Chapter 4
Experimental testing of magnetostrictive LOS stabilization system

4.1 Background

Experimental testing of the magnetostrictive LOS stabilization system is described in this chapter. The tests are motivated and the goals of the tests are spelt out. Performance, mass and dimensional parameters of the test samples, i.e. the two actuators, optical instument and its support structure, are given. These parameters are used to prescribe the test equipment and to design the test signals. The test setups and equipment are described. The tests are designed and carried out. Processing of the results is done. The results are presented, discussed and compared with the modelled results obtained in chapter 2.

Experimental tests are carried out for the following reasons: The test results will firstly indicate whether the degree of complexity of the model developed in chapter 2, was sufficient. In the second place, a measure of accuracy of the modelled Terfenol-D material and system characteristics will be provided. Thirdly, experimentally determined characteristics will be required in chapter 5 to update and improve model accuracy. The fourth and most important reason, is that an experimentally verified model will be required in chapter 6 to design a controller.

Two types of tests, i.e. quasi-static and dynamic tests, are carried out. A quasi-static test is done on each actuator in order to determine its stroke length and the ratio between its output displacement and input voltage. The voltage where this ratio is a maximum, is used as the bias voltage for the dynamic tests. Dynamic tests are carried out on the system to obtain the transfer function between coil input voltage and instrument angular acceleration. From this *TF*, other important system characteristics, such as resonance and antiresonance frequencies, are obtained.

The experimental tests are systematically covered in the following sections. The test specimens, i.e. the two actuators, optical instrument and its support structure, are discussed in short in section 4.2. The test setup and equipment are described in section 4.3, followed by the test design and test procedure in section 4.4. Section 4.5 covers the test results. Processing of the test data is described in section 4.5.1. *TF* spectra are calculated and shown in section 4.5.2. A discussion of the dynamic test results is given in section 4.5.3. The experimental and modelled results are compared, reasons for the differences are discussed and the need for an updated model is given in section 4.5.4. A summary of chapter 4 and a preview of chapter 5 are given in section 4.6.

4.2 Technical details of the test specimens

Technical details of the test specimens are given in this section. The details are required for two purposes. Firstly, the performance requirements of the test equipment, such as signal generator frequency bandwidth, measurement ranges of the displacement transducer and accelerometers, and power output of the amplifier, must be determined. Secondly, the technical details will serve as design inputs for the quasi-static and dynamic test signals.

For the purpose of this study, three specimens are considered, i.e. the two actuators, which will be individually tested quasi-statically, and the entire system, which will be tested dynamically. All the appropriate specimen parameters are tabled and dimensions are shown schematically.

The dimensional parameters are the length, width and height of the test specimens. The performance characteristics are: Actuator stroke length, maximum *translational* acceleration at each end of the optical instrument, frequency bandwidth and coil resistance, voltage, current and power. Note that the *translational* acceleration at the ends of the optical instrument is given, rather than the *angular* acceleration. The reasons are twofold. In the first place, it is easier to measure translational acceleration and to divide it by the instrument length in order to obtain its angular acceleration, than to directly measure angular acceleration. Secondly, this method of measurement will facilitate a direct comparison with the modelled characteristics obtained in section 2.8 and to update the model, as will be discussed in chapter 5.

Actuator and system dimensions are obtained from sections 3.5 and 3.6, while the performance parameters are obtained from sections 2.7, 2.8 and 3.2. Figures 4.2.1 and 4.2.2 respectively show the dimensions of the actuators and LOS stabilization system. The technical and performance parameters are summarized in table 4.2.1.

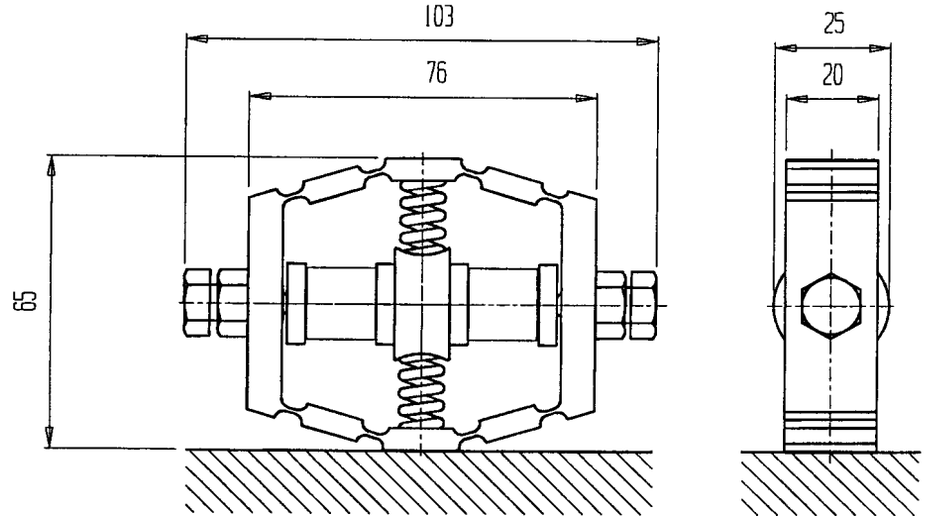

Figure 4.2.1: Terfenol-D actuator dimensions

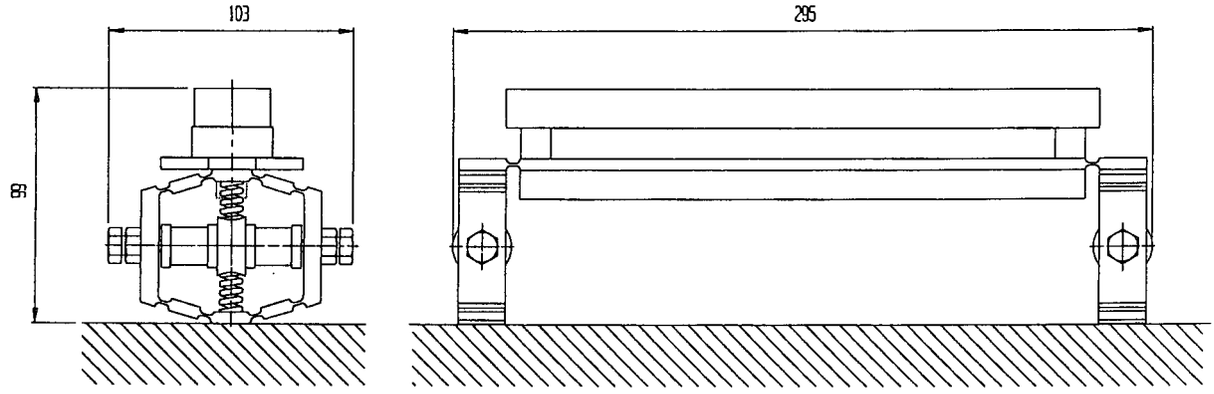

Figure 4.2.2: LOS stabilization system dimensions

Table 4.2.1: Actuator and system test parameters

Parameter	Value
System length	0,295 m
System width	0,103 m
System height	0,099 m
Actuator length	0,103 m
Actuator width	0,025 m
Actuator height	0,065 m
Actuator stroke length	75.10^{-6} m
Translational acceleration at actuator	4,26 m/s^2
Coil static resistance per actuator	3,2 Ω
Coil voltage input per actuator	17,5 V (p-p)
Coil current per actuator	5,47 A (p-p)
Coil power per actuator	98,7 W

One performance parameter that is not shown in the table, is the system frequency bandwidth (333 Hz). The reason is that this bandwidth is considerably higher than the disturbance bandwidth of 2,5 Hz to 100 Hz. The latter bandwidth, instead of the former, will be used to design the dynamic test signals.

The parameters given in this section, will be used to in section 4.3 to determine the technical requirements of the test equipment and to design the quasi-static and dynamic test signals in section 4.4.

4.3 Test setups and equipment

The test setups and equipment are described in this section. The equipment consists of a personal computer, digital signal processing equipment, test bench, sensors, signal analyzer and power amplifiers. The test bench provides a base for attachment of the LOS stabilization system and sensors. A personal computer (PC) is used to generate the test input signals in digital form. The PC contains a digital signal processing (DSP) card, which converts the signals to analogue form. A power amplifier is used to drive the actuator coils.

Two types of sensors are used to measure the outputs, i.e. displacement transducers, to measure actuator and system quasi-static displacements, and accelerometers, to measure base and system accelerations. A voltage divider is used to facilitate measurement of the input signal. A signal analyzer captures the coil input voltage and sensor output signals. The PC is used for post-processing of the test results.

The test setups are described in section 4.3.1, followed by a discussion on the signal generation equipment in section 4.3.2. The sensors, signal acquisition and processing equipment are discussed in section 4.3.3.

4.3.1 Test setups

Test setups for the quasi-static and dynamic tests are shown and discussed in this section. Two dynamic test setups are considered, i.e. an ideal setup and an available setup. The ideal setup makes simultaneous characterization of the system possible for all the known inputs. However, this setup is not feasible, since all the required equipment is not available. An alternative setup, which makes use of available equipment, is used instead. The limitations of this setup are mentioned and discussed.

The actuator quasi-static test setup is shown in figure 4.3.1.1. The actuator is attached to a fixed base. The input signal is coil voltage (V) and the output signal is actuator displacement. An inductive (eddy current) displacement transducer, mounted on a fixed base, is used for measuring actuator displacement.

The reason for attaching the actuators to a fixed base is that the quasi-static tests are mainly done to determine the most suitable coil bias voltages to be used in the dynamic tests. The effect of base motion is not of importance for this purpose.

The dynamic test setup is designed to facilitate controller design and testing in chapter 6. The controlled system will be excited by two inputs, i.e. the coil voltage (controllable input) and the base acceleration (uncontrollable input or disturbance). The controllable input must be commanded in such a way that its behaviour will cancel the uncontrollable input behaviour. In order to determine the latter behaviour, the system is attached to an elastically-mounted base, connected to an external shaker. The shaker will be used in chapter 6 to excite the base.

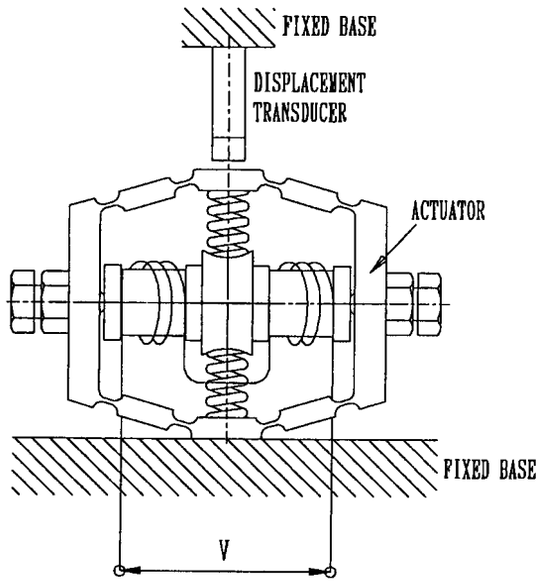

Figure 4.3.1.1: Actuator quasi-static test setup

An ideal dynamic test setup is shown in figure 4.3.1.2. Each actuator is attached to a moving base, in the form of a rigid beam. Each base is suspended by a spring, guided by a linear bearing and connected to an electrodynamic shaker by means of a string (also known as a stinger). The two actuator coils are excited 180 °out-of-phase to excite angular motion of the optical instrument. Accelerometers are mounted at each end of the optical instrument and on each moving base (i.e. four accelerometers in total). The advantage of this test setup is that it makes simultaneous measurement of all the *TF*'s of the system possible, provided the test equipment is available.

However, the equipment required for the above setup, is not available. Available equipment is limited to the following: The test bench contains only one moving base and only one shaker is available. Furthermore, the signal analyzer used to capture measured data has only two analogue input channels, therefore only one coil voltage and one acceleration can be measured during a test.

It is therefore necessary to simplify the setup by making use of available equipment. Such a setup is shown in figure 4.3.1.3. Actuator 1 is attached to a fixed base, while actuator 2 is attached to an elastically-mounted base. The coil of actuator 2 is excited by a voltage signal, while that of actuator 1 has an open circuit. The coil voltage signal and one accelerometer signal are measured during a test. The test is conducted as many times as the number of accelerometers.

The advantage of this setup is its simplicity in comparison with the ideal setup. The disadvantage is that separate tests must be done to obtain the various *TF*'s of the system. With this setup, tests will necessarily take longer to conduct than with the ideal setup. This setup will however be used, due to the problem with availability of test equipment.

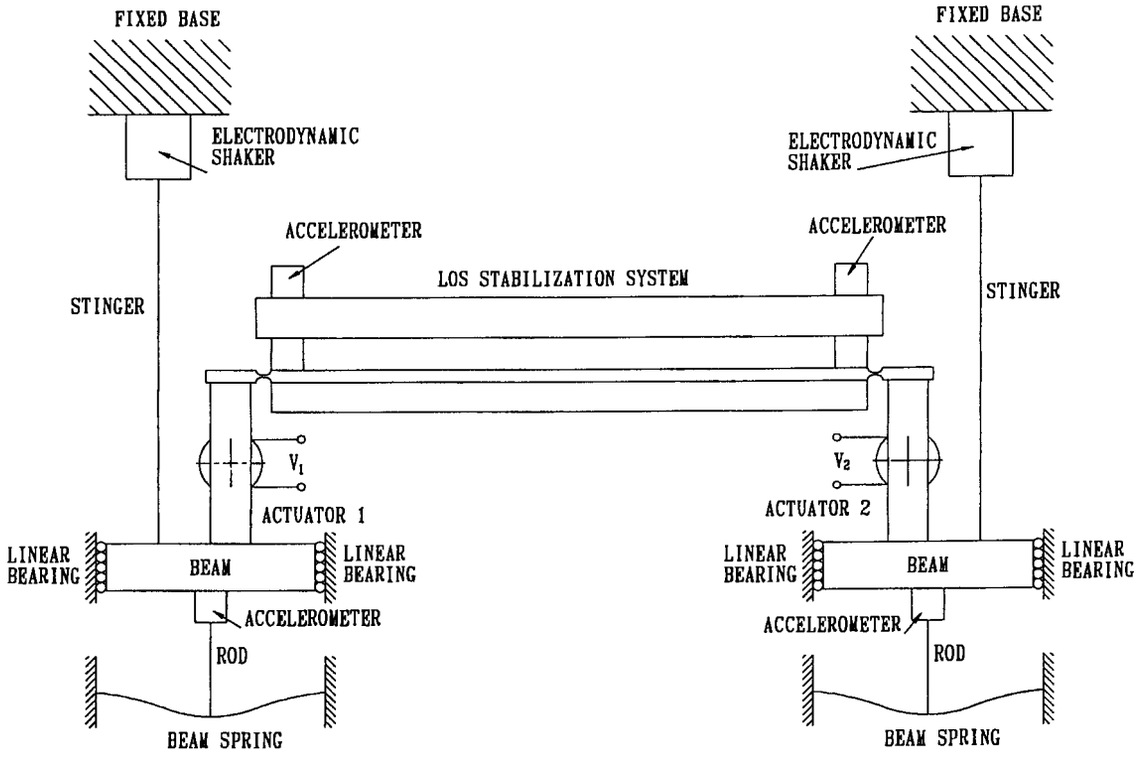

Figure 4.3.1.2: Ideal dynamic test setup

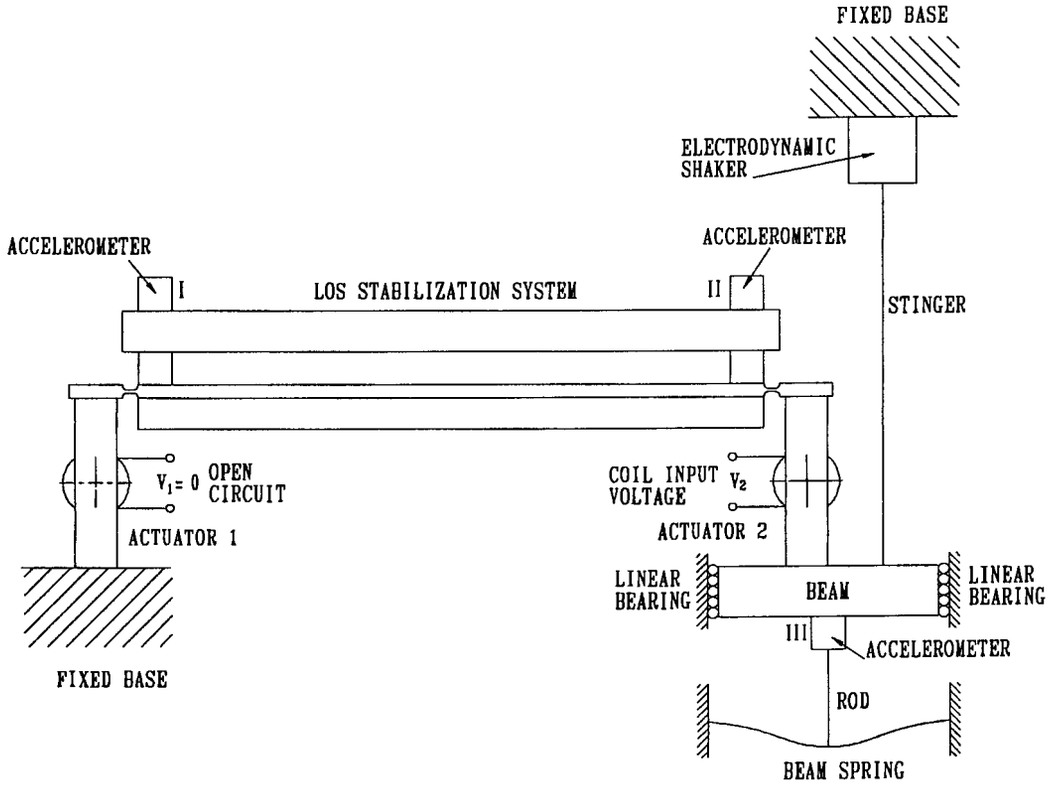

Figure 4.3.1.3: Available dynamic test setup

The system is excited by applying a voltage signal to the coil of actuator 2. The voltage and accelerometer signals are captured and processed to obtain system *TF*'s. The signal generation equipment is discussed in the next section.

4.3.2 Signal generation equipment

The test signal generation equipment is shown schematically in figure 4.3.2.1. The signals are generated in Simulink, which is a Matlab real-time simulation environment. Using Simulink, the following basic time-domain input signals can be generated: Constant, step, delayed step, sine, sine sweep, square wave, sawtooth, random and band-limited white-noise.

Arbitrary signals can be obtained in a number of ways. The signals can either be imported from Matlab or from external files. Alternatively, the abovementioned basic signals can be combined to build the required signal. For instance, a signal can be added to, subtracted from, multiplied with, or multiplexed with another signal. Furthermore, a signal can, inter alia, be clipped, rate-limited, integrated, differentiated, filtered and resampled.

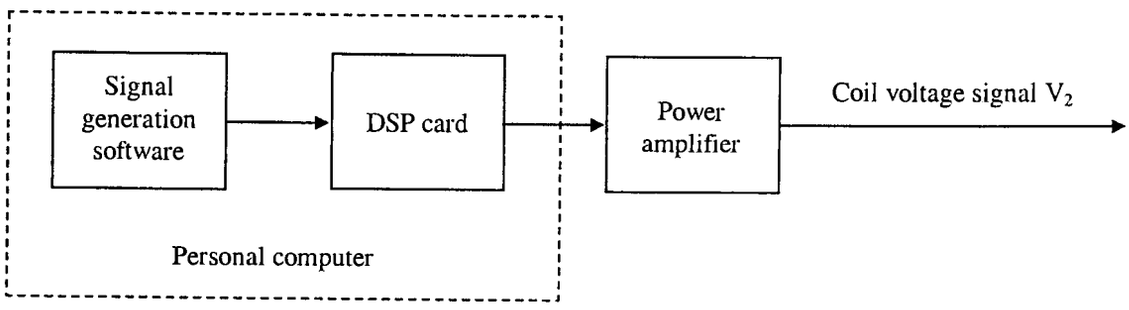

Figure 4.3.2.1: Test signal generation equipment

A signal can be generated and viewed in real time. For this purpose, algorithms such as the linear, Euler, Heun, 3rd order Runge-Kutta, 5th order Runge-Kutta, Adams, Gear and Adams/Gear algorithms are supplied. Sample frequencies can be arbitrarily selected and adaptive time-stepping is possible.

Digital signal processing card

The DSP card is a floating point card manufactured by dSpace. It is provided with a built-in processor, the clock of which runs at 40 MHz. The card has the facility to directly code a Simulink-generated signal in the C-programming language, as well as to compile the signal to an object file.

Execution speed of the compiled signal is determined by the clock speed of the card only, and not by that of the PC's central processing unit. Adaptive time-stepping is not available for

coding. Sampling frequency is strongly dependent on the number of operations executed per time step.

The card gain, i.e. the ratio between the amplitude of the simulated signal and that of the card output signal, is 10. The card has four digital-to-analogue (D/A) channels and four analogue-to-digital (A/D) channels.

Power amplifier

An MB Dynamics SS 250 power amplifier is available for the tests. The amplifier is matched to an electrodynamic shaker normally used for modal testing of structures. Amplifier frequency bandwidth, according to the manufacturer, is 0 Hz to 30 kHz. Output power is controlled by a rheostat. Maximum power output is 750 W and automatic clipping takes place in case of overloading. For the purpose of this study, a bandwidth of 100 Hz and a power output of 98,7 W are required.

An important amplifier characteristic applicable to this study is its input to output transfer function. Since the amplifier will be used to power the actuator coils during control, a minimum phase shift of the commanded signal will be required. To determine the phase shift, *TF*'s were measured for random input signals with three different power levels. The signals were low-pass filtered at 100 Hz. Power levels were -8,94 dB, -10,88 dB and -13,21 dB, relative to maximum power output. A sample frequency of 1280 Hz was used. Measured *TF* spectra are shown in figure 4.3.2.2. The maximum phase shift at 100 Hz is 0,14°, which can be considered negligible for all practical purposes.

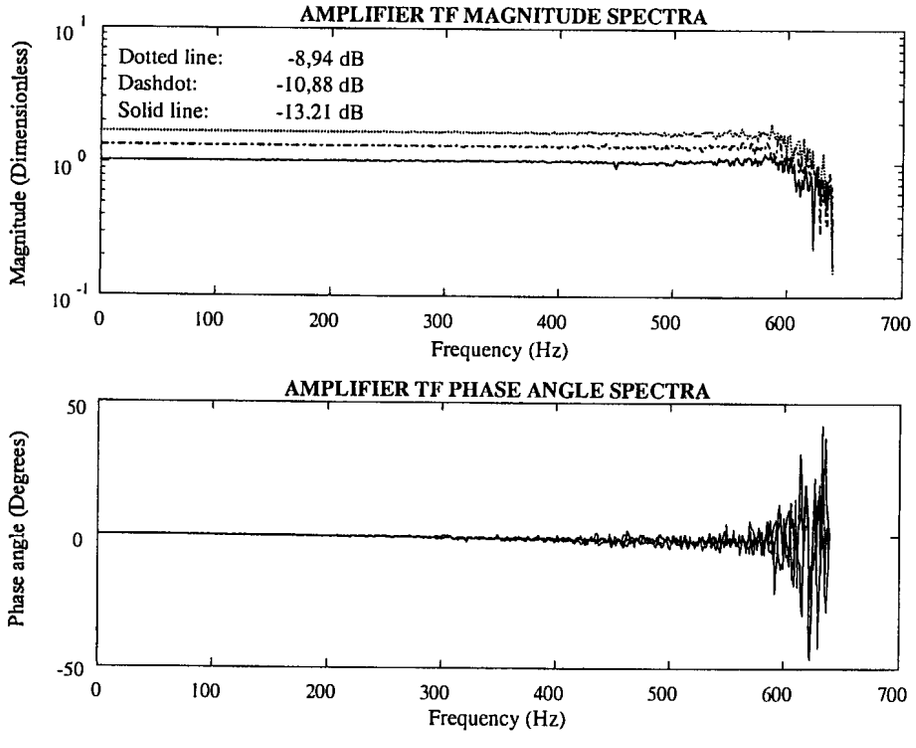

Figure 4.3.2.2: Amplifier transfer function spectra for three power output levels

4.3.3 Signal measuring, acquisition and analyzing equipment

The sensors, sensor amplifiers and signal analyzer are described in this section. A schematic layout of the equipment is shown. Sensor types and manufacturers, calibration factors, ranges and amplifier gains are given. The displacement transducer is described first, followed by the accelerometers and signal analyzer.

A schematic layout of the signal measurement, acquisition and analyzing equipment is shown in figure 4.3.3.1. The type of sensor used depends on the type of test: A displacement transducer is used for the quasi-static tests, while accelerometers are used for the dynamic tests. The sensor output signal is amplified in order to capture it with the signal analyzer.

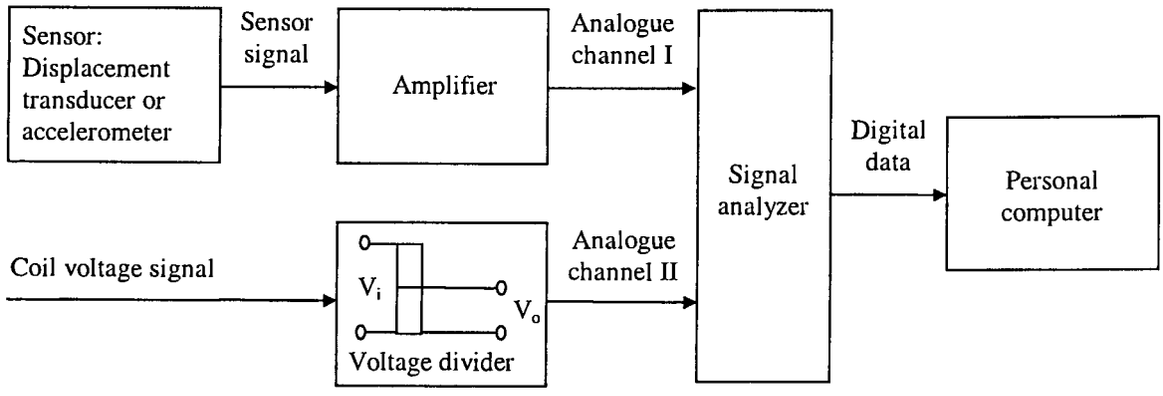

Figure 4.3.3.1: Signal measurement, acquisition and analyzing equipment layout

The signal analyzer has two analogue input channels. The two channels are respectively used for capturing the sensor output and coil input voltage signals. The amplitude of the latter signal (17,5 V as simulated- see sections 2.7 and 2.8) exceeds the input range of the analyzer (± 10 V) and is therefore reduced to a measurable level by means of a voltage divider. The divider gain is 0,25.

Captured data can be processed in real-time, using the analyzer, or can be off-loaded to the computer for post-processing. The latter option is preferred, since the available analyzer can only process two signal characteristics at a time. If, for instance, the *TF* between two signals is required in magnitude and phase format, other characteristics, such as time traces, PSD's, CSD's and coherence spectra, cannot be obtained during the same test. In order to obtain these characteristics, the tests must be repeated.

Computer post-processing, on the other hand, can be relatively easily done using signal processing software. Overlaps can be adjusted and frequency resolution can be changed without repeating the tests. In this study, the signal analyzer is only used to capture and view the data, whereafter the signal processing is done on the computer.

Displacement transducer

An inductive (eddy current) transducer, manufactured by SKF, is used for the displacement measurements. The transducer measures the distance between its tip and a magnetic material placed close to its tip. A gap is normally left between the transducer and the actuator to protect the transducer tip from damage. Due to this gap, the measured output has a DC offset, which has to be subtracted from the measured output to obtain actuator displacement. The transducer output is in volts and its calibration factor is 125 μm/V. A 24V DC driver, type CMSS665, by the same manufacturer, powers the transducer.

Accelerometers

Two accelerometers, manufactured by Setra, are available for the characterization tests. Accelerometer ranges are 15 g and 30 g respectively. Nominal natural frequencies, as claimed by the manufacturer, are 800 Hz for the 15 g accelerometer and 1150 Hz for the 30 g accelerometer. Claimed ± 3 dB flat response ranges are 0 Hz to 400 Hz and 0 Hz to 700 Hz for the 15 g and 30 g accelerometers respectively. The lower cutoff frequencies were checked and found to be 5 Hz, instead of 0 Hz, for both accelerometers. The accelerometers do however respond below 5 Hz, but response is outside the ± 3 dB range. Experimentally determined calibration factors of the two accelerometers are 29,32 mV/g for the 15 g accelerometer and 46 mV/g for the 30 g accelerometer.

Signal analyzer

A Diagnostic Instruments type PL 202 signal analyzer is used for data acquisition purposes. The analyzer has two analogue input channels. The maximum signal input range is ± 10 V per channel. Any input outside this range is clipped. Single-capture or continuous acquisition is possible.

Frequency bandwidth ranges from 25 Hz to 40 kHz. Acquisition time ranges from 2,5 ms to 64 s, depending on the bandwidth and number of data points. The latter is adjustable from 256 to 4096 in fixed steps. A manually selectable anti-alias filter is provided.

The following signal characteristics can be obtained in real time: Frequency spectrum, PSD, time trace, difference between time traces of the two measured signals, FRF, coherence, octave bands and 1/3 octave bands. Real-time averaging of data, including RMS calculation, is possible. Four window types are provided, i.e. exponential (for pulse-type inputs), Hanning, flat top and rectangular.

Automatic or manual screen ranging can be selected. The latter is logarithmically adjustable in fixed steps from 10 mV to 10 V. Axis display formats include real and imaginary, logarithmic, linear magnitude, logarithmic magnitude and phase.

Captured data can be stored in files. The files can be recalled, reviewed, erased, copied and off-loaded, for instance to a personal computer, through a standard RS 232 port. Software for data off-loading is provided by the manufacturer.

4.4 Test design and procedure

The quasi-static and dynamic test design and procedures are described in this section. Quasi-static test signal generation is discussed in section 4.4.1, followed by a description of the quasi-static test execution in section 4.4.2. In section 4.4.3, quasi-static test data processing is described and the test results are shown and discussed. The most suitable coil bias voltage for the dynamic tests is calculated in section 4.4.4. Dynamic test signal selection, design and generation are described in section 4.4.5, followed by a description of the dynamic test execution in section 4.4.6.

4.4.1 Quasi-static test signal generation

Truncated ramp voltage signals are used as inputs for the quasi-static tests. The desired signal characteristics are: A low rate-of-rise to prevent the excitation of dynamic behaviour such as overshoot, sufficient amplitude to excite the actuator over its entire voltage and displacement ranges, and a relatively short time duration to minimize the risk of coil overheating.

The maximum voltage applied to the coil depends on the coil resistance and amplifier output power. For an amplifier power of 400 W (approximately 53% of full amplifier power, see section 4.2) and static coil resistance of 3,2 Ω (see section 3.5.2), a voltage of 36 V is achievable. To prevent coil overheating, the signal time duration is limited to 4 s. The rate-of-rise of the ramp is 250 V/s.

The signal generation block diagram is shown in figure 4.4.1.1. The signal is generated in Simulink, using the available input functions. The truncated ramp input is constructed from two rate-limited step inputs. The first step, with a height of H, is applied at time t = 0. The ramp is terminated by adding a delayed, rate-limited step with height -H, to the first step. The resulting signal is shown in figure 4.4.1.1.

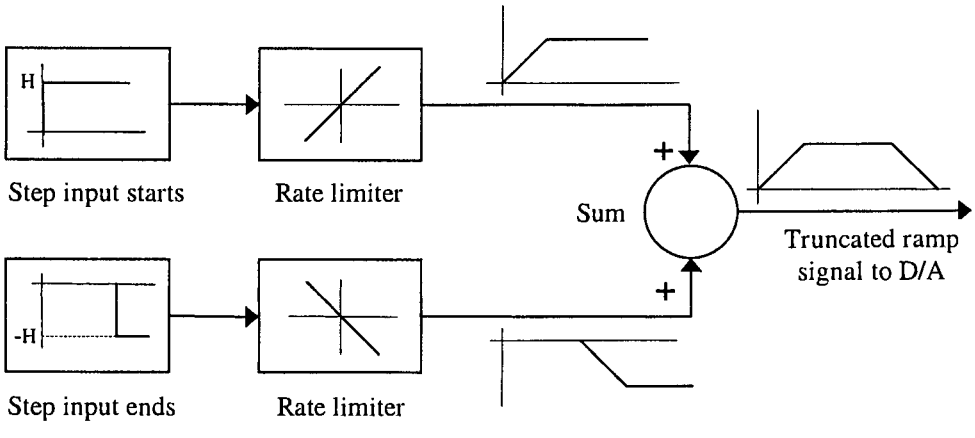

Figure 4.4.1.1: Block diagram for quasi-static signal generation

Analogue-to-digital conversion of the signal is done by means of the DSP card. The card has a gain of 10 and its maximum output voltage is 10 V (see section 4.3.2). The card characteristics must be compensated for in the Simulink model. Failure to do so may lead to

clipping of the signal. To prevent this, the height H and rate-of-rise of the signal are respectively adjusted to 0,96 V and 6,7 V/s. The signal is coded in the C-programming language, compiled to an object file and viewed on the analyzer display screen.

4.4.2: Quasi-static test execution

The two actuators are tested separately. The test procedure is as follows. A voltage divider with a gain of 0,25 is connected in parallel with the coil in order to facilitate input voltage measurement. The displacement transducer is attached on a fixed base above the actuator, as shown in figure 4.3.1.1. A gap is left between the actuator and the transducer tip. The transducer is connected to its driver. The DSP card output is connected to the input of the power amplifier, whose output is connected to the actuator coil (see figure 4.3.2.1). The amplifier gain is adjusted to give the required coil voltage.

The test signal is applied to the actuator coil. The voltage across the divider and the transducer output voltage, are measured and captured using the signal analyzer. Captured data is transferred to a personal computer for processing. The input and output signals are multiplied with their respective calibration and gain factors. (The transducer calibration factor is 125 μm/V - see section 4.3.3, while the coil voltage gain is the inverse of the divider gain, i.e. 4 V/V). It is important to note that the actuator will give a negative displacement for a positive coil voltage. This is due to the geometry of the octagonal displacement gain mechanism (see figure 3.4.1.5) The actuator output signal is therefore multiplied with an additional gain factor of –1.

Output displacement versus input voltage curves of the two actuators are plotted. The characteristics of the two actuators are compared. If the characteristics display unduly large differences, adjustments are made to the actuators and the tests are repeated.

A possible cause for differences between the actuator characteristics is Terfenol-D rod prestress. Prestress can be easily adjusted, either by changing the torque in the prestress bolts, or by replacing the prestress springs. However, measuring rod prestress is not as simple. Due to space limitations, measuring equipment, such as load cells and strain gauges, cannot be placed inside the actuators. Rod prestress is therefore adjusted iteratively. The characteristic of the actuator with the highest output displacement is used as reference. The rod prestress of the other actuator is adjusted and the test is repeated. The characteristics are compared again and the process is repeated until sufficient correspondence between the characteristics is obtained. The test results are displayed and discussed in section 4.4.3.

4.4.3 Quasi-static test results and discussion of results

Output displacement versus input voltage characteristics of the two actuators are shown in figure 4.4.3.1. Voltage and displacement ranges are 40 V and 120 μm respectively. The loading and unloading curves are indicated, together with the required actuator stroke length of 75 μm.

The maximum output displacements, for a 36 V coil input, are 110 μm for actuator I and 113 μm for actuator II. The percentage difference between the maximum output displacements, relative to that of actuator I, is 2,7%. From the loading curves, it can be seen that the required stroke lengths of actuators I and II are produced with input voltages of 13,2 V and 12,3 V respectively.

The linear and saturation ranges are not clearly demarcated. In section 2.2, it was mentioned that subjective judgment is required to determine the transition point between the ranges. From figure 4.4.3.1, it can be judged that the linear ranges of the two actuators end at the required stroke length of 75 μm.

A dead zone of 2,5 V appears in each loading curve. During loading from a state of 0 V and 0 μm displacement, displacement initially remains at 0 μm, but increases as soon as the voltage reaches 2,5 V. The dead zone is a result of magnetostrictive hysteresis, which was discussed in more detail in section 2.3. In short, the closer the spacing between the loading and unloading curves, the less significant the effects of hysteresis. From figure 4.4.3.1, it can be seen that, at lower voltages, spacing between the curves is wider than at higher voltages.

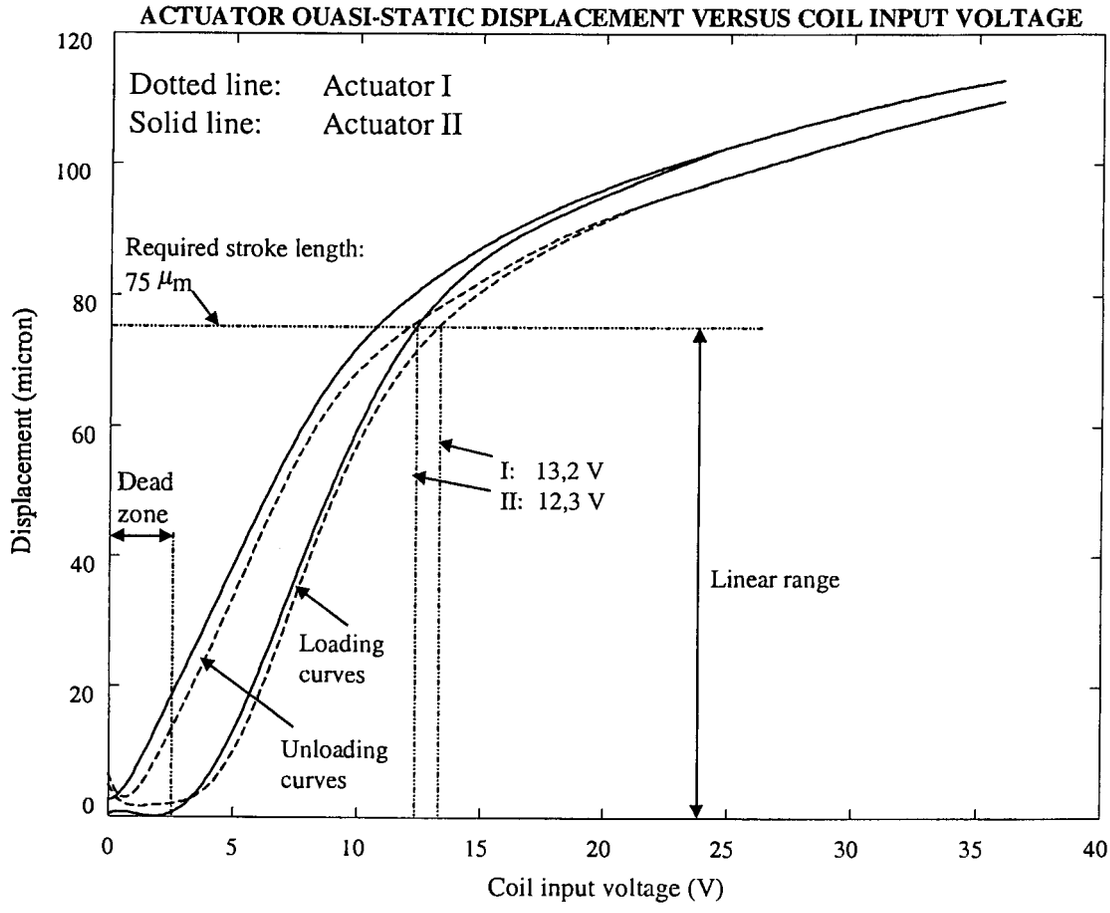

Figure 4.4.3.1: Actuator quasi-static displacement versus coil input voltage

The differences between the characteristics of the two actuators remain, even after adjustment of the rod prestress, using the iterative method described above. The following reasons can be given for the differences: Firstly, during actuator assembly, fitting the prestress springs may have caused slight twisting of the flexures. The flexures are relatively soft and can be easily damaged.

Secondly, the magnetostrictive characteristics of the rods may differ slightly. The rod manufacturer, Etrema, does however include a measured quasi-static (strain versus field) characteristic with each rod upon delivery. Differences in rod characteristics are therefore known before actuator assembly.

The quasi-static characteristics shown in figure 4.4.3.1 are not expressed in terms of rod strain and induced magnetic field. The reason is that, for the purpose of analyzing actuator and system performance, parameters such as output displacement, stroke length and input voltage, are more important. These parameters are also directly measurable.

However, in the interest of facilitating future designs and for updating the model, it is necessary to determine the rod strain. If gain mechanism stiffness and passive rod length are neglected and equal strains in the two rods are assumed, the maximum strain achieved with actuator II, is 1100 $\mu\varepsilon$. If passive rod length and gain mechanism stiffness (3,28 MN/m – as calculated by means of the FE method in section 3.5.1) are included, the maximum strain in the rods of actuator II is 1410 $\mu\varepsilon$. The maximum linear strain, which occurs at a stroke length of 75 μm, is 944 $\mu\varepsilon$ (see also section 3.5.1).

From the quasi-static test results, the most suitable bias voltage for the dynamic tests is determined. This is done in section 4.4.4.

4.4.4 Calculation of bias voltage for dynamic tests

The following procedure is followed to calculate the bias voltage. The first step is to obtain the dehysterized displacement versus coil voltage characteristic for each actuator. The dehysterized characteristic is the average of the loading and unloading curves (this definition was adopted in section 2.3, where the hysteresis effect on the strain versus field characteristics was studied):

$$x_{dehysterized}(V) = \frac{1}{2}\left\{x_{loading}(V) + x_{unloading}(V)\right\} \qquad \textbf{(4.4.4.1)}$$

where V is coil input voltage and x is output displacement.

Equation 4.4.4.1 is differentiated numerically with respect to coil voltage to obtain the displacement derivatives, or gradients, of the dehysterized characteristics. The curves of displacement derivative versus coil voltage of the two actuators are shown in figure 4.4.4.1.

It can be seen from figure 4.4.4.1 that the *shapes* of the displacement derivative curves resemble those of the modelled dehysterized strain constant curve (see figure 2.2.1.5). For low coil voltages, the gradients are low. The gradients increase with an increase in voltage

and reach a peak. The maximum displacement gradient of actuator I is 9,3 μm/V at 6,7 V, while that of actuator II is 8,8 μm/V at 6,4 V. For further increases in coil voltage, the gradients decay to zero in the saturation region.

Theoretically, the voltage where the gradient peaks, can be selected as the bias voltage. For this bias voltage, coil voltage will range from 0 V to approximately twice the bias voltage. (Actuator I, for example, produces a stroke length of 75 μm at 13,2 V, while the theoretical bias voltage is 6,7 V). However, it is undesirable to extend the voltage range below 2,5 V, since hysteresis losses are more significant at lower voltages (see discussion in section 4.4.3).

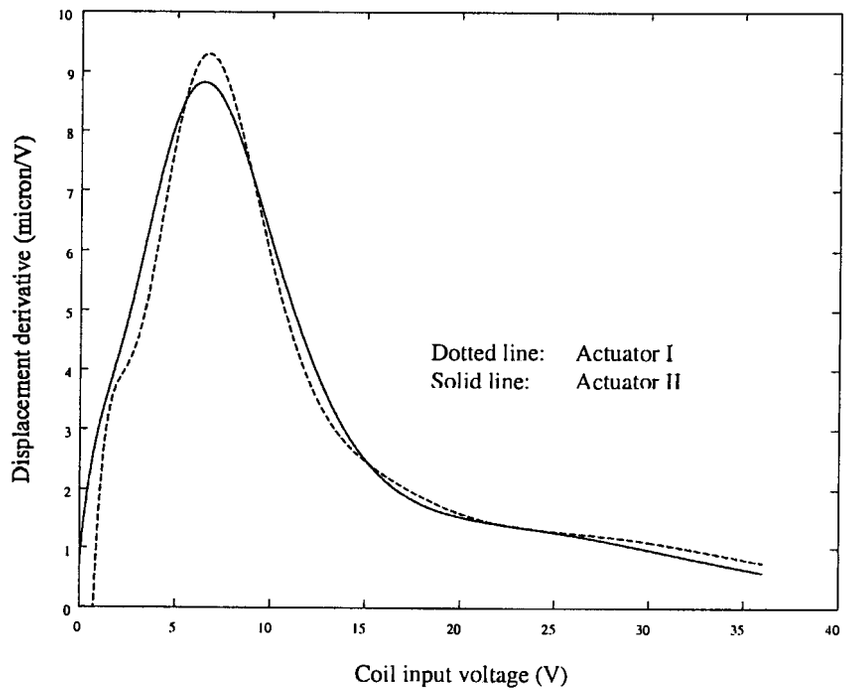

Figure 4.4.4.1: Displacement derivatives versus coil voltage of the two actuators

In order to limit hysteresis losses, it is necessary to increase the coil voltages. The required increase is unknown at this stage. The coil voltages are therefore arbitrarily raised by 2,5 V (the dead zone voltage), resulting in bias voltages of 9,1 V and 8,75 V for actuators I and II respectively. These voltages respectively differ by only 3,4% and 0,5% from the design bias voltage of 8,8 V (see table 3.5.2.3).

The disadvantage of increasing the coil voltage is that the maximum voltage is moved into the saturation region. The maximum voltage of actuator I, for instance, will be 15,7 V, an increase of approximately 20%. The problem can, to a large extent, be solved with permanent magnet biasing.

4.4.5 Dynamic test signal selection, design and generation

The selection, design and generation of the dynamic test signals are described in this section. A number of signal types are considered and a suitable test signal type is selected. Signal parameters, such as duration, amplitude and bandwidth are determined and tabulated. A block diagram for dynamic signal generation is shown.

Dynamic test signal types and selection of the most suitable signal type

Signal types to be considered for dynamic characterization purposes, are steady-state harmonic, stepped-sine, sine-sweep, wide-band random (white noise) and transient type signals. A short description of each input signal type, from Ewins [1991], is given below. The application, advantages and disadvantages of each signal type are discussed in short. The most suitable dynamic test signal type is selected.

Steady-state harmonic inputs are mainly applied to obtain the *TF* magnitude and phase of a system at a single frequency. If the *TF*'s are required at more than one frequency, a characterization test must be carried out at each frequency of interest. Wide-band, high-resolution characterization of systems using harmonic inputs is therefore not recommended.

Stepped-sine inputs can be used for system characterization over a limited bandwidth. A harmonic input is applied, preferably at the lowest or highest frequency in the band. The frequency is fixed for a sufficiently long period to ensure that steady-state conditions are attained before measurements are made. The frequency is adjusted stepwise and the procedure is repeated. The test is stopped when measurements have been made at all the frequencies in the band. Input amplitude is held constant with time.

Sine sweep inputs are in a sense similar to stepped-sine inputs, but the frequency is varied continuously, instead of stepwise. A harmonic input is applied at the lowest or highest frequency in the band. The frequency is varied slowly to ensure that steady-state conditions are attained before making measurements. Frequency can be varied linearly or logarithmically with time. Input amplitude is held constant with time. Sine sweep tests are not recommended for combinations of short test times, wide frequency bands and high resolutions. Under these circumstances, steady-state conditions are difficult to attain.

Random inputs are often used for wide-band characterization of systems. A special type of random input is the so-called "white noise" signal, with an approximately constant amplitude spectrum and a random phase. During testing, the signal time trace is recorded in samples of equal duration. The amplitude spectra of the individual samples are averaged. Sequential or overlap averaging can be performed. For a given bandwidth, data reliability is improved with an increase in sample duration and number of samples.

Data reliability is indicated by the "statistical degrees of freedom" κ, given by the following equation:

$$\kappa = 2mT\ BW \qquad \textbf{(4.4.5.1)}$$

where m is the number of samples, T is the sample duration and BW is the frequency bandwidth. The higher κ, the more reliable the data. As an example, Ewins [1991] recommends a κ-value of 10 for an 80% probability that the estimated spectrum is within 50% of the true spectrum at any given frequency. For an 80% probalility that the estimated spectrum is within 18% of the true spectrum, κ should approach 100.

Transient inputs are mainly applied to obtain the pulse- or impact behaviour of a system. Input time duration is relatively short in comparison with the lowest natural period of the system. The input amplitude spectrum normally decays exponentially with frequency. This type of test is not suitable for wide-band characterization where constant amplitudes are required over the frequency spectrum.

In this study, wide band random inputs are used for dynamic system characterization. Harmonic excitation is ruled out because the disturbance frequency band is too wide to conduct a test at each frequency (0 to 100 Hz, with a resolution of 1/3 Hz). Stepped-sine and sine-sweep inputs are undesirable, since steady-state conditions will be difficult to attain in a short test time. Lastly, transient tests will give unwanted exponentially decaying amplitude spectra.

Dynamic test input signal design

The dynamic test input signal parameters are bias voltage, voltage amplitude, voltage RMS-to-peak ratio, frequency bandwidth, time duration and sample frequency. The peak-to-peak voltages, for a quasi-static stroke length of 75 μm, are 13,2 V for actuator I and 12,3 V for actuator II. The amplitude is 50% of the peak-to-peak voltage, i.e. 6,6 V for actuator I and 6,25 V for actuator II. The bias voltages are 9,1 V for actuator I and 8,75 V for actuator II.

It was mentioned in section 4.3 that, due to a problem with availability of test equipment, it is possible to excite the coil of one actuator only. In the interest of safety, the bias voltage and voltage amplitude are selected to correspond with those of the actuator with the maximum peak-to-peak voltage, i.e. 9,1 V and 6,6 V respectively. The corresponding minimum and maximum voltages are 2,5 V and 15,7 V respectively.

Test signal bandwidth is mainly determined by the disturbance bandwidth. As was motivated in the previous section, a wide-band, white noise, random signal is used for system characterization. However, this signal contains frequencies well above the disturbance bandwidth. The signal must therefore be low-pass filtered above 100 Hz. In order to prevent filter interference in the disturbance band, the signal is filtered at a 30% higher frequency, i.e. at 130 Hz. A 4^{th} order filter is used for this purpose. High-pass filtering of the signal is not desirable, since the signal must be DC-biased. Test signal bandwidth is therefore 0 Hz to 130 Hz.

As an unwritten rule, sampling frequency should be in the order of five to ten times the maximum disturbance frequency, i.e. 500 Hz to 1 kHz. The DSP card, however, allows the use of significantly higher sampling frequencies. To make full use of its performance, the test signal is sampled at 2 kHz, which is 20 times that of the maximum disturbance frequency.

The crest factor of a signal is the inverse of its RMS-to-peak ratio. The disturbance crest factor is 2,17 (see table 3.2.1), i.e. its RMS-to-peak ratio is 0,46. Using the same crest factor, the required RMS voltage of the test signal, for an amplitude of 6,6 V, is 3,03 V. The RMS-to-peak ratio of a wide-band random signal is normally in the order of 0,25. In order to obtain a 0,46 RMS-to-peak ratio, the random signal is gained to raise the peak and then clipped. Due to the high sampling rate, clipping of the signal does not occur inside the 0-100 Hz disturbance band.

The reliability of test signal data is determined by the bandwidth, number of test samples and sample duration (see equation 4.4.5.1). In this study, test signal duration is limited to 3,2 s per sample. The number of samples is arbitrarily selected as 37. The total test duration is the product of the number of samples and duration per sample, i.e. 118 s. For a bandwidth of 100 Hz, the statistical degrees of freedom κ, from equation 4.4.5.1, is 23680. This value of κ is 237 times the value of 100, as recommended by Ewins [1991], for an 80% probability that the measured value is within 18% of the true value. The dynamic test signal parameters are summarized in table 4.4.5.1.

Table 4.4.5.1: Dynamic test signal parameters

Bias voltage	9,1 V
Voltage amplitude	6,6 V
Maximum voltage	15,7 V
Minimum voltage	2,5 V
RMS voltage	3,03 V
Crest factor	2,17
Frequency bandwidth	0 Hz to 130 Hz
Sampling frequency	2 kHz
Total duration	118 s
Number of test samples	37
Duration per sample	3,2 s

Dynamic test signal generation

As with the quasi-static signals, the signals are generated in Simulink. A signal generation block diagram is shown in figure 4.4.5.1. The signals are constructed from standard Simulink input functions, i.e. step and random functions. Every time the test signal is applied, a new random signal, with the same frequency band, RMS and peak values, is generated.

Gradual application of the input signal is desirable to prevent the excitation of unwanted transients. To this end, the random signal is multiplied with a truncated ramp function. The ramp function is created from two rate-limited step functions, as described in section 4.4.1.

The signal is low-pass filtered at 130 Hz, i.e. 30% above the maximum frequency of the disturbance band. Gains and saturation elements are used to adjust the amplitude and crest factor. The bias voltage is created using the same method as in section 4.4.1 and added to the random function.

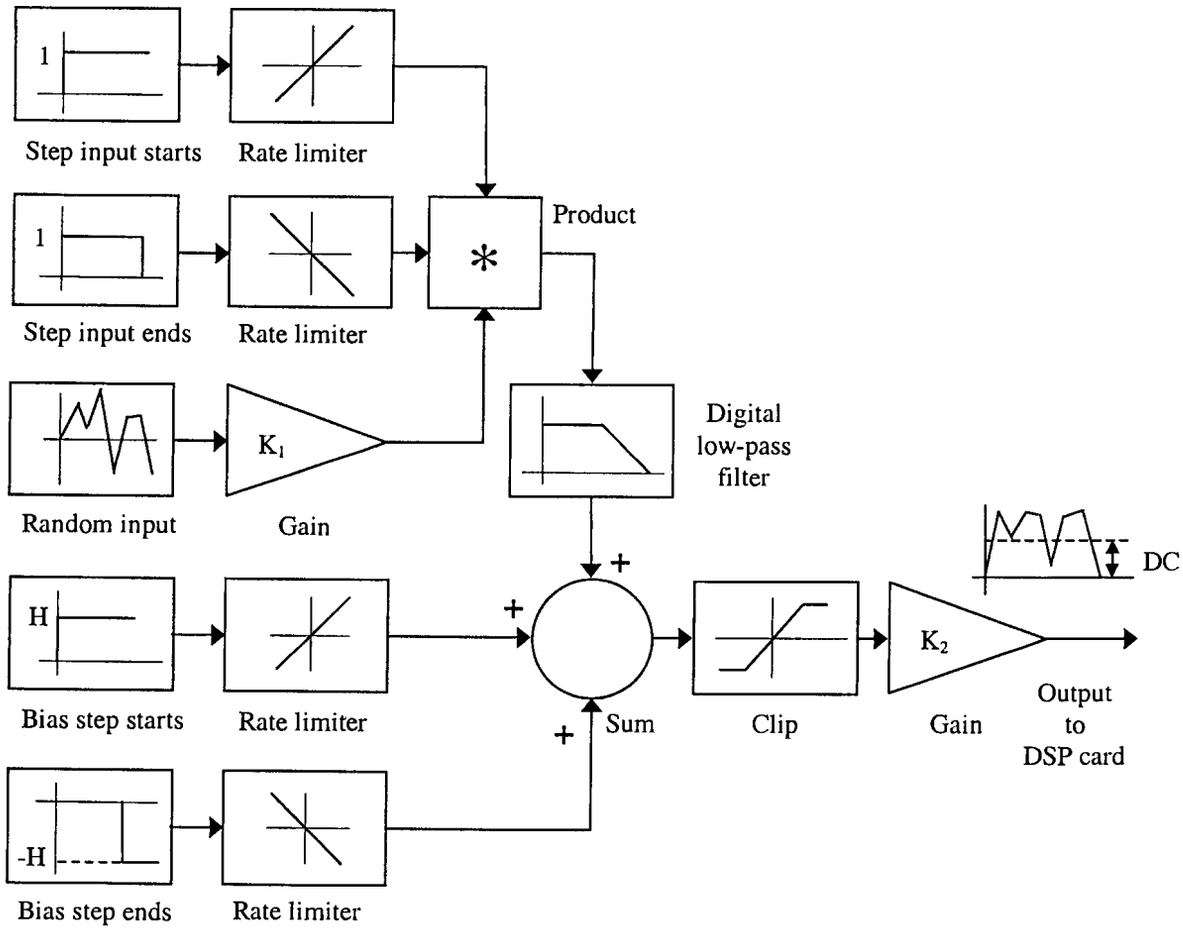

Figure 4.4.5.1: Block diagram for dynamic signal generation

The test signal is simulated and viewed using the Simulink scope. It is then divided by the DSP card gain factor (see section 4.4.1 for the procedure), coded in C and compiled to an object file. It is captured and viewed using the signal analyzer.

4.4.6 Dynamic test execution

A voltage divider with a gain of 0,25 is connected in parallel with the coil. Accelerometers are attached at the measurement positions (see figure 4.3.1.3). The DSP card output is connected to the input of the power amplifier, whose output is connected to the actuator coil. The amplifier output power is adjusted to –8,94 dB, relative to maximum power. The test signal is applied to the actuator. The coil voltage signal and one accelerometer signal are captured using the signal analyzer. A signal analyzer sampling frequency of 1280 Hz is used. This is

12,8 times the maximum frequency of the disturbance band and 8,8 times the predicted first natural frequency (see table 2.8.4.2).

A new test signal is generated and the test is repeated until all 37 tests have been completed. Total test time is 118 s. Captured data of each test is viewed on the signal analyzer screen. The data is stored in a file and transferred to the PC for processing. The tests are repeated for the other accelerometer positions. In total, 111 tests are conducted, i.e. 37 per accelerometer.

4.5 Dynamic test results

The dynamic test results are processed, presented and discussed in this section. The data processing method is explained. Transfer function magnitudes and phase spectra are calculated and shown graphically. Frequency domain characteristics, such as resonance and anti-resonance frequencies, are indicated. The dynamic test results are discussed and compared with the modelled results. It is shown that the modelled results currently compare poorly with the experimental results. Reasons for differences between experimental and modelled results are given.

Dynamic test data processing is explained in section 4.5.1. *TF* magnitude and phase angle spectra are shown in section 4.5.2. Resonance and anti-resonance frequencies are indicated. The dynamic test results are discussed in section 4.5.3. A comparison between the experimental and modelled results is drawn in section 4.5.4 and reasons for differences are given.

4.5.1 Dynamic test data processing

The data is processed in Matlab, using the signal processing toolbox. Each measured signal is multiplied with its calibration factor. The voltage signal is multiplied with the inverse of the voltage divider gain, i.e. 4 V/V. The accelerometer calibration factors are converted from mV/g to $m/s^2/V$ and multiplied with the accelerometer output signals.

The accelerations and coil input voltage are used to calculate the *TF* between coil input voltage and rotational (angular) acceleration of the instrument. The *TF* between coil input voltage and translational acceleration is also calculated. Although this *TF* does not influence LOS accuracy of the instrument, it is a valuable tool to identify the modes of excitation of the instrument. The three accelerations at the accelerometer positions, together with the rotational and translational accelerations, are shown diagrammatically in figure 4.5.1.1.

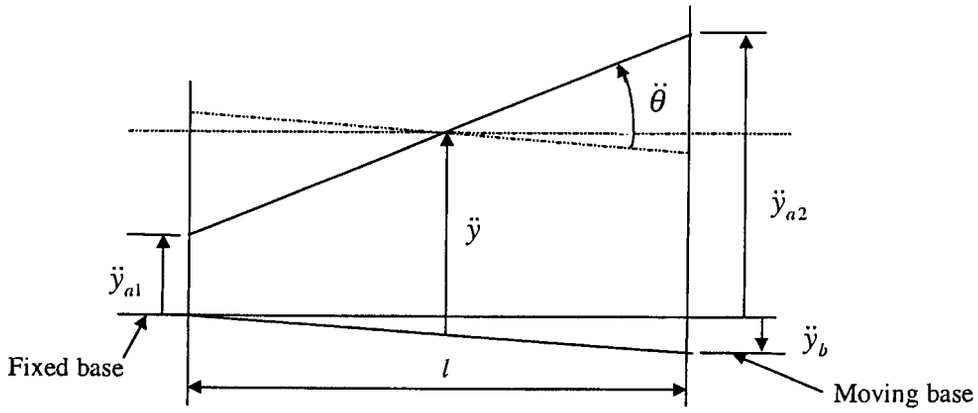

Figure 4.5.1.1: Diagram indicating measured, rotational and translational accelerations

In figure 4.5.1.1, $\ddot{y}_{a1}$ is the acceleration at accelerometer I (see figure 4.3.1.3), $\ddot{y}_{a2}$ is the acceleration at accelerometer II and $\ddot{y}_b$ is the acceleration at accelerometer III, i.e. the base acceleration. Note that $\ddot{y}_b$ is positive downward, since the accelerometer is mounted upside down under the beam. $\ddot{\theta}$ is the instrument rotational (angular) acceleration and $\ddot{y}$ is the translational acceleration of the instrument centre of mass. l is the instrument length.

TF spectra between the output accelerations and input voltage are calculated using the following equation, from Ewins [1991]:

$$G(\omega) = \frac{P_{\ddot{y}u}(\omega)}{P_{uu}(\omega)} \qquad \textbf{(4.5.1.1)}$$

where $P_{\ddot{y}u}(\omega)$ is the cross-spectral density (CSD) between input voltage and output acceleration and $P_{uu}(\omega)$ is the input voltage power spectral density (PSD).

Using equation 4.5.1.1, the following spectra are calculated: $\ddot{y}_{a1}/V$, $\ddot{y}_{a2}/V$ and $\ddot{y}_b/V$. Data overlapping is done to smooth the spectra. The number of overlaps is 256 per test, for 37 tests per accelerometer. For 256 overlaps, a test duration of 3,2 s and sampling frequency of 1280 Hz, the frequency resolution is 1/3 Hz.

The averages $G_{a1}(\omega)$, $G_{a2}(\omega)$ and $G_b(\omega)$ of the test spectra are calculated using the following equations:

$$G_{a1}(\omega) = \frac{1}{37}\sum_{i=1}^{37}\left(\frac{P_{\ddot{y}_{a1}V}}{P_{VV}}\right)_i \qquad \textbf{(4.5.1.2a)}$$

$$G_{a2}(\omega) = \frac{1}{37}\sum_{i=1}^{37}\left(\frac{P_{\ddot{y}_{a2}V}}{P_{VV}}\right)_i \qquad \textbf{(4.5.1.2b)}$$

$$G_b(\omega) = \frac{1}{37}\sum_{i=1}^{37}\left(\frac{P_{\ddot{y}_bV}}{P_{VV}}\right)_i \qquad \textbf{(4.5.1.2c)}$$

where i is the test number.

The transfer function $G_{parallel}$ for parallel excitation, i.e. excitation at actuator II and measurements at accelerometers II and III, is calculated using the following equations:

$$G_{parallel}(\omega) = G_{a2}(\omega) + G_b(\omega) \tag{4.5.1.3}$$

The sign of $G_b(\omega)$ is positive, in agreement with the sign convention in figure 4.5.1.1.

The transfer function $G_{crisscross}$ for crisscross excitation, i.e. excitation at actuator II and measurement at accelerometer I, is given by:

$$G_{crisscross}(\omega) = G_{a1}(\omega) \tag{4.5.1.4}$$

The *TF* between coil input voltage and optical instrument rotational acceleration is the difference between the parallel and crisscross accelerations, divided by the instrument length:

$$G_{rotation} = \frac{\ddot{\theta}}{V} = \frac{1}{l}\left(G_{parallel} - G_{crisscross}\right) \tag{4.5.1.5}$$

The *TF* between coil input voltage and instrument translational acceleration is the average of the parallel and crisscross *TF*'s:

$$G_{translation} = \frac{\ddot{y}}{V} = \frac{1}{2}\left(G_{parallel} + G_{crisscross}\right) \tag{4.5.1.6}$$

The parallel, crisscross, rotational and translational *TF* magnitude and phase spectra are calculated from equations 4.5.1.3 to 4.5.1.6 respectively. The spectra are shown graphically in section 4.5.2.

4.5.2 Transfer function spectra

TF magnitude and phase spectra for parallel and crisscross excitations, for a frequency band of 0 Hz to 500 Hz, are shown in figure 4.5.2.1. The figure also shows the disturbance bandwidth (*BW*) and input filter frequencies.

TF magnitude and phase spectra for rotational motion of the optical instrument are shown in figure 4.5.2.2. For the purpose of clarity, the resonance and anti-resonance frequencies for rotational motion, together with the magnitudes and phases at these frequencies, are given in table 4.5.2.1. *TF* magnitude and phase spectra for translational motion are shown in figure 4.5.2.3.

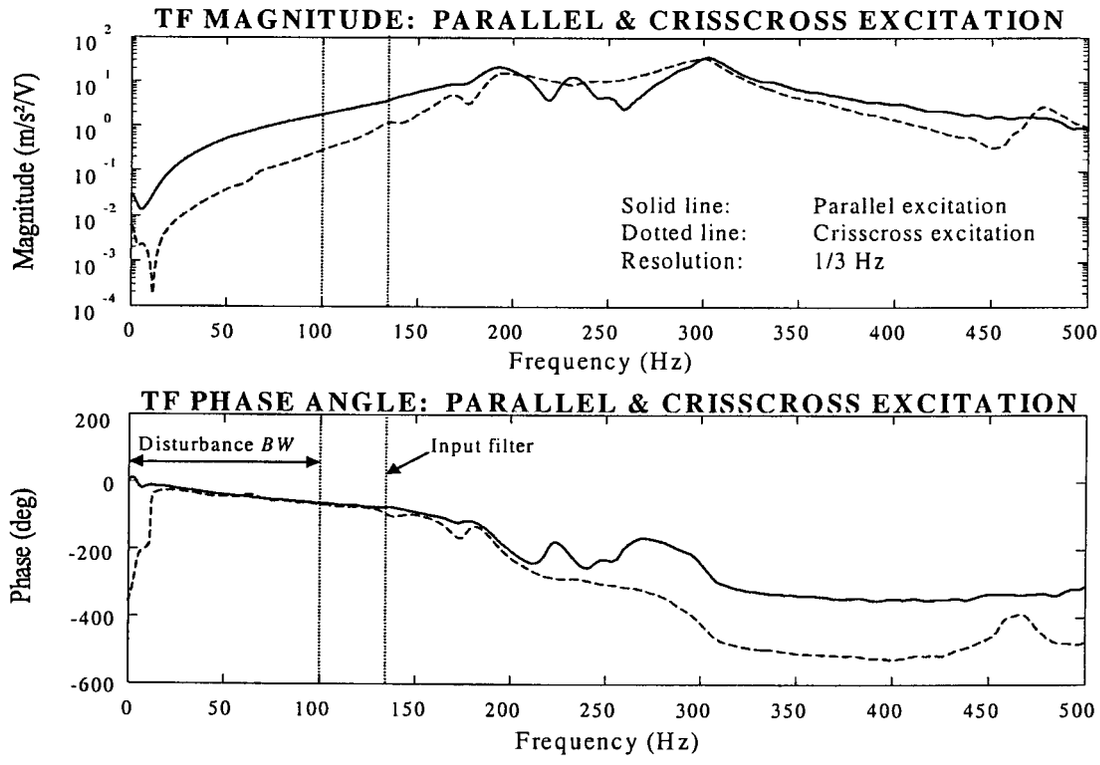

Figure 4.5.2.1: Parallel and crisscross excitation transfer function frequency spectra

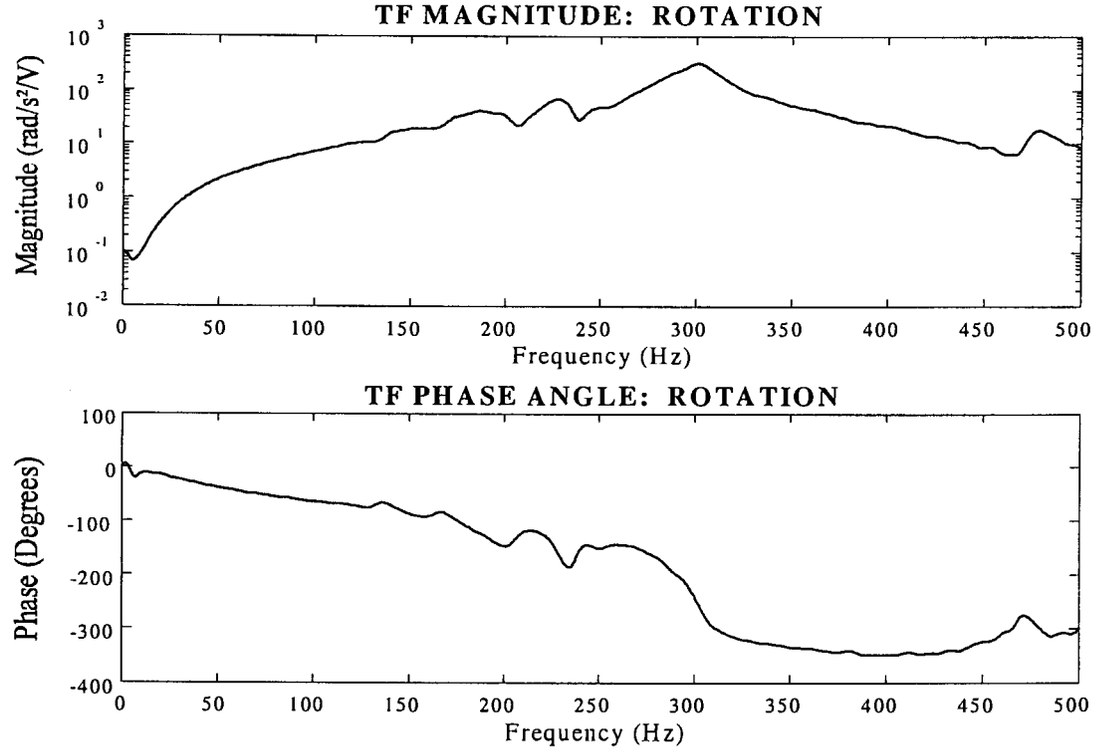

Figure 4.5.2.2: Transfer function magnitude and phase spectra for rotation

Table 4.5.2.1: Resonance and anti-resonance frequencies, magnitudes & phases for rotation

Frequency (Hz)	Resonance	Anti-resonance	Magnitude (rad/s²/V)	Phase (°)
186,3	✓	×	40,47	-128,0
206,7	×	✓	22,21	-130,4
227,3	✓	×	67,98	-153,9
238,7	×	✓	28,19	-162,0
247,0	✓	×	45,42	-147,2
254,3	×	✓	48,14	-146,3
301,0	✓	×	320,5	-246,8
466,0	×	✓	6,53	-297,2
478,3	✓	×	18,11	-294,4

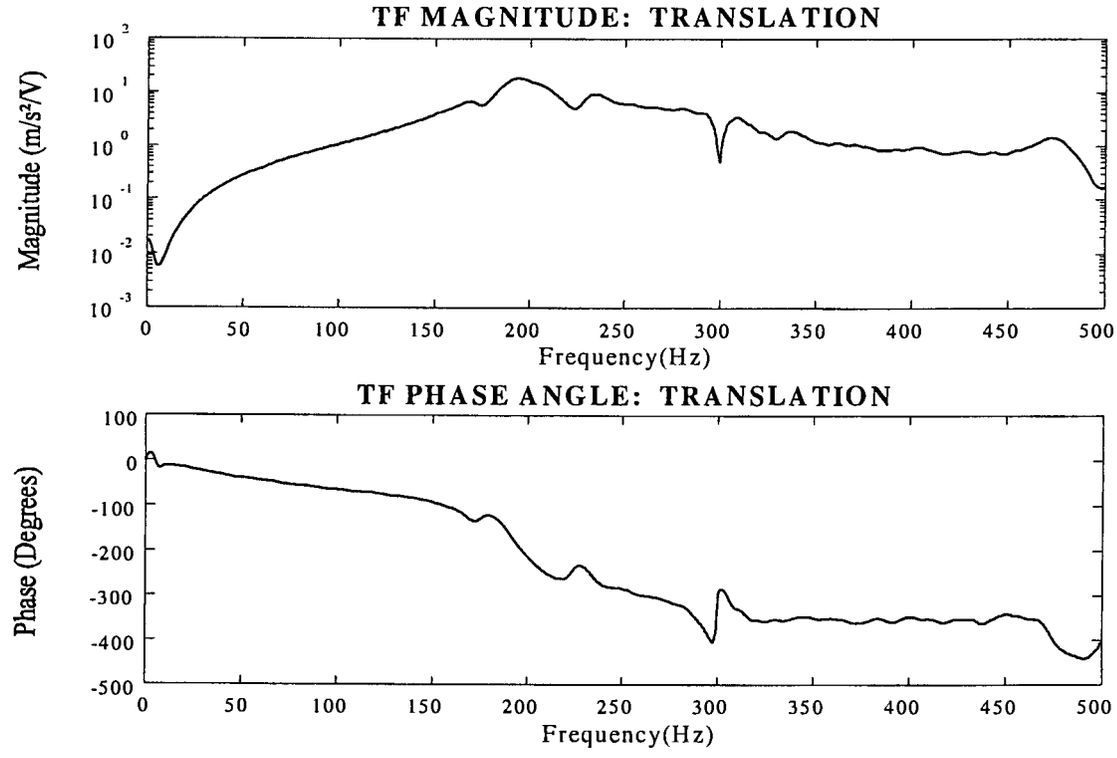

Figure 4.5.2.3: Transfer function magnitude and phase spectra for translation

4.5.3 Discussion of dynamic test results

Magnitude and phase of the rotational DOF at the end of the disturbance band, i.e. at 100 Hz, are 7,21 rad/s²/V and -63,1° respectively. All the resonance and anti-resonance frequencies are well above the disturbance band. Dominant rotational resonance frequencies are 227,3 Hz and 301 Hz. The magnitude peak at 478,3 Hz is due to base resonance. This peak also appears in the translational *TF* magnitude. An anti-resonance frequency, i.e. at 5 Hz, is

noticable in the magnitude graph in figure 4.5.2.2. This is not a system anti-resonance frequency, but rather a notch in the accelerometer transfer function.

From figure 4.5.2.3, it can be judged that the peak at 186,3 Hz, is a dominant translational resonance frequency. At this frequency, a peak also appears in the rotational *TF* spectrum. This may be attributed to different actuator stiffnesses. At 238,7 Hz, a slight peak appears in the translational *TF* magnitude, while at 301 Hz, a notch occurs in the translational magnitude, where the dominant rotational resonance frequency occurs.

It can be seen from figures 4.5.2.1 to 4.5.2.3, that the phase angles gradually drop with an increase in frequency from 0 Hz. This phenomenon also appeared in the modelled *TF* (see figure 2.8.5.3). The phase drop can be attributed to coil inductance.

The -3 dB bandwidth of the coil cannot be directly obtained from the *TF* spectra. The reason is that the system consists of two coupled (mechanical and electrical) subsystems. The coil bandwidth can however be calculated after separating the electrical characteristic of the coil (I/V-spectrum) from the mechanical characteristic. This will be done in chapter 5.

4.5.4 Comparison between experimental and modelled results

The modelled and experimentally determined input voltage to output acceleration *TF*'s, for parallel and crisscross excitation, are shown in figures 4.5.4.1 and 4.5.4.2 respectively. Modelled spectra are obtained from coil input voltage to output displacement characteristics as simulated in section 2.8.5. The modelled *TF*'s are multiplied with $-\omega^2$ to obtain voltage to angular acceleration *TF*'s. Figure 4.5.4.3 shows the modelled and experimentally determined input voltage to output angular acceleration *TF*'s.

It is clear from the abovementioned three figures that correspondence between the modelled and experimental results is poor. It can be deduced that the model is currently highly inaccurate and must therefore be improved before a controller can be designed.

Possible reasons for differences between the modelled and experimental results are as follows: Firstly, in chapter 2, an ideal SDOF model was used for each actuator. It is however obvious from this section that the experimental *TF* spectra display more resonant frequencies than the modelled spectra. This can be attributed to actuator dynamics, i.e. each actuator behaves like an excited structure, with more than one degree of freedom.

Furthermore, natural frequencies depend on a number of other factors, such as Young's modulus of the Terfenol-D rods, system distributed and concentrated mass, strain constant, gain mechanism stiffness and gain factor. Parameters such as Young's modulus and the strain constant are prestress-dependent (see section 2.2). The problems of determining prestress were discussed in more detail in sections 4.4.2 and 4.4.3.

In the third place, actuator output (displacement or acceleration) must be multiplied by -1, since a positive Terfenol-D rod elongation produces a negative actuator output displacement (see figure 3.4.1.5). The model developed in chapter 2 did not take this characteristic into

consideration, which partly explains the large differences between modelled and measured phase spectra.

Lastly, a hysteresis damping model, which was derived from quasi-static hysteresis loops published in the literature, was used in chapter 2 (see section 2.3). An effort was made to derive a dynamic damping model from the hysteresis loops. However, it was mentioned in section 2.3 that experimentally measured results are required to obtain an accurate damping model. Updating of the damping model will be explained in chapter 5, where a modal damping model will be described.

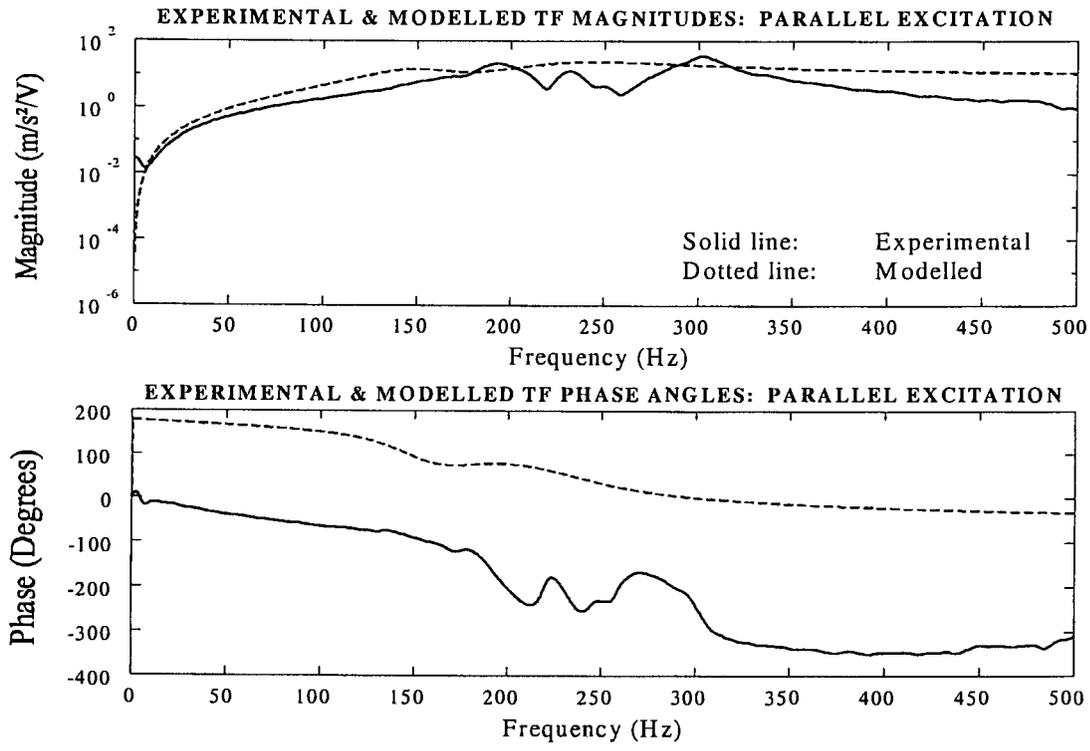

Figure 4.5.4.1: **Experimental and modelled *TF* magnitude and phase spectra for parallel excitation**

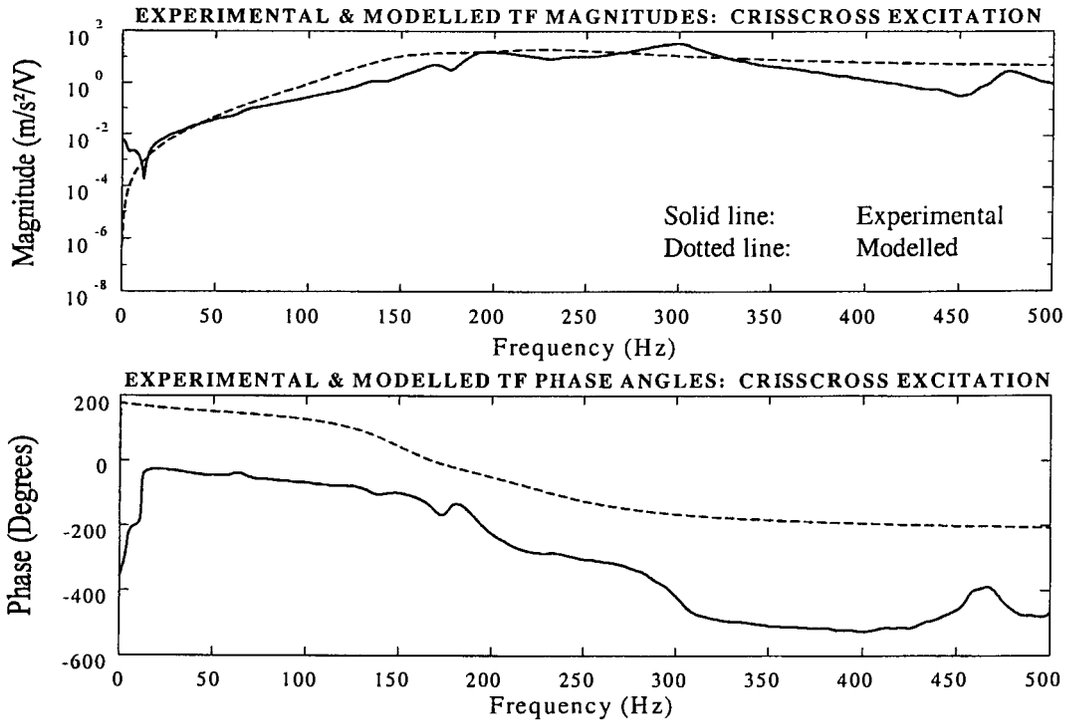

Figure 4.5.4.2: **Experimental and modelled *TF* magnitude and phase spectra for crisscross excitation**

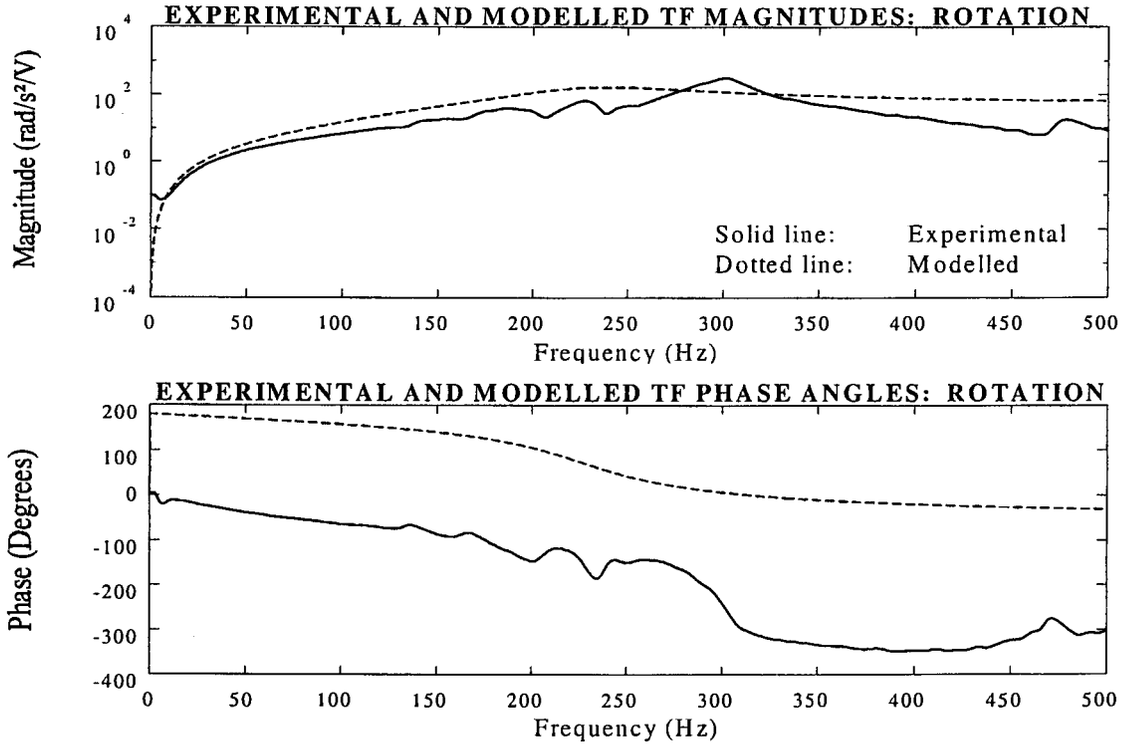

Figure 4.5.4.3: **Experimental and modelled *TF* magnitude and phase spectra for angular motion (rotation)**

4.6 Summary of chapter 4 and preview of chapter 5

The Terfenol-D actuator and LOS stabilization system characteristics were determined experimentally in this chapter. The actuators were tested quasi-statically. The system, consisting of the two actuators, optical instrument and its support structure, was tested dynamically. The purpose of the quasi-static tests was to determine the actuator linear ranges, maximum stroke length, input voltages required to produce the stroke length and bias voltage for the dynamic tests. The dynamic tests were carried out to obtain system frequency-domain *TF*'s between coil voltage and instrument angular acceleration, as well as resonance and anti-resonance frequencies. These characteristics are required to update the model and to design a controller.

The test specimens were discussed in short. Quasi-static and dynamic test setups and equipment were described and shown diagrammatically. The tests were carried out and the measured signals were processed. The results were shown graphically and discussed. It was shown that all the resonance and anti-resonance frequencies are well above the disturbance bendwidth. The dynamic test results were compared with the modelled results. Reasons for differences between the modelled and measured results were given. It was shown that the model is inaccurate and must therefore be updated to represent the measured results more accurately. Model updating will be described in chapter 5.

The model updating procedure is as follows: A 2DOF discrete model is developed for each actuator and an SDOF model of the elastically mounted base is included. The distributed model of the optical instrument is left unchanged. The electrical and mechanical subsystems are analyzed separately. The actuator, base and optical instrument equations of motion are coupled using component mode synthesis. The *TF* spectra are recalculated and compared with the experimentally determined spectra. It will be shown that the accuracy of this model is sufficient.

Chapter 5
Identification of system parameters and updating of system model

5.1 Background

In this chapter, two model updating approaches are considered. The first approach is direct identification from measured transfer function spectra, by using system identification theory. The second approach is updating of a physical model, by means of iterative parameter adjustment.

A motivation for updating the model is given and the procedure is explained. System identification theory is discussed and a suitable identification technique is selected. The selected technique is described in detail.

An updated *TF* model is obtained from the experimentally determined *TF* magnitude and phase spectra, by means of linear frequency domain identification. The *TF* is presented in numerator and denominator polynomial form. *TF* spectra of the updated model are compared with the experimentally determined *TF* spectra. It is shown that the model is sufficiently accurate. This identification technique generally gives high accuracy without a thorough knowledge of the system and is relatively quick and easy to apply.

The limitations of the *TF* model are, firstly, that no physical insight is provided into certain system characteristics, such as normal modes, modal forcing functions, coupling between mechanical and electrical subsystems, or the effects of base motion on system transmissibility. Secondly, depending on the order of the approximation model, an overdetermined system may be required to ensure high accuracy. Although the model may closely approximate the experimental data, excessive computational effort may be required to model noise, instead of system characteristics.

In order to overcome the abovementioned limitations of the *TF* model, a physical model is also derived. The model parameters are selected and adjusted until the calculated *TF* magnitude and phase spectra closely match the experimentally determined *TF* spectra. The advantage of a physical model is that it can be derived from first principles and that all the characteristics can be related to physical system parameters, such as mass, stiffness, damping and input force. The disadvantage is that the model updating procedure may be tedious.

The physical model is subsequently separated into two models, i.e. one for the electrical subsystem (coil) and one for the mechanical subsystem. Reasons for separating the models are given and the difficulties of identifying the electrical and mechanical subsystem models are mentioned. A method of analyzing the models separately is described. The coil model is presented in canonical state-space and *TF* forms. Coil *TF* magnitude and phase spectra are shown and the *TF* poles and zeroes are discussed. The relationship between coil current and modal excitation force is given.

The equations of motion of the mechanical subsystem, which consists of the two actuators, elastically mounted base and the optical instrument and support structure, are derived.

Different methods of coupling the component equations of motion are discussed. The component mode synthesis method is selected as the most suitable method for this purpose. The undamped natural frequencies and normal mode shapes are calculated. Modal damping and forcing terms are added. The latter terms are obtained from the coil model. The overall system *TF* spectra are calculated and compared with the experimentally determined *TF* spectra. It is shown that the model is sufficiently accurate.

The system open-loop transmissibility (*TR*), i.e. the base angular acceleration to optical instrument angular acceleration transfer function, is obtained by means of the physical model. The open-loop transmissibility will be required in chapter 6 to design a controller.

Motivation for updating the system model

It was shown in section 4.5 that the modelled and experimentally determined system *TF*'s differed considerably. The following reasons were mentioned. In the first place, the experimental *TF* spectra displayed more resonant frequencies than the modelled spectra. This was attributed to the fact that the SDOF actuator models were insufficient and that MDOF actuator models would be required to accurately describe system characteristics.

Secondly, due to the geometry of the gain mechanisms, a positive rod elongation would produce a negative actuator displacement (see figure 3.4.1.5). The model developed in chapter 2 did not take this characteristic into consideration, which partly explains the large differences between modelled and measured phase spectra. The problem can however be solved relatively easily, by multiplying the output with -1.

Lastly, in chapter 2, damping was modelled by means of a hysteresis damping model, which was derived from quasi-static hysteresis loops published in the literature (see section 2.3). Since the system is required to operate over a wide frequency range, a quasi-static damping model would necessarily be inaccurate. The damping model can be improved by making use of viscous modal damping.

Layout of this chapter

Model updating is systematically described in the following sections. Identification theory is discussed in short in section 5.2. A classification of identification techniques is given. Linear and nonlinear system identification techniques are respectively mentioned in sections 5.2.1 and 5.2.2. A suitable identification technique is selected in section 5.2.3, followed by a discussion of linear least-squares frequency domain identification in section 5.2.4.

In section 5.3, an updated frequency domain *TF* model is obtained from the measured spectra by means of a least-squares data fit. Model order is determined iteratively. The model parameters, i.e. the numerator and denominator polynomial coefficients, are given and the *TF* poles and zeroes are calculated. The updated model *TF* is compared with the experimentally determined *TF*.

Identification of the coil characteristics is covered in section 5.4. Separation of the coil and mechanical subsystem models is motivated and described in section 5.4.1. The coil model is presented in section 5.4.2.

The undamped equations of motion of the mechanical subsystem, for natural behaviour, are derived in section 5.5, using the component mode synthesis method. Damping and forcing terms are added in section 5.6. The latter terms are obtained from the coil model. Updated system state-space and *TF* models are derived. The updated model *TF* magnitude and phase spectra are compared with the experimentally determined *TF* spectra and it is shown that accuracy of the updated model is acceptable. The *TF* poles and zeroes are calculated and a pole-zero diagram is shown. The *TF*'s of the individual mode shapes are calculated and the dominating mode is identified. The system bandwidth is calculated. The open-loop transmissibility is calculated by means of the physical model.

A summary of chapter 5 and a preview of chapter 6 are given in section 5.7.

5.2 System identification theory

System identification theory is summarized in this section. A broad classification of identification model types is given. Linear and nonlinear, as well as time and frequency domain identification models and techniques are discussed in short. A suitable identification technique is selected for this study and described.

Linear time-domain and frequency-domain identification models and techniques are mentioned in section 5.2.1. In section 5.2.2, nonlinear time- and frequency domain identification models and techniques are mentioned. The most suitable identification technique is selected in section 5.2.3, followed by a detailed discussion of the technique in section 5.2.4.

The process of constructing models and estimating unknown system parameters from experimental data, is called system identification [Franklin et al, 1990]. A broad classification of estimation methods is given by Schoukens & Pintelon [1991]. The methods are classified in three categories, i.e. nature of the selected model, application of the model and stochastic characteristics of the measurements. A classification of identification methods is summarized in table 5.2.1.

Table 5.2.1: Classification of system identification methods [Schoukens & Pintelon, 1991]

Category	
Selected model:	Parametric versus nonparametric Time domain versus frequency domain Linear-in-the-parameters versus nonlinear-in-the-parameters
Application:	Time invariant systems versus time varying systems Linear systems versus nonlinear systems
Stochastic characteristics:	Noise on the input and output versus noise on the input only versus noise on the output only

A category which can be added to the above, is on-line (real-time) versus off-line (classical) identification. On-line and off-line identification are discussed in more detail by Sinha & Kuszta [1983]. The determination of frequency spectra, e.g. those shown in section 4.5, can be done on-line, using modern signal analyzers. Extraction of model parameters, such as natural frequencies, damping factors and modal amplitudes, is mostly done off-line.

Parametric actuator and LOS stabilization system models were developed in chapter 2. The state-space and *TF* models were derived in terms of the Terfenol-D magnetostrictive and magnetization parameters and the actuator, coil and system dynamic parameters (see sections 2.4 to 2.8). Nonparametric models were obtained from the experimental test results in chapter 4, where the actuator and system *TF*'s were represented by their respective spectra (see figure 4.5.2.2). Time domain simulations of the actuator behaviour were done in chapter 2 (see section 2.7.3), while the system frequency domain *TF's* were derived from the complex Laplace domain *TF's* in section 2.8.5.

A distinction is made between a linear system and a linear-in-the-parameters system. A model is called linear-in-the-parameters if there is a linear relationship between its parameters and its output [Franklin et al, 1990]. The actuator and system frequency domain *TF's* are nonlinear-in-the-parameters. Consider for instance the modelled SDOF actuator frequency domain output equation, which, from equation 2.5.3.5, can be written as:

$$Y(j\omega) = \frac{p_0}{\left(q_0 - q_2\omega^2\right) + j\omega\left(q_1 - \omega^2\right)} U(j\omega) \qquad \textbf{(5.2.1)}$$

where ω is the angular excitation frequency, $U(j\omega)$ and $Y(j\omega)$ are the complex frequency domain coil voltage input and actuator displacement output respectively. The parameters p_0, q_0, q_1 and q_2 are the *TF* numerator and denominator polynomial coefficients. It can be seen from the above equation that $Y(j\omega)$ is a nonlinear function of the *parameters*.

A system is linear if there is a linear relationship between its input and output. In equation 5.2.1, the ratio of the output $Y(j\omega)$ to the input $U(j\omega)$ at any given frequency ω, is linear.

5.2.1 Linear system identification models and techniques

The objective of linear identification is to obtain a system model in transfer function or state-space form, from measured data. Linear identification models and techniques include the following: The ARMA method for discrete time-domain identification of linear systems, time-domain models from free-decay response, identification models for time-varying systems, regression techniques to determine model coefficients, Laplace- and frequency-domain *TF* models from discrete time-domain models, frequency-domain models from measured *TF* spectra and state-space identification of linear systems. The abovementioned models are not discussed here. A summary of each of the methods is given in appendix U.

5.2.2 Nonlinear system identification models and techniques

Techniques for determining the parameters of nonlinear systems from measured data can broadly be classified as time-domain techniques, frequency-domain techniques, force-state component identification and identification using neural networks. The methods are summarized in appendix U.

5.2.3 Selection of a suitable identification technique

For the purpose of this study, the system models that will be identified, will mainly be parametric, time invariant, linear, frequency *(ω)* domain *TF* and state-space models. Time-varying, nonlinear and time-domain models will not be considered.

The reasons are, firstly, that the models developed in chapter 2 are state-space and frequency-domain *TF* models. These models will serve as a guide for updating the system model from experimentally-determined *TF* spectra. A second reason is that *TF* and state-space models are mostly used for the design of classical and optimal controllers. Adaptive controllers, which adjust control parameters in real time using learning algorithms, are an exception. Adaptive controllers will not be considered in this study. A third reason is that experimentally-determined spectra already exist. These spectra were obtained during the test phase, as described in chapter 4. The last reason is that ω-domain spectra give physical insight into dynamic characteristics, such as magnitude, phase angle, number of DOF's, resonance and anti-resonance frequencies, DC gains and frequency bandwidths.

The disadvantages are firstly that ω-domain models are nonlinear-in-the-parameters, as discussed before. Secondly, processing is almost always done off-line. Real-time determination of *TF* polynomial coefficients is not possible with the currently available equipment. Thirdly, during conversion from a *TF* model to a state-space model, a canonical model almost always results. The canonical model states do not necessarily correspond with the selected model states. The latter must be obtained by a similarity transform. Lastly, frequency-domain identification requires longer data records than time-domain identification [Liu & Miller, 1995].

In this chapter, the coil voltage to angular acceleration *TF* of the optical instrument is obtained from measured spectra in the frequency-domain, using the Gauss-Newton technique. A physical system model is also derived. The coil and mechanical subsystem models are separated and a canonical coil model is developed.

Actuator characteristics are modelled by means of 2DOF discrete models, instead of the SDOF models used in chapter 2. Substructure synthesis is used to couple the actuator, optical instrument and base models. The actuator and base stiffnesses are adjusted until the modelled *TF* spectra match the experimentally determined natural frequencies with an acceptable degree of accuracy. The normal mode shapes of the optical instrument are subsequently calculated. The mechanical subsystem model is coupled to the coil model in state-space. The system *TF* magnitude and phase spectra are calculated and compared with the experimentally determined spectra. The coil back-emf is not modelled.

5.2.4 Least-Squares method for frequency-domain identification

The frequency domain *TF* model which approximates the measured spectra, can be written as follows in complex form:

$$\hat{G}(j\omega)=\frac{\hat{P}(j\omega)}{\hat{Q}(j\omega)} \tag{5.2.4.1}$$

where $\hat{G}(j\omega)$ is the approximate *TF* and $\hat{P}(j\omega)$ and $\hat{Q}(j\omega)$ respectively represent the numerator and denominator of $\hat{G}(j\omega)$. $\hat{P}(j\omega)$ and $\hat{Q}(j\omega)$ are polynomials in $j\omega$:

$$\hat{P}(j\omega)=\sum_{k=0}^{M} p_k (j\omega)^k \tag{5.2.4.2a}$$

$$\hat{Q}(j\omega)=\sum_{l=0}^{N} q_l (j\omega)^l \tag{5.2.4.2b}$$

where M is the order of the numerator polynomial and N is the order of the denominator polynomial. p_k and q_l are the numerator and denominator polynomial coefficients respectively. For the sake of convenience, the polynomial coefficients are written as follows in vector form:

$$\{C_p\}=\{p_0, p_1, \cdots, p_M\}^T \tag{5.2.4.3a}$$

$$\{C_q\}=\{q_0, q_1, \cdots, q_N\}^T \tag{5.2.4.3b}$$

where $\{C_p\}$ and $\{C_q\}$ are the numerator and denominator polynomial coefficient vectors respectively. These two vectors are combined as follows in one coefficient, or parameter, vector $\{C\}$:

$$\{C\}=\{\{C_p\},\ \{C_q\}\}^T=\{p_0, p_1, \cdots, p_M,\ \ q_0, q_1, \cdots, q_N\}^T \tag{5.2.4.4}$$

It is desirable to obtain a model which is proper, i.e. a model whose numerator order is less than or equal to the denominator order:

$$M \le N \tag{5.2.4.5}$$

In order to ensure a high degree of accuracy, large values of M and N are required. However, the larger M and N, the more computationally intensive the identification procedure becomes. Furthermore, in a physical system model, such as an equation of motion, M and N are determined by the number of normal modes.

The purpose of the model is to represent the experimentally-determined *TF* spectra as accurately as possible. The difference between the modelled *TF* and experimentally-determined *TF* is known as the estimation error and is given by:

$$e = G - \hat{G} \tag{5.2.4.6}$$

where e is the error, $\hat{G}$ is the modelled *TF* and G is the experimentally determined *TF*. G is known at discrete frequencies (see section 4.5), thus the error can only be evaluated at these frequencies.

The error e_r at the r-th frequency is:

$$e_r = G_r - \hat{G}_r \tag{5.2.4.7}$$

where $\hat{G}_r$ and G_r are the approximate *TF* and measured *TF* at the r-th frequency, given by:

$$\hat{G}_r = \hat{G}(j\omega_r) \tag{5.2.4.8a}$$
$$G_r = G(j\omega_r) \tag{5.2.4.8b}$$

It can be seen from equations 5.2.4.7 and 5.2.4.8, it can be seen that the error varies with frequency. As a globally accurate model is required, the error squared is summed and minimized over the frequency band.

The global error is given by the following equation:

$$E = \sum_{r=1}^{N} |e_r|^2 \tag{5.2.4.9}$$

where E is the global error of the model and N is the number of discrete frequencies.

Both $\hat{G}$ and G are complex (see equations 5.2.4.8). The global error can therefore be expressed as the sum of the error of the real term squared plus the error of the imaginary term squared [Schoukens & Pintelon, 1991]:

$$E = \sum_{r=1}^{N} \left[\left(\mathrm{Re}\{G_r\} - \mathrm{Re}\{\hat{G}_r\} \right)^2 + \left(\mathrm{Im}\{G_r\} - \mathrm{Im}\{\hat{G}_r\} \right)^2 \right] \tag{5.2.4.10}$$

E is a nonlinear function of the polynomial coefficient vector C:

$$E = E(C) \tag{5.2.4.11}$$

For the global error to be a minimum, the partial derivative of the error with respect to the model parameters, must be zero:

$$\frac{\partial E}{\partial C_l} = 0, \quad l = 1, 2, \cdots, M + N + 2 \qquad \textbf{(5.2.4.12)}$$

where C_l is the l-th element of the model parameter vector, given by equation 5.2.4.4. The coefficients which will minimize E, must be determined. Methods for solving LS problems are discussed next.

Methods for solving least-squares problems

Least-squares (LS) problems can, inter alia, be classified as linear and nonlinear problems. The following linear LS solution techniques are described by Chen et al [1989]: Gaussian elimination, Cholesky decomposition, classical and modified Gram-Schmidt methods, Householder transformation, Givens method and singular value decomposition (SVD). These techniques are applicable to linear-in-the-parameters systems.

Frequency-domain models are nonlinear-in-the-parameters (see equation 5.2.1). The following nonlinear LS solution techniques, for nonlinear-in-the-parameters systems, are described by Schoukens & Pintelon [1991]: The gradient method, Newton-Raphson algorithm, Gauss-Newton algorithm and the method of Levenberg-Marquardt. Methods to obtain linear-in-the-parameters models for frequency-domain identification purposes are described by Schoukens & Pintelon [1991]. These methods have however become obsolete due to the rapid development of computers.

The main drawback of the gradient method is its slow convergence. Speed of convergence can be improved using the Newton-Raphson method, which gives quadratic convergence. However, to make this possible, 2nd order derivatives must be calculated, which may be time-consuming. Furthermore, the Newton-Raphson method does not gurarantee convergence.

The problem of calculating 2nd order derivatives can be avoided by using the Gauss-Newton method. For most problems the Gauss-Newton method demands less computation time per iteration step than the Newton-Raphson algorithm. In the neighbourhood of the solution, the Newton-Raphson method will generally converge faster than the Gauss-Newton method. However, the convergence region of the Gauss-Newton method is larger than that of the Newton-Raphson method. As with the Newton-Raphson method, the Gauss-Newton method does not guarantee convergence.

A method which assures unconditional convergence, at least to a local minimum, is the Levenberg-Marquardt method. The method is a combination between the gradient and Gauss-Newton methods.

The Gauss-Newton method is well-established for nonlinear-in-the-parameter LS identification. This method is also used in this study to obtain the *TF* numerator and denominator coefficients from experimentally-determined *TF* frequency spectra. The method is described in appendix V.

5.3 Updated system *TF* model from least-squares data fit

In this section, an approximate transfer function is obtained by doing a least-squares data fit to the experimentally determined frequency domain spectra. The *TF* is written in numerator and denominator polynomial form and the polynomial coefficients are tabled. The approximate *TF* magnitude and phase spectra are shown graphically and compared with the experimentally determined spectra. The poles and zeroes are tabled.

The approximate frequency domain transfer function $\hat{G}(j\omega)$ is written in the following form:

$$\hat{G}(j\omega) = \frac{\hat{P}(j\omega)}{\hat{Q}(j\omega)} \tag{5.3.1}$$

$\hat{P}(j\omega)$ and $\hat{Q}(j\omega)$ respectively represent the *TF* numerator and denominator polynomials in $j\omega$, given by:

$$\hat{P}(j\omega) = \sum_{k=0}^{M} p_k (j\omega)^k \tag{5.3.2a}$$

$$\hat{Q}(j\omega) = \sum_{l=0}^{N} q_l (j\omega)^l \tag{5.3.2b}$$

where p_k and q_l are the k-th numerator and l-th denominator polynomial coefficients respectively. M and N are the numerator and denominator polynomial orders respectively.

M and N are determined iteratively. Initial values of M and N are determined from the number of resonance and anti-resonance frequencies of the experimentally determined *TF* (see table 4.5.2.1). A pole is added to model the coil *TF*. The total number of poles is therefore 2 per resonance frequency, plus one coil pole. The number of zeroes is 2 per anti-resonance frequency. Two zeroes, in the origin of the complex plane, are added. The notch, which appears at approximately 5 Hz in the *TF* spectra (see figure 4.5.2.2), is not accounted for, since it is assumed that it is an accelerometer characteristic, rather than a system characteristic (see also section 4.3.3).

Five resonance and four anti-resonance frequencies are listed in table 4.5.2.1. Applying the method set out above, M and N are:

$$M = 10 \tag{5.3.3a}$$
$$N = 11 \tag{5.3.3b}$$

The difference between M and N is the relative degree of freedom of the *TF*, given by:

$$M - N = 1 \tag{5.3.4}$$

With the above values of M and N, the Gauss-Newton method is used to fit an approximate transfer function $\hat{G}(j\omega)$, to the experimental spectra. The numerator and denominator polynomial coefficients are obtained from the data fit.

$\hat{G}(j\omega)$ is calculated using equations 5.3.2. The magnitude and phase of $\hat{G}(j\omega)$ are calculated and compared with the experimental spectra. If the accuracy of the fit is poor, M and N are each increased by 2. The process is repeated until the poles and zeroes coincide. Coinciding poles and zeroes are then eliminated. After two iterations, the following values of M and N result:

$$M = 14 \qquad \textbf{(5.3.5a)}$$
$$N = 15 \qquad \textbf{(5.3.5b)}$$

The *TF* numerator and denominator polynomial coefficients p_k and q_l, which minimize the LS error for the above values of M and N, are given in table 5.3.1.

Table 5.3.1: Polynomial numerator and denominator coefficients

Coefficient	Value
p_0	0
p_1	0
p_2	$-1{,}0667.10^{43}$
p_3	$-6{,}9076.10^{39}$
p_4	$-2{,}6194.10^{37}$
p_5	$-1{,}5266.10^{34}$
p_6	$-2{,}3520.10^{31}$
p_7	$-1{,}2339.10^{28}$
p_8	$-9{,}4729.10^{24}$
p_9	$-4{,}5154.10^{21}$
p_{10}	$-1{,}6358.10^{18}$
p_{11}	$-7{,}3367.10^{14}$
p_{12}	$-8{,}0479.10^{10}$
p_{13}	$-4{,}0799.10^{7}$
p_{14}	$1{,}7934.10^{3}$
q_0	$4{,}3672.10^{47}$
q_1	$1{,}3445.10^{45}$
q_2	$2{,}1924.10^{42}$
q_3	$4{,}1830.10^{39}$
q_4	$3{,}9207.10^{36}$
q_5	$5{,}2226.10^{33}$
q_6	$3{,}4152.10^{30}$
q_7	$3{,}3812.10^{27}$
q_8	$1{,}5984.10^{24}$
q_9	$1{,}2220.10^{21}$
q_{10}	$4{,}0475.10^{17}$
q_{11}	$2{,}4539.10^{14}$
q_{12}	$5{,}1186.10^{10}$
q_{13}	$2{,}5149.10^{7}$
q_{14}	$2{,}4468.10^{3}$
q_{15}	1

The magnitude and phase spectra of the approximate transfer function $\hat{G}(j\omega)$, together with the experimentally determined spectra, are shown in figure 5.3.1. The poles and zeroes of $\hat{G}(j\omega)$ are given in table 5.3.2.

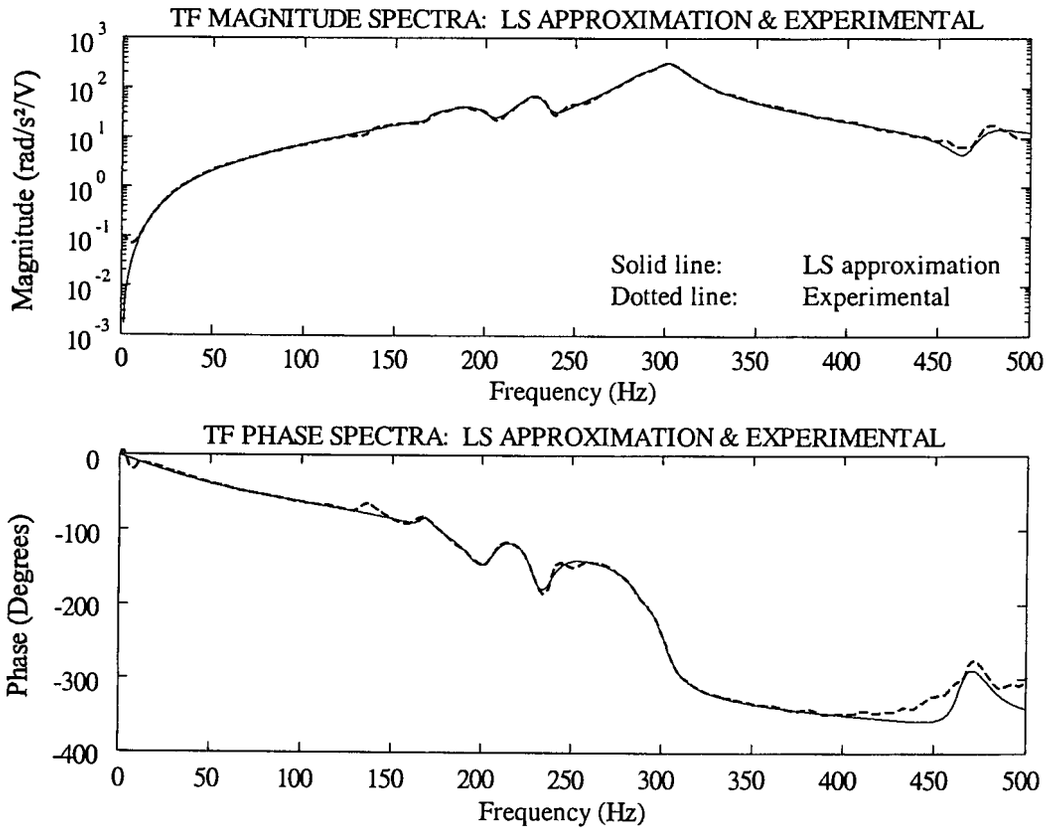

Figure 5.3.1: LS approximation and experimentally determined TF spectra

It can be seen from figure 5.3.1 that the accuracy of the magnitude spectrum is acceptable for a frequency band of 10 Hz to 430 Hz. For frequencies below 10 Hz, inaccuracies are caused by the two zeroes in the origin of the complex plane. A more accurate low-frequency model can for instance be obtained by detailed accelerometer modelling. Accuracy of the phase spectrum is acceptable for a frequency band of 10 Hz to 350 Hz. The phase is slightly inaccurate at 130 Hz and 240 Hz.

Table 5.3.2: Transfer function poles and zeroes:

Frequency (Hz)	Damping factor (%)	Pole	Zero	Type	Sign of real part
0		×	✓	Real	
0		×	✓	Real	
68,74		✓	×	Real	Negative
167,5	2,29	×	✓	Complex conjugate pair	Negative
168,4	2,48	✓	×	Complex conjugate pair	Negative
197,3	6,48	✓	×	Complex conjugate pair	Negative
205,2	3,96	×	✓	Complex conjugate pair	Negative
228,6	2,69	✓	×	Complex conjugate pair	Negative
237,0	3,21	×	✓	Complex conjugate pair	Negative
263,2	40,76	✓	×	Complex conjugate pair	Negative
287,7	3,25	✓	×	Complex conjugate pair	Negative
291,0	3,53	×	✓	Complex conjugate pair	Negative
301,2	2,61	✓	×	Complex conjugate pair	Negative
323,7		×	✓	Real	Negative
463,7	1,29	×	✓	Complex conjugate pair	Negative
474,7	2,68	✓	×	Complex conjugate pair	Negative
4016,1		×	✓	Real	Positive

All the poles and zeroes but one, are inside the test band of 0,33 Hz to 500 Hz. The zero at 4016 Hz is well above the test band. The real pole at 69 Hz is inside the isolation bandwidth of the system, i.e. 2,5 Hz to 100 Hz. The real parts of all the poles are negative. The real parts of all the zeroes, except for the two zeroes in the origin of the complex plane and the zero at 4016 Hz, are negative. The sign of the latter zero indicates that $\hat{G}(j\omega)$ is non-minimum phase.

5.4 Identification of coil characteristics

The system spectra shown in figures 4.5.2.1 to 4.5.2.3 are spectra of a system which consists of two coupled subsystems, i.e. electrical and mechanical subsystems. The electrical subsystem consists of the coils, while the mechanical subsystem consists of the actuators, elastically-mounted base, optical instument and its support structure. The coil input is the supply voltage V and the output is current I. The mechanical subsystem input is actuator force and the output is the optical instrument angular acceleration $\ddot{\theta}$. Actuator force is related to coil current by the equation:

$$F = F_I I \qquad \textbf{(5.4.1)}$$

where F_I is force per unit current.

A block diagram of the system is shown in figure 5.4.1. The two subsystems and the subsystem coupling element are also shown.

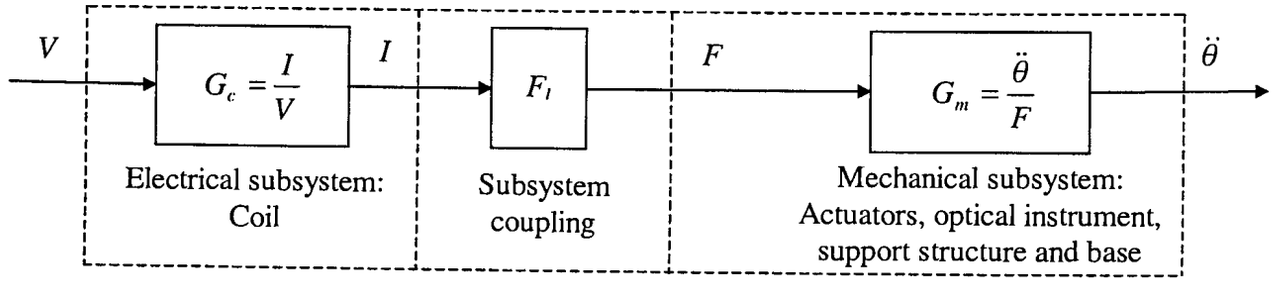

Figure 5.4.1: System block diagram

The system *TF* is given by:

$$G = G_c F_I G_m \tag{5.4.2}$$

where G_c is the coil transfer function and G_m is the mechanical subsystem transfer function.

5.4.1 Separation of electrical and mechanical subsystem models

It is convenient to separate the coil and mechanical subsystem characteristics, since this measure will make it possible to obtain the coil *TF*, true normal mode shapes, natural frequencies, damping factors and forces. One method of directly obtaining the coil characteristics, would be to measure voltage and current during the test phase and to calculate the coil *TF*, i.e. *I/V*. A signal analyzer with three analogue input channels, i.e. one for each of the voltage, current and acceleration signals, would be required for this purpose. Alternatively, an additional set of tests could be done to measure the coil current, using the available signal analyzer.

Obtaining the mechanical subsystem *TF*, in isolation of the electrical characteristics, would be more difficult, since both output angular acceleration and input force would be required for this purpose. Firstly, angular acceleration cannot be measured directly. Angular acceleration can however be calculated from measured vertical accelerations, as was explained in section 4.5. Secondly, force could not be measured directly, since the sensors required for this purpose are load cells, which would not fit between the actuators and support structure. A relatively flat, washer-type, load cell would be a welcome solution to the problem. Although this type of load cell is currently under development, it is not ready for use in this study.

An alternative identification method is to obtain the coil and mechanical subsystem *TF*'s from the system *TF*. To make this technique possible, a number of assumptions must be made. It is firstly assumed that all the peaks and notches in the *TF* spectra are mechanical subsystem characteristics, with the peaks occuring at resonance frequencies and the notches occuring at anti-resonance frequencies. It is further assumed that coil damping is high. A consequence of this assumption is that the coil *TF* will not display sharp resonance peaks.

A frequency domain *TF* of the system is obtained from an LS data fit, using the Gauss-Newton method (see appendix V). The resonance and anti-resonance frequencies are identified and their corresponding poles and zeroes are calculated. Using the poles and zeroes, the

mechanical subsystem *TF* is derived. The quotient of the system *TF* and the mechanical subsystem *TF* gives the coil *TF*.

An advantage of this identification technique is that the subsystem *TF*'*s* can be relatively easily determined. Furthermore, the mechanical subsystem *TF* can be written in modal form and the dominating mode can be identified. The disadvantage, however, is that the back-emf cannot be obtained using this technique.

5.4.2 Coil model

The coil *TF* is the ratio between current I and voltage V. The complex frequency domain transfer function $G_c(j\omega)$ is given by:

$$G_c(j\omega) = \frac{I(j\omega)}{V(j\omega)} = \frac{\sum_{ck=0}^{M_C} p_{ck}(j\omega)^{ck}}{\sum_{cl=0}^{N_C} q_{cl}(j\omega)^{cl}} \qquad \textbf{(5.4.2.1)}$$

where p_{ck} and q_{cl} are the k-th numerator and l-th denominator polynomial coefficients respectively. The coefficicents for $M_c = 2$ and $N_c = 3$ are given in table 5.4.2.1. The *TF* magnitude and phase spectra are shown in figure 5.4.2.1.

Table 5.4.2.1: Coil *TF* numerator and denominator polynomial coefficients

Coefficient:	$p_{c0}(\text{x}10^8)$	$p_{c1}(\text{x}10^5)$	$p_{c2}(\text{x}10^1)$	$q_{c0}(\text{x}10^9)$	$q_{c1}(\text{x}10^6)$	$q_{c2}(\text{x}10^3)$	$q_{c3}(\text{x}10^0)$
Value:	4,1629	1,0574	1,3316	1,3321	3,4874	1,8168	1

The coil Laplace-domain *TF* is obtained by substitution of $j\omega$ with s in equation 5.4.2.1:

$$G_c(s) = \frac{\sum_{ck=0}^{M_C} p_{ck} s^{ck}}{\sum_{cl=0}^{N_C} q_{cl} s^{cl}} \qquad \textbf{(5.4.2.2)}$$

where the p_{ck} and q_{cl} coefficients are equal to those in equation 5.4.2.1.

The coil *TF* has two complex conjugate zeroes, one real pole and two complex conjugate poles. The undamped frequency and damping ratio of the zeroes are 889,9 Hz and 71,01 % respectively. The frequency of the zeroes is above the maximum frequency of the measurenent band (500 Hz). The frequency of the real pole is 74,19 Hz. The undamped frequency and damping ratio of the poles are 269,1 Hz and 39,95% respectively. The real parts of all the coil poles and zeroes are negative.

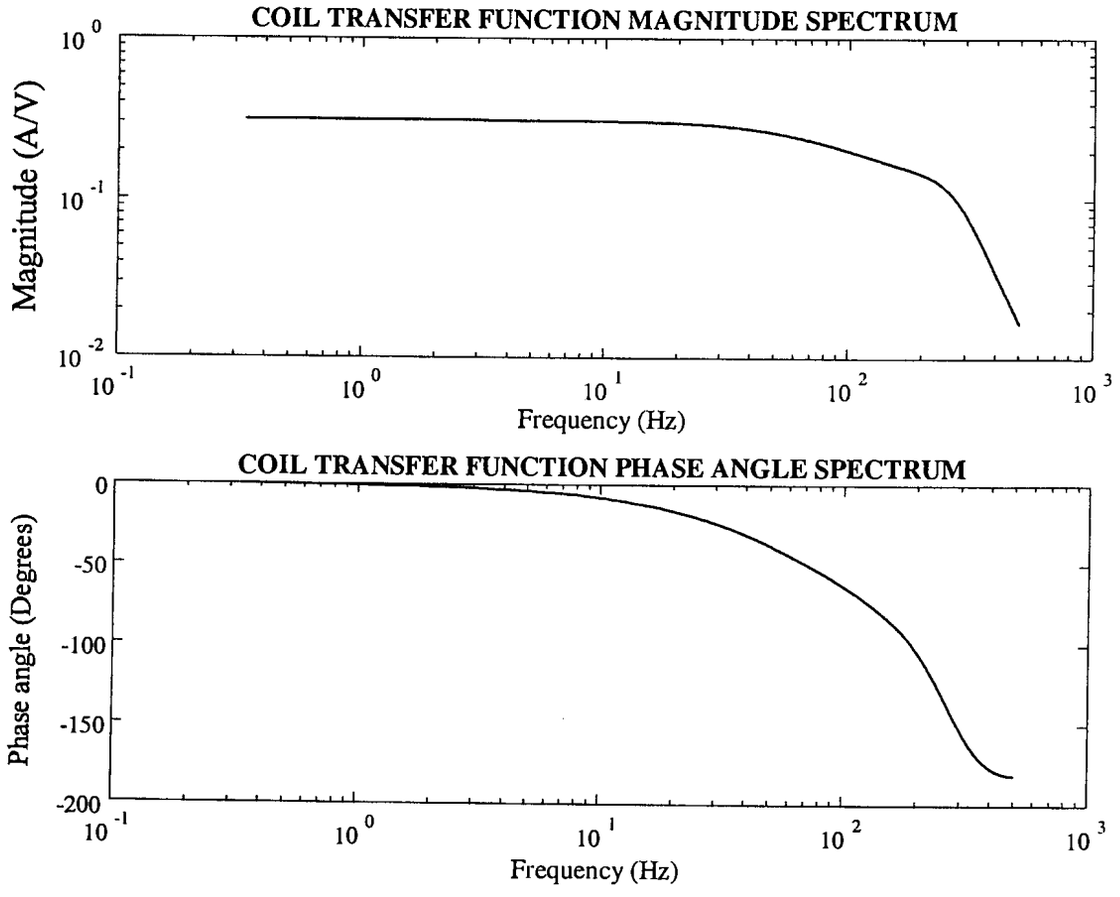

Figure 5.4.2.1: Coil transfer function magnitude and phase spectra

The coil *TF* at DC is the ratio of p_0/q_0, which is equal to the inverse of the coil resistance of 3,2 Ω, i.e. 0,3125 A/V. The coil *TF* magnitude at 100 Hz is 3,69 dB lower than the DC magnitude. The -3 dB bandwidth of the coil is 84 Hz. The coil bandwidth is lower than the required bandwidth of 100 Hz and the design bandwidth of 150 Hz (see section 3.5.2). This can mainly be attributed to the presence of the real pole at 74 Hz. It will however be shown in section 5.6, that, due to the presence of mechanical subsystem poles above 100 Hz, the overall system bandwidth is 199 Hz, which exceeds the required bandwidth by 99 Hz. The complex poles and zeroes of the coil *TF* are well above the disturbance bandwidth of 100 Hz.

The coil state-space model is given by:

$$\dot{x}_c = A_c x_c + B_c V \qquad \textbf{(5.4.2.3a)}$$
$$I = C_c x_c + D_c V \qquad \textbf{(5.4.2.3b)}$$

where x_c is the coil state vector and A_c, B_c, C_c and D_c are the coil state and output matrices, given by:

$$A_c = \begin{bmatrix} 0 & 1 & 0 \\ 0 & 0 & 1 \\ -q_{c0} & -q_{c1} & -q_{c2} \end{bmatrix} \qquad \textbf{(5.4.2.4a)}$$

$$B_c = \{0 \quad 0 \quad 1\}^T \qquad \textbf{(5.4.2.4b)}$$

$$C_c = \{p_{c0} \quad p_{c1} \quad p_{c2}\} \qquad \textbf{(5.4.2.4c)}$$

$$D_c = 0 \qquad \textbf{(5.4.2.4d)}$$

Actuator force, in terms of the state vector and input, is obtained by substitution of equation 5.4.2.3b into equation 5.4.1:

$$F = F_I C_c x_c + F_I D_c V \qquad \textbf{(5.4.2.5)}$$

The individual modal forces Q_i are given by:

$$Q_i = \phi_i^T F_{I_i} \left(C_c x_c + D_c V \right) \qquad \textbf{(5.4.2.6)}$$

where ϕ_i is the i-th normal mode shape vector and F_{I_i} is the i-th normal mode input force per unit coil current. Equation 5.4.2.6 will be used in section 5.6 to describe the modal forcing terms.

5.5 Mechanical subsystem model using component mode synthesis

It was shown in section 4.5.4 that the system model derived in chapter 2 is inadequate, due to the fact that simple SDOF models were used to describe actuator behaviour. It was also mentioned in chapter 4 that a dynamic model would be required to describe motion of the elastically-mounted base. In this section, each actuator will be modelled with a 2DOF discrete spring-mass model. The original distributed mass and stiffness model developed for the optical instrument and support structure in section 2.8, is retained. An SDOF model is added to represent the base.

The total number of DOF's required to update the model is 15, i.e. 2 for each actuator, 10 for the optical instrument and support structure, and one for the base. This number of DOF's exceeds the number of DOF's used in the original model by five (see section 2.8).

The increase in DOF's does not pose any problems for updating the model. A number of modelling techniques that can be considered for this purpose, are the Rayleigh-Ritz method, Newton's 2nd law, FEM, the mechanical impedance method and component mode synthesis. The main shortcoming of the Rayleigh-Ritz method, for this application, is that coupling of discrete and distributed models may be difficult. This is also a drawback of Newtons's 2nd law, which is clumsy in defining boundary values between discrete and continuous subsystems. Another limitation, which is of secondary importance, is that displacement of an internal DOF of a particular component may be difficult to obtain.

The mechanical impedance method is relatively easy to apply, but gives twice the required number of eigenvalues, since the resulting system DE is 4th order per DOF. Lastly, unless the system is enlarged significantly, no real need exists to use FEM. The only method that is powerful, yet simple enough for this purpose, is component mode synthesis. This method deals with the coupling of component equations of motion using modal displacement vectors. A coupling matrix is used to express boundary values in terms of component modal displacements. System mass and stiffness matrices are derived using energy methods. Normal mode shapes and natural frequencies are obtained from a Rayleigh-Ritz type eigenvalue analysis.

The component mode shapes used in the analysis, may either be component normal modes or component assumed modes. If normal modes are used, boundary values between substructures will not necessarily be satisfied. Additional coupling modes may be required for this purpose. Coupling modes include constraint modes, rigid body modes, attachment modes and inertia relief attachment modes. A description of these modes is given by Craig [1981]. If, on the other hand, assumed modes are used, the modes can be initially selected to satisfy all the boundary values. This method, as explained by Thomson [1993], is also used is in this study. Mode shapes which satisfy the boundary values, will be selected below.

More detail about substructure synthesis is provided by Meirovitch [1990], Kubomura [1987], Béliveau & Souci [1985], Kubomura [1982], Craig [1981], Hintz [1975], Rubin [1975], Klein & Dowell [1974], Benfield & Hruda [1971] and Craig & Bampton [1968].

The system, with its components, is shown shematically in figure 5.5.1. Discrete spring-mass models of the two actuators and base are shown in figure 5.5.2.

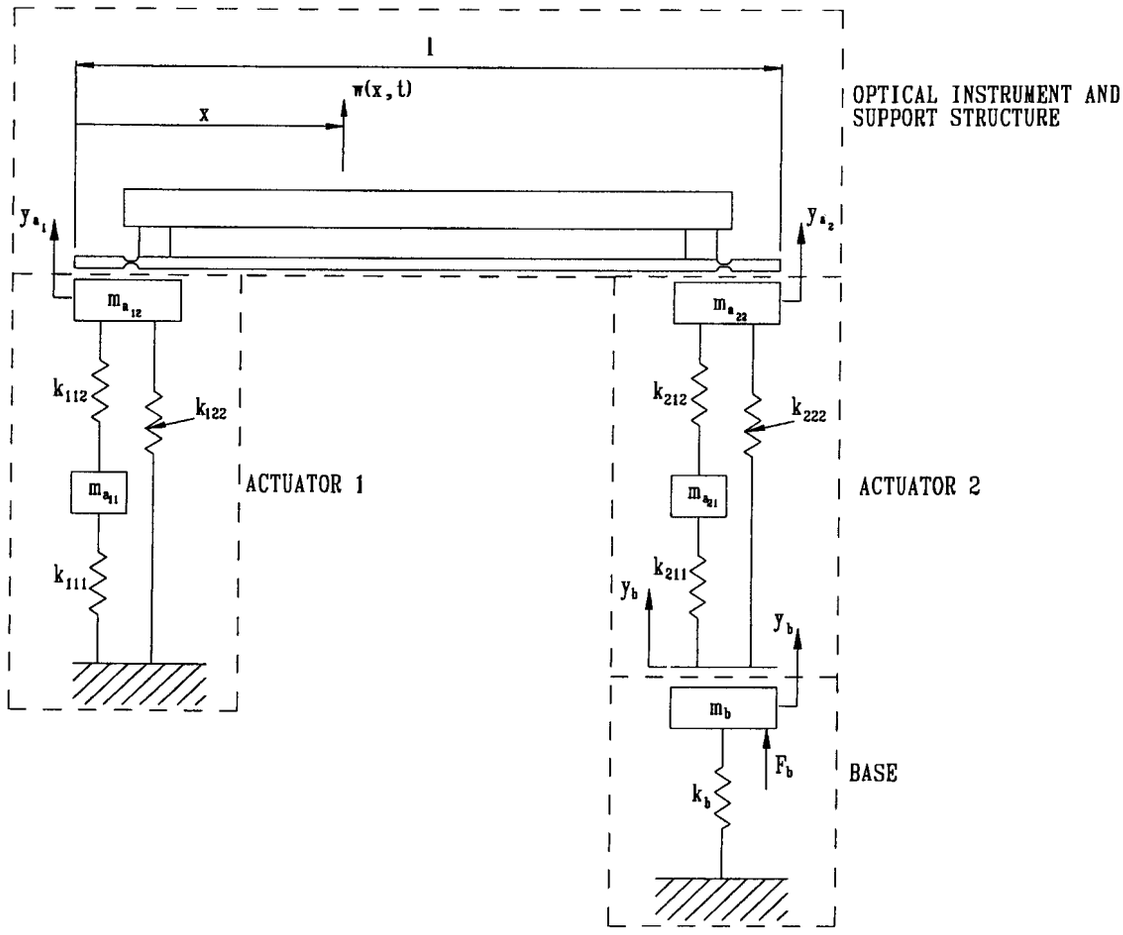

Figure 5.5.1: System model, with substructures

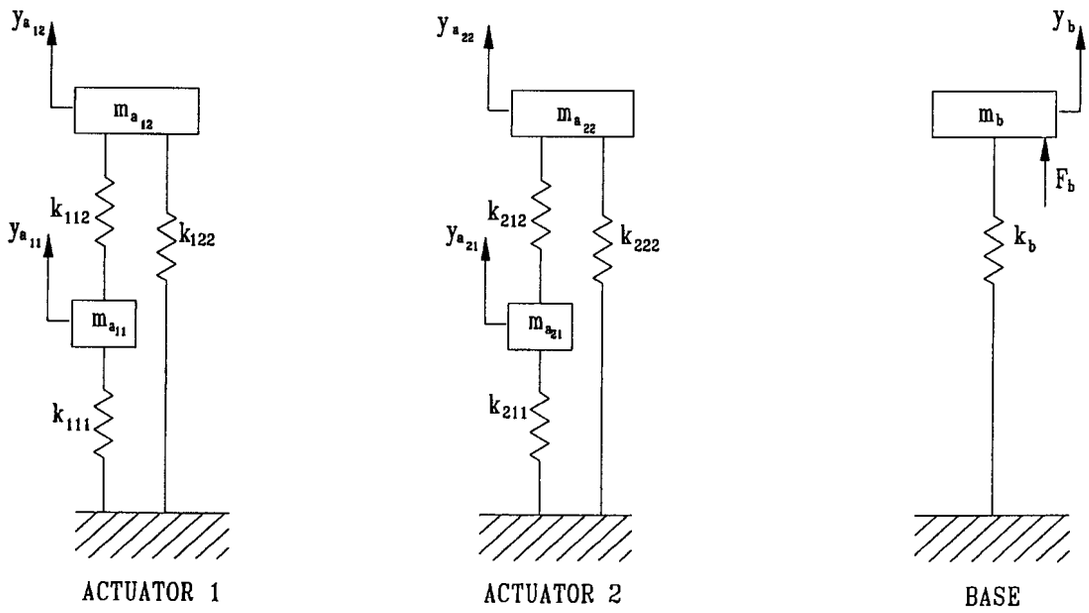

Figure 5.5.2: Actuator and base discrete models

System equation of motion in terms of component displacements

The equation of motion of a linear mechanical system is:

$$m\ddot{y} + c\dot{y} + ky = F \tag{5.5.1}$$

where m, c, k, y and F respectively represent mass, damping, stiffness, displacement and force. F and y are functions of time t:

$$y = y(t) \tag{5.5.2a}$$
$$F = F(t) \tag{5.5.2b}$$

The system described in this section, consists of the actuators, the optical instrument and its support structure, and the elastically-mounted base. Discrete models are used for the actuators and base, while a distribured model is used for the instrument and support structure.

The system equation of motion is firstly derived for natural motion of an undamped system. This is done in order to obtain real normal mode shapes. The assumption is made that damping does not change the mode shapes. This technique was also used in section 2.8. Damping and forcing terms will be added in section 5.6.

The system equation of motion is written in the following general form:

$$m\ddot{y} + ky = 0 \tag{5.5.3}$$

where m and k are the system mass and stiffness matrices. m and k contain component mass and stiffness matrices on the diagonal, as well as off-diagonal matrices which describe coupling between adjacent components. y is the system displacement vector, given by:

$$y = \left\{ \{y_{a1}\},\quad w(x),\quad \{y_{a2}\},\quad y_b \right\}^T \tag{5.5.4}$$

where $\{y_{a1}\}$ and $\{y_{a2}\}$ are the displacement vectors of actuators I and II respectively, $w(x)$ is the distributed displacement of the optical instrument and support structure and y_b is the base displacement.

System modal analysis

The system displacement vector y is determined by the superposition of r number of normal modes:

$$y = \sum_{i=1}^{r} \phi_i q_i(t) \tag{5.5.5}$$

where ϕ_i is the i-th normal mode shape and q_i is the i-th normal mode displacement as a function of time. The number of normal modes r depends on the total number of component

modes n_t and the number of constraint equations. The constraint equations describe motion at boundaries between adjacent components.

Equation 5.5.5 is written concisely in matrix form as:

$$y = \Phi q_n \tag{5.5.6}$$

where Φ is the system normal mode shape matrix and q_n is the modal displacement vector. Φ is given by:

$$\Phi = \begin{bmatrix} [\Phi_1] \\ \{\Phi_s(x)\} \\ [\Phi_2] \\ \{\Phi_b\} \end{bmatrix} \tag{5.5.7}$$

where $[\Phi_1]$ is the 2 x r normal mode shape matrix of actuator I, $\{\Phi_s(x)\}$ is the 1 x r normal mode shape vector, as a function of x, of the optical instrument, $[\Phi_2]$ is the 2 x r normal mode shape matrix of actuator II and Φ_b is the 1 x r normal mode vector of the base. The size of Φ is 6 x r. The elements of Φ are derived later.

The system modal equation of motion, for undamped natural motion, is:

$$M^* \ddot{q}_n + K^* q_n = 0 \tag{5.5.8}$$

where M^* and K^* are the diagonal modal mass and stiffness matrices of the system. The sizes of M^* and K^* are n_t-r each.

The normal mode shapes and mass and stiffness matrices are currently unknown. In order to solve equation 5.5.3, a number of mode shapes must be assumed for each component. The component assumed mode shapes are given in the next section.

Component assumed mode shapes

Assumed mode shapes for each component are given in this section. As opposed to the Rayleigh-Ritz method, which requires that all the assumed mode satisfy the boundary values, the component mode synthesis method only requires that the *combination* of assumed modes of each component satisfy the boundary values [Thomson, 1993].

The boundary values are:

$$w_s(0) = y_{a12} \tag{5.5.9a}$$

$$w_s(l) = y_{a22} + y_b \tag{5.5.9b}$$

$$w_s'(0) = 0 \tag{5.5.9c}$$

$$w_s'(l) = 0 \tag{5.5.9d}$$

The assumed mode shapes ψ_{a1} and ψ_{a2} of actuators I and II are:

$$\psi_{a1} = \begin{bmatrix} 1 & 1 \\ 1 & -1 \end{bmatrix} \tag{5.5.10a}$$

$$\psi_{a2} = \begin{bmatrix} 1 & 1 \\ 1 & -1 \end{bmatrix} \tag{5.5.10b}$$

The sizes of ψ_{a1} and ψ_{a2} are 2 x 2 each.

Three types of assumed modes were used for the optical instrument and support structure in section 2.8.3, i.e. symmetric bending modes (see figure 5.5.3), asymmetric bending modes (see figure 5.5.4) and a rigid body mode, with unity displacement along the length of the instrument.

The assumed mode vector of the instrument and structure can be written as:

$$\psi_s(x) = \left\{ \{\psi_{symm}(x)\} \quad \{\psi_{asymm}(x)\} \quad \psi_{rigid}(x) \right\} \tag{5.5.11}$$

where ψ_{symm} and ψ_{asymm} are the symmetric and asymmetric assumed mode vectors and ψ_{rigid} is the rigid body mode of the following form:

$$\psi_{rigid}(x) = 1 \tag{5.5.12}$$

The size of $\psi_s(x)$ is 1 x 10.

The assumed mode ψ_b of the base is:

$$\psi_b = 1 \tag{5.5.13}$$

ψ_b is a 1 x 1 scalar.

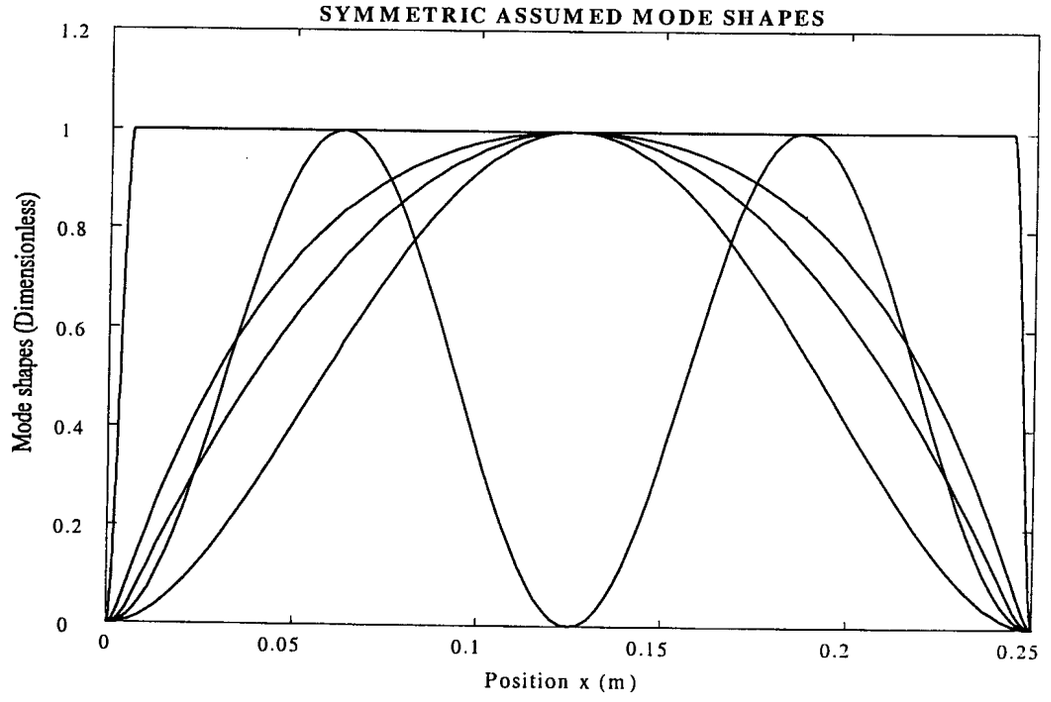

Figure 5.5.3: Symmetric assumed mode shapes for the optical instrument and support structure

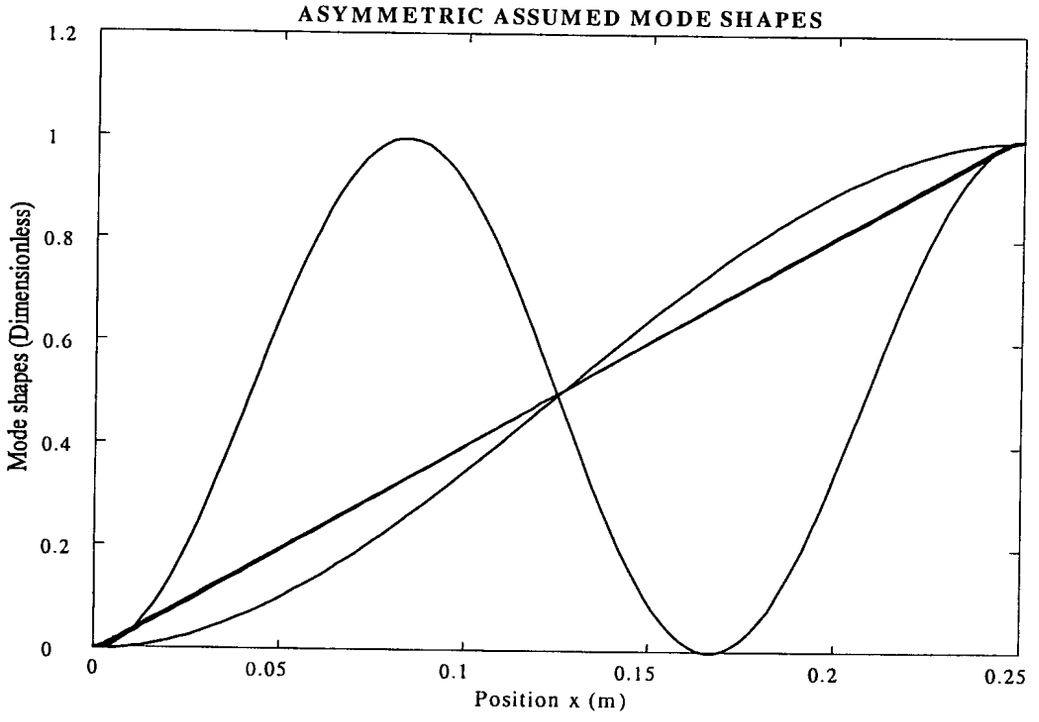

Figure 5.5.4: Asymmetric assumed mode shapes for the optical instrument and support structure

The system assumed mode matrix ψ is compiled from the component assumed modes as follows:

$$\psi = \begin{bmatrix} [\psi_{a1}] & & & \\ & \{\psi_s(x)\} & & \\ & & [\psi_{a2}] & \\ & & & \psi_b \end{bmatrix} \tag{5.5.14}$$

The size of ψ is 6 x 15.

Component displacements in terms of assumed mode displacements

The actuator displacements, in terms of their assumed mode shapes and modal displacements, are:

$$y_{a1} = \psi_{a1} q_{a1} \tag{5.5.15a}$$
$$y_{a2} = \psi_{a2} q_{a2} \tag{5.5.15b}$$

where y_{a1} and y_{a2} are given by:

$$y_{a1} = \{y_{a11}, \quad y_{a12}\}^T \tag{5.5.16a}$$
$$y_{a2} = \{y_{a21}, \quad y_{a22}\}^T \tag{5.5.16b}$$

The actuator modal displacement vectors are given by:

$$q_{a1} = \{q_{a11}, \quad q_{a12}\}^T \tag{5.5.17a}$$
$$q_{a2} = \{q_{a21}, \quad q_{a22}\}^T \tag{5.5.17b}$$

The displacement of the optical instrument, in terms of its assumed mode shapes and modal displacements, is:

$$w(x) = \psi_s(x) q_s \tag{5.5.18}$$

where $w(x)$ is the vertical translational displacement of the instrument, as a function of x, and q_s is its modal displacement vector, given by:

$$q_s = \{q_{s1}, \quad q_{s2}, \quad \cdots, \quad q_{s10}\}^T \tag{5.5.19}$$

The displacement of the base, in terms of its assumed mode shape and modal displacement, is:

$$y_b = q_b \tag{5.5.20}$$

Component modal mass and stiffness matrices

The modal mass matrices M_{a1} and M_{a2} of actuators I and II are:

$$M_{a1} = \psi_{a1}^{T} m_{a1} \psi_{a1} \quad \textbf{(5.5.21a)}$$

$$M_{a2} = \psi_{a2}^{T} m_{a2} \psi_{a2} \quad \textbf{(5.5.21b)}$$

where ψ_{a1} and ψ_{a2} are given in equations 5.5.10. m_{a1} and m_{a2} are the mass matrices of actuators I and II respectively, for the displacement coordinate systems y_{a1} and y_{a2} given in equations 5.5.16. m_{a1} and m_{a2} are given by:

$$m_{a1} = \begin{bmatrix} m_{a11} & 0 \\ 0 & m_{a12} \end{bmatrix} \quad \textbf{(5.5.22a)}$$

$$m_{a2} = \begin{bmatrix} m_{a21} & 0 \\ 0 & m_{a22} \end{bmatrix} \quad \textbf{(5.5.22b)}$$

Since each actuator is modelled as a 2DOF discrete system (see figure 5.5.2), m_{a1} and m_{a2} are diagonal matrices. The sizes of M_{a1} and M_{a2} are 2 x 2 each.

The modal stiffness matrices K_{a1} and K_{a2} of actuators I and II are:

$$K_{a1} = \psi_{a1}^{T} k_{a1} \psi_{a1} \quad \textbf{(5.5.23a)}$$

$$K_{a2} = \psi_{a2}^{T} k_{a2} \psi_{a2} \quad \textbf{(5.5.23b)}$$

where k_{a1} and k_{a2} are the stiffness matrices of actuators I and II respectively, for the displacement coordinate systems y_{a1} and y_{a2} given in equations 5.5.16. k_{a1} and k_{a2} can be derived as:

$$k_{a1} = \begin{bmatrix} (k_{111} + k_{112}) & -k_{112} \\ -k_{112} & (k_{112} + k_{122}) \end{bmatrix} \quad \textbf{(5.5.24a)}$$

$$k_{a2} = \begin{bmatrix} (k_{211} + k_{212}) & -k_{212} \\ -k_{212} & (k_{212} + k_{222}) \end{bmatrix} \quad \textbf{(5.5.24b)}$$

The sizes of K_{a1} and K_{a2} are 2 x 2 each.

The modal mass and stiffness matrices of the optical instrument and support structure, from

equations 2.8.3.10, are:

$$M_s = \int_{x=0}^{x=l} \rho_s(x) A_s(x) \psi_{si}(x) \psi_{sj}(x) dx \qquad \textbf{(5.5.25a)}$$

$$K_s = \int_{x=0}^{x=l} E_s(x) I_s(x) \psi''_{si}(x) \psi''_{sj}(x) dx \qquad \textbf{(5.5.25b)}$$

where $\psi_s(x)$ are the assumed mode shapes of the optical instrument and support structure as shown in figures 5.5.3 and 5.5.4. The mass per unit length $\rho_s A_s$ and flexural rigidity $E_s I_s$, as functions of x, are shown in figures 2.8.4.1 and 2.8.4.2. The sizes of M_b and K_b are 10 x 10 each.

The modal mass and stiffness matrices of the base are:

$$M_b = \psi_b^T m_b \psi_b \qquad \textbf{(5.5.26a)}$$

$$K_b = \psi_b^T k_b \psi_b \qquad \textbf{(5.5.26b)}$$

M_b and K_b are 1 x 1 scalars.

System modal equation of motion

The modal equation of motion of the system is:

$$M\ddot{q} + Kq = 0 \qquad \textbf{(5.5.27)}$$

where M and K are the system modal mass and stiffness matrices respectively, given by:

$$M = \begin{bmatrix} [M_{a1}] & [0] & \cdots & [0] \\ [0] & [M_s] & \ddots & \vdots \\ \vdots & \ddots & [M_{a2}] & [0] \\ [0] & \cdots & [0] & [M_b] \end{bmatrix} \qquad \textbf{(5.5.28a)}$$

$$K = \begin{bmatrix} [K_{a1}] & [0] & \cdots & [0] \\ [0] & [K_s] & \ddots & \vdots \\ \vdots & \ddots & [K_{a2}] & [0] \\ [0] & \cdots & [0] & [K_b] \end{bmatrix} \qquad \textbf{(5.5.28b)}$$

M and K respectively contain the component modal mass and stiffness matrices in square blocks, of different sizes, on the diagonal. Off-diagonal submatrices of M and K are zero. The sizes of M and K are 15 x 15 each.

The system displacement vector q is:

$$q = \left\{ \{q_{a1}\} \quad \{q_s\} \quad \{q_{a2}\} \quad q_b \right\}^T \tag{5.5.29}$$

The size of q is the sum of the sizes of the different component modal displacement vectors, i.e. 15 x 1. The modal displacement vectors q_{a1}, q_{a2}, q_s and q_b are currently uncoupled. Modal coupling is done in the next section.

System coupled modal displacements

The displacement at the boundary between actuator I and the support structure, i.e. at $x = 0$, is:

$$w_s(0) = y_{a12} \tag{5.5.30}$$

The displacement at the boundary between actuator II and the support structure, i.e. at $x = l$, is the sum of the base displacement and the deflection of actuator II:

$$w_s(l) = y_{a22} + y_b \tag{5.5.31}$$

Combination of equations 5.5.10, 5.5.15 to 5.5.18, 5.5.30 and 5.5.31, gives:

$$\psi_s(0) q_s = q_{a11} - q_{a12} \tag{5.5.32a}$$
$$\psi_s(l) q_s = q_{a21} - q_{a22} + q_b \tag{5.5.32b}$$

or:

$$q_{a12} = q_{a11} - \psi_s(0) q_s \tag{5.5.33a}$$
$$q_{a22} = q_{a21} - \psi_s(l) q_s + q_b \tag{5.5.33b}$$

Equations 5.5.33a and 5.5.33b are combined and written as follows in matrix form:

$$\begin{Bmatrix} q_{a12} \\ q_{a22} \end{Bmatrix} = \begin{bmatrix} 1 & 0 & -\psi_s(0) & 0 \\ 0 & 1 & -\psi_s(l) & 1 \end{bmatrix} \begin{Bmatrix} q_{a11} \\ q_{a21} \\ q_s \\ q_b \end{Bmatrix} \tag{5.5.34}$$

Substitution of equation 5.5.34 into equation 5.5.29, gives the system modal displacements as:

$$\begin{Bmatrix} \begin{Bmatrix} q_{a11} \\ q_{a12} \end{Bmatrix} \\ --- \\ \{q_s\} \\ --- \\ \begin{Bmatrix} q_{a21} \\ q_{a22} \end{Bmatrix} \\ --- \\ q_b \end{Bmatrix} = \begin{bmatrix} 1 & \{0\} & 0 & 0 \\ 1 & -\{\psi_s(0)\} & 0 & 0 \\ \{0\} & [I] & \{0\} & \{0\} \\ 0 & \{0\} & 1 & 0 \\ 0 & -\{\psi_s(l)\} & 1 & 1 \\ 0 & \{0\} & 0 & 1 \end{bmatrix} \begin{Bmatrix} q_{a11} \\ \{q_s\} \\ q_{a21} \\ q_b \end{Bmatrix} \tag{5.5.35}$$

Equation 5.5.35 is written in matrix notation as:

$$q = Cq_r \tag{5.5.36}$$

where q is the uncoupled system modal displacement vector given by equation 5.5.29 and q_r is the reduced modal displacement vector, given by:

$$q_r = \{q_{a11} \quad \{q_s\} \quad q_{a21} \quad q_b\}^T \tag{5.5.37}$$

C is the coupling matrix, given by:

$$C = \begin{bmatrix} 1 & \{0\} & 0 & 0 \\ 1 & -\{\psi_s(0)\} & 0 & 0 \\ \{0\} & [I] & \{0\} & \{0\} \\ 0 & \{0\} & 1 & 0 \\ 0 & -\{\psi_s(l)\} & 1 & 1 \\ 0 & \{0\} & 0 & 1 \end{bmatrix} \tag{5.5.38}$$

The sizesof q and q_r are 15 x 1 and 13 x 1 respectively. The size of C is 15 x 13.

System coupled modal equation of motion

The uncoupled modal equation of motion of the system is given in equation 5.5.27. Substitution of the coupling equation 5.5.36 into equation 5.5.27, gives:

$$MC\ddot{q}_r + KCq_r = 0 \qquad \textbf{(5.5.39)}$$

Premultiplication of equation 5.5.39 with C^T gives:

$$M_r\ddot{q}_r + K_r q_r = 0 \qquad \textbf{(5.5.40)}$$

where M_r and K_r are the reduced-order mass and stiffness matrices, respectively given by:

$$M_r = C^T MC \qquad \textbf{(5.5.41a)}$$
$$K_r = C^T KC \qquad \textbf{(5.5.41b)}$$

The sizes of M_r and K_r are 13 x 13 each. The off-diagonal elements of M_r and K_r are non-zero and the reduced coordinate equation of motion (5.5.40), is coupled. The normal mode shapes, natural frequencies, mass and stiffness matrices of the system are derived next.

Normal mode shapes, natural frequencies, mass and stiffness matrices

The reduced coordinate vector q_r can be expressed as follows in terms of the eigenvector U and the normal mode displacement vector q_n:

$$q_r = Uq_n \qquad \textbf{(5.5.42)}$$

The sizes of U and q_n are 13 x 13 and 13 x 1 respectively.

Substitution of equation 5.5.42 into equation 5.5.40 and premultiplication of the resulting equation with U^T gives:

$$U^T M_r U\ddot{q}_n + U^T K_r U q_n = 0 \qquad \textbf{(5.5.43)}$$

For natural motion

$$\ddot{q}_n = -\Omega^2 q_n, \qquad \textbf{(5.5.44)}$$

where Ω^2 the 13 x 13 diagonal eigenvalue matrix.

Substitution of equation 5.5.44 into equation 5.5.43 and simplification of the resulting equation, gives:

$$\left(K_r - M_r\Omega^2\right)Uq_n = 0 \qquad \textbf{(5.5.45)}$$

The eigenvalues are the values of Ω^2 for which:

$$\left|K_r - M_r\Omega^2\right| = 0 \tag{5.5.46}$$

The natural frequency f_i of the i-th normal mode is:

$$f_i = \frac{1}{2\pi}\Omega_{ii} \tag{5.5.47}$$

The uncoupled, normal mode mass and stiffness matrices, from equations 5.5.8 and 5.5.43, are:

$$M^* = U^T M_r U \tag{5.5.48a}$$
$$K^* = U^T K_r U \tag{5.5.48b}$$

The sizes of M^* and K^* are 13 x 13 each.

The normal mode shape matrix Φ is given by:

$$\Phi = \psi C U \tag{5.5.49}$$

where ψ and C are respectively given by equations 5.5.14 and 5.5.38 and U is the eigenvector. The size of Φ is 6 x 13.

The component normal mode shapes are given by:

$$\begin{bmatrix} [\Phi_1] \\ \{\Phi_s(x)\} \\ [\Phi_2] \\ \{\Phi_b\} \end{bmatrix} = \begin{bmatrix} [\psi_{a1}][C_{rows\,1,2}] \\ \{\psi_s(x)\}[C_{rows\,3-12}] \\ [\psi_{a2}][C_{rows\,13,14}] \\ \psi_b\{C_{row\,15}\} \end{bmatrix} U \tag{5.5.50}$$

The system displacement vector, in terms of the normal mode matrix and modal displacement vector, is given by:

$$y = \Phi q_n \tag{5.5.51}$$

y is a 6 x 1 vector.

Component displacements are given by:

$$\begin{Bmatrix} y_{a1} \\ w(x) \\ y_{a2} \\ y_b \end{Bmatrix} = \begin{bmatrix} [\Phi_1] \\ \{\Phi_s(x)\} \\ [\Phi_2] \\ \{\Phi_b\} \end{bmatrix} q_n \qquad \textbf{(5.5.52)}$$

The first five natural frequencies of the system were experimentally determined in section 4.5. The first five natural frequencies and mode shapes of the system will be calculated in the next section, using the equations derived in this section. The stiffnesses and masses of the actuators and base will be selected and adjusted until the calculated natural frequencies correspond sufficiently accurately with the experimentally determined natural frequencies. The equation of motion will be written in state-space form and coupled to the coil state equations. The state equations will be converted to *TF* form, *TF* spectra will be calculated and compared with the experimentally determined spectra.

5.6 Updated system model

An updated system model is presented in this section. The actuators are modelled by means of 2DOF discrete models, instead of the SDOF models developed in chapter 2. An additional SDOF model is included to represent the elastically mounted base. The distributed mass and stiffness model of the optical instrument and support structure, as developed in chapter 2, is left unchanged.

The updating procedure is as follows: Model parameters are selected and adjusted until the calculated natural frequencies closely match the experimentally determined natural frequencies. The model parameters are the actuator, optical instrument and base stiffnesses and masses. Damping is initially ignored in order to obtain real mode shapes. The component mode synthesis method, as described in section 5.5, is used to calculate the normal mode shapes of the optical instrument and support structure. Once the mode shapes have been determined, modal damping and excitation forces are added.

Modal equations of motion are derived and written in state-space form. From the state-space equations, the system transfer function between input voltage and instrument angular acceleration is obtained. As with the masses and stiffness, damping and force parameters are adjusted until the calculated system *TF* closely matches the experimentally determined *TF*. The modelled *TF* is compared with the experimentally determined *TF* and it is shown that the updated model is sufficiently accurate.

A system block diagram is included to show the coil and mechanical subsystem models and to indicate coupling between the subsystems. The modal *TF*'s are calculated and the dominating mode is indicated. A pole-zero diagram of the *TF* is shown. The system bandwidth is calculated and it is shown that it exceeds the required bandwidth.

Base motion and its effect on system behaviour are also analyzed in order to obtain the open-loop transmissibility (*TR*) of the system. (The *TR* is the ratio of instrument angular acceleration to base angular acceleration). The *TR*, together with the system transfer function, is required for control system design purposes, which will be described in chapter 6.

Updated natural frequencies and normal mode shapes

The normal mode shapes and natural frequencies are calculated by means of the component mode synthesis method, described in section 5.5. The actuator and base masses and stiffnesses are selected and the natural frequencies are calculated. The latter are compared with the experimentally determined natural frequencies and, if the comparison is poor, the masses and stiffnesses are updated until the model gives sufficiently accurate natural frequencies. The resulting masses and stiffnesses are given in table 5.6.1.

These masses and stiffnesses, together with the assumed mode shapes, as given in section 5.5, are substituted into equations 5.5.21 to 5.5.28 to obtain the component modal mass and stiffness matrices *M* and *K*. The assumed mode shapes are substituted into equation 5.5.38 to obtain the coupling matrix *C*. The coupled mass and stiffness matrices are calculated using equations 5.5.41. The eigenvector *U* and natural frequencies f_i are obtained by solving the eigenvalue problem, the solution of which is given in equations 5.5.45 to 5.5.47. The normal mode shapes are obtained by application of equation 5.5.50.

Table 5.6.1: Updated actuator and base stiffnesses and masses

Component	Parameter	Symbol	Value
Actuator I	Stiffness	k_{111}	$7{,}34.10^5$ N/m
	Stiffness	k_{112}	$9{,}9672.10^4$ N/m
	Stiffness	k_{122}	$1{,}0972.10^6$ N/m
	Displacement gain	G_1	2,7
	Mass (ungained)	m_{a11}/G_1	0,1482 kg
	Mass (ungained)	m_{a12}/G_1	0,0456 kg
	Mass (gained)	m_{a11}	0,4 kg
	Mass (gained)	m_{a12}	0,1231 kg
Actuator II	Stiffness	k_{211}	$8{,}7327.10^5$ N/m
	Stiffness	k_{212}	$1{,}1761.10^5$ N/m
	Stiffness	k_{222}	$1{,}0863.10^6$ N/m
	Displacement gain	G_2	2,7
	Mass (ungained)	m_{a21}/G_2	0,1482 kg
	Mass (ungained)	m_{a22}/G_2	0,0456 kg
	Mass (gained)	m_{a21}	0,4 kg
	Mass (gained)	m_{a22}	0,1231 kg
Base	Stiffness	k_b	$7{,}1559.10^7$ N/m
	Mass	m_b	8 kg

The first five normal mode shapes of the optical instrument and support structure, together with their corresponding natural frequencies, are shown in figure 5.6.1. Each mode shape is normalized with respect to the maximum displacement of the particular mode. A short discussion of the mode shapes follows.

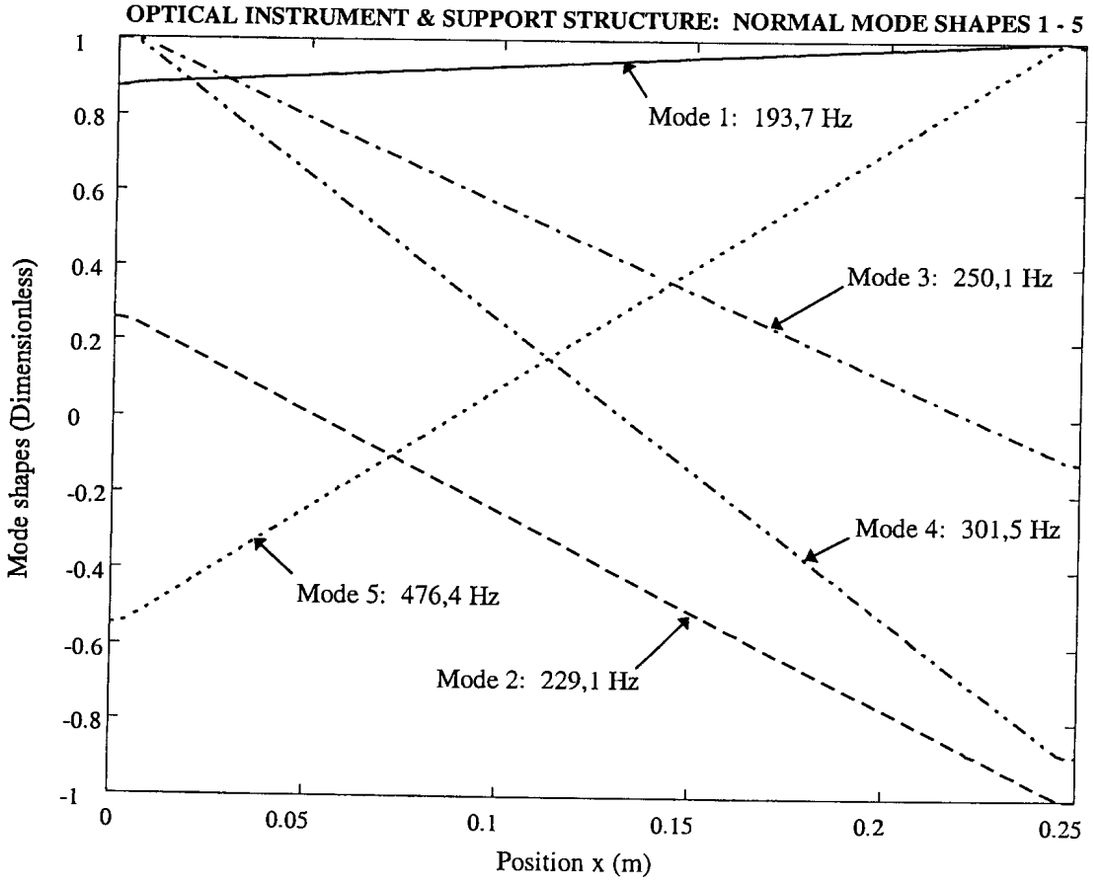

Figure 5.6.1: First five mode shapes of the optical instrument and support structure

It can be seen from figure 5.6.1 that translational motion dominates in the 1st mode. The modal displacements at the ends of the support structure, i.e. at x = 0 and x = 0,25 m, differ by approximately 10%. The mode shape is not entirely translational, which can be attributed to unequal actuator stiffnesses, as shown in table 5.6.1. (A possible cause of the unequal stiffnesses is slight distortion of the actuator flexures during assembly). It can further be seen from figure 5.6.1, that rotational motion dominates in the 4th mode. The modal displacement at x = 0 is approximately equal to that at x = 0,25 m, but of opposite sign.

An almost constant displacement separates the 2nd and 3rd mode shapes. A possible explanation is that, at 229 Hz and 250 Hz, the two actuators behave like dynamic absorbers. At 229 Hz, actuator I *passively* cancels the motion at x = 0, with the result that the support structure displacement is relatively small at that position. Similarly, at 250 Hz, actuator II cancels the support structure motion at x = 0,25 m. Note that the 2nd and 3rd mode shapes, as shown in figure 5.6.1, did not appear in the original mode shapes calculated in section 2.8.

The 5th normal mode shape results from the elastically mounted base. This mode is not closely coupled to the other four normal modes.

The 1st to 4th natural frequencies of the updated model differ from the experimentally determined frequencies by 3,9%, 0,79%, 1,2% and 0,17% respectively (see also table 4.5.2.1). Accuracy of the model will be further improved in the next section, when damping and forcing terms are added and the mechanical subsystem model is coupled to the coil model.

The 6th to 13th normal mode shapes are not shown. These mode shapes occur at frequencies ranging from 5 kHz to 710 kHz. Since the acquisition frequency of the signal analyzer used in the experimental tests was 1280 Hz (see section 4.4.6), the model can only be updated for frequencies up to the Nyquist frequency, i.e. 640 Hz.

Updated system state-space and transfer function model

The system modal equations of motion are given by:

$$M^*\ddot{q}_n + C^*\dot{q}_n + K^*q_n = \Phi_s^T F_I I \tag{5.6.1}$$

where M^*, C^* and K^* respectively represent the modal mass, modal damping coefficient and modal stiffness. Φ_s is the optical instrument normal mode shape vector, I is the coil current and F_I is the force per unit current. The current is given by equations 5.4.2.3 and 5.4.2.4.

Premultiplication of equation 5.6.1 with M^{*-1} and simplification of the resulting equation gives:

$$\ddot{q}_n + 2Z\Omega\dot{q}_n + \Omega^2 q_n = M^{*-1}Q \tag{5.6.2}$$

where Z is the modal damping matrix, Ω is the modal natural frequency matrix and Q is the modal force input vector, given by:

$$Q = \Phi_s^T F_I I \tag{5.6.3}$$

Z and Ω are diagonal matrices, whose sizes correspond with the number of normal modes in a given frequency band. For the first five normal modes, Z and Ω are 5 x 5 square matrices each. Q is a 5 x 1 vector.

The optical instrument angular acceleration, in terms of the modal accelerations, is:

$$\ddot{\theta} = \frac{\Phi_s(x_2) - \Phi_s(x_1)}{x_2 - x_1}\ddot{q}_n \tag{5.6.4}$$

where x_1 and x_2 respectively represent the longitudinal coordinates of the accelerometer attachment points.

Equations 5.6.2 and 5.6.4 are written as follows in state-space form:

$$\begin{Bmatrix}\dot{q}_n\\ \ddot{q}_n\end{Bmatrix}=\begin{bmatrix}[0] & [I]\\ -\Omega^2 & -2Z\Omega\end{bmatrix}\begin{Bmatrix}q_n\\ \dot{q}_n\end{Bmatrix}+\begin{bmatrix}[0]\\ M^{*-1}\end{bmatrix}Q \tag{5.6.5a}$$

$$\ddot{\theta}=\frac{\Phi_s(x_2)-\Phi_s(x_1)}{x_2-x_1}\begin{bmatrix}-\Omega^2 & -2Z\Omega\end{bmatrix}\begin{Bmatrix}q_n\\ \dot{q}_n\end{Bmatrix}+\frac{\Phi_s(x_2)-\Phi_s(x_1)}{x_2-x_1}M^{*-1}Q \tag{5.6.5b}$$

Combination of equations 5.4.2.3 to 5.4.2.5, 5.6.3 and 5.6.5 results in the following state equation for the coupled system:

$$\begin{Bmatrix}\dot{q}_n\\ \ddot{q}_n\\ \dot{x}_c\end{Bmatrix}=\begin{bmatrix}[0] & [I] & [0]\\ -\Omega^2 & -2Z\Omega & M^{*-1}\Phi_s^T F_l C_c\\ [0] & [0] & A_c\end{bmatrix}\begin{Bmatrix}q_n\\ \dot{q}_n\\ x_c\end{Bmatrix}+\begin{bmatrix}\{0\}\\ \{0\}\\ B_c\end{bmatrix}V \tag{5.6.6}$$

where A_c, B_c and C_c are the coil state and output matrices given in equations 5.4.2.4. Numerical values of the coil state matrix elements are given in table 5.4.2.1.

The system output equation is given by:

$$\ddot{\theta}=\frac{\Phi_s(x_2)-\Phi_s(x_1)}{x_2-x_1}\begin{bmatrix}-\Omega^2 & -2Z\Omega & M^{*-1}\Phi_s^T F_l C_c\end{bmatrix}\begin{Bmatrix}q_n\\ \dot{q}_n\\ x_c\end{Bmatrix} \tag{5.6.7}$$

The system state and output equations are written as follows:

$$\begin{aligned}\dot{x}&=Ax+B_V V\\ y&=Cx+D_V V\end{aligned} \tag{5.6.8}$$

where A, B_V, C and D_V are respectively given by:

$$A=\begin{bmatrix}[0] & [I] & [0]\\ -\Omega^2 & -2Z\Omega & M^{*-1}\Phi_s^T F_l C_c\\ [0] & [0] & A_c\end{bmatrix} \tag{5.6.9a}$$

$$B_V=\begin{bmatrix}\{0\} & \{0\} & B_c\end{bmatrix}^T \tag{5.6.9b}$$

$$C=\frac{\Phi_s(x_2)-\Phi_s(x_1)}{x_2-x_1}\begin{bmatrix}-\Omega^2 & -2Z\Omega & M^{*-1}\Phi_s^T F_l C_c\end{bmatrix} \tag{5.6.9c}$$

$$D_V=0 \tag{5.6.9d}$$

The sizes of the A, B_V, C and D_V matrices are 13 x 13, 13 x 1, 1 x 13 and 1 x 1 respectively. Note that the order of the system is lower than that of the frequency domain TF described in section 5.3.

The undamped angular natural frequencies (Ω), damping factors (Z) and input forces per unit current per unit mass $\left(M^{*-1}\Phi_s^T F_I\right)$ of the first five normal modes are given in table 5.6.2.

Table 5.6.2: Modal frequency, damping factor and force per unit mass per unit current

Mode number	f_n (Hz)	Ω (rad/s)	Z (%)	$M^{*-1}\Phi_s{}^T F_I$ (N/kg/A)
1	193,62	1216,6	4,00	35,242
2	230,17	1446,2	1,75	-7,9059
3	250,10	1571,4	3,55	-2,9391
4	299,11	1879,4	3,04	-103,72
5	476,37	2993,1	1,20	65,347

The signs of the $M^{*-1}\Phi_s^T F_I$ terms for the 2nd to 4th modes differ from those of the 1st and 5th modes. The reason is that the signs of the displacements of the 2nd to 4th modes at the attachment point of actuator II, i.e. at x = 0,25 m, differ from those of the 1st and 5th modes (see figure 5.6.1).

The transfer function between input voltage and output angular acceleration is obtained by substitution of equations 5.6.9 into equation 2.5.2.1. The transfer function $G(s)$, in numerator and denominator polynomial form, is:

$$G(s) = \frac{\sum_{k=0}^{M} p_k s^k}{\sum_{l=0}^{N} q_l s^l} \qquad \textbf{(5.6.10)}$$

The TF numerator and denominator polynomial coefficients are given in table 5.6.3.

A block diagram of the system is shown in figure 5.6.2. The electrical and mechanical subsystems, subsystem inputs and outputs, subsystem coupling, modal excitation forces, accelerations, velocities and displacements, as well as system output angular acceleration, are indicated.

In figure 5.6.2, V is the coil input voltage, G_c is the coil transfer function, I is the coil current, F_I is the force per unit current, Φ_s is the normal mode shape vector and Q is the modal excitation force. M^*, C^* and K^* respectively represent the modal mass, modal damping coefficient and modal stiffness. $\ddot{\theta}$ is the angular acceleration of the optical instrument, s is the complex Laplace domain differential operator, x_1 and x_2 are the longitudinal coordinates of the accelerometer attachment points.

Table 5.6.3: *TF* numerator & denominator polynomial coefficients

Coefficient	Value
p_0	0
p_1	0
p_2	$-8{,}4062.10^{36}$
p_3	$-3{,}3157.10^{33}$
p_4	$-1{,}4211.10^{31}$
p_5	$-4{,}8225.10^{27}$
p_6	$-8{,}4473.10^{24}$
p_7	$-2{,}4310.10^{21}$
p_8	$-2{,}0674.10^{18}$
p_9	$-4{,}8705.10^{14}$
p_{10}	$-1{,}7883.10^{11}$
p_{11}	$-3{,}0275.10^{7}$
p_{12}	$-3{,}6572.10^{3}$
q_0	$3{,}2766.10^{41}$
q_1	$9{,}1519.10^{38}$
q_2	$1{,}2393.10^{36}$
q_3	$2{,}0897.10^{33}$
q_4	$1{,}6119.10^{30}$
q_5	$1{,}8762.10^{27}$
q_6	$9{,}8145.10^{23}$
q_7	$8{,}4358.10^{20}$
q_8	$3{,}0026.10^{17}$
q_9	$1{,}9869.10^{14}$
q_{10}	$4{,}3527.10^{10}$
q_{11}	$2{,}2966.10^{7}$
q_{12}	$2{,}2632.10^{3}$
q_{13}	1

The updated model *TF* magnitude and phase spectra, for a frequency band of 0 Hz to 500 Hz, are shown in figure 5.6.3. A comparison between the updated model *TF* spectra and the experimentally determined spectra is shown in figure 5.6.4. A pole-zero diagram of the updated model *TF* is shown in figure 5.6.5. The poles and zeroes are respectively indicated by crosses and circles. All the real parts of the poles and zeroes are negative, indicating that the updated system model is stable and minimum phase.

The input voltage to angular acceleration *TF*'s of the individual normal modes are shown in figure 5.6.6. From the figure, it can be seen that the 4th mode is the dominating mode in the frequency range of 0 Hz to 500 Hz. The relative contributions of the 1st and 2nd modes are approximately one order below that of the 4th mode, while those of the 3rd and 5th modes are approximately two orders below that of the 4th mode.

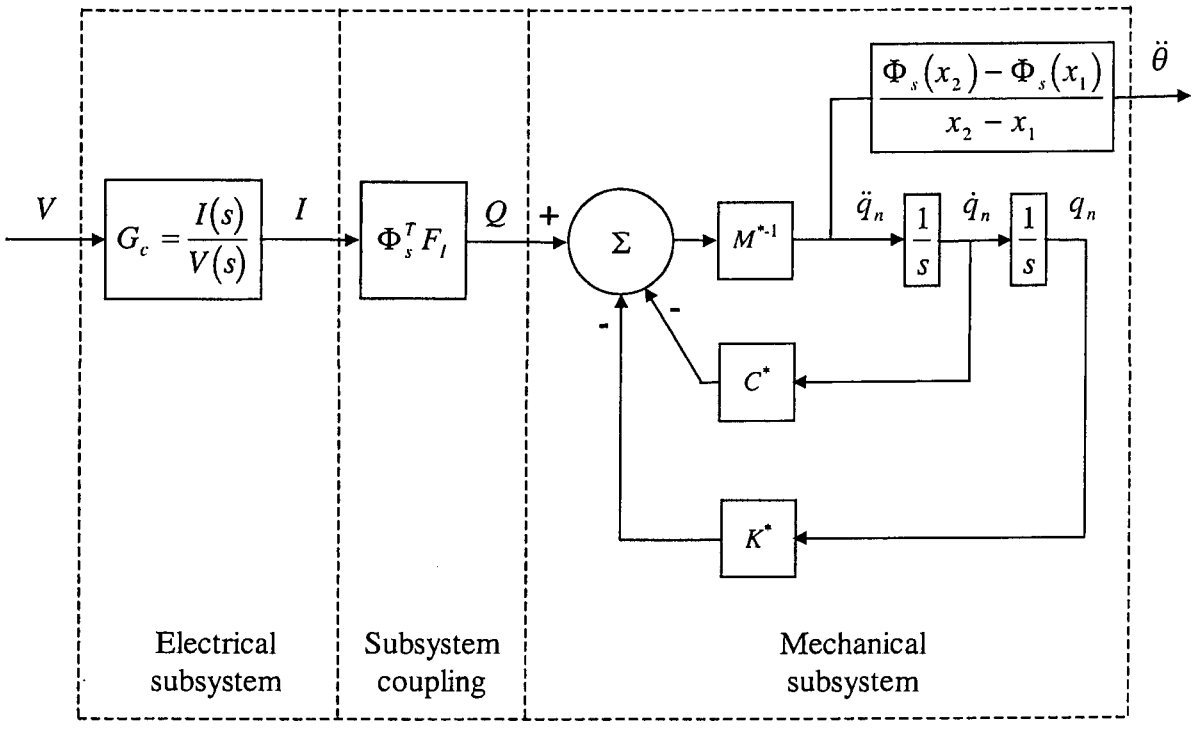

Figure 5.6.2: Updated system model block diagram

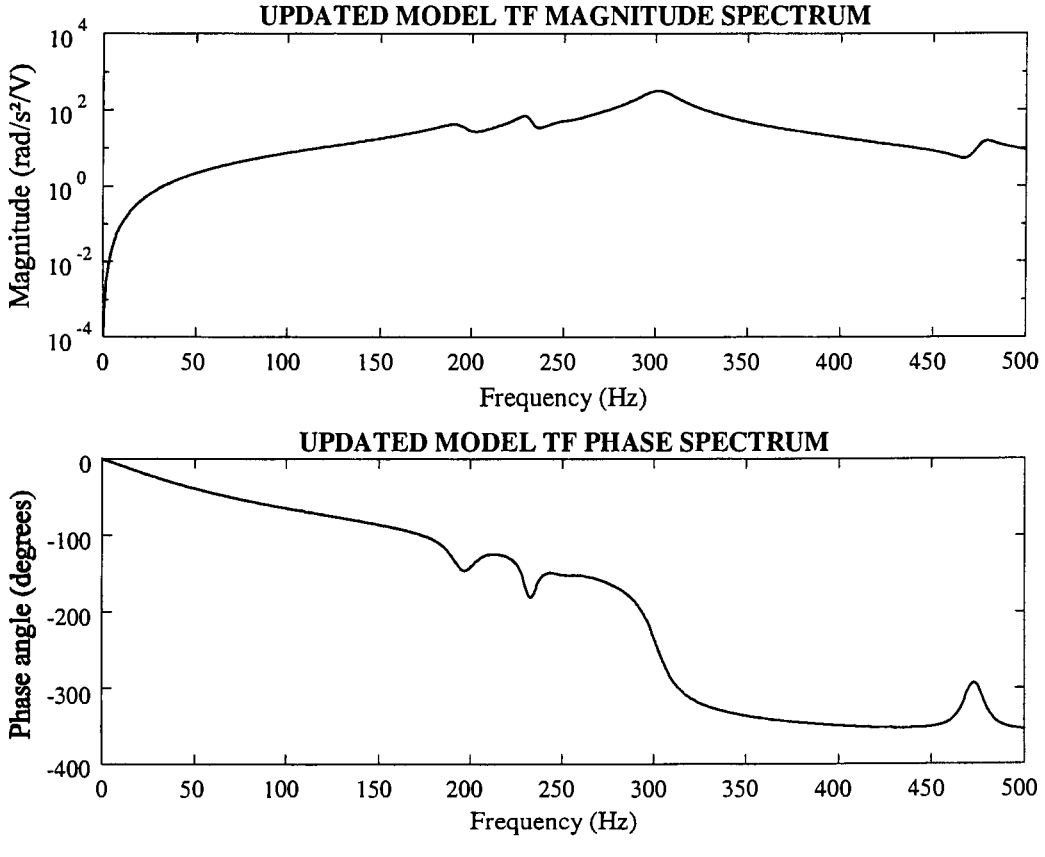

Figure 5.6.3: Updated model *TF* spectra

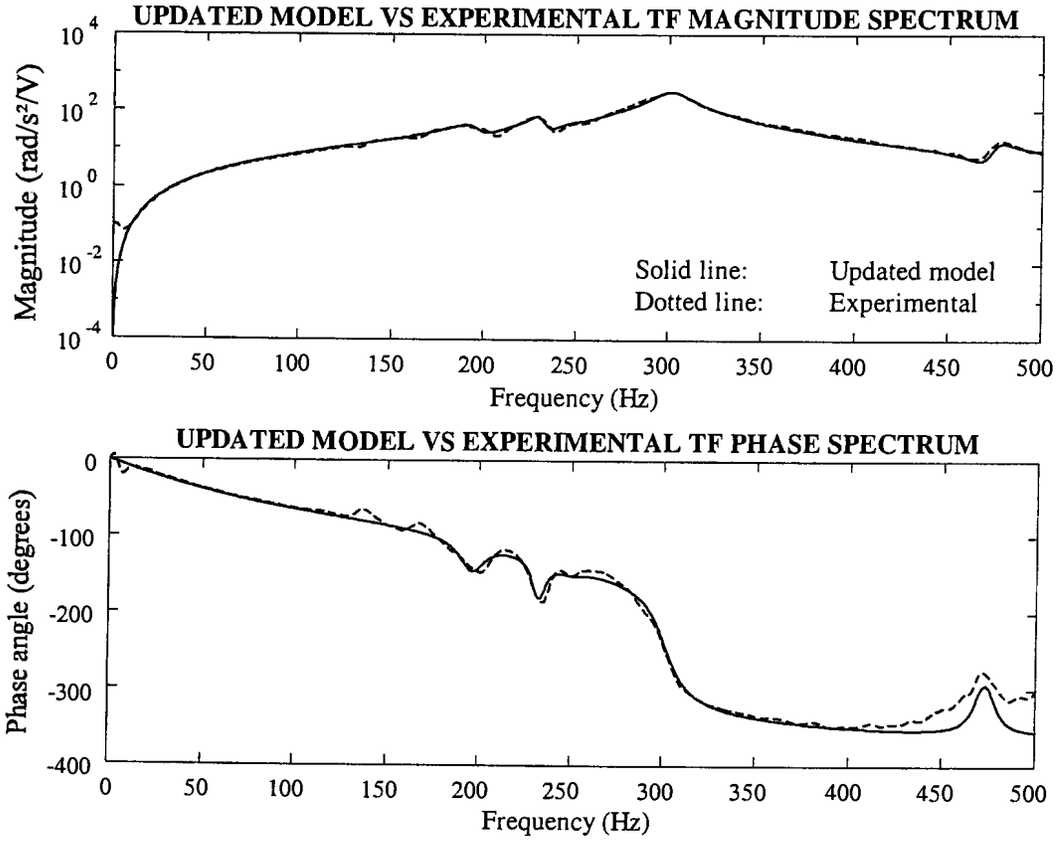

Figure 5.6.4: Comparison between updated model *TF* and experimental *TF* spectra

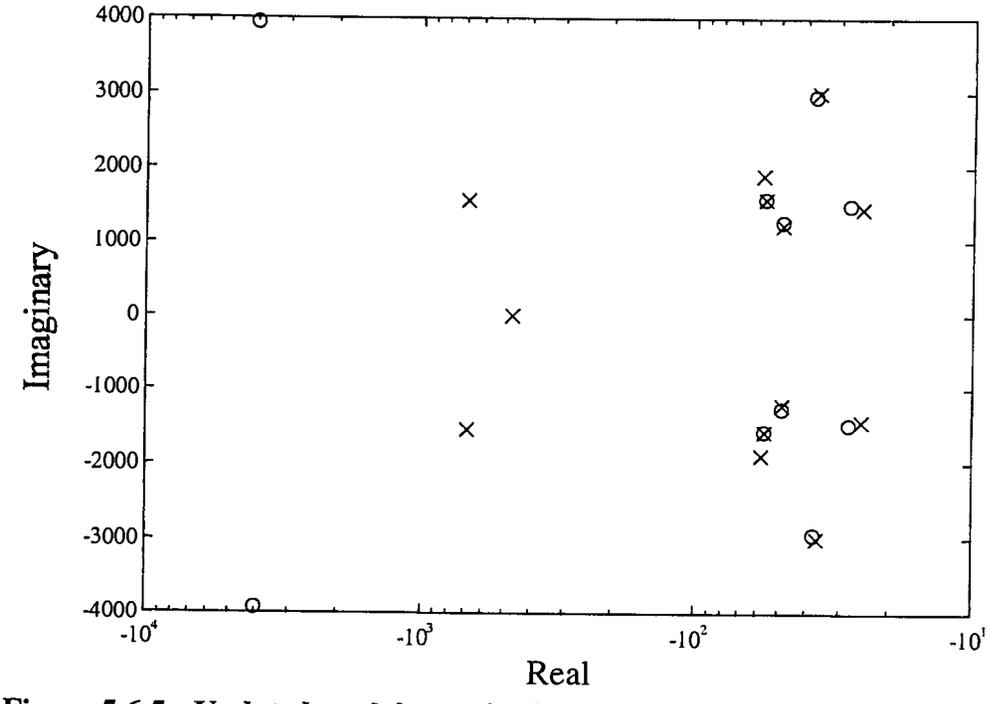

Figure 5.6.5: Updated model transfer function pole-zero diagram

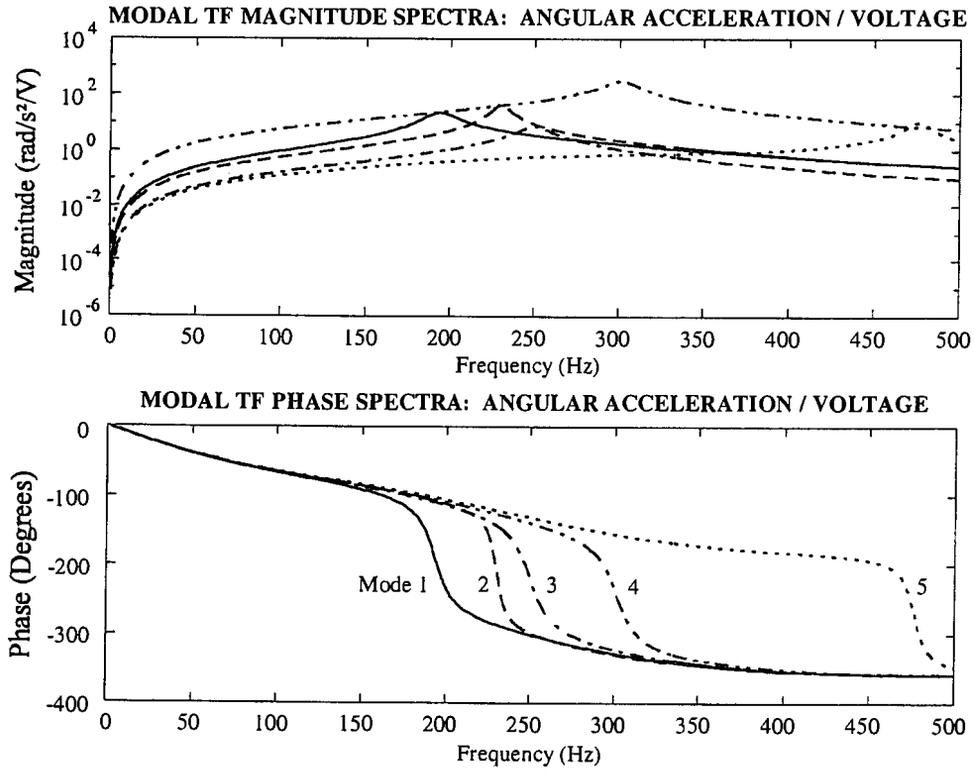

Figure 5.6.6: Modal transfer function spectra

In order to determine the system isolation bandwidth (BW), the coil voltage to instrument angular *displacement TF* is analyzed, instead of the voltage to angular *acceleration TF*. The *TF* magnitude is shown in figure 5.6.7, together with the -3 dB and disturbance bandwidths.

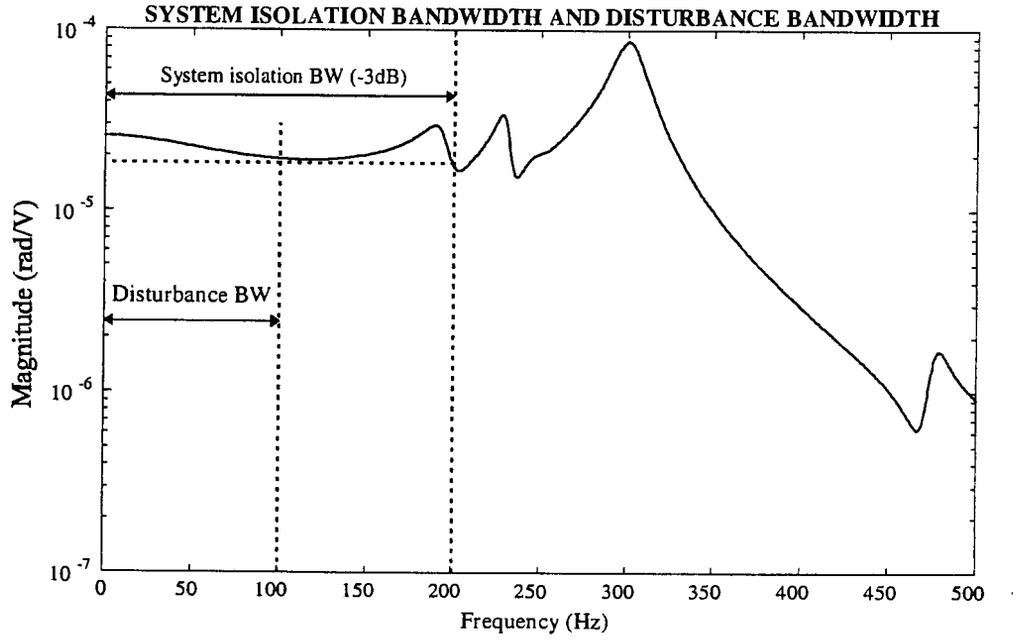

Figure 5.6.7: System isolation bandwidth and disturbance bandwidth

The *TF* magnitude at 0 Hz is $2{,}57.10^{-5}$ rad/V. The lowest frequency where the magnitude is 3 dB below this value, i.e. $1{,}81.10^{-5}$ rad/V, is 199 Hz. This frequency is almost double the maximum frequency of the disturbance, i.e. 100 Hz. It can therefore be concluded that the system isolation bandwidth is sufficient, despite the fact that the coil bandwidth is only 84 Hz (see section 5.4.2).

System base to output transmissibility

System transmissibility (*TR*) can be expressed in terms of a number of transfer functions, such as the input force to output force *TF*, base angular displacement to output angular displacement *TF* (θ/θ_b), base angular velocity to output angular velocity *TF* ($\dot{\theta}/\dot{\theta}_b$) and base angular acceleration to output angular acceleration *TF* ($\ddot{\theta}/\ddot{\theta}_b$). The most appropriate transfer function, is mainly determined by the sensors used for system characterization and control.

Accelerometers were used for dynamic system characterization in chapter 4. The measured vertical accelerations were subsequently used to calculate the base and output angular accelerations (see section 4.5.1). Accelerometers will also be used as sensors during testing of the control system, which will be described in more detail chapter 6. It is therefore appropriate to express the *TR* as the transfer function between base angular acceleration and output angular acceleration ($\ddot{\theta}/\ddot{\theta}_b$).

The transmissibility is required in terms of system characteristics, such as state and output parameters, natural frequencies, damping factors and normal mode shapes. A derivation of the *TR* is given in appendix W. In order to simplify the derivation, an assumption is made that the *TR* is independent of sensor dynamics. The consequence of this assumption is that the transfer functions, θ/θ_b, $\dot{\theta}/\dot{\theta}_b$ and $\ddot{\theta}/\ddot{\theta}_b$, are equal over a wide frequency bandwidth. This makes it possible to derive the transfer function θ/θ_b and set it equal to $\ddot{\theta}/\ddot{\theta}_b$:

$$TR = \frac{\ddot{\theta}}{\ddot{\theta}_b} = \frac{-\omega^2\theta}{-\omega^2\theta_b} = \frac{\theta}{\theta_b} \qquad \textbf{(5.6.11)}$$

The component mode synthesis method, which was described in detail section 5.5, is used to determine the *TR*. The *TR* is determined independently of any coil voltage input, and therefore does not contain any coil parameters. A state-space model is obtained for the mechanical subsystem, which is subsequently written in *TF* form.

The modal equation of motion (see appendix W), is:

$$\ddot{q}_n + 2Z\Omega\dot{q}_n + \Omega^2 q_n = M^{*-1}Q \qquad \textbf{(5.6.12)}$$

where Q is the modal force vector (see appendix W).

The modal state and output equations are written as follows:

$$\dot{x} = A_b x + B_b \theta_b \tag{5.6.13a}$$

$$\theta = C_b x + D_b \theta_b \tag{5.6.13b}$$

The state vector x is:

$$x = \begin{Bmatrix} q_n \\ \dot{q}_n \end{Bmatrix} \tag{5.6.14}$$

A_b, B_b, C_b and D_b are respectively given by:

$$A_b = \begin{bmatrix} 0 & I \\ -\Omega^2 & -2Z\Omega \end{bmatrix} \tag{5.6.15a}$$

$$B_b = \begin{Bmatrix} \{0\} \\ M^{*-1} U^T C^T \begin{Bmatrix} \{0\} \\ \{0\} \\ l\psi_{a2}^T \begin{Bmatrix} k_{211} \\ k_{222} \end{Bmatrix} \end{Bmatrix} \end{Bmatrix} \tag{5.6.15b}$$

$$C_b = \begin{Bmatrix} \dfrac{\Phi_s(x_2) - \Phi_s(x_1)}{x_2 - x_1} & \{0\} \end{Bmatrix} \tag{5.6.15c}$$

$$D_b = 0 \tag{5.6.15d}$$

The sizes of A_b, B_b, C_b and D_b are 24 x 24, 24 x 1, 1 x 24 and 1 x 1 respectively (see appendix W).

Combination of equations 5.6.13 to 5.6.15 gives:

$$\begin{Bmatrix}\dot{q}_n\\ \ddot{q}_n\end{Bmatrix}=\begin{bmatrix}0 & I\\ -\Omega^2 & -2Z\Omega\end{bmatrix}\begin{Bmatrix}q_n\\ \dot{q}_n\end{Bmatrix}+\begin{Bmatrix}\{0\}\\ M^{*-1}U^TC^T\begin{Bmatrix}\{0\}\\ \{0\}\\ l\psi_{a2}^T\begin{Bmatrix}k_{211}\\ k_{222}\end{Bmatrix}\end{Bmatrix}\end{Bmatrix}\theta_b \qquad \textbf{(5.6.16a)}$$

$$\theta=\begin{bmatrix}\dfrac{\Phi_s(x_2)-\Phi_s(x_1)}{x_2-x_1} & \{0\}\end{bmatrix}\begin{Bmatrix}q_n\\ \dot{q}_n\end{Bmatrix} \qquad \textbf{(5.6.16b)}$$

The system transmissibility is the *TF* between θ_b and θ is given by:

$$\frac{\theta}{\theta_b}=C_b\left[sI-A_b\right]^{-1}B_b \qquad \textbf{(5.6.17)}$$

By application of equation 5.6.11, the *TR*, which is also the *TF* between $\ddot{\theta}_b$ and $\ddot{\theta}$, is given by:

$$\frac{\ddot{\theta}}{\ddot{\theta}_b}=C_b\left[sI-A_b\right]^{-1}B_b \qquad \textbf{(5.6.18)}$$

The number of state equations, for the selected number of actuator and optical instrument assumed modes, is 24. The system as described by equations 5.6.16, has 24 eigenvalues in complex conjugate pairs. However, many of the eigenvalues occur at high frequencies, well above the bandwidth, and have no significant effect on system performance inside the band. States corresponding with these frequencies, can therefore be eliminated. This was also done for the coil voltage input, where, apart from the three coil states, only the first ten mechanical subsystem states were retained. For the base input, the 5th and 10th states (corresponding with the 5th normal mode) are eliminated, while the 1st to 4th and 6th to 9th states (corresponding with the first four normal modes) are retained.

The transmissibility magnitude and phase spectra , for a frequency bandwidth of 0 to 500 Hz, are shown in figure 5.6.8.

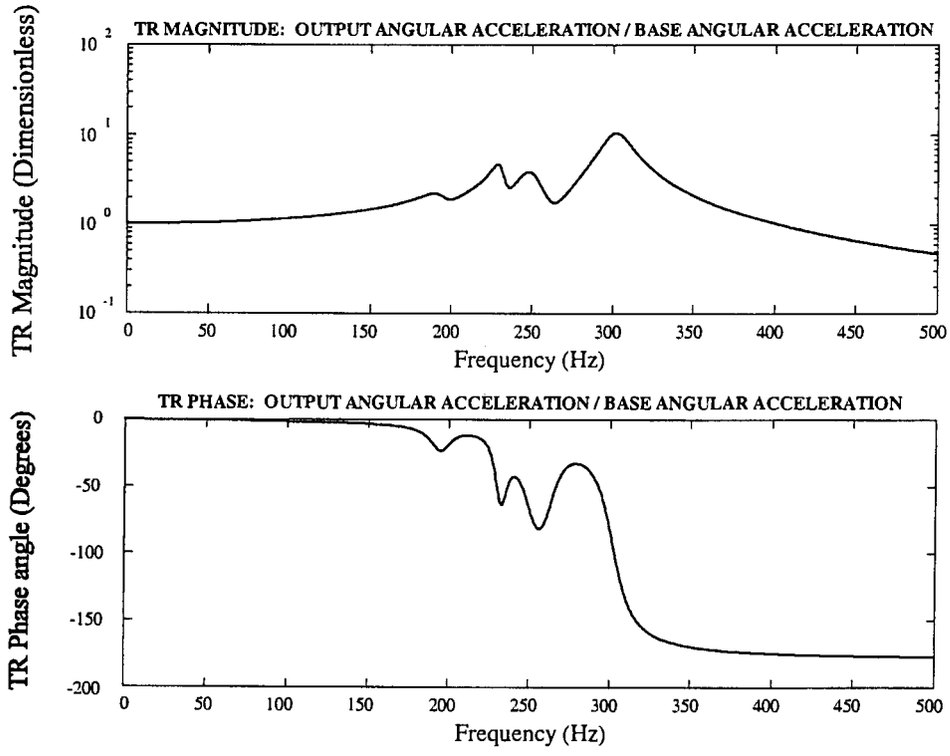

Figure 5.6.8: System base to output transmissibility spectra

Two-input state-space model for control system analysis and design purposes

The state-space model of the system currently consists of two separate state models, one for the coil voltage input, given by equations 5.6.6 to 5.6.9, and one for the base angular acceleration input, given by equations 5.6.13 to 5.6.18. For the purpose of analyzing and designing the control system, it is convenient to combine the two state models into a single state model, with two simultaneous inputs, i.e. coil voltage and base angular acceleration. The coil voltage is the controllable input, while the base motion is the uncontrollable input, or disturbance. The state and output equations, for these two inputs, are:

$$\dot{x} = Ax + B\begin{Bmatrix} V \\ \ddot{\theta}_b \end{Bmatrix} \qquad \textbf{(5.6.19a)}$$

$$\ddot{\theta} = Cx + D\begin{Bmatrix} V \\ \ddot{\theta}_b \end{Bmatrix} \qquad \textbf{(5.6.19b)}$$

The state vector, from equation 5.6.6, is:

$$x = \begin{Bmatrix} q_n \\ \dot{q}_n \\ x_c \end{Bmatrix} \qquad \textbf{(5.6.20)}$$

A is the system coefficient matrix, given in equation 5.6.9a:

$$A = \begin{bmatrix} [0] & [I] & [0] \\ -\Omega^2 & -2Z\Omega & M^{*-1}\Phi_s^T F_l C_c \\ [0] & [0] & A_c \end{bmatrix} \tag{5.6.21}$$

The first ten rows and columns of A correspond with A_b in equation equation 5.6.15a.

B is a matrix with two vector columns:

$$B = [B_V \quad B_{\ddot{\theta}b}] \tag{5.6.22}$$

B_V is given by equation 5.6.9b:

$$B_V = \begin{Bmatrix} \{0\} \\ \{0\} \\ B_c \end{Bmatrix} \tag{5.6.23a}$$

For the first four normal modes $B_{\ddot{\theta}b}$ is given by:

$$B_{\ddot{\theta}b} = \begin{Bmatrix} \{B_b\}_{rows\,1-4} \\ 0 \\ \{B_b\}_{rows\,13-16} \\ 0 \\ \begin{Bmatrix} 0 \\ 0 \\ 0 \end{Bmatrix} \end{Bmatrix} \tag{5.6.23b}$$

C is the output matrix given in equation 5.6.9c:

$$C = \frac{\Phi_s(x_2) - \Phi_s(x_1)}{x_2 - x_1}\begin{bmatrix} -\Omega^2 & -2Z\Omega & M^{*-1}\Phi_s^T F_l C_c \end{bmatrix} \tag{5.6.24}$$

D is a row vector with two zero elements:

$$D = \{0 \quad 0\} \tag{5.6.25}$$

Note that the C-matrix in equation 5.6.24 corresponds with the C-matrix in equation 5.6.9c. However, this C-matrix does not correspond with C_b in equation 5.6.15c. In order to obtain a C-matrix, which is valid for both inputs, the elements of $B_{\ddot{\theta}b}$ are modified as explained in short in the following paragraphs. A more complete explanation is provided in appendix W.

The procedure is as follows: Equations 5.6.16 are written in canonical form, whereby uncoupled state and output equations for each normal mode are obtained. Each modal state equation is then written as follows in *TF* form, using equation 5.6.11:

$$\left(\frac{\ddot{\theta}}{\ddot{\theta}_b}\right)_i = \left(\frac{\theta}{\theta_b}\right)_i = C_i\left[sI - A_i\right]^{-1} B_i \qquad \textbf{(5.6.26)}$$

where the subscript i denotes the i-th normal mode. The sizes of A_i, B_i, C_i and D_i are respectively 2 x 2, 2 x 1, 1 x 2 and 1 x 1.

For the i-th mode, equation 5.6.26 can be expressed as follows in numerator and denominator polynomial form:

$$\left(\frac{\ddot{\theta}}{\ddot{\theta}_b}\right)_i = \left(\frac{p_1 s + p_0}{s^2 + q_1 s + q_0}\right)_i \qquad \textbf{(5.6.27)}$$

where the numerator and denominator polynomial coefficients are given by:

$$p_{0i} = \left(-A_{11}B_2C_2 + A_{12}B_2C_1 + A_{21}B_1C_2 - A_{22}B_1C_1\right)_i \qquad \textbf{(5.6.28a)}$$

$$p_{1i} = \left(B_1C_1 + B_2C_2\right)_i \qquad \textbf{(5.6.28b)}$$

$$q_{0i} = \left(A_{11}A_{22} - A_{12}A_{21}\right)_i \qquad \textbf{(5.6.28c)}$$

$$q_{1i} = \left(-A_{11} - A_{22}\right)_i \qquad \textbf{(5.6.28d)}$$

Equations 5.6.9 are subsequently written in canonical form to obtain an uncoupled state and output equation for each of the first four normal modes. The modal state equation for the i-th mode is then written as follows, in the *TF* form of equation 5.6.26:

$$\left(\frac{\ddot{\theta}}{V}\right)_i = C_i\left[sI - A_i\right]^{-1} B_i \qquad \textbf{(5.6.29)}$$

From equations 5.6.28a and 5.6.28b, B_{1i} and B_{2i} for the i-th mode are determined as follows:

$$\begin{Bmatrix} B_1 \\ B_2 \end{Bmatrix}_i = \begin{bmatrix} C_1 & C_2 \\ A_{21}C_2 - A_{22}C_1 & A_{12}C_1 - A_{11}C_2 \end{bmatrix}_i^{-1} \begin{Bmatrix} p_1 \\ p_0 \end{Bmatrix}_i \qquad \textbf{(5.6.30)}$$

where C_1 and C_2 are the elements of C_i in equation 5.6.29.

The resulting $B_{\ddot{\theta}b}$ -vector, is:

$$B_{\ddot{\theta}_b} = \left\{(B_1)_{i=1} \quad (B_1)_{i=2} \quad (B_1)_{i=3} \quad (B_1)_{i=4} \quad 0 \quad (B_2)_{i=1} \quad (B_2)_{i=2} \quad (B_2)_{i=3} \quad (B_2)_{i=4} \quad 0 \quad 0 \quad 0 \quad 0\right\}^T \qquad \textbf{(5.6.31)}$$

Equations 5.6.19 therefore become:

$$\begin{Bmatrix} \dot{q}_n \\ \ddot{q}_n \\ \dot{x}_c \end{Bmatrix} = \begin{bmatrix} [0] & [I] & [0] \\ -\Omega^2 & -2Z\Omega & M^{*-1}\Phi_s^T F_l C_c \\ [0] & [0] & A_c \end{bmatrix} \begin{Bmatrix} q_n \\ \dot{q}_n \\ x_c \end{Bmatrix} + \begin{bmatrix} B_V & B_{\ddot{\theta}b} \end{bmatrix} \begin{Bmatrix} V \\ \ddot{\theta}_b \end{Bmatrix} \qquad \textbf{(5.6.32a)}$$

$$\ddot{\theta} = \frac{\Phi_s(x_2) - \Phi_s(x_1)}{x_2 - x_1} \begin{bmatrix} -\Omega^2 & -2Z\Omega & M^{*-1}\Phi_s^T F_l C_c \end{bmatrix} \begin{Bmatrix} q_n \\ \dot{q}_n \\ x_c \end{Bmatrix} \qquad \textbf{(5.6.32b)}$$

Equations 5.6.32 will be used to design a suitable control system. Controller design, testing and implementing will be discussed in more detail in chapter 6.

5.7 Summary of chapter 5 and preview of chapter 6

Updating of the system model was described in this chapter. Model updating was motivated in section 5.1 and an updating procedure was given. Identification theory was discussed in short in section 5.2 and linear least-squares frequency domain identification was selected as the most suitable technique for this study.

In section 5.3, an updated *TF* model was obtained from the experimentally determined *TF* spectra, using the Gauss-Newton method. The order of the model was determined iteratively. The *TF* numerator and denominator polynomial coefficients were determined by means of a least-squares data fit to the experimentally determined spectra. The *TF* magnitude and phase spectra were calculated and compared with the measured spectra. It was shown that the accuracy of the updated model was sufficient. The poles and zeroes of the updated *TF* were calculated. It was shown that all the poles and zeroes, with the exception of one zero, have negative real parts and are inside the test band.

Separation of the coil and mechanical subsystem models was motivated in section 5.4 and the procedure was described. The coil *TF* model was separated from the system *TF* and written in canonical state-space form. 2DOF actuator models were developed in section 5.5 to replace the original SDOF models. The distributed mass and stiffness model developed for the optical instrument and support structure in section 2.8 was retained. An SDOF model was included to represent the elastically mounted base. Coupling of the actuator, base and optical instrument models by means of component mode synthesis was explained.

In section 5.6, a physical model was developed to aid in updating the natural frequencies and normal mode shapes. The model parameters were selected and adjusted until the modelled natural frequencies matched the exprimentally-determined frequencies. The normal mode shapes were calculated and modal damping and -force terms were added. A system state model was derived and written in *TF* form. The *TF* spectra were calculated and compared with the experimentally-determined *TF* spectra. *TF* poles and zeroes were calculated and it was shown that all the poles and zeroes have negative real parts. System open-loop transmissibility was obtained and shown graphically. A two-input state-space model was subsequently derived, with coil voltage and base angular acceleration as inputs.

Controller design, implementation and testing will be described in chapter 6. Various controller types will be discussed in section 6.2, followed by a discussion on disturbance attenuation methods in section 6.3. The controller design will be described in detail in section 6.4. The experimental test setup and test equipment will be discussed in section 6.5, followed by the test execution procedure in section 6.6. Test results will be presented and discussed in section 6.7. Chapter 6 will be summarized in section 6.8.

Chapter 6
Design, implementation and testing of a controller for the LOS stabilization system

6.1 Background

Control system design, implementation and testing are described in this chapter. General control theory is given as a background. Various controller types, i.e. feedforward, output and state feedback controllers, linear and nonlinear controllers, tracking controllers, regulators and optimal controllers, are discussed in short.

Principles of disturbance attenuation are discussed in more detail. The attenuation factor is defined and the nature of the disturbance is discussed. Requirements for disturbance and noise attenuation are given. An attenuation method for a known disturbance entering a system at a given point, is described. A short summary of optimal control, in terms of H_2 and H_∞ optimal criteria, is given. Other modern disturbance attenuation techniques, such as preshaping of command inputs, attenuation of a continuous disturbance by means of digital regulation, and "two-way" isolation, are discussed. Motion controllers, i.e. relative and absolute motion controllers, are described in detail.

Control system design specifications are given, followed by a discussion of general control system requirements, such as accuracy, stability, sensitivity, reaction speed, control effort, robustness, observability and controllability. The specifications and general requirements are used to select a suitable controller type. The control system design procedure is described and a detailed exposition of the controller design is given. The design of a suboptimal controller, coupled to a suboptimal observer, is described. These designs are derived from optimal controller and observer designs. Controller characteristics are expressed in terms of state-space models, transfer functions, and closed-loop poles and zeroes. In order to facilitate implementation of the controller, the controller transfer functions are converted to digital filter form.

The test apparatus, test procedure and execution are described. Three controller configurations, i.e. disturbance feedforward, output feedback and feedforward plus feedback configurations, are tested. Test data is processed and the test results are presented. The attenuation factor spectra are shown graphically and RMS attenuation factors are given. The test results are discussed.

The various controller types are discussed in section 6.2, followed by the disturbance attenuation methods in section 6.3. The controller design is described in detail in section 6.4. The test setup is shown in section 6.5 and the test equipment is discussed. A description of the test execution follows in section 6.6. The test results are presented and discussed in section 6.7. Finally, chapter 6 is summarized in section 6.8.

6.2 Summary of various controller types

A concise summary of various controllers is given in this section. The controllers are classified according to type and compared in terms of application, principles of operation, advantages and disadvantages.

A large number of controller types exist. These controllers can broadly be classified in one or more of the following categories: Open-loop feedforward-, closed-loop feedback-, linear-, nonlinear-, output-, state-, optimal-, reduced-order-, tracking controllers and regulators. These categories are discussed in short below.

6.2.1 Open-loop feedforward controllers

The principle of operation of open-loop controllers can be summarized as follows: On the basis of knowledge about the system and of past experience, a prediction is made of what the input should be to give the desired output; the input is adjusted accordingly [Schwarzenbach & Gill, 1986]. The output may, or may not, be measured. A feedforward controller is also known as a prefilter, series compensator, or feedforward compensator.

The purpose of a feedforward controller is to cancel out a significant part of a disturbance before it enters the system. Computation of the control requires a model of the system. The more closely the disturbance can be monitored and the more accurate the system model, the better will be the control [Schwarzenbach & Gill, 1986].

Open-loop controllers can perform well if external disturbances are relatively insignificant [Meirovitch, 1990]. However, the control depends only on the expected system behaviour, and not on the actual behaviour. If some unexpected factor causes the output to deviate from the desired output, there is no way of correcting the deviation.

A vast number of uncertainties, in the form of disturbances or plant variations, may cause the deviations, and every possible uncertainty may require a different design. In order to avoid repetitive design and testing, adaptive controllers can be used to do real-time adjustment of controller characteristics. Adaptive controllers are described in detail by Goodwin & Sin [1984], and will not be discussed any further in this study. Alternatively, open-loop control can be used in combination with closed-loop control, where the feedforward compensator attenuates the disturbance, and the feedback compensator provides the necessary corrective action, stability and robustness.

6.2.2 Closed-loop feedback controllers

In feedback control, the control takes into consideration the actual system behaviour, instead of the expected behaviour [Meirovitch, 1990]. Feedback is used in closed-loop controllers to decrease the sensitivity of the system to plant variations, to enable adjustment of the system transient response, to reject disturbances and to reduce steady-state tracking errors [Bishop, 1993]. Two main types of closed-loop controllers can be distinguished, i.e. output feedback

controllers and state feedback controllers. These two controller types are discussed in short in the next two sections.

6.2.3 Output feedback controllers

Output feedback controllers often used are PID controllers, rate feedback controllers, lead-lag compensators and frequency-shaping filters. The choice of a suitable controller depends on the control objective and the controller characteristic.

If accurate transient behaviour, in terms of overshoot, rise-time, settling-time and DC error is required, a PID controller is normally used. This controller type consists of a parallel combination of a proportional (P)-element, an integral (I)-element and a differential (D)-element, placed in the forward path of the closed-loop, with unity feedback. The P-element gains the output error to increase the control effort, the I-element integrates the error to obtain accurate steady-state behaviour, while the D-element lowers the overshoot peak. Simpler variations of PID controllers include PI- and PD controllers. PID controller design is described in detail by Schwarzenbach & Gill [1986].

In order to eliminate large initial transients that may damage a plant or may cause system malfunctioning, the PID controller discussed above may be removed and replaced by a minor feedback loop, which differentiates the output. This method of feedback control is known as rate feedback, or negative velocity feedback. Since it is not good practice to differentiate the output signal, due to the presence of noise, measurement of the output rate may be directly done, using an output rate sensor [Schwarzenbach & Gill, 1986].

If both control accuracy and high stability margins are essential, a phase compensator, such as a phase-lead-, phase-lag- or lead-lag filter, may be used. A phase lead compensator is a 1^{st} order filter, with high-pass characteristics, which increases the phase of the closed-loop system. The filter numerator and denominator coefficients determine the phase spectrum. Phase-lead compensation generally improves rise-time and reduces the amplitude of transient oscillations, but increases the bandwidth [Schwarzenbach & Gill, 1986].

A phase-lag filter is a 1^{st} order filter with low-pass filtering characteristics. Lag compen-sation reduces overshoot, but at the expense of rise-time. The limitations of lead- and lag filters are partially overcome by lead-lag filters. The lead- and lag elements may be combined into a single filter, or may be placed in series, separated by a buffer [Schwarzen-bach & Gill, 1986].

A frequency-shaping filter can be placed in the feedback loop to obtain the required plant frequency-domain behaviour. This can be achieved by, inter alia, pole assignment and optimal frequency shaping filter design techniques. Optimal frequency shaping is possible with LQG design, by including frequency-shaped weighting matrices in the quadratic cost functional [Meirovitch, 1990]. Pole assignment using output feedback is described by Brogan [1985]. Practically, output controllers can be implemented by placing digital filters between the sensors and plant.

6.2.4 State feedback controllers

In state-feedback control, the plant states are combined, either linearly or nonlinearly, to obtain the control signal. A large variety of state feedback controllers exist. Since it is impossible to discuss all the varieties here, a brief discussion is given on optimal-, static-, dynamic-, full-state feedback- and reduced-order controllers, as well as state feedback controllers using observers.

An optimal state feedback gain matrix can be determined which stabilizes the system, minimizes the control effort and meets the disturbance rejection criterion. Two of the most popular versions of optimal state feedback controllers, are H_2 and H_∞ controllers, the names of which are derived from their respective optimality criteria. Other versions of optimal controllers include bang-bang controllers, and optimal controllers designed by variational methods, as discussed in detail by Kirk [1970] and Meirovitch [1990]. More recently, optimal controllers have also been designed by application of genetic algorithms. A serious limitation of optimal state controllers is that they are seldom robust [Kuo, 1982]. In order to obtain sufficient robustness, modification of the controller design may be required. Robust design will be discussed in short in section 6.4.

State control can be directly done if the output is invertible, i.e. if the states can be obtained by inversion of the linear, or nonlinear, function $y(x)$, that expresses the outputs in terms of the states. This type of state control is known as static state control. The term "static" indicates that the relationship between the output and control is either a constant factor, or a nonlinear function of the output, but is independent of frequency. Static state controllers have no dynamics of their own, which limits their performance in terms of criteria such as optimality, stability and robustness. Static state controller design and stabilization are, however, relatively simple. Stability of the closed-loop system is only determined by its gain and phase margins.

If $y(x)$ is not invertible, for instance if the output matrix is singular, a state observer is required to reconstruct the states from measured outputs. This type of state control is known as dynamic state control, since the observer has its own dynamic behaviour, independent of that of the plant. Observer order is normally equal to, or less than, the plant order. If the observer order is equal to that of the plant, the observer is known as a full-state observer, and the controller is known as a full-state feedback controller. Observability and controllability are conditions for full-state feedback, and will be discussed in short in section 6.4.

In order to avoid interference of the observer with the plant, observer poles can be arbitrarily placed at twice the plant natural frequencies, as a rule-of-thumb. However, if plant natural frequencies are high, high sample rates may be required for accurate control, which may lead to excessively noisy measurement signals. As an alternative, optimal linear quadratic gaussian (LQG) observer design can be done, where both disturbance and output noise energy levels are taken into account to determine the observer gain matrix.

Estimation of all the plant states is impossible if the plant is not observable. However, in general, it is still possible to estimate the observable components of the states of such a plant; if the unobservable components decay extremely rapidly, this partial estimation may be adequate [Anderson & Moore, 1989]. Observers used for this purpose are known as reduced-order observers, the design of which is discussed in more detail by Anderson & Moore [1989]

and Meirovitch [1990]. It will be shown in section 6.4 that the magnetostrictive LOS stabilization system is observable.

Stability of a closed-loop linear state-feedback controlled system is determined by the signs of the real parts of the closed-loop eigenvalues. If the real parts of all the eigenvalues are negative, the system is unconditionally stable. The stability margin of a closed-loop state-controlled system can be obtained by means of the Nyquist criterion.

6.2.5 Linear controllers

A comprehensive range of linear controllers exists; a detailed description of which is beyond the scope of this study. Linear controllers can broadly be classified as linear state- and linear output controllers. The control signal generated by a linear state controller, is a linear combination of the states, while that generated by a linear output controller, is the product of the output and a transfer function with constant coefficients. The number of transfer functions depends on the number of controls and outputs. A single-input-single-output (SISO) controller has only one *TF*. The number of *TF*'s of a multiple-input-multiple-output (MIMO) controller, is the product of the number of output and control variables. For large MIMO systems, state control is generally more powerful than output control.

Linear control is applied to systems whose characteristics stay constant, or vary slightly with changes in states or outputs (e.g. weakly nonlinear systems), over the range of operation. Linear control is particularly popular because system characteristics and behaviour can be analyzed using the well-established linear systems theory.

Linear controllers make use of linear feedback and / or feedforward elements, with constant coefficients, to generate the plant control signal. Linear control design methods are, inter alia, optimal design (H_2 and H_∞) methods, robust design methods, frequency shaping and arbitrary pole placement. Stability of a linear closed-loop system is determined by the eigenvalues of the system coefficient matrix, or poles of the transfer functions.

Disadvantages of linear control arise from the fact that most dynamic systems display some degree of nonlinearity. This characteristic limits the application of linear controllers to weakly nonlinear systems. Where large changes in characteristics are encountered, linear control may lead to instability, unduly high input energy and inaccurate control [Slotine & Li, 1991]. Linear control is therefore not recommended for highly nonlinear systems. Nonlinear controllers are recommended for this purpose.

6.2.6 Nonlinear controllers

In nonlinear control, the control signal may either be a nonlinear function of the outputs, or a nonlinear function of the states. The former is known as nonlinear output control, while the latter is known as nonlinear state control.

Nonlinear control methods include input-output linearization, input-state linearization, sliding mode control, linearization by means of describing functions, nonlinear control using nonlinear

observers, and adaptive control. Nonlinear control design methods are described in detail by Gelb & VanderVelde [1968], Slotine & Li [1991] and Vidyasagar [1978].

If applied to highly nonlinear systems, the advantages of nonlinear control are higher accuracy, better stability and lower control effort. The disadvantages are a higher degree of complication in mathematical analysis and control hardware. One of the most difficult tasks in nonlinear control design is to find a feedback function that will linearize, as well as stabilize, the system. In the case of weakly nonlinear systems, however, linearization is less complicated, and linear control may often be directly applied.

6.2.7 Tracking controllers

Tracking control is defined as follows by Meirovitch [1990]: "The tracking problem is defined as the problem of designing a control input so as to cause the plant state to follow a given reference state. The linear tracking problem is the one in which the control is a linear function of the state".

Tracking control can be applied to this study, by controlling the relative angular acceleration between the base and instrument. The base and instrument accelerations are measured and the relative acceleration is calculated. The tracking error, which is the difference between the relative acceleration and (negative) base acceleration, is driven to zero.

The advantage of using a tracking controller for this application is that the relative acceleration is large, ideally equal in magnitude to the disturbance, and is therefore easily measurable. Sensor noise is comparatively small and therefore does not significantly influence controller performance, as long as the controller is operated outside the sensor noise frequency band.

The disadvantage is that, although control is closed-loop, the relative acceleration, instead of the output acceleration, is controlled. The main objective of LOS stabilization of the optical instrument is to minimize the output. A controller that drives the output to zero, or as close to zero as possible, will therefore be more applicable. This controller type is known as a regulator.

An example of a tracking controller that is of importance to this study, is a state observer. The observer estimates the states from the measured plant output, estimated output and control input. The observer error, which is the difference between the true states and estimated states, is driven to zero. The control is obtained from the estimated states.

More information on tracking controllers is given by Anderson & Moore [1989] and Kirk [1970].

6.2.8 Regulators

The following definition of the regulator problem is given by Meirovitch [1990]: "The regulator problem is defined as the problem of designing a control input so as to drive the plant from some initial state to a constant final state. Another way of defining the regulator problem is as one in which the reference input is constant. Because a simple coordinate transformation can translate the origin of the state-space to any constant point in the space, the regulator problem can be redefined as the problem of designing a control input, so as to drive the plant to the zero state. The linear regulator problem is the one in which the control is a linear function of the state." Since the output of a linear system can be described as a linear combination of the states, a controller that drives the output to zero, can also be classified as a regulator.

The presence of noise may make it difficult to drive the output to zero. For this reason, regulator design is often aimed at minimizing the output, instead of driving it to zero. Generally, regulated systems with low output magnitudes, wide disturbance frequency bands and high system cutoff frequencies, may experience serious noise effects.

The objective of this study is to minimize the output, in the presence of the base disturbance and measurement noise. The output is the angular acceleration of the optical instument, the base disturbance is the base angular acceleration, and the control is the actuator coil voltage. For this application, the aim is to obtain the coil voltage, which will attenuate the effects of the disturbance to such an extent that the output is minimized. Since the required output is significantly smaller than the base disturbance, any regulator considered for attenuation purposes, will therefore also have to be designed to minimize the effects of measurement noise.

6.2.9 Optimal controllers

Optimality of a control system is expressed in terms of a performance measure, the concept of which was originally introduced in classical controller design. Typical performance criteria are system response to a step or ramp input, characterized by rise-time, settling-time, peak overshoot and steady-state accuracy, and the frequency response of the system, characterized by gain and phase margin, peak amplitude and bandwidth [Kirk, 1970].

In modern, or optimal, control, the main goal is to minimize the performance measure, or performance index ("PI"), of a particular system or control problem. Typical optimal control problems are minimum-time, terminal control, minimum control effort, tracking control and regulator problems. (The PI's of each of these problems are given by Kirk [1970]).

Formulation of the PI is necessarily influenced by the control objective. The objective of a regulator, or instance, is to minimize the control effort required to drive the states (for a state regulator), or outputs (for an output regulator), to zero, or as close to zero as possible. Optimization of a regulator therefore requires that both the control and the states (or outputs), be minimized. Weights can be placed on any of the terms in the PI, to emphasize the relative importance of the particular term. For example, an increase in control weight will lower the control effort, while an increase in output weight will lower the output.

The PI may be expressed in linear quadratic (LQ) form, where the squared values of the relevant performance terms are weighed, summed and subsequently integrated over a given time period, which may be definite or indefinite. The value of the PI may be calculated to obtain the relative performance of a system. A low PI indicates better performance than a high PI, for the same plant.

If necessary, constraints can be imposed to limit, or bound, certain system variables or parameters, to ensure that the system operates within its ability. The performance of a constrained system may be the same as, or worse than, that of an unconstrained system. For instance, a regulator with a high output weight, whose control is constrained, may command a control signal in excess of the constraint. The control will be clipped as soon as it reaches the constraint, thereby sacrificing output performance. This may however not happen in the case of a regulator with a lower output weight.

Constraints may also be required to obtain relationships between the individual terms in the PI. An example is the state-space equations of a plant. The state equation provides the relationship between the states and control, while the output equation gives a relationship between the states and outputs.

State feedback gains of LQ optimal linear regulators are obtained from, inter alia, the solution of the steady-state Riccati equation. Derivation of the equation, from the PI and state equations, is described in detail by Anderson & Moore [1989] and Kirk [1970]. The Riccati equation is nonlinear, but can be solved in linear form by Hamiltonian eigenvector decomposition, as described by Meirovitch [1990].

Optimal control design principles are also applied to observer, or estimator design. An optimal observer is also known as a linear quadratic estimator, or Kalman filter. The objective of optimal observer design is to obtain the observer feedback gain matrix that will minimize the effects of input and output noise.

Optimal control is thoroughly described by Anderson & Moore [1989], Brogan [1985], Kirk [1970] and Meirovitch [1990].

6.2.10 Conclusion of section 6.2

Controllers considered for this study are made up of combinations of two or more of the controllers discussed in the foregoing sections. A suitable controller for the magnetostrictive LOS stabilization system will typically be a linear regulator, with sufficient disturbance attenuation, stability, robustness and optimality, for a bounded control voltage. The selection of a suitable type of controller for the LOS stabilization system will be covered in section 6.4.3.

6.3 Principles of disturbance attenuation

In this study, LOS stabilization of the optical instrument can be considered as a disturbance attenuation method. The disturbance is the base motion, which is transmitted to the optical instrument by the plant. The resulting motion of the optical instrument, i.e. the plant output, is the product of the disturbance and uncontrolled transmissibility of the plant.

The objective is to attenuate the effects of the base motion on the LOS accuracy of the optical instrument. To achieve this, the transmitted base motion must be attenuated to reduce the motion of the optical instrument to a significantly low fraction of the base motion. The ratio of the remaining output to the disturbance is known as the attenuation factor.

Base and optical instrument motions may be expressed in terms of variables such as angular displacements, speeds or accelerations. The choice of the most suitable variable will necessarily depend on the sensors used for measuring the motions. Since the sensors used in this study are accelerometers, the base and instrument motions will be expressed in terms of angular accelerations. (Although the sensors can only measure translational accelerations, angular accelerations can be obtained by dividing the difference between the measured signals by the distance between the sensors).

In this section, the attenuation factor is discussed in more detail. The nature of the disturbance is subsequently discussed. Requirements for attenuation of disturbances and noise are given, followed by a description of feedforward compensation of a known disturbance entering a system at a given point. Modern attenuation methods, i.e. optimal attenuation, preshaping of command inputs, digital regulation of continuous disturbances and two-way isolation, are discussed in short.

The application of disturbance attenuation methods is extended to motion controllers of various kinds, the most basic of which are relative and absolute motion controllers, disturbance feedforward (open-loop) controllers and a combination of disturbance feedforward and absolute motion controllers. A simple method for improving the robustness of optimal motion controllers, is discussed.

6.3.1 Attenuation factor

The isolation ability of the system can be expressed in terms of an attenuation factor, which is the ratio of the attenuated output, to the disturbance:

$$\gamma = \frac{y}{d} \qquad \textbf{(6.3.1.1)}$$

where γ is the attenuation factor, y is the attenuated output and d is the disturbance.

In disturbance attenuation, the ultimate goal is to drive the output to zero, in order to achieve total isolation. However, although this may be theoretically feasible, it is practically impossible to achieve. The reason is that the measured disturbance and output signals will almost always be contaminated with noise. As the output is driven to zero, its signal-to-noise

ratio approaches zero, thereby making feedback control extremely difficult. It is therefore more realistic to minimize the output, instead of driving it to zero.

At the other end of the scale, an attenuation factor of unity indicates that all the base motion is transmitted to the optical instrument, i.e. no isolation takes place. This may for instance happen in the trivial case of total absence of a stabilization system. When a stabilization system is present, but is not controlled, the attenuation factor may exceed unity. This will for instance happen if the base excites one or more of the natural frequencies of the plant. In this case, γ represents the transmissibility (TR) of the stabilization system, for zero control input. A properly designed isolation system must be able to attenuate both the disturbance and its dynamic effects on the plant.

The TR magnitude and phase spectra of the LOS stabilization system were shown in figure 5.6.8. From the figure, it can be seen that the TR magnitude is unity at DC and gradually increases with frequency, reaching local maxima at the natural frequencies, and local minima at anit-resonant frequencies. The TR magnitude is approximately unity in the disturbance frequency BW of 0 Hz to 100 Hz.

From the above discussion, it can be seen that a practically achievable goal for γ should be between zero and one:

$$0 \leq \gamma \leq 1 \tag{6.3.1.2}$$

The lower γ, the more effective the isolation.

Mathematical expression of the attenuation factor will depend on the control objective. A number of control objectives can be formulated to suit the need. Firstly, if the objective is to reduce a peak in the time trace of the output to a given fraction of that of the disturbance, γ can be expressed as:

$$\gamma = \frac{|y(t)|_{\max}}{|d(t)|_{\max}} \tag{6.3.1.3}$$

Secondly, if the objective is to attenuate the disturbance at the dominant frequency in the BW, the attenuation factor can be expressed as:

$$\gamma = \frac{Y(j\omega_d)}{D(j\omega_d)} \tag{6.3.1.4}$$

where ω_d is the dominant disturbance frequency.

In the third place, if the objective is to obtain an output whose magnitude is a constant fraction of that of the disturbance at each frequency in the disturbance *BW*, the attenuation factor can be expressed as:

$$\gamma(j\omega) = \frac{Y(j\omega)}{D(j\omega)} = const \qquad \textbf{(6.3.1.5)}$$

To obtain this attenuation factor, an isolation system is required which rejects a constant percentage of the disturbance at all the frequencies in the disturbance *BW*.

Lastly, if the objective is to minimize the ratio of output energy to disturbance energy over a given frequency bandwidth, the attenuation factor can be expressed as the ratio of the *RMS* of the output to that of the disturbance:

$$\gamma = \frac{y_{RMS}}{d_{RMS}} \qquad \textbf{(6.3.1.6)}$$

In this case, the attenuation factor is a constant scalar. It will however not necessarily be constant with frequency and may contain a spectrum of frequencies.

6.3.2 Nature of the disturbance

A disturbance can broadly be classified in terms of its type, whether the disturbance is known, and its position of entering the system. Disturbance types include, inter alia, wide-band random, band-limited random, narrowband, harmonic, transient, and DC disturbances, as well as measurement and system noise.

A distinction is often made between noise and disturbances, since the system characteristics required for disturbance attenuation differ from those required for noise attenuation [Anderson & Moore, 1989]. Disturbance and noise attenuation requirements will be discussed in section 6.3.3. A thorough comparison between different control methods for narrowband disturbance attenuation is given by Sievers & von Flotow [1992]. DC disturbance attenuation is described in detail by Kuo [1982].

A disturbance can be termed a known disturbance if it can be measured before control system design. The disturbance is measured and characterized in terms of parameters such as magnitude and phase spectra, power spectral density and RMS value. These parameters are used to design the controller in order to meet the control objective, e.g. to achieve a required RMS output. The control objective will be met as long as the known disturbance is the only disturbance entering the system. Unknown disturbances are necessarily more difficult to attenuate. To achieve this, sufficient robustness must be supplied by the feedback loop in order to compensate for the uncertainties. Attenuation of a known disturbance entering a system at a given position, by means of feedforward compensation, is described by Schwarzenbach & Gill [1986].

Disturbances may enter the system at the input or output, or may originate inside the system. An example of a disturbance entering the system at the input, is measurement noise

contaminating the reference signal of a tracking controller. An example of a disturbance entering the system at the output, is measurement noise contaiminating the output signal of a regulator. Input noise and output noise mainly originate from sensors and electromagnetic radiation, infiltrating the system through unscreened wires. System noise may originate from loose, rattling or faulty system components.

In the case of the LOS stabilization system, which is the topic of this study, the known disturbance is the angular acceleration of the mounting base of the optical instrument. The disturbance enters the system at the input. The unknown disturbances are base and output measurement noise, as well as seismic motion of the test setup, caused by environmental disturbances such as traffic.

6.3.3 Requirements for disturbance and noise attenuation

The requirements for disturbance and noise attenuation are discussed in short in this section. Sensitivity and complementary sensitivity functions, which provide an indication of the dependence of the tracking error, output and control signals, on the reference, disturbance and noise signals, are defined. The requirements for accurate tracking, disturbance and noise attenuation are expressed in terms of these functions.

The block diagram of a closed-loop controller is shown in figure 6.3.3.1. The reference input, output and tracking error signals are respectively denoted by r, y and e, while the output measurement noise and disturbance signals are represented by n and d. The control signal is denoted by u. The plant and controller transfer functions are represented by $G_p(s)$ and $G_c(s)$. (The TF's may either be vectors or scalars, depending on the number of inputs and outputs).

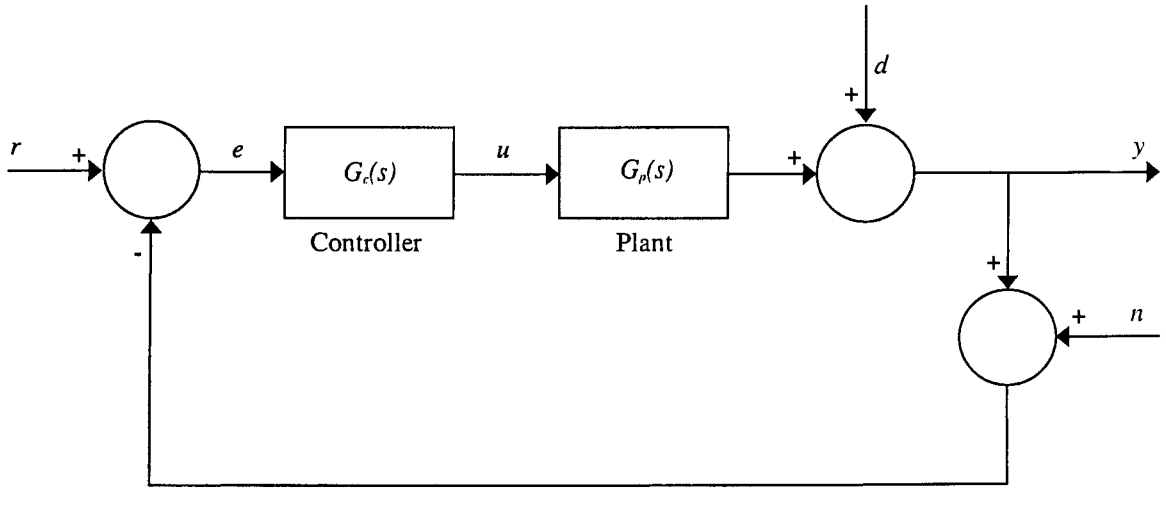

Figure 6.3.3.1: Block diagram of closed-loop controller, with disturbance and noise entering the system at the output [Anderson & Moore, 1989]

The sensitivity function S and complementary sensitivity function T, from Anderson & Moore, [1989], are given by:

$$S = \left(I + G_p G_c\right)^{-1} \tag{6.3.3.1a}$$

$$T = G_p G_c \left(I + G_p G_c\right)^{-1} \tag{6.3.3.1b}$$

where T is the complement of S:

$$S + T = I \tag{6.3.3.2}$$

The plant output y, measured tracking error e and control u can be expressed as follows in terms of S and T (the derivations are not done here, only the results are given):

$$y = T(r - n) + Sd \tag{6.3.3.3a}$$

$$e = S(r - n - d) \tag{6.3.3.3b}$$

$$u = G_c S(r - n - d) \tag{6.3.3.3c}$$

Requirements for accurate tracking, disturbance attenuation and noise attenuation, in terms of the sensitivity and complementary sensitivity functions, are discussed in detail by Anderson & Moore [1989].

The requirement for accurate tracking and good disturbance attenuation is:

$$\overline{\sigma}[S(j\omega)] << 1 \tag{6.3.3.4}$$

where $\overline{\sigma}$ denotes the largest singular value of S.

The requirement for good noise attenuation is:

$$\overline{\sigma}[T(j\omega)] << 1 \tag{6.3.3.5}$$

It can be seen from equations 6.3.3.2, 6.3.3.4 and 6.3.3.5, that there is an inconsistency between the requirements for good tracking and disturbance attenuation on the one hand, and noise attenuation on the other.

6.3.4 Attenuation of a known disturbance entering the system at a given point

A known disturbance entering a system at a given point can be attenuated by means of a feedforward compensator, in conjunction with a unit feedback loop [Schwarzenbach & Gill, 1986]. The disturbance signal is monitored and a control signal is obtained that partially attenuates the disturbance before it affects the system. This attenuation method is particularly applicable to this study, since the disturbance and its position of entering the system, i.e. the angular acceleration of the base, are known in advance.

The block diagram of a feedback controller with feedforward compensation is shown in figure 6.3.4.1.

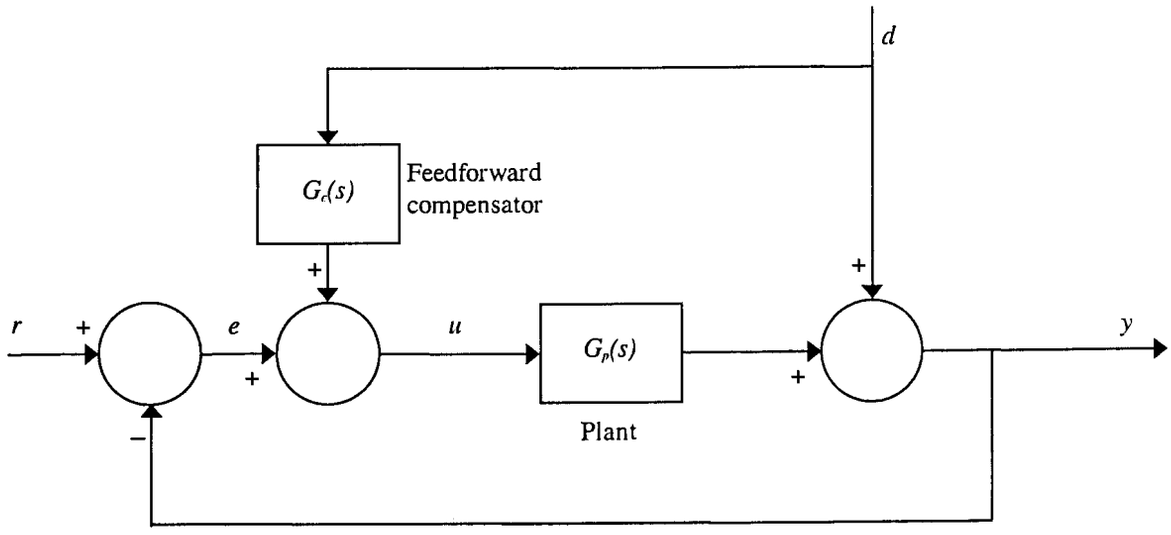

Figure 6.3.4.1: Block diagram of feedback controller with feedforward compensator [Schwarzenbach & Gill, 1986]

The output, tracking error and control are given by:

$$y = G_p u + d \qquad \textbf{(6.3.4.1a)}$$

$$e = r - y \qquad \textbf{(6.3.4.1b)}$$

$$u = e + G_c d \qquad \textbf{(6.3.4.1c)}$$

The output, tracking error and control can be expressed as follows in terms of the reference and disturbance inputs:

$$y = G_p\left(I + G_p\right)^{-1} r + \left(G_p G_c - I\right)\left(I + G_p\right)^{-1} d \qquad \textbf{(6.3.4.2a)}$$

$$e = \left(I + G_p\right)^{-1} r - G_p G_c\left(I + G_p\right)^{-1} d \qquad \textbf{(6.3.4.2b)}$$

$$u = \left(I + G_p\right)^{-1} r + \left(G_c - I\right)\left(I + G_p\right)^{-1} d \qquad \textbf{(6.3.4.2c)}$$

A special case is that of a regulator, whose reference input r is zero. The output of a regulator, in terms of the disturbance, from equation 6.3.4.2a, is given by:

$$y = \left(G_p G_c - I\right)\left(I + G_p\right)^{-1} d \qquad \textbf{(6.3.4.3)}$$

The attenuation factor γ, from equation 6.3.1.1, is given by:

$$\gamma = \frac{y}{d} \qquad \textbf{(6.3.4.4)}$$

Substitution of equation 6.3.4.3 into equation 6.3.4.4 gives:

$$\gamma = \left(G_p G_c - I\right)\left(I + G_p\right)^{-1} \tag{6.3.4.5}$$

For a specified disturbance attenuation factor γ, the required feedforward compensator transfer function G_c is:

$$G_c = \gamma + \left(I + \gamma\right)G_p^{-1} \tag{6.3.4.6}$$

The control u, in terms of the disturbance d and output y, is given by:

$$u = G_c d - y \tag{6.3.4.7}$$

Substitution of equation 6.3.4.6 into equation 6.3.4.7 gives:

$$u = \left[\gamma + \left(I + \gamma\right)G_p^{-1}\right]d - y \tag{6.3.4.8}$$

Equation 6.3.4.8 is only valid for static unit feedback. A similar equation can be derived for an arbitrary dynamic feedback gain $H_c(s)$.

6.3.5 Optimal disturbance attenuation using H_2 and H_∞ optimization techniques

The objective of disturbance attenuation in this study is to make the angular motion of the optical instrument less sensitive to the angular motion of the base. To achieve this, the output of the plant must be minimized.

The control required for this purpose can be obtained in a number of ways, e.g. by classical controller design methods, such as pole placement. However, this method only involves the output, and takes no account of the control effort required to achieve the objective. Necessarily, the output will increase if the control decreases, and vice versa. In order to obtain an efficient controller, the control effort must be weighed against the output. This process is known as optimization.

Various control optimization techniques exist, such as variational optimization and linear quadratic (H_2) optimization. The latter technique is applicable if the disturbance is fixed or has a fixed power spectrum [Doyle et al, 1989]. H_2 optimization is therefore applicable to this study, since the disturbance spectrum is known.

The H_2 performance measure is defined as follows in the frequency domain for a stable transfer function matrix $G(s)$ [Doyle et al, 1989]:

$$\|G\|_2 := \left(\frac{1}{2\pi}\int_{-\infty}^{\infty} trace\left[G(j\omega) * G(j\omega)\right]d\omega\right)^{1/2} \tag{6.3.5.1}$$

Linear quadratic optimization will be discussed in more detail in section 6.4, where the control design will be described in detail.

A modern control optimization technique still under development, which gives better robustness to uncertainties, is H_∞ control. The H_∞ performance measure performance is defined as follows in the frequency domain [Doyle et al, 1989]:

$$\|G\|_\infty := \sup_\omega \sigma_{max}[G(j\omega)] \qquad \textbf{(6.3.5.2)}$$

where σ_{max} is the maximum singular value.

The H_∞ criterion corresponds to designing for the worst disturbance signal [Doyle et al, 1989]. If a full-state feedback controller is used, the feedback gain matrix can be obtained from a solution of a single Riccati equation. State-space solutions to H_∞ control problems and disturbance attenuation by means of H_∞ control, are discussed in detail by Doyle et al [1989], Petersen [1987] and Petersen [1989].

6.3.6 Preshaping of command inputs

Preshaping of command inputs is often used for open-loop disturbance attenuation. The method can however be applied successfully if the input shaping accounts for the dynamic characteristics of the closed-loop plant [Singer & Seering, 1990].

The behaviour of the system to a series of impulses is used to attenuate endpoint vibration. The first impulse excites transient behaviour of the system, which is cancelled by the transient behaviour of subsequent impulses. A short delay, of the order of the period of the first mode of vibration, is incurred. Disturbances other than impulses are expressed as series of impulses.

The impulse amplitude and delay between impulses depend on the frequency and damping factor of the first natural mode. For example, the amplitudes for a two-impulse input are:

$$A_1 = \frac{1}{1+K} \qquad \textbf{(6.3.6.1a)}$$

$$A_2 = \frac{K}{1+K} \qquad \textbf{(6.3.6.1b)}$$

where K is a dimensionless constant, given as follows in terms of the damping factor ζ of the first natural mode of vibration:

$$K = e^{-\zeta\pi/\sqrt{1-\zeta^2}} \qquad \textbf{(6.3.6.2)}$$

The time delay ΔT is given by:

$$\Delta T = \frac{\pi}{\omega_n \sqrt{1-\zeta^2}} \qquad \textbf{(6.3.6.3)}$$

where ω_n is the natural frequency of the first mode of vibration of the system.

6.3.7 Attenuation of a continuous disturbance by means of digital regulation

Digital control is almost universally used in modern control, mainly for its simplicity of implementation and ease of changing control parameters. For these reasons, a digital controller will be used to drive the LOS stabilization system discussed in this study. The principle of operation of the controller is discussed in short below. The system block diagram, from Jacquot [1981], is shown in figure 6.3.7.1.

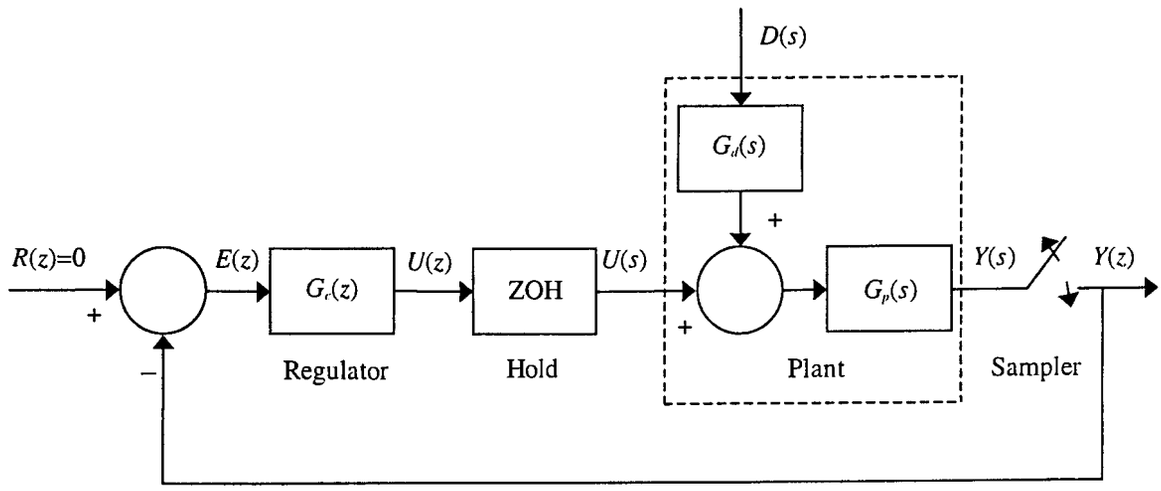

Figure 6.3.7.1: Block diagram of digital regulator for continuous disturbance attenuation [Jacquot, 1981]

A disturbance $D(s)$ enters the plant, with disturbance-to-output and input-to-output transfer functions $G_d(s)$ and $G_p(s)$, at the input. The plant output $Y(s)$ is sampled at a rate T and the sampled output $Y(z)$ is fed back into a digital regulator, with output $U(z)$. A zero order hold is applied to the control to obtain a continuous control signal $U(s)$, which drives the plant to attenuate the disturbance.

6.3.8 Motion controllers

Motion controllers are discussed in this section. A translational SDOF spring-mass-damper system is used to explain the principles of motion control. Although rotational pitch DOF's are of importance in this study, the translational model is used in the interest of simplicity. Analytical equations are obtained which give clear insight into the system characteristics. The principle can easily be extended to a rotational system, such as the LOS stabilization system. This will be done in section 6.4, where the controller design will be covered in detail.

Motion controllers can conveniently be divided into relative motion controllers and absolute motion controllers. A better understanding of the various types of motion controllers is provided with the aid of figure 6.3.8.1. The figure shows a linear spring-mass-damper system, with mass m, spring stiffness k and viscous damping coefficient c, mounted on a moving base with vertical displacement d, speed $\dot{d}$ and acceleration $\ddot{d}$. The vertical displacement, speed and acceleration of the mass are y, $\dot{y}$ and $\ddot{y}$ respectively. The actuator force, which excites the mass to attenuate the transmission of the base motion through the system, is F_a.

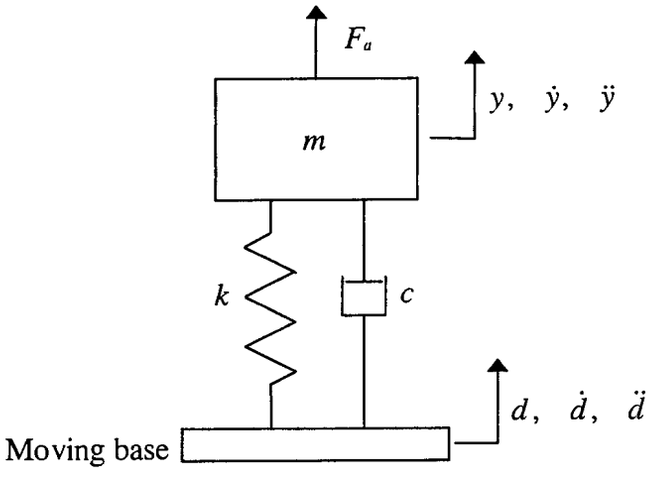

Figure 6.3.8.1 SDOF spring-mass-damper system excited by base motion and actuator force

The motion variable that is controlled depends on the sensor type, e.g. accelerometer, eddy probe (proximity sensor), or linear variable differential transformer (LVDT). In this study, the dynamic motion variables are translational accelerations, measured by means of accelerometers. Transmissibilities of the open-loop and closed-loop systems discussed below will therefore be expressed as ratios of accelerations.

The equation of motion is normally expressed in terms of all the motion variables, i.e. displacement, speed and acceleration. The equation of motion of the system shown in figure 6.3.8.1 is:

$$m\ddot{y} = -c(\dot{y} - \dot{d}) - k(y - d) + F_a \qquad \textbf{(6.3.8.1)}$$

Equation 6.3.8.1 is subsequently used to obtain the open- and closed-loop transmissibilities of the various motion controller types.

6.3.8.1 Relative motion controller

Relative motion control is done by measuring both the base and absolute accelerations, and by feeding back the difference between the two measured signals into the controller, to obtain the actuator force.

In order to derive the equation of motion, consider figure 6.3.8.1 and equation 6.3.8.1. The equation of motion of the SDOF system, for relative motion, is obtained by subtraction of $m\ddot{d}$ on both sides of equation 6.3.8.1:

$$m(\ddot{y} - \ddot{d}) = -c(\dot{y} - \dot{d}) - k(y - d) - m\ddot{d} + F_a \qquad \textbf{(6.3.8.1.1)}$$

Equation 6.3.8.1.1 can be written as:

$$\ddot{y}_r + \frac{c}{m}\dot{y}_r + \frac{k}{m}y_r = -\ddot{d} + \frac{1}{m}F_a \qquad \textbf{(6.3.8.1.2)}$$

where y_r is the relative displacement between the base and mass:

$$y_r = y - d \qquad \textbf{(6.3.8.1.3)}$$

The acceleration of the mass, in terms of the relative and base accelerations, from equation 6.3.8.1.3, is given by:

$$\ddot{y} = \ddot{y}_r + \ddot{d} \qquad \textbf{(6.3.8.1.4)}$$

Selecting the relative displacement and relative speed as states, the base acceleration and actuator force as inputs and the relative acceleration as the output, the state-space equations of the system can be written as:

$$\begin{Bmatrix} \dot{y}_r \\ \ddot{y}_r \end{Bmatrix} = \begin{bmatrix} 0 & 1 \\ -\frac{k}{m} & -\frac{c}{m} \end{bmatrix} \begin{Bmatrix} y_r \\ \dot{y}_r \end{Bmatrix} + \begin{Bmatrix} 0 \\ -1 \end{Bmatrix} \ddot{d} + \begin{Bmatrix} 0 \\ \frac{1}{m} \end{Bmatrix} F_a \qquad \textbf{(6.3.8.1.5a)}$$

$$\ddot{y}_r = \begin{bmatrix} -\frac{k}{m} & -\frac{c}{m} \end{bmatrix} \begin{Bmatrix} y_r \\ \dot{y}_r \end{Bmatrix} - \ddot{d} + \frac{1}{m}F_a \qquad \textbf{(6.3.8.1.5b)}$$

For relative motion control, the actuator force can expressed as follows as a linear combination of the relative displacement and speed:

$$F_a = \begin{bmatrix} -K_1 & -K_2 \end{bmatrix} \begin{Bmatrix} y_r \\ \dot{y}_r \end{Bmatrix} \tag{6.3.8.1.6}$$

where K_1 and K_2 are the relative displacement and relative speed feedback gains respectively. Because the relative displacement and speed are the plant states, the control law given in equation 6.3.8.1.6 describes state feedback control. State control requires that the states be known, either by direct measurement, or by state estimation. Since the output is the relative acceleration, instead of the relative displacement and speed, the states must be reconstructed from the output. This is done as follows, by direct integration of the relative acceleration:

$$y_r = \iint \ddot{y}_r dt dt \tag{6.3.8.1.7a}$$

$$\dot{y}_r = \int \ddot{y}_r dt \tag{6.3.8.1.7b}$$

where $\ddot{y}_r$ is the relative acceleration, which is obtained by subtraction of the measured acceleration of the base, from the measured acceleration of the mass:

$$\ddot{y}_r = \ddot{y} - \ddot{d} \tag{6.3.8.1.8}$$

The closed-loop state-space equations of the system are obtained by substitution of equation 6.3.8.1.6 into equations 6.3.8.1.5a and 6.3.8.1.5b:

$$\begin{Bmatrix} \dot{y}_r \\ \ddot{y}_r \end{Bmatrix} = \begin{bmatrix} 0 & 1 \\ -\dfrac{k+K_1}{m} & -\dfrac{c+K_2}{m} \end{bmatrix} \begin{Bmatrix} y_r \\ \dot{y}_r \end{Bmatrix} + \begin{Bmatrix} 0 \\ -1 \end{Bmatrix} \ddot{d} \tag{6.3.8.1.9a}$$

$$\ddot{y}_r = \begin{bmatrix} -\dfrac{k+K_1}{m} & -\dfrac{c+K_2}{m} \end{bmatrix} \begin{Bmatrix} y_r \\ \dot{y}_r \end{Bmatrix} - \ddot{d} \tag{6.3.8.1.9b}$$

The closed-loop transmissibility of the system, which is the *TF* between the acceleration of the base and the *absolute* accleration of the mass, is obtained from equations 6.3.8.1.4 and 6.3.8.1.9b as:

$$TR = \frac{\ddot{y}}{\ddot{d}} = \frac{\dfrac{c+K_2}{m}s + \dfrac{k+K_1}{m}}{s^2 + \dfrac{c+K_2}{m}s + \dfrac{k+K_1}{m}} \tag{6.3.8.1.10}$$

The poles of the closed-loop system are given by:

$$s = -\frac{c + K_2}{2m} \pm \frac{1}{2}\sqrt{\left(\frac{c + K_2}{m}\right)^2 - 4\frac{k + K_1}{m}} \qquad \textbf{(6.3.8.1.11)}$$

The zero of the closed-loop system is given by:

$$s = -\frac{k + K_1}{c + K_2} \qquad \textbf{(6.3.8.1.12)}$$

The natural frequency f_n and dimensionless damping factor ζ are respectively given by:

$$f_n = \frac{1}{2\pi}\sqrt{\frac{k + K_1}{m}} \qquad \textbf{(6.3.8.1.13a)}$$

$$\zeta = \frac{c + K_2}{2\sqrt{(k + K_1)m}} \qquad \textbf{(6.3.8.1.13b)}$$

The DC transmissibility is unity, and is independent of the feedback gains.

The transmissibility given by equation 6.3.8.1.10 corresponds with the transfer function of a passive low-pass (LP) filter. The filtering characteristic is such that the system will attenuate above $\sqrt{2}$ times the closed-loop natural frequency, i.e. above $f = (1/2\pi)\sqrt{2(k + K_1)/m}$.

Below the attenuation frequency, i.e. in the pass-band, the system will amplify the base motion, in other words, the acceleration of the mass will exceed that of the base. The attenuation band can be widened by reducing the natural frequency. This is achieved by reducing K_1; the lower K_1, the wider the attenuation band.

K_1 can however not be reduced indefinitely, since this will inevitably cause instability. Similarly, instability will result if K_2 is reduced to such an extent that the damping factor becomes negative. The lower limits of K_1 and K_2 are determined by the gain and phase margins of the plant.

In the attenuation band, the *TR* increases with damping, therefore damping is undesirable in this band. However, in the pass-band, the *TR* decreases with damping. In this band, damping must be as high as possible. In order to provide efficient damping in both the attenuation and pass bands, an optimum damping factor is required. For white-noise base motion, the optimum damping factor is 70,7 %.

The controller feedback transfer function $H_c(s)$ between the relative acceleration and actuator force is:

$$H_c(s) = -\frac{K_1}{s^2} - \frac{K_2}{s} \qquad \textbf{(6.3.8.1.14)}$$

The block diagram of the relative motion controller described above, is shown in figure 6.3.8.1.1. The inputs to the plant are the actuator force F_a and base acceleration $\ddot{d}$. The

plant output, which is also the controller input, is the relative acceleration $\ddot{y} - \ddot{d}$. The controller output is the actuator force F_a.

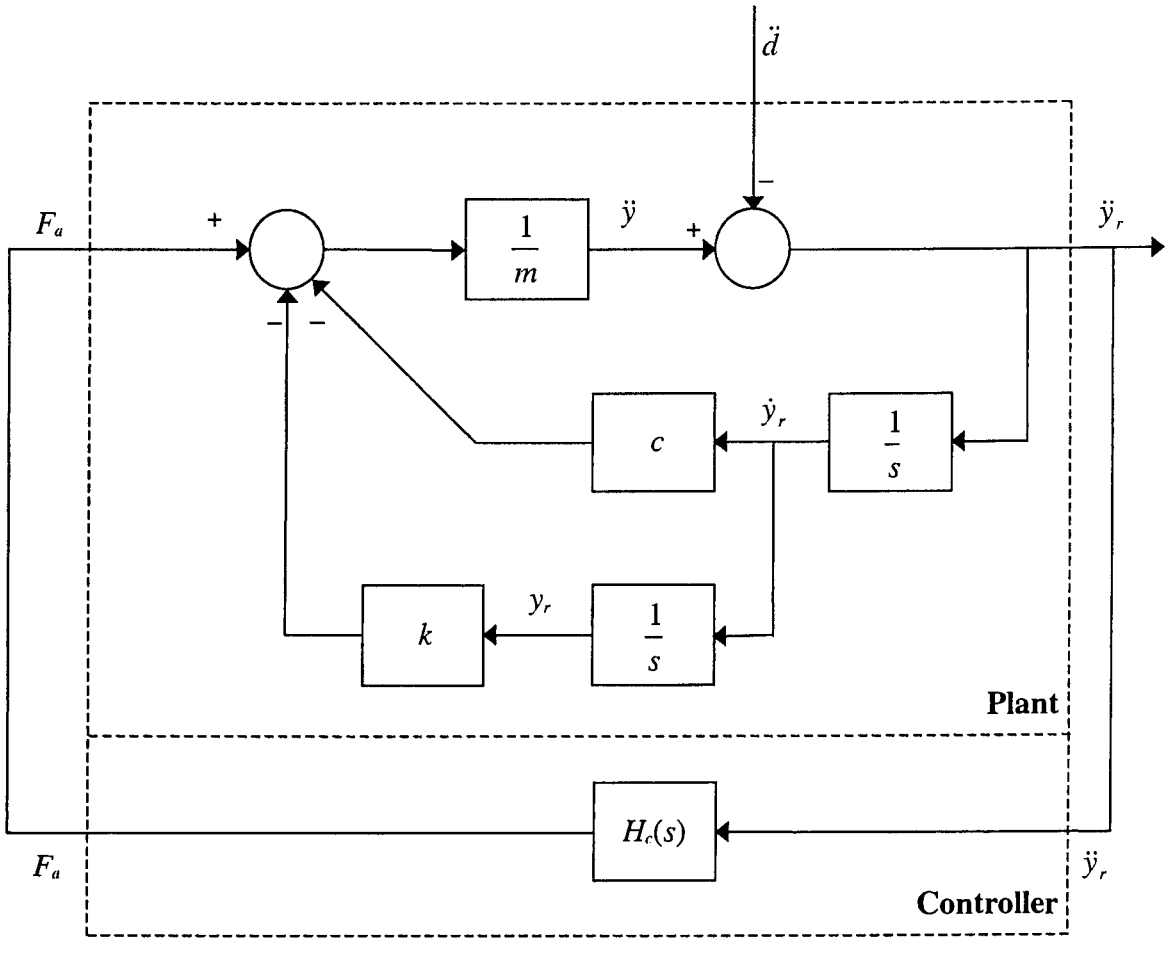

Figure 6.3.8.1.1: Block diagram of relative motion controller

An advantage of the relative motion controller is that it can be implemented passively, and does not require an actuator. The LP characteristics may be desirable from a measurement point of view, since the system can operate at low sample frequencies.

The disadvantages of the system are firstly, that it cannot attenuate at DC. However, depending on the nature of the disturbance, this may not be a necessity, for example where the disturbance does not contain a significant DC component. Secondly, since relative motion, instead of absolute motion, is controlled, the system is incapable of taking any corrective action if the motion of the mass deviates from the required motion. The system is therefore relatively non-robust in comparison with an absolute motion controller.

6.3.8.2 Absolute motion controller

An absolute motion controller measures the acceleration of the mass and feeds this signal back into the controller to obtain the control signal.

In order to derive the equation of motion, consider figure 6.3.8.1. The equation of motion of the system, from equation 6.3.8.1, is:

$$m\ddot{y} + c\dot{y} + ky = c\dot{d} + kd + F_a \qquad \textbf{(6.3.8.2.1)}$$

Equation 6.3.8.2.1 can be written as:

$$m\ddot{y} + c\dot{y} + ky = F_b + F_a \qquad \textbf{(6.3.8.2.2)}$$

where F_b is the equivalent base excitation force, given by:

$$F_b = c\dot{d} + kd \qquad \textbf{(6.3.8.2.3)}$$

The base excitation force is obtained as follows from the base acceleration:

$$F_b = c\int(\ddot{d})dt + k\iint(\ddot{d})dt\,dt \qquad \textbf{(6.3.8.2.4)}$$

The base-excited spring-mass-damper system shown in figure 6.3.8.1 can be replaced with an equivalent base-force excited system, as shown in figure 6.3.8.2.1.

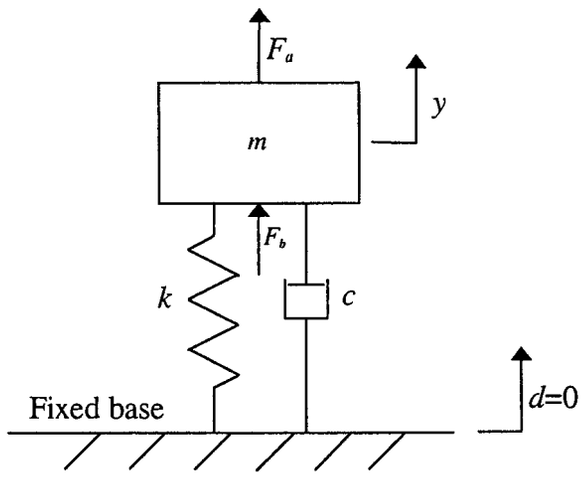

Figure 6.3.8.2.1: Equivalent spring-mass-damper system excited by base and actuator forces

Selecting the absolute displacement and speed of the mass as states, the base excitation and actuator forces as inputs and the acceleration of the mass as the output, the state-space equations of the system can be written as:

$$\begin{Bmatrix} \dot{y} \\ \ddot{y} \end{Bmatrix} = \begin{bmatrix} 0 & 1 \\ -\frac{k}{m} & -\frac{c}{m} \end{bmatrix} \begin{Bmatrix} y \\ \dot{y} \end{Bmatrix} + \begin{Bmatrix} 0 \\ \frac{1}{m} \end{Bmatrix} F_b + \begin{Bmatrix} 0 \\ \frac{1}{m} \end{Bmatrix} F_a \qquad \textbf{(6.3.8.2.5a)}$$

$$\ddot{y} = \begin{bmatrix} -\frac{k}{m} & -\frac{c}{m} \end{bmatrix} \begin{Bmatrix} y \\ \dot{y} \end{Bmatrix} + \frac{1}{m} F_b + \frac{1}{m} F_a \qquad \textbf{(6.3.8.2.5b)}$$

For relative motion control, the actuator force can be expressed as follows as a linear combination of the absolute displacement and speed of the mass:

$$F_a = \begin{bmatrix} -K_1 & -K_2 \end{bmatrix} \begin{Bmatrix} y \\ \dot{y} \end{Bmatrix} \qquad \textbf{(6.3.8.2.6)}$$

where K_1 is the abolute displacement feedback gain and K_2 is the absolute speed feedback gain.

The closed-loop state-space equations are obtained by substitution of equation 6.3.8.2.6 into equations 6.3.8.2.5a and 6.3.8.2.5b:

$$\begin{Bmatrix} \dot{y} \\ \ddot{y} \end{Bmatrix} = \begin{bmatrix} 0 & 1 \\ -\frac{k+K_1}{m} & -\frac{c+K_2}{m} \end{bmatrix} \begin{Bmatrix} y \\ \dot{y} \end{Bmatrix} + \begin{Bmatrix} 0 \\ \frac{1}{m} \end{Bmatrix} F_b \qquad \textbf{(6.3.8.2.7a)}$$

$$\ddot{y} = \begin{bmatrix} -\frac{k+K_1}{m} & -\frac{c+K_2}{m} \end{bmatrix} \begin{Bmatrix} y \\ \dot{y} \end{Bmatrix} + \frac{1}{m} F_b \qquad \textbf{(6.3.8.2.7b)}$$

The transfer function between the base force and output acceleration is:

$$\frac{\ddot{y}}{F_b} = \frac{\frac{1}{m} s^2}{s^2 + \frac{c+K_2}{m} s + \frac{k+K_1}{m}} \qquad \textbf{(6.3.8.2.8)}$$

The transmissibility, which is the transfer function between the base acceleration and absolute acceleration, is obtained from equations 6.3.8.2.3 and 6.3.8.2.8 as:

$$TR = \frac{\ddot{y}}{\ddot{d}} = \frac{\frac{c}{m}s + \frac{k}{m}}{s^2 + \frac{c + K_2}{m}s + \frac{k + K_1}{m}} \qquad \textbf{(6.3.8.2.9)}$$

The poles of the closed-loop system are given by:

$$s = -\frac{c + K_2}{2m} \pm \frac{1}{2}\sqrt{\left(\frac{c + K_2}{m}\right)^2 - 4\frac{k + K_1}{m}} \qquad \textbf{(6.3.8.2.10)}$$

The zero is given by:

$$s = -\frac{k}{c} \qquad \textbf{(6.3.8.2.11)}$$

The natural frequency, damping factor and DC transmissibility of the closed-loop system are respectively given by:

$$f_n = \frac{1}{2\pi}\sqrt{\frac{k + K_1}{m}} \qquad \textbf{(6.3.8.2.12a)}$$

$$\zeta = \frac{c + K_2}{2\sqrt{(k + K_1)m}} \qquad \textbf{(6.3.8.2.12b)}$$

$$TR_{DC} = \frac{k}{k + K_1} \qquad \textbf{(6.3.8.2.12c)}$$

The controller feedback transfer function $H_c(s)$ between the acceleration of the mass and actuator force is:

$$H_c(s) = -\frac{K_1}{s^2} - \frac{K_2}{s} \qquad \textbf{(6.3.8.2.13)}$$

The block diagram of the absolute motion controller is shown in figure 6.3.8.2.1. The controller input is the absolute acceleration of the mass $\ddot{y}$. The controller output is the actuator force F_a. The plant inputs are the actuator and base excitation forces F_a and F_b. The plant output is the absolute acceleration of the mass $\ddot{y}$.

It can be seen from equation 6.3.8.2.9 that only the denominator of the TR is affected by the feedback gains. The numerator is unaffected. The natural frequency increases with an increase in K_1, while the damping factor increases with an increase in K_2. For a positive K_1, k/m is smaller than $(k+K_1)/m$, giving a DC transmissibility of less than unity.

The DC transmissibility and natural frequency are coupled by K_1, i.e. a change in K_1 changes both the DC transmissibility and natural frequency. These two parameters can for instance be separately adjusted by using acceleration feedback in conjunction with displacement and speed feedback. In this case, the feedback law is:

$$F_a = K_1 y + K_2 \dot{y} + K_3 \ddot{y} \qquad \textbf{(6.3.8.2.14)}$$

where K_3 is the acceleration feedback gain.

The closed-loop transmissibility is:

$$\frac{\ddot{y}}{\ddot{d}} = \frac{\frac{c}{m+K_3}s + \frac{k}{m+K_3}}{s^2 + \frac{c+K_2}{m+K_3} + \frac{k+K_1}{m+K_3}} \qquad \textbf{(6.3.8.2.15)}$$

The natural frequency, damping factor and DC transmissibility are respectively given by:

$$f_n = \frac{1}{2\pi}\sqrt{\frac{k+K_1}{m+K_3}} \qquad \textbf{(6.3.8.2.16a)}$$

$$\zeta = \frac{c+K_2}{2\sqrt{(k+K_1)(m+K_3)}} \qquad \textbf{(6.3.8.2.16b)}$$

$$TR_{DC} = \frac{k}{k+K_1} \qquad \textbf{(6.3.8.2.16c)}$$

The transfer function $H_c(s)$ between the acceleration of the mass and actuator force is:

$$H_c(s) = -\frac{K_1}{s^2} - \frac{K_2}{s} - K_3 \qquad \textbf{(6.3.8.2.17)}$$

The block diagram of this controller is shown in figure 6.3.8.2.1.

Advantages of this system type are that the controller is capable of detecting the output, irrespective of what happens at the input. Corrective action can therefore be taken if the output deviates from the required output. Being a feedback controller, the system can be designed to be sufficiently robust. Furthermore, contrary to the relative motion controller, the system can be designed to attenuate at DC.

A disadvantage of this system type is that the control signal, which only depends on the output, may be contaminated by measurement noise. Since the output is a relatively small signal in comparison with the disturbance, the signal-to-noise ratio is low.

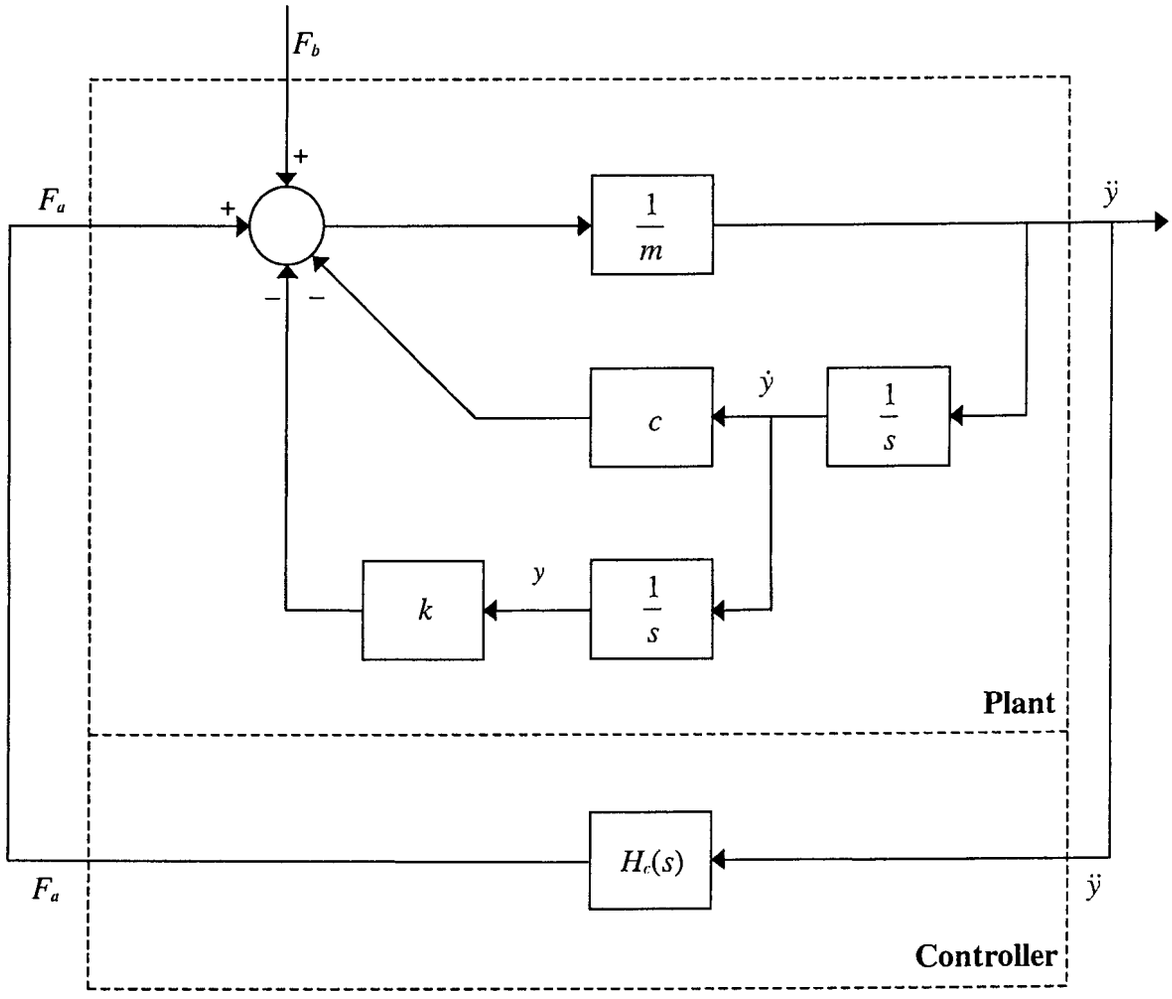

Figure 6.3.8.2.1: Block diagram of absolute motion controller

6.3.8.3 Disturbance feedforward (open-loop) controller

The disturbance feedforward controller measures the acceleration of the base and feeds this signal into the controller to obtain the actuator force.

The actuator force is expressed as follows as a linear combination of the base displacement and speed:

$$F_a = K_1 d + K_2 \dot{d} \qquad \textbf{(6.3.8.3.1)}$$

where K_1 is the base displacement gain and K_2 is the base speed gain.

Substitution of equations and 6.3.8.3.1 into equation 6.3.8.2.1 and simplification of the resulting equation gives the equation of motion as follows:

$$\ddot{y} + \frac{c}{m}\dot{y} + \frac{k}{m}y = \frac{c + K_2}{m}\dot{d} + \frac{k + K_1}{m}d \qquad \textbf{(6.3.8.3.2)}$$

The transmissibility equation of the system is:

$$\frac{\ddot{y}}{\ddot{d}} = \frac{\frac{c + K_2}{m}s + \frac{k + K_1}{m}}{s^2 + \frac{c}{m}s + \frac{k}{m}} \qquad \textbf{(6.3.8.3.3)}$$

The poles of the feedforward-controlled system are given by:

$$s = -\frac{c}{2m} \pm \frac{1}{2}\sqrt{\left(\frac{c}{m}\right)^2 - 4\frac{k}{m}} \qquad \textbf{(6.3.8.3.4)}$$

The zero is given by:

$$s = -\frac{k + K_1}{c + K_2} \qquad \textbf{(6.3.8.3.5)}$$

The natural frequency, damping factor and DC transmissibility are respectively given by:

$$f_n = \frac{1}{2\pi}\sqrt{\frac{k}{m}} \qquad \textbf{(6.3.8.3.6a)}$$

$$\zeta = \frac{c}{2\sqrt{km}} \qquad \textbf{(6.3.8.3.6b)}$$

$$TR_{DC} = 1 + \frac{K_1}{k} \qquad \textbf{(6.3.8.3.6c)}$$

The transfer function $G_c(s)$ between the base acceleration and actuator force is:

$$G_c(s) = \frac{K_1}{s^2} + \frac{K_2}{s} \qquad \textbf{(6.3.8.3.7)}$$

It can be seen from equations 6.3.8.3.6a and 6.3.8.3.6b that the natural frequency and damping factor correspond to those of an uncontrolled SDOF system. The DC transmissibility depends on the base displacement feedforward gain K_1. A DC transmissibility of less than unity can be obtained if K_1 is negative.

The block diagram of the open-loop controller is shown in figure 6.3.8.3.1. The input to the controller is the base acceleration, $\ddot{d}$. The controller output is the actuator force F_a. The plant inputs are the actuator force F_a and the base disturbance force F_b. The plant output is the acceleration of the mass $\ddot{y}$.

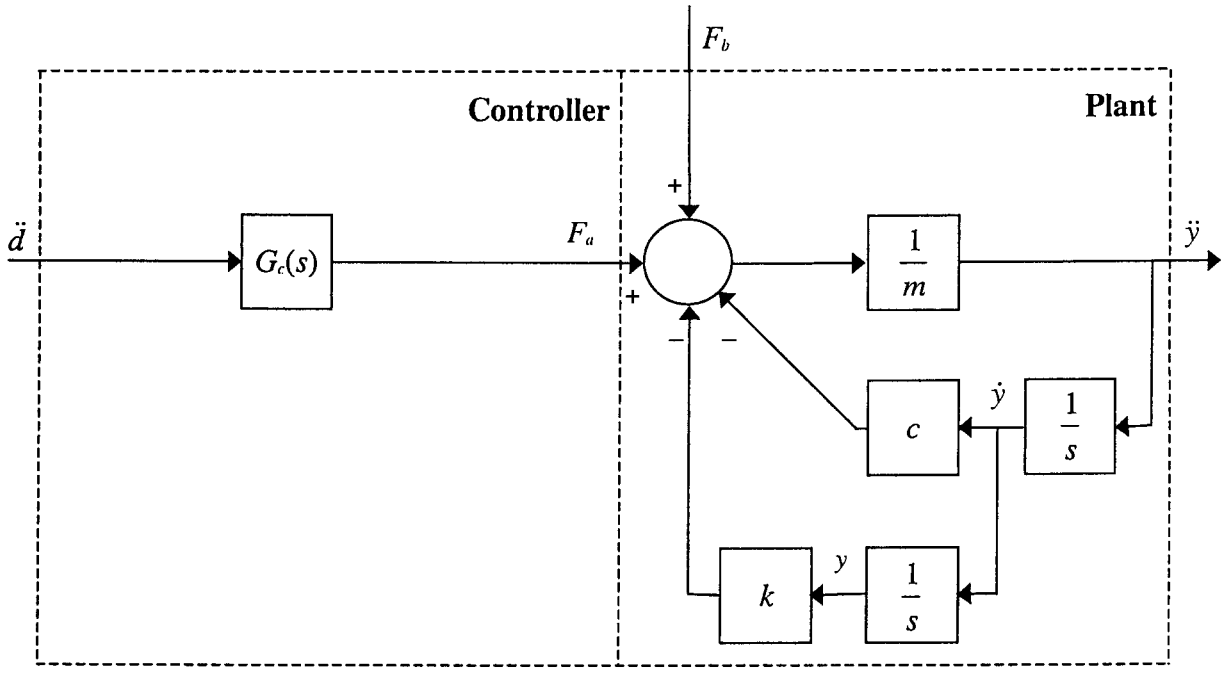

Figure 6.3.8.3.1: Block diagram of disturbance feedforward controller

An advantage of the disturbance feedforward controller is that it is unconditionally stable for any K_1 and K_2. Furthermore, since the base acceleration will be larger than the acceleration of the mass, a higher signal-to-noise ratio will result than in the case of the absolute output controller. This makes it possible to use a relatively high sample rate, which is required for accurate control.

The disadvantage of a disturbance feedforward controller is that there is no feedback loop. The controller can therefore not take any corrective action to compensate for disturbances other than the known base motion. Furthermore, the absence of a feedback loop prevents the system from compensating for shifts of plant poles due to uncertainties.

6.3.8.4 Absolute plus base motion controller

The absolute plus base motion controller measures both the base and mass accelerations and feeds these signals into the controller to obtain the actuator force.

The actuator force is a linear combination of the displacement of the mass, speed of the mass, displacement of the base and speed of the base:

$$F_a = -K_1 y - K_2 \dot{y} + K_3 d + K_4 \dot{d} \qquad \textbf{(6.3.8.4.1)}$$

where K_1 is the absolute displacement gain, K_2 is the absolute speed gain, K_3 is the base displacement gain and K_4 is the base speed gain. K_1 and K_2 are output feedback gains, while K_3 and K_4 are disturbance feedforward gains. This controller is a combination of the absolute acceleration and open-loop controllers, respectively discussed in sections 6.3.8.2 and 6.3.8.3.

Substitution of equations 6.3.8.4.1 into equation 6.3.8.2.1 and simplification of the resulting equation gives the equation of motion as follows:

$$\ddot{y} + \frac{c + K_2}{m}\dot{y} + \frac{k + K_1}{m}y = \frac{c + K_4}{m}\dot{d} + \frac{k + K_3}{m}d \qquad \textbf{(6.3.8.4.2)}$$

The transmissibility equation of the controlled system is:

$$\frac{\ddot{y}}{\ddot{d}} = \frac{\frac{c + K_4}{m}s + \frac{k + K_3}{m}}{s^2 + \frac{c + K_2}{m}s + \frac{k + K_1}{m}} \qquad \textbf{(6.3.8.4.3)}$$

The natural frequency, damping factor and DC transmissibility are respectively given by:

$$f_n = \frac{1}{2\pi}\sqrt{\frac{k + K_1}{m}} \qquad \textbf{(6.3.8.4.4a)}$$

$$\zeta = \frac{c + K_2}{2\sqrt{(k + K_1)m}} \qquad \textbf{(6.3.8.4.4b)}$$

$$TR_{DC} = \frac{k + K_3}{k + K_1} \qquad \textbf{(6.3.8.4.4c)}$$

The feedback transfer function $H_c(s)$ between the absolute acceleration and actuator force is:

$$H_c(s) = -\frac{K_1}{s^2} - \frac{K_2}{s} \qquad \textbf{(6.3.8.4.5)}$$

The feedforward transfer function $G_c(s)$ between the base acceleration and actuator force is:

$$G_c(s) = \frac{K_3}{s^2} + \frac{K_4}{s} \qquad \textbf{(6.3.8.4.6)}$$

It can be seen from equation 6.3.8.4.3 that both the TR numerator and denominator are affected by the controller gains. Poles and zeroes can therefore be shifted independently. Stability of the system only depends on K_1 and K_2, and is independent of K_3 and K_4.

The controller block diagram is shown in figure 6.3.8.4.1. The inputs to the controller are the absolute acceleration of the mass $\ddot{y}$ and the acceleration of the base $\ddot{d}$. The controller output is the actuator force F_a. The inputs to the plant are the actuator force F_a and the base excitation force F_b. The plant output is the absolute acceleration of the mass $\ddot{y}$.

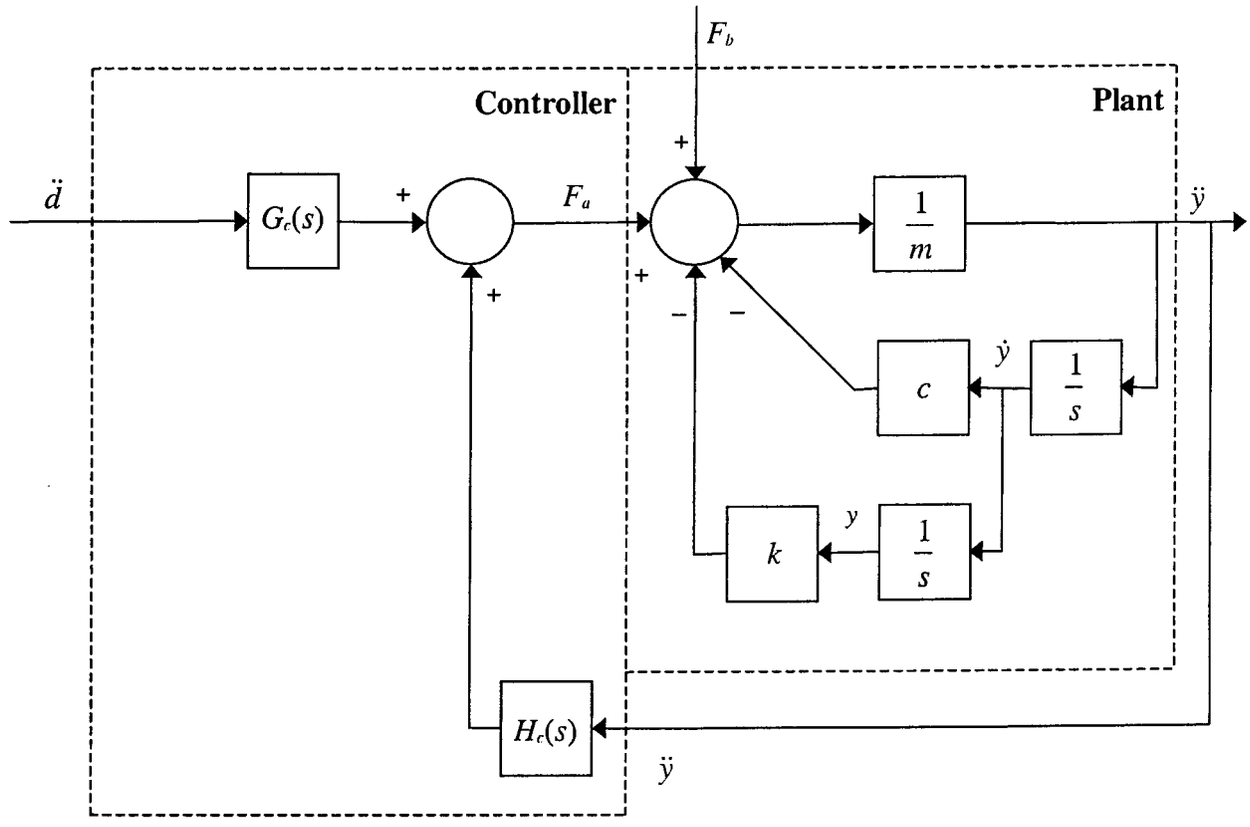

Figure 6.3.8.4.1: Block diagram of disturbance feedforward plus absolute motion controller

A special case of this controller is the relative motion controller discussed previously, which results if $K_3 = K_1$ and $K_4 = K_2$.

The first advantage of this controller type is that its poles and zeroes can be determined independently, since both base motion and absolute motion are used for control. Secondly, as was mentioned in section 6.3.4, a known disturbance may be partially attenuated before entering the system. Thirdly, in the case of a sensor failure, the controller may still operate, albeit at the cost of performance.

A disadvantage of the system is that, because it is not a pure feedback controller, robustness will be lower that that of the absolute motion controller.

6.3.8.5 Robustness improvement

Optimal state controllers are often non-robust. The main reason is that the transmissibilities of optimal controllers are, in many cases, characterized by pole-zero cancellation. The poles will be exactly cancelled by the zeroes, as long as the frequencies and damping factors of the poles and zeroes are constant. This is however not guaranteed, since either the poles or the zeroes may shift, due to, inter alia, plant nonlinearities. If, for instance, the poles shift, but the zeroes

are unaffected, pole-zero cancellation will no longer be effective, resulting in inadequate controller performance. Optimal controllers with low pole damping, in particular, are prone to this problem.

Robustness improvement can be achieved by proper robust feedback design, employing methods such as loop transfer recovery (LTR), as described in detail by Maciejowski [1989], Skogestad & Postlethwaite [1997] and Tsui [1996]. An alternative method of robustness improvement is to place an output integrator in parallel with the state feedback elements [Kuo, 1982, and Anderson & Moore, 1989]. The controller consists of two loops, i.e. an inner state-feedback loop and an outer output integrator loop. This method or robust control is often applied to reject DC disturbances in electric motors [Kuo, 1982].

This control method can also be applied to improve the robustness of motion controllers. A simple example is the absolute motion controller described in section 6.3.8.2. In the case of acceleration output, integral feedback will alter the speed feedback gain, thereby altering the damping factor of the poles.

The actuator force is obtained as follows in terms of the absolute displacement, speed and acceleration of the mass:

$$F_a = \begin{bmatrix} -K_1 & -K_2 \end{bmatrix} \begin{Bmatrix} y \\ \dot{y} \end{Bmatrix} - H_I \int \ddot{y} dt \qquad \textbf{(6.3.8.5.1)}$$

where K_1 and K_2 are the optimal state feedback gains and H_I is the acceleration integral feedback gain.

Simplification of equation 6.3.8.5.1 gives:

$$F_a = -K_1 y - \left(K_2 + H_I\right)\dot{y} \qquad \textbf{(6.3.8.5.2)}$$

Substitution of equation 6.3.8.5.2 into equation 6.3.8.2.1 gives the equation of motion of the closed-loop system as follows:

$$\ddot{y} + \frac{c}{m}\dot{y} + \frac{k}{m}y = -\frac{K_1}{m}y - \frac{\left(K_2 + H_I\right)}{m}\dot{y} + \frac{c}{m}\dot{d} + \frac{k}{m}d \qquad \textbf{(6.3.8.5.3)}$$

The transmissibility equation of the closed-loop system is:

$$\frac{\ddot{y}}{\ddot{d}} = \frac{\frac{c}{m}s + \frac{k}{m}}{s^2 + \frac{c + K_2 + H_I}{m}s + \frac{k + K_1}{m}} \qquad \textbf{(6.3.8.5.4)}$$

The poles are given by:

$$s = -\frac{c + K_2 + H_I}{2m} \pm \frac{1}{2}\sqrt{\left(\frac{c + K_2 + H_I}{m}\right)^2 - 4\left(\frac{k + K_1}{m}\right)} \qquad \textbf{(6.3.8.5.5)}$$

The zero is given by:

$$s = -\frac{k}{c} \qquad \textbf{(6.3.8.5.6)}$$

The natural frequency, damping factor and DC transmissibility are respectively given by:

$$f_n = \frac{1}{2\pi}\sqrt{\frac{k + K_1}{m}} \qquad \textbf{(6.3.8.5.7a)}$$

$$\zeta = \frac{c + K_2 + H_I}{2\sqrt{(k + K_1)m}} \qquad \textbf{(6.3.8.5.7b)}$$

$$TR_{DC} = \frac{k}{k + K_1} \qquad \textbf{(6.3.8.5.7c)}$$

The inner and outer feedback loops can be replaced by a single feedback loop. The transfer function $H_c(s)$ between the acceleration of the mass and the actuator force, from equation 6.3.8.5.2, is:

$$H_c(s) = -\frac{K_1}{s^2} - \frac{K_2 + H_I}{s} \qquad \textbf{(6.3.8.5.8)}$$

Comparison of equation 6.3.8.2.12b with equation 6.3.8.5.7b shows that the relative increase in damping, from the optimal damping, is $H_I/(c + K_2)$.

6.3.9 "Two-way" isolation

The methods discussed so far in section 6.3 are mainly applicable to the attenuation of disturbances exciting a system with a rigid base and mass, through the moving base. This section focusses on the attenuation of disturbances entering the structure at the base and mass, both of which are flexible. The actuator is mounted in between, from where it excites both the base and mass. This attenuation method is appropriately known as "two-way isolation" [Hyde, 1996].

The control system operates on the principle of dual sensor feedback. The absolute motion (speed) of the mass and the actuator force are measured and fed back into the controller, through two control loops, i.e. an inner (unit) force feedback loop and an outer motion feedback loop. The inner feedback loop makes it possible to control the actuator force, as follows. The measured motion signal is gained to give the commanded force signal. The measured actuator force signal is subtracted from the commanded force signal and the

difference is gained and supplied to the actuator. Two-way isolation and dual sensor feedback are described in detail by Hyde [1996].

6.4 Control system design

The design of a controller for the LOS stabilization system is described in this section. Controller specifications are given in section 6.4.1. Factors which influence controller design are mentioned in section 6.4.2. The selection of a suitable controller type is motivated in section 6.4.3. The controller design procedure is described in section 6.4.4. The plant and controller design parameters are given in section 6.4.5.

6.4.1 Control system design specifications

Control system specifications include the particular system performance requirements, and general controller requirements applicable to all types of controllers. Particular performance requirements, applicable to the LOS stabilization system, are the closed-loop attenuation factor, limits to the maximum and minimum values of the control signal, and frequency bandwidth. General requirements, which are almost universal for all types of controllers, are inter alia, stability, robustness and reaction speed. General control system requirements will be given in section 6.4.2.

The required attenuation factor, in terms of RMS of the output, as a fraction of the RMS of the disturbance, is 15%, over a frequency range of 2,5 Hz to 100 Hz. The upper limit of the coil supply voltage is + 28 V. The lower voltage limit is not specified, but 0 V can be accepted as a guide. (This constraint is applied to ensure that the coils are magnetically biased - see section 3.4).

Time-domain performance parameters such as rise-time, settling-time, overshoot and DC error are not specified. Although DC tracking error is not applicable, since the controller required for the LOS stabilization system will be a regulator, a DC voltage of 9,1 V is required to bias the actuator coil.

6.4.2 General control system requirements

General controller requirements are normally expressed in terms of performance factors such as accuracy, stability, sensitivity, reaction speed, control effort, robustness, observability and controllability. These factors are not discussed here. Instead, a summary of each of the factors is given in appendix X.

6.4.3 Selection of a suitable controller type

The controller which is selected for the magnetostrictive LOS stabilization system in this study, is a digital, suboptimal output feedback plus disturbance feedforward regulator, with output integral feedback. The reasons for the choice are as follows: If the advantages and

disadvantages of digital and analogue controllers are compared (see appendix X), the relative ease of implementation and adjustment of control parameters outweigh the cost disadvantage of a digital controller. If a digital controller is available, as it is in this study, it is the logical choice.

Tracking controllers and regulators were respectively discussed in sections 6.2.7 and 6.2.8. The objective in this study is to minimize the output, i.e. the angular acceleration of the optical instrument. This is a regulator objective. Although a tracking controller could also be considered for this application, a relative motion controller would be required, whose control objective would be to drive the relative motion between the base and output to the (negative of the) base motion. An absolute motion controller is however preferred, since it controls the parameter to be minimized, i.e. the absolute angular acceleration of the optical instrument, instead of the relative angular acceleration.

Disturbance feedforward is included because the disturbance is known and enters the system through the base. It can therefore be attenuated to a large extent, before affecting the system.

Optimal feedback controllers are seldom robust. Robustness of optimal controllers can be improved by placing an output integral feedback loop, in parallel with the output feedback loop. (This method of robustness improvement is discussed in appendix X). A disadvantage of this control method is that it slightly complicates the system, since an additional control loop is required. However, a considerable improvement in robustness can be achieved, as will be illustrated in section 6.4.5.

An alternative to the above controller, is a full-state controller. Robustness set aside, state controller design techniques are generally more powerful than *TF* design techniques, especially for systems with large numbers of states, inputs and outputs. State control design techniques also make it possible to convert the dynamic equations of a state controller to analogue *TF* form. Conversion of the continuous *TF*'s to digital filter form (in terms of the discrete delay element $1/z$) is also relatively easy, provided that the frequencies of the closed-loop system poles and zeroes do not exceed the Nyquist frequency.

The advantages of both state and digital controllers will be exploited in the design and implementation of the controller for the LOS stabilization system. The design will be carried out by means of optimal linear quadratic state controller and observer design techniques. The state and output equations will subsequently be written in analogue *TF* form and converted to digital filter form.

The block diagram of the plant and digital regulator is shown in figure 6.4.3.1. The plant inputs are the disturbance d (base angular acceleration) and control u (actuator coil voltage). The plant output y is the absolute angular acceleration of the optical instrument. The regulator inputs are the sampled disturbance $D(z)$ and plant output $Y(z)$. The controller output is the control $U(z)$, supplied to the plant through a zero-order hold ("zoh").

The digital regulator feedforward and feedback filter *TF*'s are $G(z)$ and $H(z)$ respectively. The digital output feedback integrator *TF*, which is the zero-order-hold equivalent of $1/s$, is $T/(z-1)$. The integrator gain is H_I, a constant. The analogue plant disturbance and control input *TF*'s are $G_d(s)$ and $G_u(s)$ respectively.

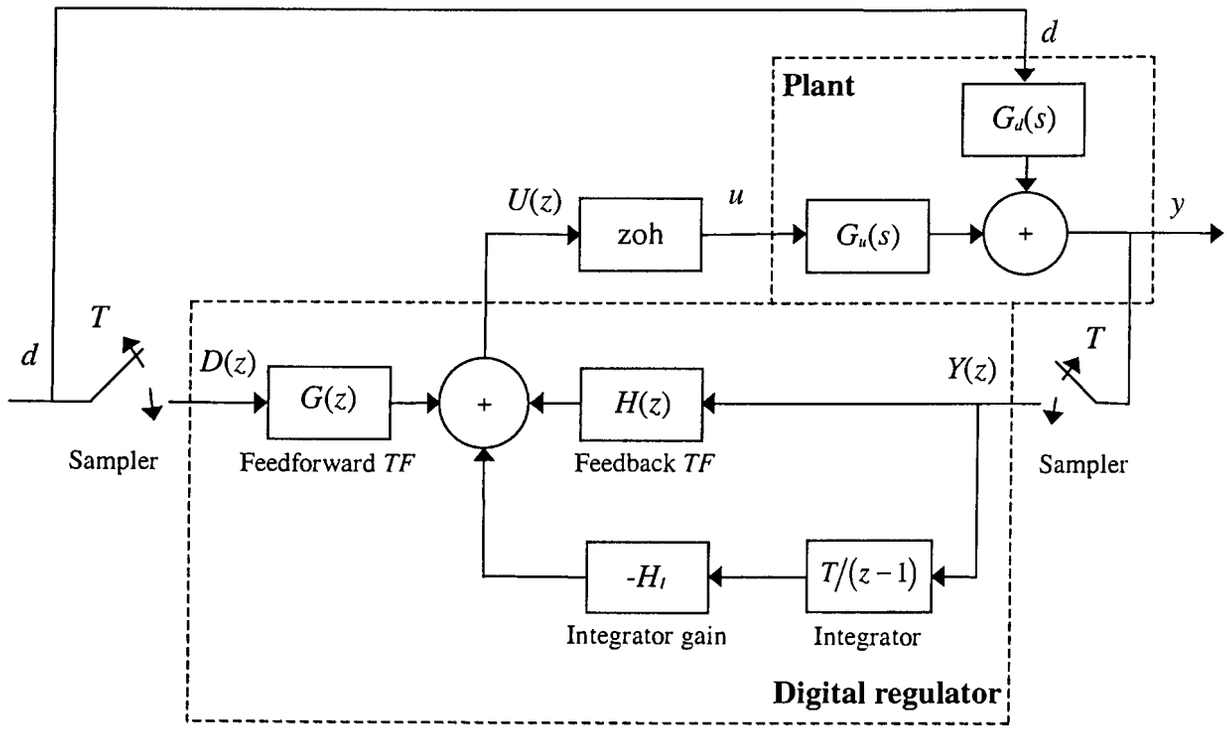

Figure 6.4.3.1: Block diagram of plant and digital regulator

6.4.4 Control system design method

An iterative method is followed in the design of the controller. The process is started by designing an optimal controller and an optimal observer. For the controller design, output and control weights are arbitrarily selected, while MS values of measured disturbance and output noise signals are used as weights for the observer design. Robustness is improved by designing a suboptimal controller and a suboptimal observer. The plant, controller and observer state-space equations are coupled and stability of the closed-loop system is verified. The disturbance-to-control and output-to-control *TF*'s are obtained and converted to digital form. The output integrator gain is arbitrarily selected.

A real-time simulation of the expected closed-loop system behaviour is done, with disturbance and noise signals acting as the extraneous inputs. The RMS-value of the output, in a frequency bandwidth of 0 Hz to 100 Hz, is compared with that of the disturbance. If the output RMS exceeds the specified value, the output weight and integrator feedback gains are adjusted and the process is repeated until the required output RMS is obtained.

The above design method is aimed at attenuating a known disturbance, entering the system through the base. The design is disturbance specific, meaning that the controller will, for example, not be able to reject the disturbance if a harmonic disturbance with the same amplitude as that of the dominating disturbance, i.e. at 96,75 Hz, occurs at 50 Hz.

The magnitude of the disturbance used in the design is 50% of that of the true disturbance, since only one actuator can be controlled. (The reason is that only two power amplifiers are

available for the experimental tests, i.e. one to excite the base and one to drive an actuator coil - see also section 4.3.1).

Detailed description of design procedure

The linear quadratic objective function of the controller is expressed in terms of the control and output. Control and output weights are arbitrarily selected and an optimal linear quadratic regulator (LQR) is designed. The Riccati equation is solved and the optimal feedback gain vector is determined from the Riccati matrix. The closed-loop state-space equations are obtained and converted to *TF* form. The poles and zeroes of the closed-loop transmissibility are determined and graphically displayed on a pole-zero map. It is shown that the optimal controller is characterized by pole-zero cancellation. The frequency spectrum of the closed-loop attenuation factor is shown. The effect of output weight on the attenuation factor is investigated. It is shown that an increase in output weight, reduces the attenuation factor.

A suboptimal controller is subsequently designed. The optimal controller is used as the point of departure. In order to eliminate pole-zero cancellation, the damping factors of most of the zeroes are increased and the frequency of the pole with the lowest frequency is raised. The poles and zeroes of the closed-loop *TR* are shown on a pole-zero map. It is shown that the suboptimal controller *TF* is nonminimum-phase. The frequency spectrum of the closed-loop attenuation factor of the suboptimal controller is shown and compared with that of the optimal controller. It is shown that the suboptimal controller is inferior in terms of attenuation, in comparison with the optimal controller, but is superior in terms of robustness, since it does not display pole-zero cancellation.

An optimal linear quadratic estimator (LQE) is designed. Results obtained from noise measurements are used to determine the disturbance and output weights. The Riccati equation for the optimal observer is solved and the optimal observer driving matrix is determined. The state-space matrices of the optimal observer and suboptimal controller are coupled. The eigenvalues of the coupled system are calculated to verify stability. A pole-zero map of the coupled system is shown. The disturbance to control (*u/d*) and output to control (*u/y*) transfer functions are calculated and their frequency spectra are shown in magnitude and phase form. The plant state-space equations are coupled to the observer and controller equations and stability of the closed-loop system is verified.

It is shown that certain elements of the optimal observer driving matrix are zero, which makes it impossible to control corresponding states from the output. The problem is rectified by designing a suboptimal observer. The zero elements in the driving matrix are replaced by non-zero elements in order to make full-state feedback control possible. The suboptimal observer is coupled to the suboptimal controller and stability of the coupled system is verified.

Equivalent digital filter *TF*'s of the continuous *TF*'s are designed. Poles and zeroes that exceed the Nyquist frequency, are eliminated. The output feedback integrator is replaced by an "equivalent" digital filter, with bounded DC gain. This is done in order to ensure that the control signal is bounded, thereby making it easier to obtain the required DC bias voltage.

Plant, controller and observer state-space, *TF* and digital filter equations

This section gives a summary of the equations required to design the controller. Additional information on different controller types, general controller requirements, configurations and block diagrams, can be found in appendix X.

The plant state and output equations are:

$$\dot{x} = Ax + B_u u + B_d d \qquad \textbf{(6.4.4.1a)}$$

$$y = Cx \qquad \textbf{(6.4.4.1b)}$$

The plant *TF* for the control input, in the absence of the disturbance input, in terms of the state and output matrices, is given by:

$$\frac{Y(s)}{U(s)} = C[sI - A]^{-1} B_u \qquad \textbf{(6.4.4.2)}$$

The plant *TF* for the disturbance input, in the absence of the control input, is given by:

$$\frac{Y(s)}{D(s)} = C[sI - A]^{-1} B_d \qquad \textbf{(6.4.4.3)}$$

The plant eigenvalues are the values of s for which:

$$|sI - A| = 0 \qquad \textbf{(6.4.4.4)}$$

The plant attenuation factor, in the absence of the control input, from equation 6.4.4.3, is:

$$\gamma(s) = C[sI - A]^{-1} B_d \qquad \textbf{(6.4.4.5)}$$

(Equation 6.4.4.5 gives the *uncontrolled* attenuation factor. This term is preferred to "open-loop" attenuation factor, because the latter may also apply to the attenuation factor of a plant controlled by an open-loop controller).

Observability matrix

The plant states are fully observable if the observability matrix

$$\left[C^T \;\vdots\; A^T C^T \;\vdots\; \left(A^T\right)^2 C^T \;\vdots\; \cdots \;\vdots\; \left(A^T\right)^{n-1} C^T\right] \qquad \textbf{(6.4.4.6)}$$

has rank n, where n is the number of plant states.

Controllability matrix

The system is fully controllable if the controllability matrix

$$\left[B \;\vdots\; AB \;\vdots\; A^2B \;\vdots\; \cdots \;\vdots\; A^{n-1}B\right] \tag{6.4.4.7}$$

has rank n.

State and *TF* equations for a state feedback controlled system

For linear state control, the control is a linear combination of the states:

$$u = -Kx \tag{6.4.4.8}$$

where K is the state feedback gain vector.

The closed-loop state space matrices are obtained by substitution of equation 6.4.4.8 into equation 6.4.4.1:

$$\dot{x} = (A - B_u K)x + B_d d \tag{6.4.4.9a}$$

$$y = Cx \tag{6.4.4.9b}$$

The closed-loop eigenvalues are the values of s for which:

$$\left|sI - (A - B_u K)\right| = 0 \tag{6.4.4.10}$$

The closed-loop attenuation factor is given by:

$$\gamma_{cl}(s) = \left.\frac{Y(s)}{D(s)}\right|_{cl} = C\left[sI - (A - B_u K)\right]^{-1} B_d \tag{6.4.4.11}$$

where the subscript *cl* denotes "closed-loop".

Optimal control design equations

The cost function to be minimized, is:

$$J = \int_{t=0}^{t=T} \left[Q_y y^2(t) + Ru^2(t)\right] dt \tag{6.4.4.12}$$

where Q_y and R are the output and control weights, respectively. For a SISO system, both Q_y and R are scalars.

The relationship between the state weight matrix Q_x and Q_y is:

$$Q_x = C^T Q_y C \tag{6.4.4.13}$$

The Riccati equation, in its steady-state version, has to be solved to determine the state feedback gain vector K, which minimizes J for prescribed values of Q_y and R. The steady-state algebraic Riccati equation (ARE), is:

$$Q_x + A^T S_{ss} + S_{ss} A - S_{ss} B_u R^{-1} B_u^T S_{ss} = 0 \tag{6.4.4.14}$$

where S_{ss} is the steady-state solution of the Riccati equation. The optimal state feedback gain matrix is given in terms of the Riccati matrix as:

$$K = R^{-1} B_u^T S_{ss} \tag{6.4.4.15}$$

The optimal state feedback gain matrix gives a linear relationship between the state vector and optimal control.

State-space and *TF* equations of coupled plant, observer and controller

The observer state-space equations are:

$$\dot{\hat{x}} = A\hat{x} + B_u u + B_d d + L(y - \hat{y}) \tag{6.4.4.16a}$$

$$\hat{y} = C\hat{x} \tag{6.4.4.16b}$$

In equation 6.4.4.16a, the observer inputs are the control input u, disturbance d, plant output y and observed output $\hat{y}$.

Substitution of equation 6.4.4.16b into equation 6.4.4.16a gives the observer state equation in the following form:

$$\dot{\hat{x}} = (A - LC)\hat{x} + B_u u + B_d d + Ly \tag{6.4.4.17}$$

In equation 6.4.4.17, the control, disturbance and plant output are the observer inputs. Equation 6.4.4.17 is required to couple the plant, observer, controller and output feedback integrator equations. The coupled equations will be given in the next section.

For state control by means of an observer, the control is a linear combination of the observed states:

$$u = -K\hat{x} \tag{6.4.4.18}$$

Substitution of equation 6.4.4.18 into equation 6.4.4.17, gives the observer state equation in yet another form:

$$\dot{\hat{x}} = (A - B_u K - LC)\hat{x} + B_d d + Ly \tag{6.4.4.19}$$

In equation 6.4.4.19, the disturbance and plant output are the observer inputs.

The coupled plant, observer and controller state-space equations are obtained by combining equations 6.4.4.1, 6.4.4.16b, 6.4.4.18 and 6.4.4.19, as follows:

$$\begin{Bmatrix} \dot{x} \\ \dot{\hat{x}} \end{Bmatrix} = \begin{bmatrix} A & -B_u K \\ LC & A - B_u K - LC \end{bmatrix} \begin{Bmatrix} x \\ \hat{x} \end{Bmatrix} + \begin{bmatrix} B_d \\ B_d \end{bmatrix} d \tag{6.4.4.20a}$$

$$\begin{Bmatrix} y \\ \hat{y} \\ u \end{Bmatrix} = \begin{bmatrix} C & 0 \\ 0 & C \\ 0 & -K \end{bmatrix} \begin{Bmatrix} x \\ \hat{x} \end{Bmatrix} \tag{6.4.4.20b}$$

The closed-loop eigenvalues of the coupled plant, observer and state feedback controller, are the values of s for which:

$$|sI - A_{cl}| = 0 \tag{6.4.4.21}$$

where A_{cl} is the coupled coefficient matrix:

$$A_{cl} = \begin{bmatrix} A & -B_u K \\ LC & A - B_u K - LC \end{bmatrix} \tag{6.4.4.22}$$

The closed-loop attenuation factor is given by:

$$\gamma(s) = [C \quad 0][sI - A_{cl}]^{-1} \begin{bmatrix} B_d \\ B_d \end{bmatrix} \tag{6.4.4.23}$$

The controller *TF*'s, i.e. the disturbance to control and output to control *TF*'s, are given by:

$$\frac{U_f(s)}{D(s)} = -K[sI - (A - B_u K - LC)]^{-1} B_d \tag{6.4.4.24a}$$

$$\frac{U_b(s)}{Y(s)} = -K[sI - (A - B_u K - LC)]^{-1} L \tag{6.4.4.24b}$$

Design equations for LQE optimal observer

A Riccati equation similar to that of the optimal controller (see equation 6.4.4.14) can be written for the optimal LQE observer. The steady-state Riccati equation for the LQE observer is:

$$P_{ss}A^T + AP_{ss} - PC^T R^{-1} CP + B_d Q B_d^T = 0 \qquad \textbf{(6.4.4.25)}$$

where P_{ss} is the steady-state Riccati matrix, A is the plant coefficient matrix, B_d is the plant disturbance input matrix, C is the plant output matrix, and Q and R are the covariances of the uncorrelated process and output noise signals w and v, respectively given by:

$$Q = \frac{1}{T}\int_0^T w^2(t)dt \qquad \textbf{(6.4.4.26a)}$$

$$R = \frac{1}{T}\int_0^T v^2(t)dt \qquad \textbf{(6.4.4.26b)}$$

The observer gain matrix L is obtained as follows from the steady-state Riccati matrix:

$$L = R^{-1} P_{ss} C^T \qquad \textbf{(6.4.4.27)}$$

The LQE observer produces an optimal linear quadratic gaussian (LQG) estimate of the observer state vector $\hat{x}$, for $d = 0$, in equation 6.4.4.16.

State-space and *TF* equations of coupled observer and state plus output integral feedback controller

For linear state plus output integral feedback, the control is given by:

$$u = -K\hat{x} - H_I \int y dt \qquad \textbf{(6.4.4.28)}$$

where H_I is the output integral feedback gain.

Differentiation of equation 6.4.4.28 with respect to time gives:

$$\dot{u} = -K\dot{\hat{x}} - H_I y \qquad \textbf{(6.4.4.29)}$$

Combination of equations 6.4.4.1, 6.4.4.16b, 6.4.4.17 and 6.4.4.29, gives the state-space

equations of the coupled plant, observer and state plus output integral feedback controller, as:

$$\begin{Bmatrix} \dot{x} \\ \dot{\hat{x}} \\ \dot{u} \end{Bmatrix} = \begin{bmatrix} A & 0 & B_u \\ LC & A-LC & B_u \\ -(KL+H_I)C & -K(A-LC) & -KB_u \end{bmatrix} \begin{Bmatrix} x \\ \hat{x} \\ u \end{Bmatrix} + \begin{Bmatrix} B_d \\ B_d \\ -KB_d \end{Bmatrix} d \qquad \textbf{(6.4.4.30a)}$$

$$\begin{Bmatrix} y \\ \hat{y} \\ u \end{Bmatrix} = \begin{bmatrix} C & 0 & 0 \\ 0 & C & 0 \\ 0 & 0 & 1 \end{bmatrix} \begin{Bmatrix} x \\ \hat{x} \\ u \end{Bmatrix} \qquad \textbf{(6.4.4.30b)}$$

The closed-loop eigenvalues of the coupled plant, observer and state plus output integral feedback controller, are the values of s for which:

$$|sI - A_{cl}| = 0 \qquad \textbf{(6.4.4.31)}$$

where A_{cl} is the coupled coefficient matrix:

$$A_{cl} = \begin{bmatrix} A & 0 & B_u \\ LC & A-LC & B_u \\ -(KL+H_I)C & -K(A-LC) & -KB_u \end{bmatrix} \qquad \textbf{(6.4.4.32)}$$

The attenuation factor is given by:

$$\gamma(s) = [C \quad 0 \quad 0][sI - A_{cl}]^{-1} \begin{bmatrix} B_d \\ B_d \\ -KB_d \end{bmatrix} \qquad \textbf{(6.4.4.33)}$$

Equations for the digital filter equivalents of the disturbance to control and output to control *TF*'s are given next.

Digital filter equivalents of continuous *TF*'s

Two methods can be used to obtain the digital equivalents of the continuous *TF*'s. The first is by conversion of the state-space matrices to their discrete equivalents, and by subsequent conversion of the dynamic equations to digital *TF* form. The second is by direct conversion from continuous *TF* form to digital *TF* form. The first method, which is described in detail by Franklin et al [1990], will not be used in this study. The second method can be directly

applied, by transforming the plant poles and zeroes from the s-domain to the z-domain. The transformation equation depends on the type of hold, e.g. zero-order hold ("zoh"), first order hold ("foh") and bilinear transformation (Tustin's method). Application of the "zoh" method is the simplest, and is therefore popular and often used. The method will also be used here. Although other methods may be more accurate for the same sample rate, accuracy can be improved by using higher sample rates.

For a zero-order hold, the discrete domain differential operator z is related to the Laplace-domain differential operator s, by the equation:

$$z = e^{sT} \tag{6.4.4.34}$$

where T is the sample period.

The continuous *TF*'s are written in the following form:

$$G(s) = K_0 \frac{(s-r_1)(s-r_2)\cdots(s-r_m)}{(s-p_1)(s-p_2)\cdots(s-p_n)} \tag{6.4.4.35}$$

where K_0 is the overall gain, r denotes a zero, p denotes a pole and m and n are the *TF* numerator and denominator orders respectively.

By application of equation 6.4.4.34, the discrete equivalent of equation 6.4.4.35, is:

$$G(z) = K_{0z} \frac{(z-e^{r_1 T})(z-e^{r_2 T})\cdots(z-e^{r_m T})}{(z-e^{p_1 T})(z-e^{p_2 T})\cdots(z-e^{p_n T})} \tag{6.4.4.36}$$

The equivalent digital filter equation is obtained by expanding the numerator and denominator terms to obtain polynomials in z, and by subsequent division by the highest power of z of the denominator. The resulting equation is of the form:

$$G(z^{-1}) = \frac{b_0 + b_1 z^{-1} + \cdots + b_m z^{-m}}{a_0 + a_1 z^{-1} + \cdots + a_n z^{-n}} \tag{6.4.4.37}$$

where z^{-1} is the discrete delay.

The discrete equivalents of both the disturbance to control *TF* (as given by equation 6.4.4.24a) and output to control *TF* (as given by equation 6.4.4.24b) are determined by the above method.

Controller design by means of Matlab and Simulink

In this study, design calculations are done with the aid of standard Matlab and Simulink toolboxes. The use of Simulink has a number of advantages, namely that it makes it possible to simulate the behaviour of a continuous plant, controlled by a digital controller. Secondly, the block diagram developed for the simulations requires only minor adjustments, such as the addition of A/D and D/A blocks, to implement the controller and download it onto the DSP. The implementation process will be discussed in section 6.6.2. More information on the use of Matlab for control system analysis, simulation and design is provided by Bishop [1993] and Mathews and Fink [1999].

Real-time simulation of closed-loop system behaviour

After carrying out the above controller design steps, a time-domain simulation of the closed-loop system behaviour is carried out in Simulink. The simulation block diagram is shown in fiigure 6.4.4.1.

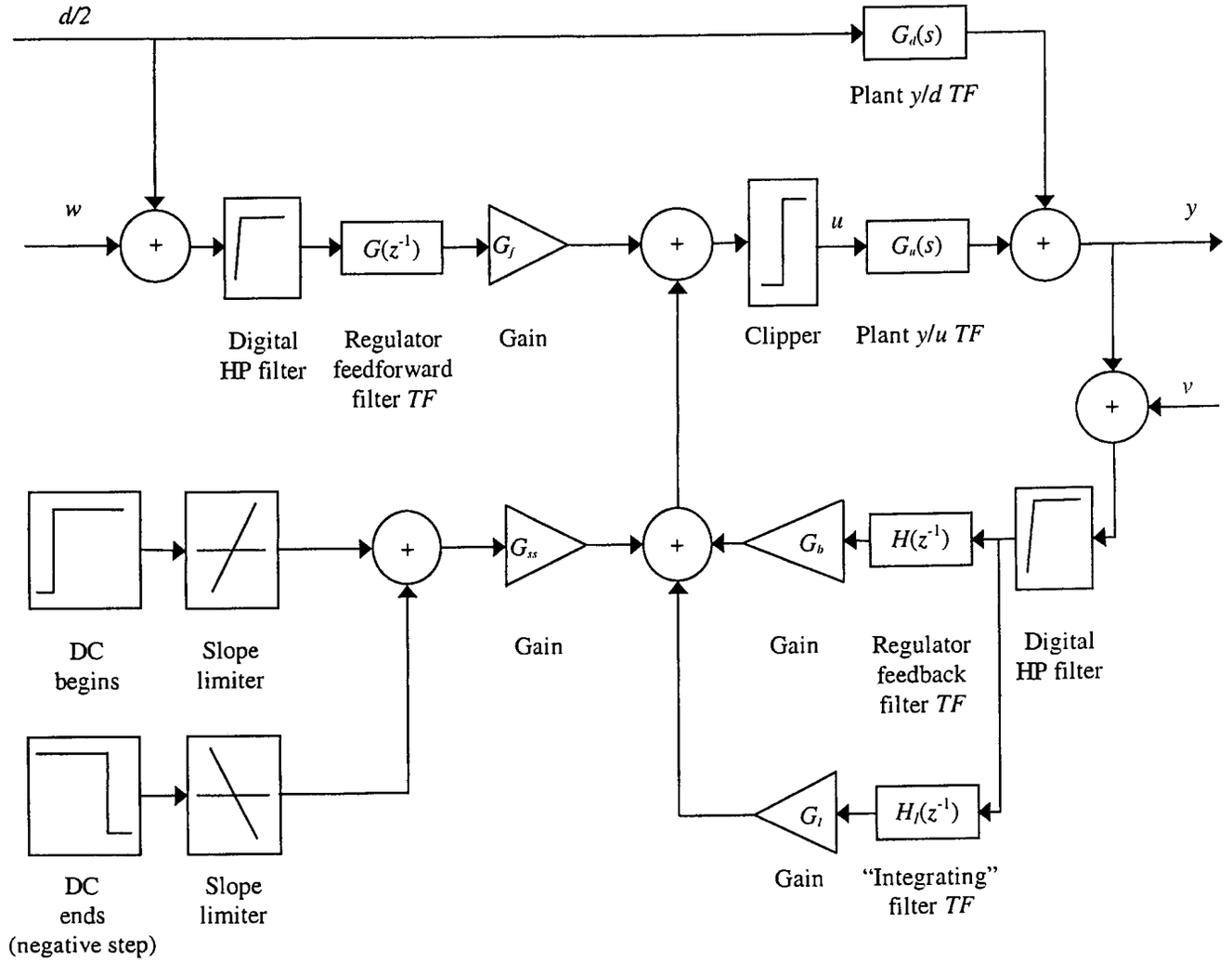

Figure 6.4.4.1: Simulation block diagram of plant and controller, with DC bias

The extraneous inputs are $d/2$, which is 50% of the disturbance, base signal measurement noise w and output signal measurement noise v. The output of the closed-loop system is y.

Third-order, elliptic high-pass (HP) filters are placed in the feedforward and feedback paths in order to demean the disturbance and output signals. Two DC bias blocks, i.e. a positive step to start the DC signal, and a negative step to stop it at the end of the simulation period, are included. The slope limiters ensure that the steps are applied and removed gradually, in order to prevent large transient overshoots. Gain elements are included in the disturbance feedforward, output feedback, output integral feedback and DC bias paths to facilitate controller implementation. Unit feedforward, feedback and DC gains are used for the simulations, while the integral feedback gain is adjustable. A clipper limits the actuator coil supply voltage in order to prevent burnout.

In the interest of high accuracy, a sample period of 4.10^{-4} s, corresponding to a sample frequency of 2,5 kHz, is used. This frequency is 25 times the maximum frequency of the disturbance band of interest (i.e. 100 Hz), 5 times the maximum frequency of the disturbance, including all frequencies (i.e. 500 Hz) and approximately 5 times the maximum measured natural frequency of the plant (476,3 Hz). In order to simulate continuous behaviour of the plant as accurately as possible, the 5^{th} order Runge-Kutta method is used to integrate the dynamic equations. The total duration of the simulation is 4s, which corresponds with that of the known disturbance.

A digital HP filter with the following *TF* is used:

$$G_{filter}\left(z^{-1}\right)=\frac{0{,}9919-2{,}9757z^{-1}+2{,}9757z^{-2}-0{,}9919z^{-3}}{1-2{,}9838z^{-1}+2{,}9677z^{-2}-0{,}9839z^{-3}} \qquad \textbf{(6.4.4.38)}$$

The upper limit of the voltage clipper is set to 28 V and the lower limit to 0 V. The DC bias voltage is 9,1 V (see also table 4.4.5.1). The bias voltage slope limit is 100 V/s.

Design of the disturbance feedforward, output feedback and output integral feedback elements is described in detail in section 6.4.5. The plant characteristics, which were discussed in detail in chapter 5, are repeated in order to provide a better understanding of the controller characteristics.

6.4.5 Plant, controller, observer and closed-loop system parameters

The plant state-space equations are:

$$\dot{x} = Ax + B_u u + B_d d \qquad \textbf{(6.4.5.1a)}$$

$$y = Cx \qquad \textbf{(6.4.5.1b)}$$

where u is the actuator coil voltage, d is the base angular acceleration and y is the optical instrument angular accceleration:

$$u = V \qquad \textbf{(6.4.5.2a)}$$

$$d = \ddot{\theta}_b \qquad \textbf{(6.4.5.2b)}$$

$$y = \ddot{\theta} \qquad \textbf{(6.4.2.5c)}$$

A consists of the following submatrices (see equation 5.6.9a):

$$A = \begin{bmatrix} 0 & I & 0 \\ -\Omega^2 & -2Z\Omega & M^{*-1}\Phi_s^T F_l C_c \\ 0 & 0 & A_c \end{bmatrix} \qquad \textbf{(6.4.5.3)}$$

Numerical values of the elements of the submatrices of A are as follows:

$$\Omega^2 = 1.10^6 \begin{bmatrix} 1{,}481 & & & & \\ & 2{,}093 & & & \\ & & 2{,}469 & & \\ & & & 3{,}588 & \\ & & & & 8{,}959 \end{bmatrix} \qquad \textbf{(6.4.5.4a)}$$

$$2Z\Omega = \begin{bmatrix} 97{,}35 & & & & \\ & 50{,}53 & & & \\ & & 111{,}6 & & \\ & & & 115{,}0 & \\ & & & & 71{,}83 \end{bmatrix} \qquad \textbf{(6.4.5.4b)}$$

$$M^{*-1}\Phi_s^T F_l C_c = \begin{bmatrix} 1{,}47.10^{10} & 3{,}734.10^{6} & 470{,}2 \\ -3{,}179.10^{9} & -8{,}075.10^{5} & -101{,}7 \\ -1{,}204.10^{9} & -3{,}058.10^{5} & -38{,}51 \\ -4{,}379.10^{10} & -1{,}112.10^{7} & -1401 \\ 2{,}723.10^{10} & 6{,}916.10^{6} & 870{,}9 \end{bmatrix} \qquad \textbf{(6.4.5.4c)}$$

$$A_c = \begin{bmatrix} 0 & 1 & 0 \\ 0 & 0 & 1 \\ -1{,}332.10^{9} & -3{,}487.10^{6} & -1817 \end{bmatrix} \qquad \textbf{(6.4.5.4d)}$$

Numerical values of the elements of the driving matrices B_u and B_d are as follows:

$$B_u = [0 \;\; 0 \;\; 0 \;\; 0 \;\; 0 \;\; 0 \;\; 0 \;\; 0 \;\; 0 \;\; 0 \;\; 0 \;\; 0 \;\; 1]^T \qquad \textbf{(6.4.5.5a)}$$

$$B_d = [-9{,}705.10^{-6} \;\; 1{,}5771.0^{-6} \;\; 6{,}437.10^{-6} \;\; 9{,}235.10^{-6} \;\; 0 \;\; 0{,}1476 \;\; -0{,}06532 \;\; -0{,}1424 \;\; -0{,}288 \;\; 0 \;\; 0 \;\; 0 \;\; 0]^T \qquad \textbf{(6.4.5.5b)}$$

Numerical values of the elements of the output matrix C are as follows:

$$C =$$
$$[5{,}14.10^{5} \;\; -3{,}24.10^{6} \;\; -3{,}72.10^{6} \;\; -7{,}94.10^{6} \;\; -1{,}82.10^{6} \;\; 33{,}8 \;\; -78{,}3 \;\; -168 \;\; -255 \;\; -146 \;\; -1{,}14.10^{11} \;\; -2{,}9.10^{7} \;\; -3657] \qquad \textbf{(6.4.5.6)}$$

The plant transfer functions for the control and disturbance inputs are given by:

$$\frac{Y(s)}{U(s)} = C[sI - A]^{-1} B_u \qquad \textbf{(6.4.5.7a)}$$

$$\frac{Y(s)}{D(s)} = C[sI - A]^{-1} B_d \qquad \textbf{(6.4.5.7b)}$$

Numerical values of the plant *TF* numerator and denominator polynomials are obtained by substitution of equations 6.4.5.4 into equation 6.4.5.3, and by subsequent substitution of the resulting equation, as well as equations 6.4.5.5 and 6.4.5.6, into equations 6.4.5.7.

The plant *TF* poles and zeroes, in frequency and damping form, are given in tables 6.4.5.1 to 6.4.5.3.

Table 6.4.5.1: Plant *TF* poles

Undamped frequency (Hz)	Damping factor (%)
74,19	* real pole
193,64	4,00
230,26	1,75
250,09	3,55
269,05	39,95
301,46	3,04
476,37	1,20

* Damping factor not given for real poles and zeroes

Table 6.4.5.2: Plant *TF* zeroes for control input

Undamped frequency (Hz)	Damping factor (%)
0	* real zero
0	* real zero
199,15	3,87
234,23	1,88
251,25	3,52
469,22	1,25
889,88	71,01

Table 6.4.5.3: Plant *TF* zeroes for disturbance input

Undamped frequency (Hz)	Damping factor (%)
74,19	* real zero
196,10	3,94
233,90	1,98
261,96	3,33
269,05	39,95
476,37	1,20

The plant pole-zero maps, for the control and disturbance inputs, are shown in figures 6.4.5.1 and 6.4.5.2 respectively. The units are in rad/s.

The *TF* magnitude and phase spectra for the control and disturbance inputs are shown in figures 6.4.5.3 and 6.4.5.4 respectively.

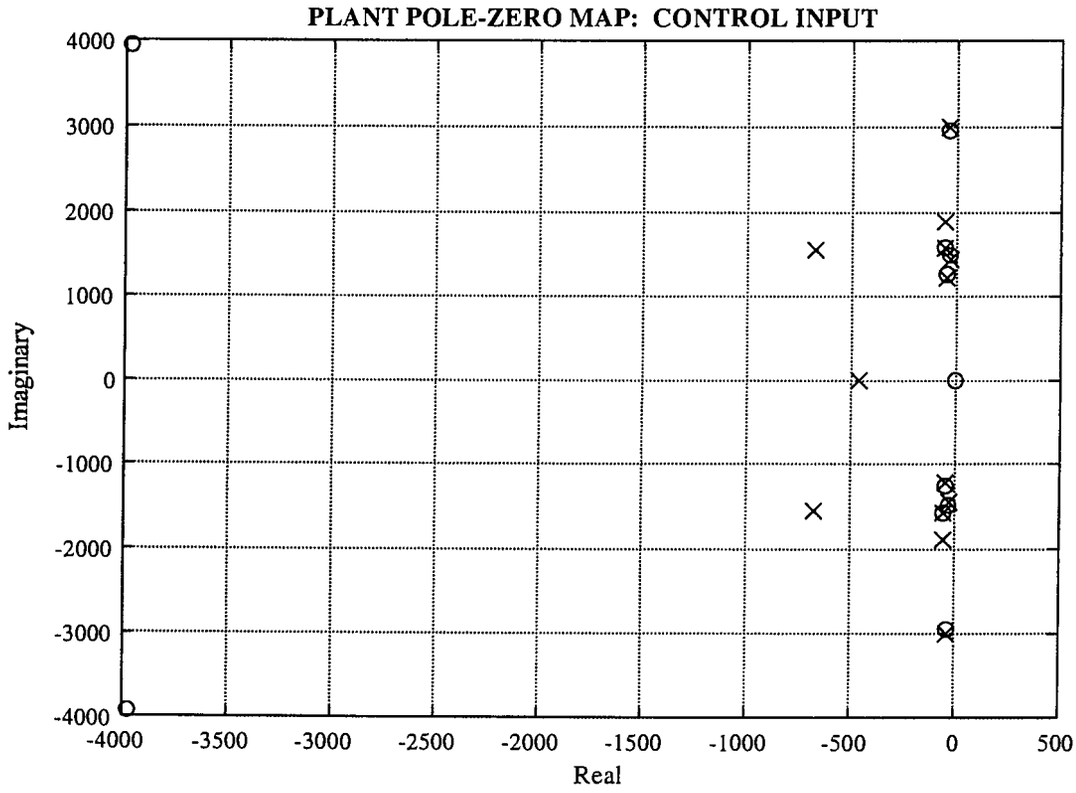

Figure 6.4.5.1: Plant pole-zero map for control input

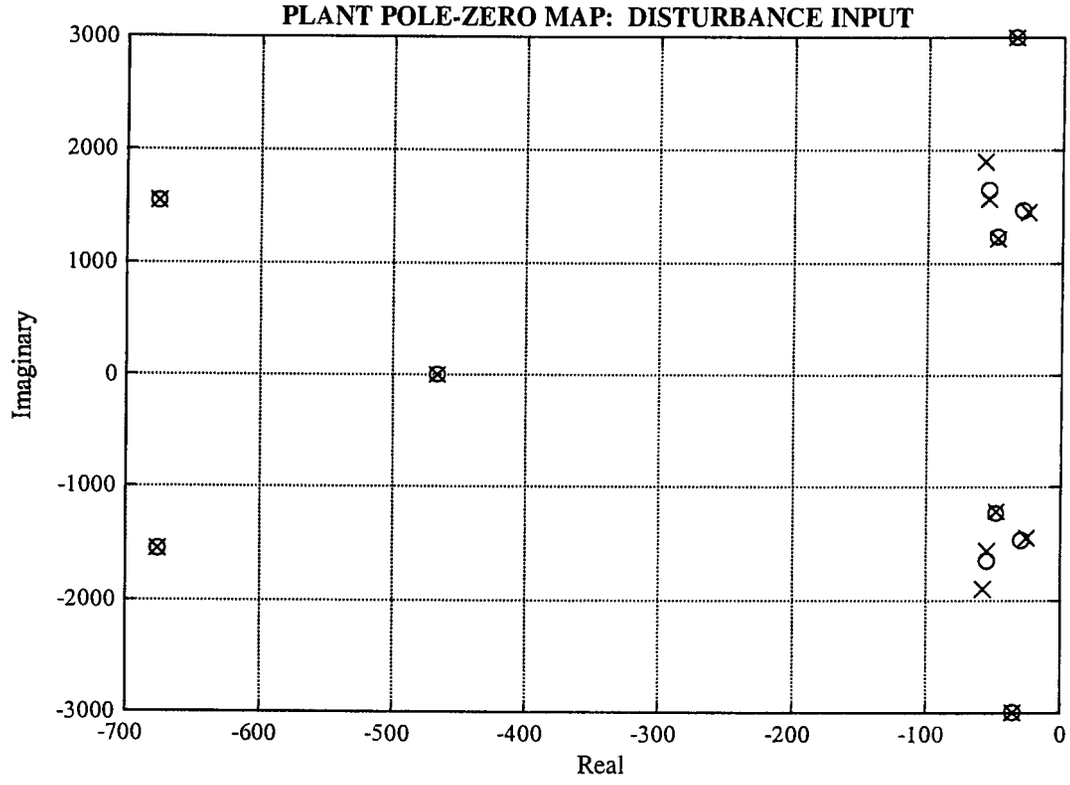

Figure 6.4.5.2: Plant pole-zero map for disturbance input

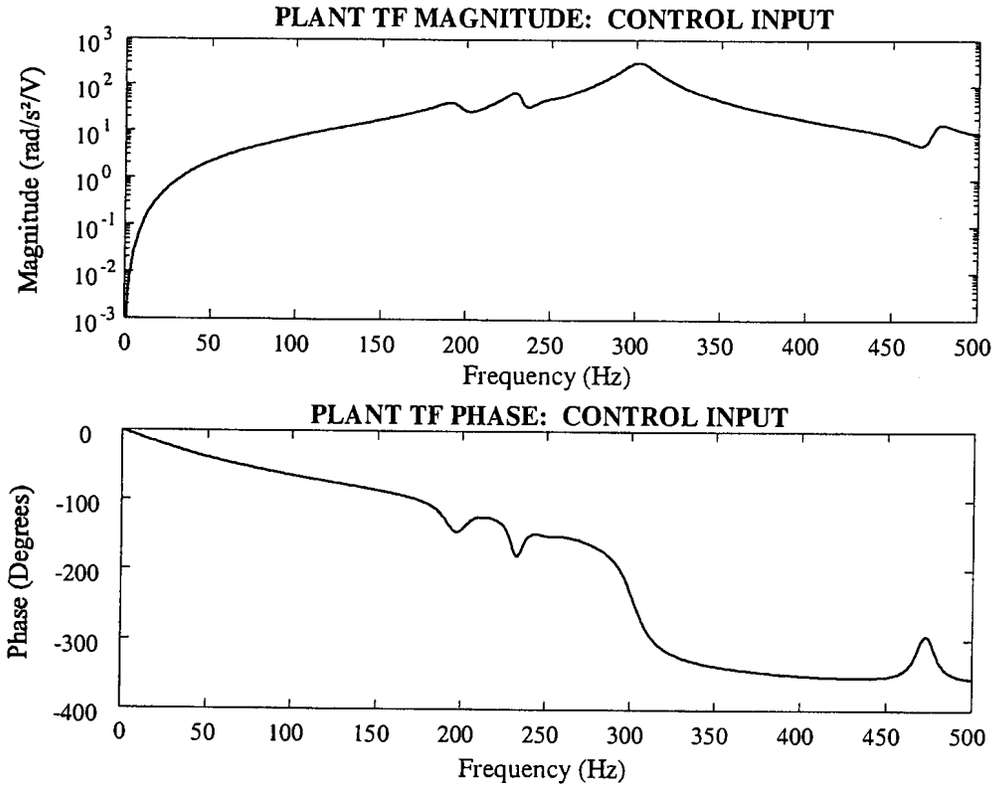

Figure 6.4.5.3: Plant *TF* magnitude and phase spectra for control input

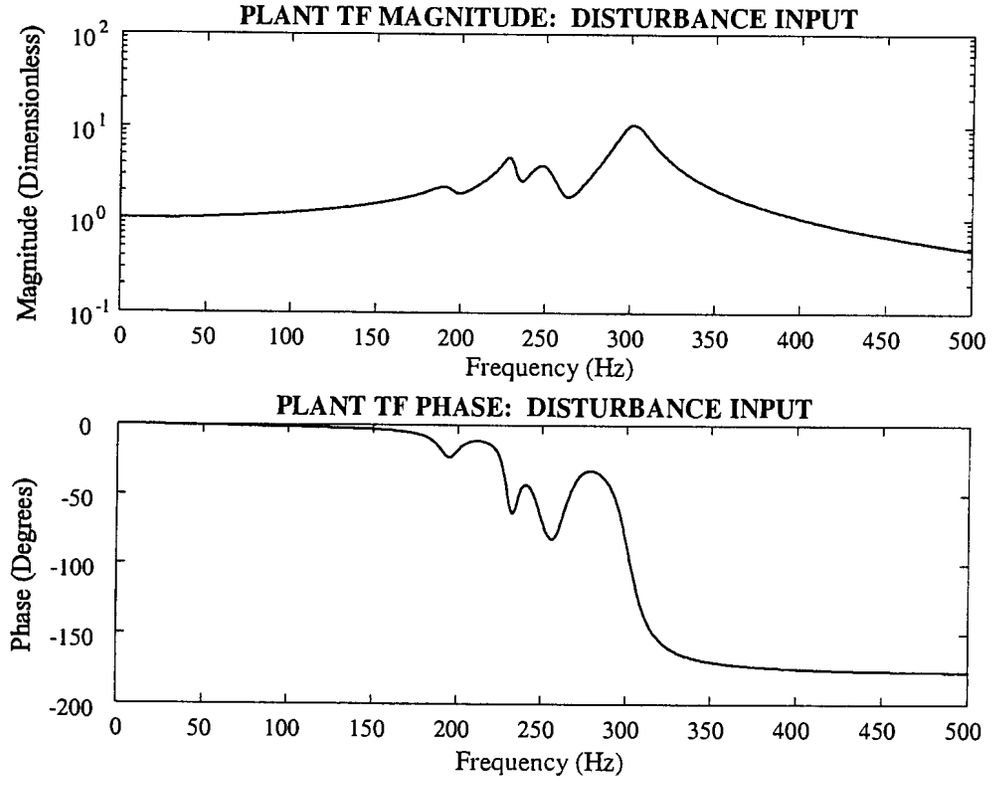

Figure 6.4.5.4: Plant *TF* magnitude and phase spectra for disturbance input

Plant canonical state-space matrices

The plant state-space matrices are expressed as follows in modal canonical form:

$$A = \begin{bmatrix} -48{,}67 & 1216 & & & & & & & & & & & \\ -1216 & -48{,}67 & & & & & & & & & & & \\ & & -25{,}27 & 1447 & & & & & & & & & \\ & & -1447 & -25{,}27 & & & & & & & & & \\ & & & & -55{,}82 & 1570 & & & & & & & \\ & & & & -1570 & -55{,}82 & & & & & & & \\ & & & & & & -57{,}53 & 1893 & & & & & \\ & & & & & & -1893 & -57{,}53 & & & & & \\ & & & & & & & & -35{,}92 & 2993 & & & \\ & & & & & & & & -2993 & -35{,}92 & & & \\ & & & & & & & & & & -466{,}1 & & \\ & & & & & & & & & & & -675{,}3 & 1550 \\ & & & & & & & & & & & -1550 & -675{,}3 \end{bmatrix}$$

(6.4.5.8a)

$$B_{tt} = \{-5{,}534 \quad -0{,}9727 \quad 0{,}2827 \quad 0{,}242 \quad 0{,}5233 \quad -0{,}8961 \quad -8{,}419 \quad 3{,}373 \quad -0{,}05148 \quad 1{,}282 \quad 2{,}550 \quad -10{,}69 \quad -4{,}101\}^T$$

(6.4.5.8b)

$$B_{il} = \{-0{,}005910 \quad 0{,}1476 \quad 0{,}00506 \quad -0{,}1424 \quad -0{,}06529 \quad -0{,}002281 \quad 0{,}2876 \quad 0{,}01749 \quad 0 \quad 0 \quad 0 \quad 0 \quad 0\}^T$$

(6.4.5.8c)

$$C = \{421{,}9 \quad 16{,}89 \quad -2365 \quad -84{,}04 \quad -78{,}25 \quad 2239 \quad 254{,}6 \quad -4186 \quad -607{,}9 \quad -7{,}296 \quad -1003 \quad -2854 \quad 2504\}$$

(6.4.5.8d)

Observability

The rank of the observability matrix in equation 6.4.4.6 is 13, which corresponds with the number of states. The system is therefore observable. (The A matrix is multiplied by a constant factor of 1.10^{-3} to calculate the observability matrix, since the magnitudes of the higher powers of A cause roundoff errors).

Controllability

The rank of the controllability matrix in equation 6.4.4.7 is 13. The system is therefore controllable. (The A matrix is scaled by a factor of 1.10^{-3}, as for the observability matrix).

Selection of output and control weights and calculation of state feedback gains

Output and control weights for use in the optimization cost function (equation 6.4.4.12) are arbitrarily selected and their influence on the closed-loop attenuation factor is investigated. Output weights Q_y of 1000, 2000 and 5000, are selected, together with a unit control weight R. The state weight Q_x is determined for each of the output weights, by application of equation 6.4.4.13. The Riccati equation (6.4.4.14) is solved and the steady state Riccati matrix is obtained, which is used to determine the state feedback gain vectors for each of the above output weights.

The state feedback gain vector K, for $Q_y = 1000$ and $R = 1$, is:

$$K = \{-13325 \quad -126{,}22 \quad 74687 \quad 1285{,}1 \quad 907{,}15 \quad -70794 \quad -6692{,}9 \quad 132290 \quad 19212 \quad 399{,}74 \quad 28390 \quad 87605 \quad -79040\} \tag{6.4.5.9}$$

The state feedback gain vector K, for $Q_y = 2000$ and $R = 1$, is:

$$K = \{-18851 \quad -245{,}34 \quad 105650 \quad 1945{,}3 \quad 1478 \quad -100130 \quad -9384{,}4 \quad 187140 \quad 27176 \quad 437{,}68 \quad 40881 \quad 124390 \quad -112110\} \tag{6.4.5.10}$$

The state feedback gain vector K, for $Q_y = 5000$ and $R = 1$, is:

$$K = \{-29816 \quad -518{,}4 \quad 167100 \quad 3411{,}8 \quad 2772{,}6 \quad -158340 \quad -14951 \quad 295970 \quad 42967 \quad 532{,}1 \quad 65900 \quad 197950 \quad -177640\} \tag{6.4.5.11}$$

Closed-loop attenuation factors for optimal state feedback gains

The closed-loop attenuation factors for each of the above state feedback gain factors are calculated by means of equation 6.4.4.11. The attenuation factors, which are also the magnitude spectra of the closed-loop TR's, are shown in figure 6.4.5.5.

It can be seen from figure 6.4.5.5 that, for the three selected weights, the lowest (i.e. best) attenuation factor is obtained with an output weight of 5000, while the highest (worst) is obtained with a weight of 1000. The suboptimal controller design will be based on the optimal controller, obtained with an output weight of 5000 and a unit control weight.

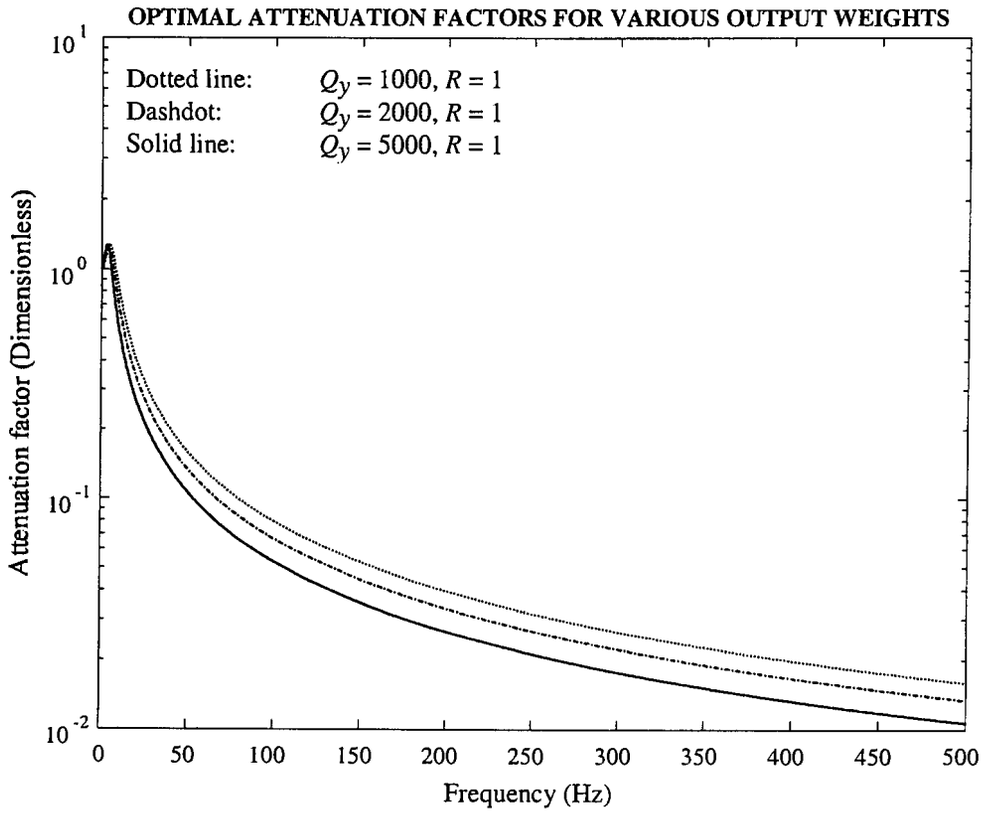

Figure 6.4.5.5: Optimal attenuation factors for Q_y = 1000, 2000 & 5000, with R = 1

The closed-loop poles and zeroes of the optimal controller, for Q_y = 5000 and R = 1, are given in tables 6.4.5.4 and 6.4.5.5 respectively. The closed-loop pole-zero map is shown in figure 6.4.5.6. (The real pole at 41,16 kHz is not shown). From tables 6.4.5.4 and 6.4.5.5, and figure 6.4.5.6, it is clear that almost all of the poles, except for the complex pole pair at 3,74 Hz, are cancelled by zeroes.

Table 6.4.5.4: Closed-loop poles for Q_y = 5000, R =1

Undamped frequency (Hz)	Damping factor (%)
3,74	70,74
199,15	3,87
234,23	1,88
251,35	3,52
469,22	1,25
889,92	71,01
41155	real

Table 6.4.5.5: Closed-loop zeroes for $Q_y = 5000$, $R = 1$

Undamped frequency (Hz)	Damping factor (%)
2,64	real
199,15	3,87
234,23	1,88
251,35	3,52
469,22	1,25
888,35	71,08

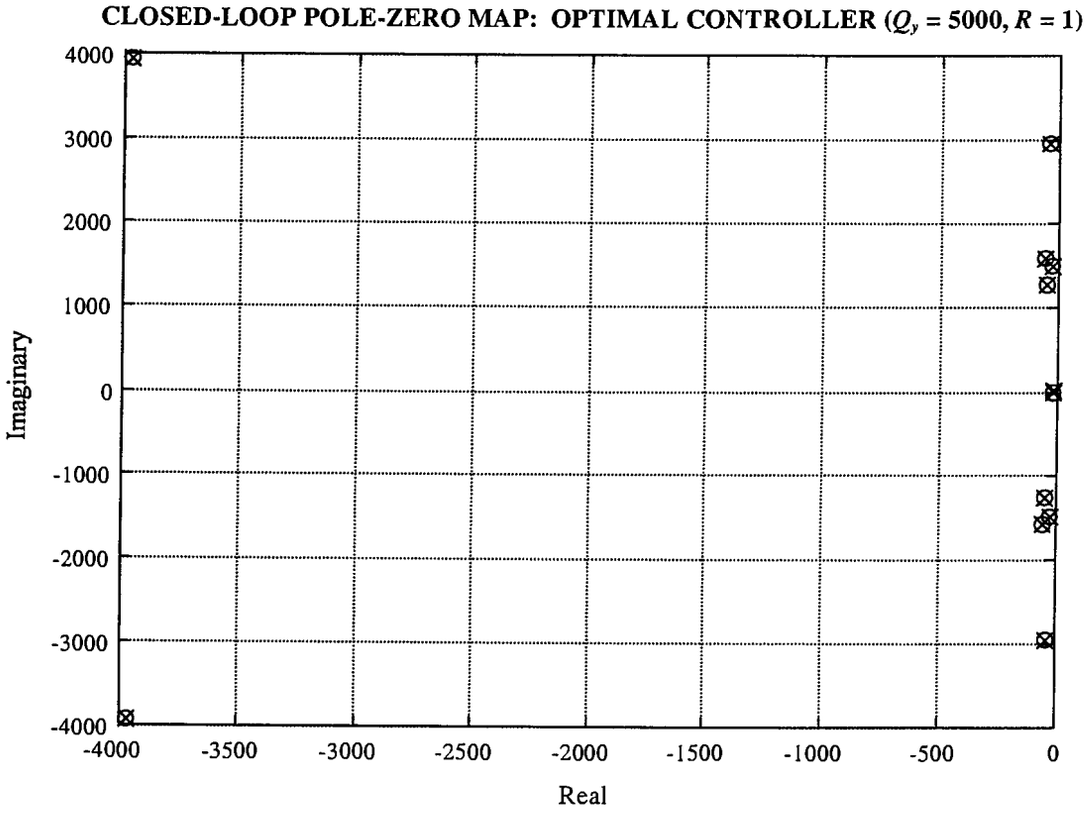

Figure 6.4.5.6: Closed-loop pole-zero map for optimal controller ($Q_y = 5000$, $R = 1$)

The attenuation factor of the optimal controller is compared with the open-loop *TR* magnitude in figure 6.4.5.7. The effect of pole-zero cancellation is clear from the figure.

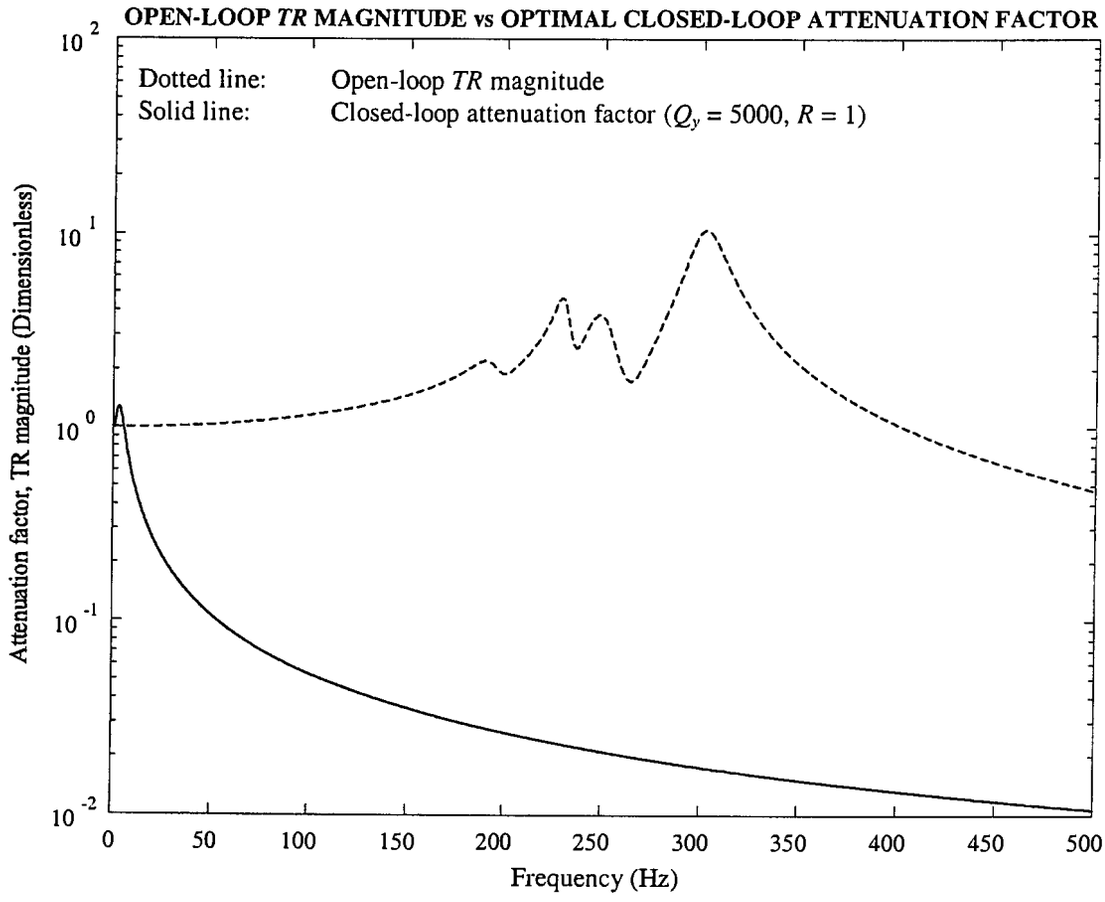

Figure 6.4.5.7: Open-loop *TR* magnitude and optimal closed-loop attenuation factor

The suboptimal control parameters are given next. The design is based on the optimal controller.

Suboptimal state feedback controller

The closed-loop pole with undamped frequency of 3,7 Hz is shifted to 5,6 Hz (i.e. an increase of 50%) and the damping factors of all the zeroes, with the exception of one, are increased to above 5%. Damping of the pole at 234 Hz is lowered from 1,88% to 1,22%. The state feedback gain vector K which places the poles accordingly, is:

$$K=\{-19871 \quad 531{,}5 \quad 107030 \quad 11421 \quad -36570 \quad -92131 \quad -13057 \quad 187250 \quad 29893 \quad 625{,}92 \quad 40340 \quad 126250 \quad -113250\} \tag{6.4.5.12}$$

The poles and zeroes of the suboptimal closed-loop system are given in tables 6.4.5.6 and 6.4.5.7 respectively. The pole-zero map is shown in figure 6.4.5.8. (The real pole at 25,42 kHz is not shown).

Table 6.4.5.6: Poles of suboptimal closed-loop system

Undamped frequency (Hz)	Damping factor (%)
5,63	70,71
199,45	3,87
234,05	1,22
251,33	3,52
468,56	1,25
901,57	71,89
25417	real

Table 6.4.5.7: Zeroes of suboptimal closed-loop system

Undamped frequency (Hz)	Damping factor (%)
3,99	real
199,04	7,41
240,04	1,78 (positive real part)
261,74	7,14
462,60	7,47
879,19	55,03

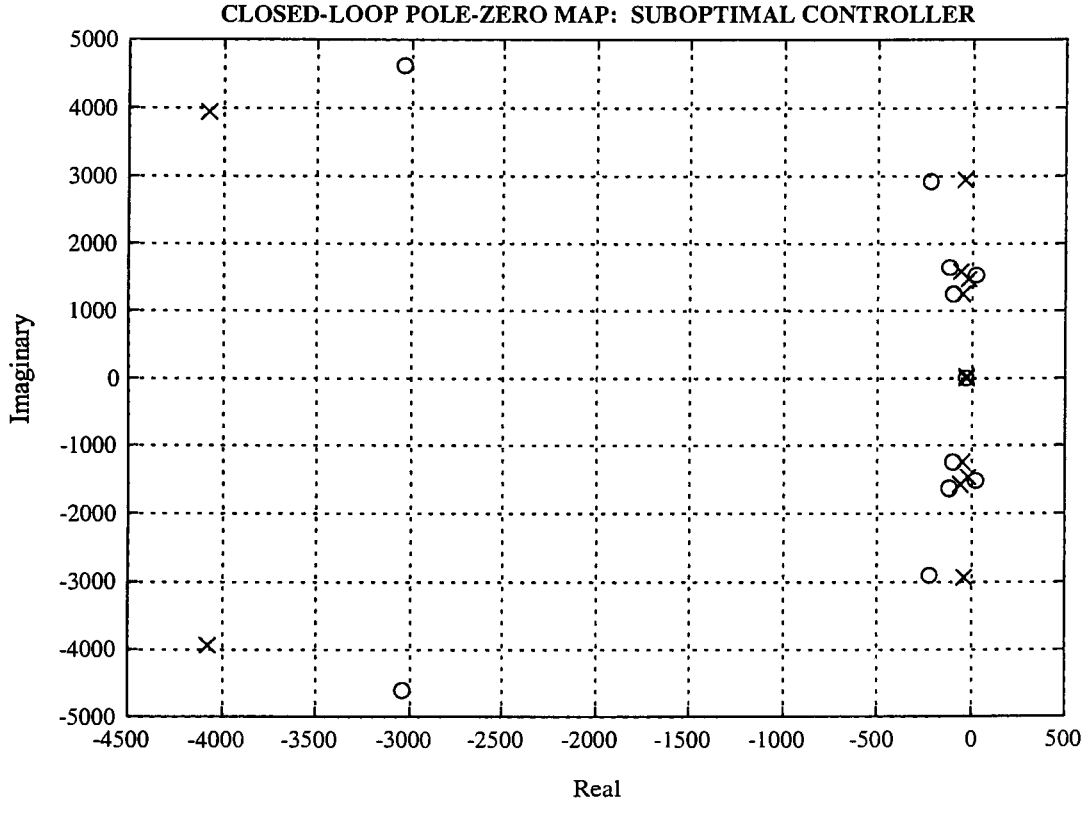

Figure 6.4.5.8: Closed-loop pole-zero map for suboptimal controller

The attenuation factor of the suboptimal controller is compared with the open-loop *TR* magnitude in figure 6.4.5.9.

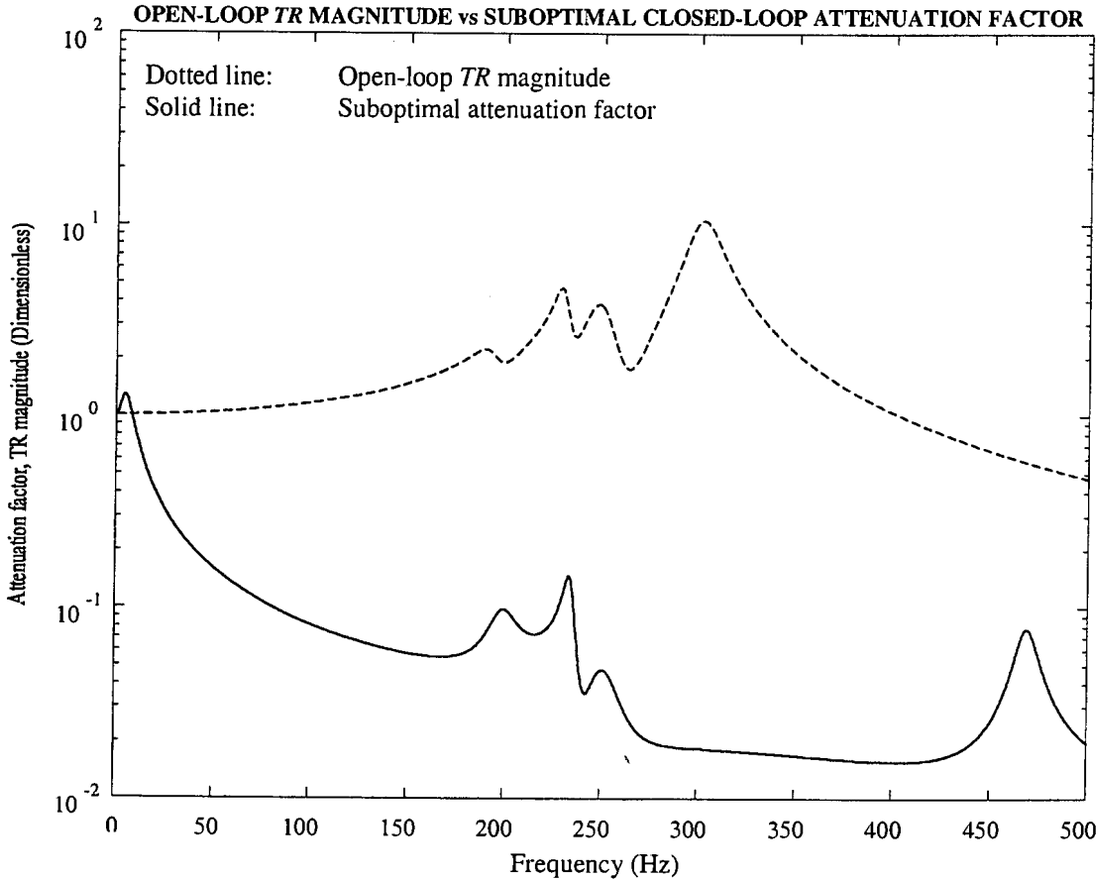

Figure 6.4.5.9: Open-loop *TR* magnitude and suboptimal closed-loop attenuation factor

A comparison between the optimal and suboptimal controller attenuation factors is shown graphically in figure 6.4.5.10. It can be seen from the figure that, unlike in the case of the optimal controller, the suboptimal attenuation factor does not display pole-zero cancellation.

The suboptimal attenuation factor graph displays a resonance peak at 476 Hz, which corresponds with the base natural frequency. The suboptimal controller excites the base mode, while the optimal controller doesn't.

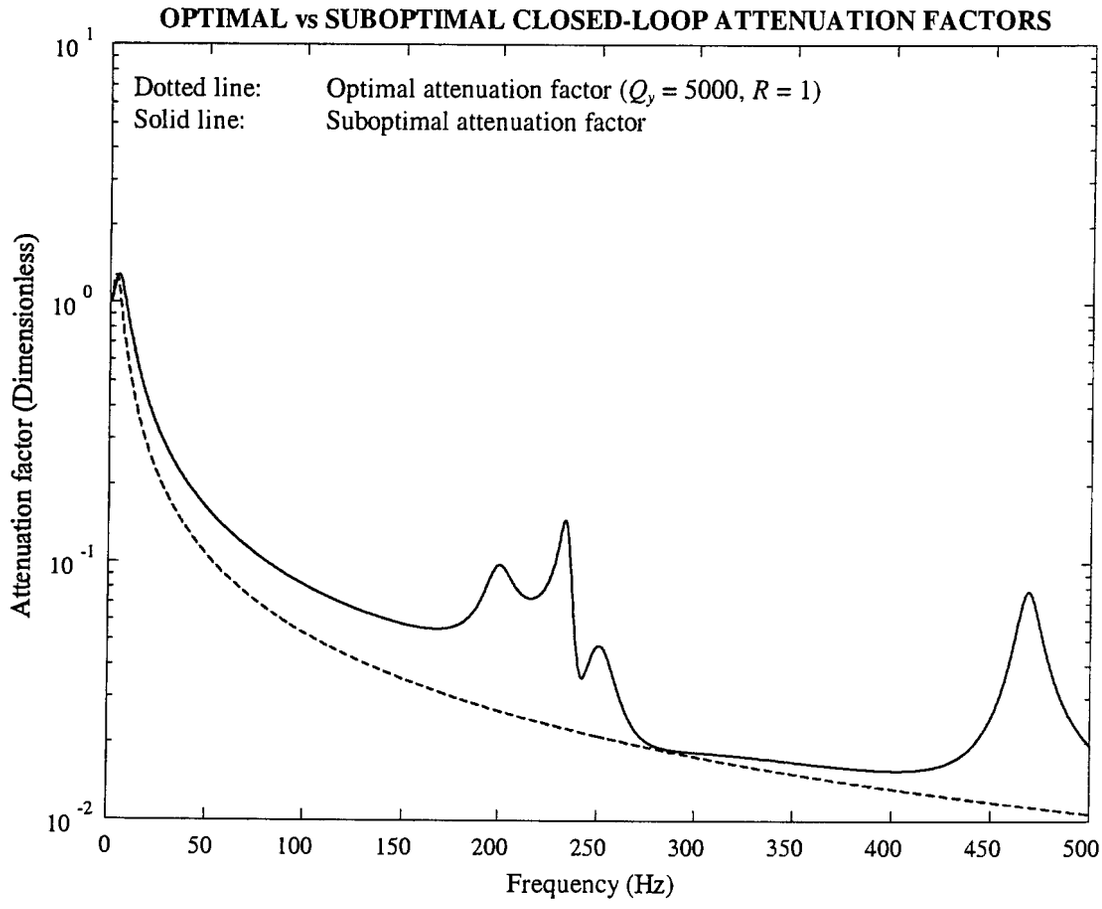

Figure 6.4.5.10: Comparison between optimal and suboptimal closed-loop controller attenuation factors

The optimal linear quadratic observer parameters are given next.

Linear quadratic optimal observer (LQE)

The solution of the optimal observer Riccati equation (6.4.4.25) is determined for measured Q and R values of 0,0103. These values correspond with 15,6% of that of the required output. The solution of the Riccati equation is subtituted into equation 6.4.4.27 to give the optimal observer gain matrix as follows:

$$L = \{0{,}07109 \quad 0{,}1065 \quad -0{,}102 \quad -0{,}0797 \quad -0{,}04247 \quad 0{,}04399 \quad 0{,}09784 \quad -0{,}2468 \quad 0 \quad 0 \quad 0 \quad 0 \quad 0\}^T \tag{6.4.5.13}$$

The disturbance-to-control and output-to-control *TF*'s are obtained by application of equations 6.4.4.24a and 6.4.4.24b. The poles of *U/*D and *U/Y* are given in table 6.4.5.8, while the zeroes of *U/D* and *U/Y* are respectively given in tables 6.4.5.9 and 6.4.5.10.

Table 6.4.5.8: Poles of *U/D* & *U/Y* for optimal observer

Undamped frequency (Hz)	Damping factor (%)
6,66	84,36
199,53	3,98
234,14	1,46
251,63	3,59
468,67	1,36
900,62	71,61
25647	real

Table 6.4.5.9: Zeroes of *U/D* for optimal observer

Undamped frequency (Hz)	Damping factor (%)
74,19	* real
196,16	3,94
233,88	1,78
261,93	3,33
269,05	39,95
476,37	1,20
17681	positive real

Table 6.4.5.10: Zeroes of *U/Y* for optimal observer

Undamped frequency (Hz)	Damping factor (%)
74,19	real
146,95	real
196,62	3,44
234,29	1,02
262,83	2,33
269,05	39,95
476,37	1,20

The pole-zero maps of *U/D* and *U/Y* for the suboptimal controller and optimal observer are shown in figures 6.4.5.11 and 6.4.5.12 respectively. (The real zero of *U/D* at 17,68 kHz is not shown).

The magnitude and phase spectra of *U/D* and *U/Y* are respectively shown in figures 6.4.5.13 and 6.4.5.14.

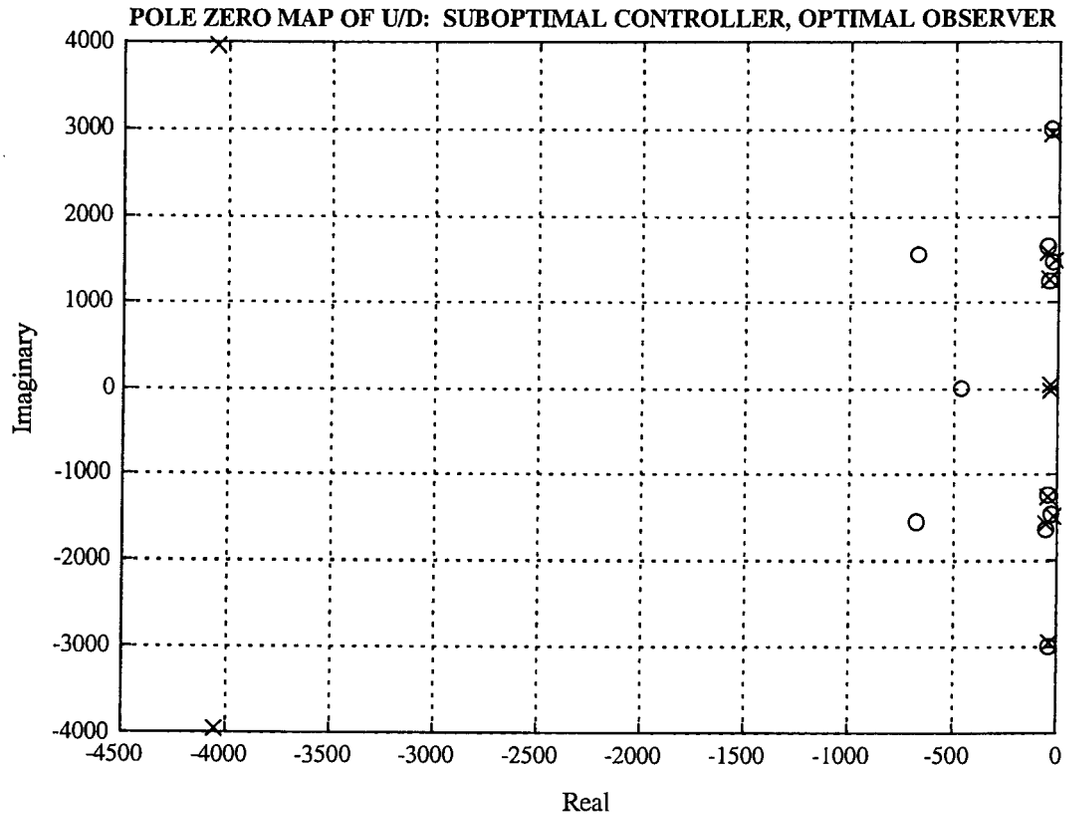

Figure 6.4.5.11: Pole-zero map of *U/D* (suboptimal controller with optimal observer)

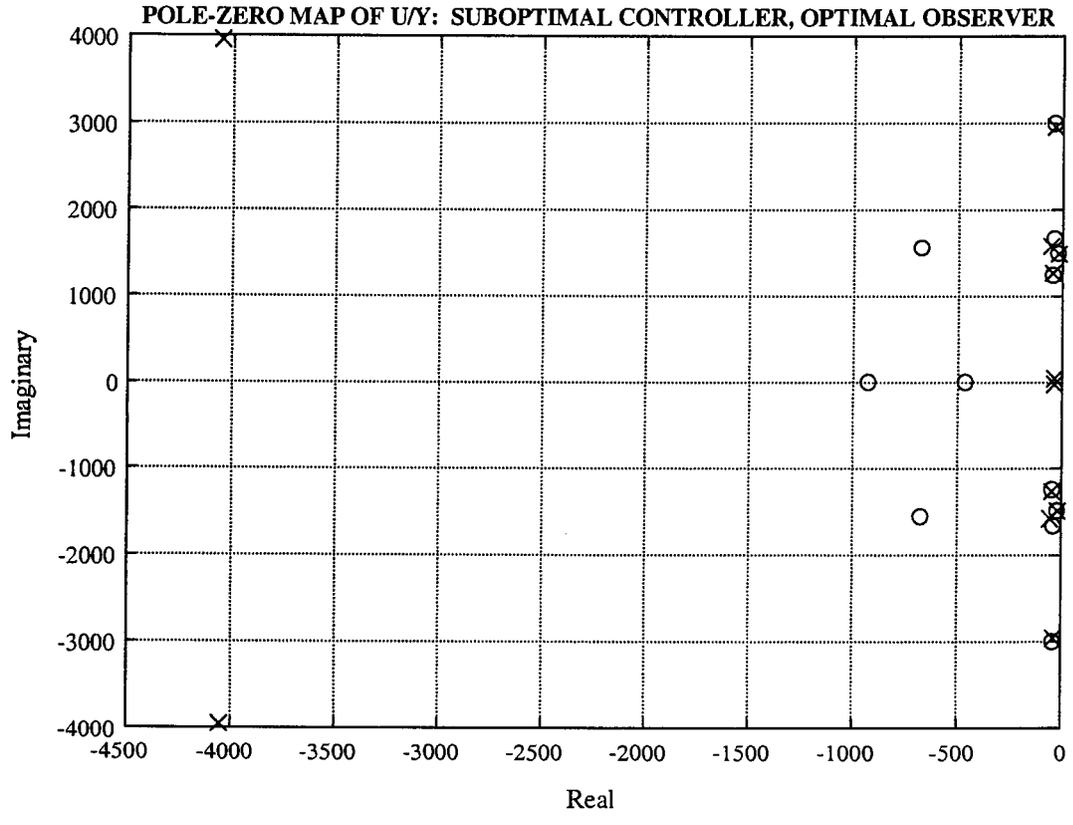

Figure 6.4.5.12: Pole-zero map of *U/Y* (suboptimal controller with optimal observer)

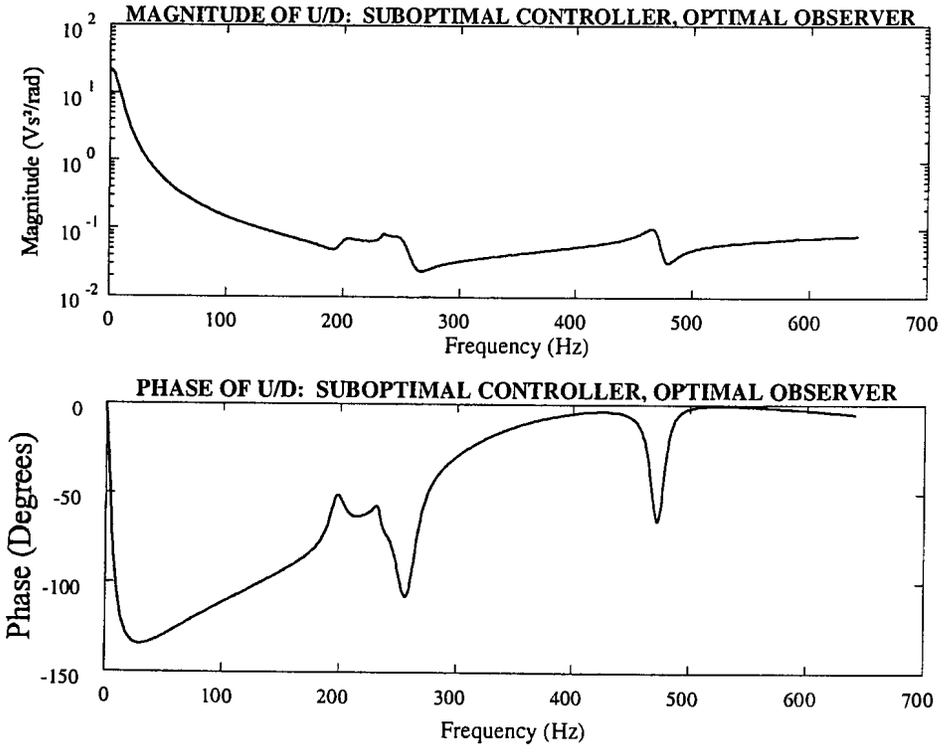

Figure 6.4.5.13: **Disturbance to control *TF* magnitude & phase spectra: Suboptimal controller with LQE optimal observer**

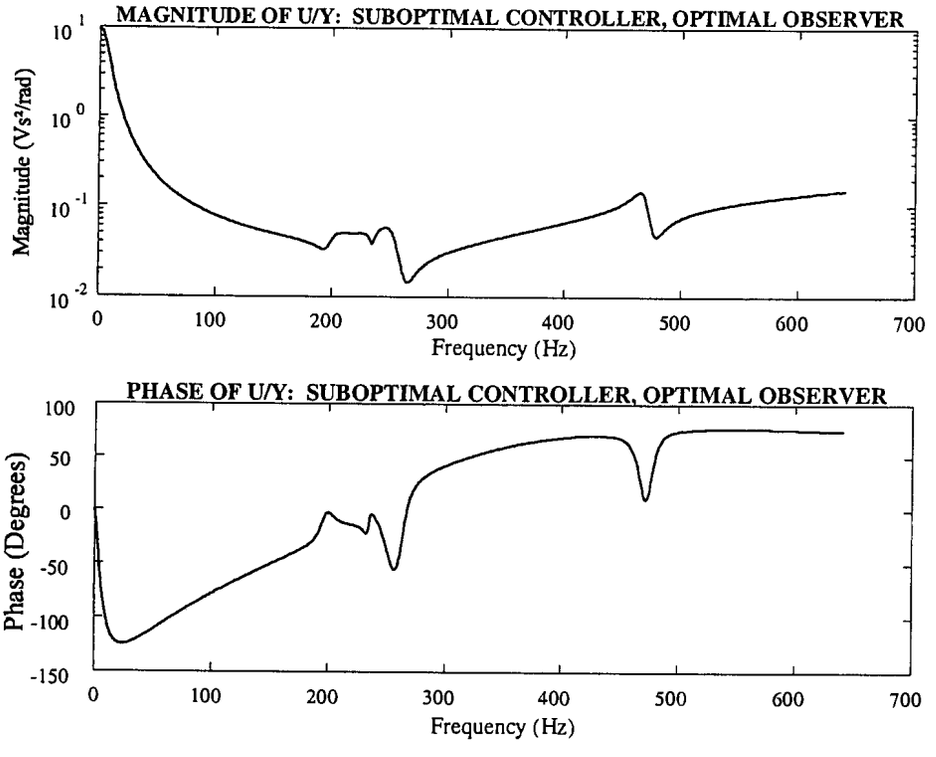

Figure 6.4.5.14: **Output to control *TF* magnitude and phase spectra: Suboptimal controller with LQE optimal observer**

The coupled state and output equations of the closed-loop system, consisting of the plant, suboptimal controller and optimal observer, are given in equations 6.4.4.20. The system is stable.

Suboptimal controller with suboptimal observer

It can be seen from equation 6.4.5.13 that the last five elements of the optimal observer gain matrix are zero. This is a consequence of the fact that the corresponding elements in the disturbance driving matrix B_d (see equation 6.4.5.8c) are zero. Although the plant is fully observable, the controller will not be able to control the last five states, i.e. the two base states and the three coil states, from the output.

In order to control these states, the corresponding elements of the observer gain matrix are changed to nonzero values. Contrary to the design of the suboptimal controller, the purpose is not to alter the frequencies and damping factors of poles and zeroes, but to control all the states. The resulting observer is necessarily suboptimal in terms of the process and output weights Q and R in equations 6.4.4.26.

The suboptimal observer gain matrix is modified as follows:

$$L=\{0{,}07109 \quad 0{,}1065 \quad -0{,}102 \quad -0{,}07697 \quad -0{,}04247 \quad 0{,}04397 \quad 0{,}09784 \quad -0{,}2468 \quad 0{,}05 \quad 0{,}05 \quad 0{,}05 \quad -0{,}02 \quad -0{,}02\}^T \tag{6.4.5.14}$$

The magnitude and phase spectra of U/D and U/Y of the suboptimal controller and suboptimal observer are shown in figures 6.4.5.15 and 6.4.5.16 respectively.

The coupled state and output equations of the closed-loop system, consisting of the plant, suboptimal controller and suboptimal observer, are given in equations 6.4.4.20. The coupled system is stable.

The TF magnitude and phase of U/Y for the suboptimal controller and suboptimal observer are compared with those of the suboptimal controller and optimal observer in figure 6.4.5.17. (The magnitude and phase spectra for U/D are not shown because the differences between the spectra are hardly visible. This is mainly because certain elements of the the L matrix are adjusted, while the B_d matrix is unaffected.)

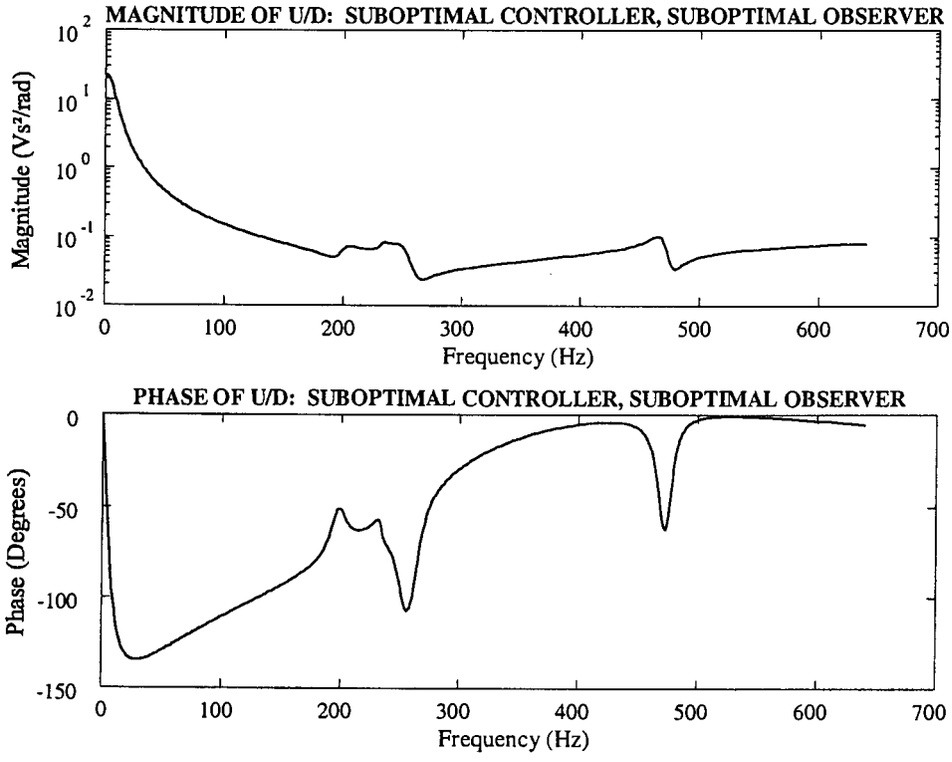

Figure 6.4.5.15: **Disturbance to control *TF* magnitude and phase spectra: Suboptimal controller with suboptimal observer**

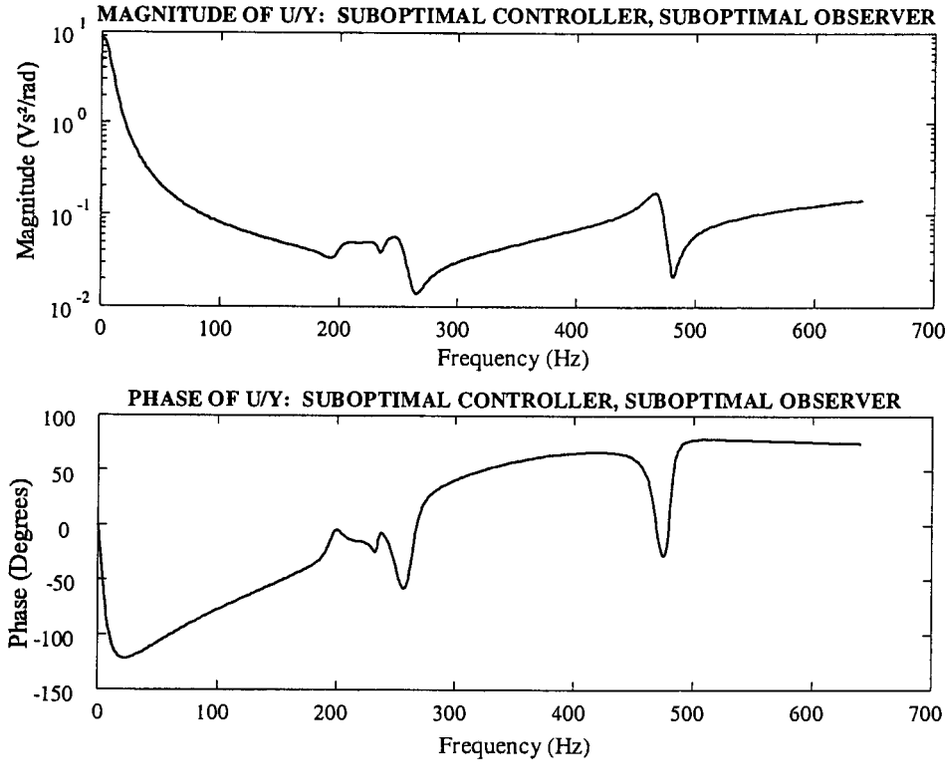

Figure 6.4.5.16: **Output to control *TF* magnitude and phase spectra: Suboptimal controller with suboptimal observer**

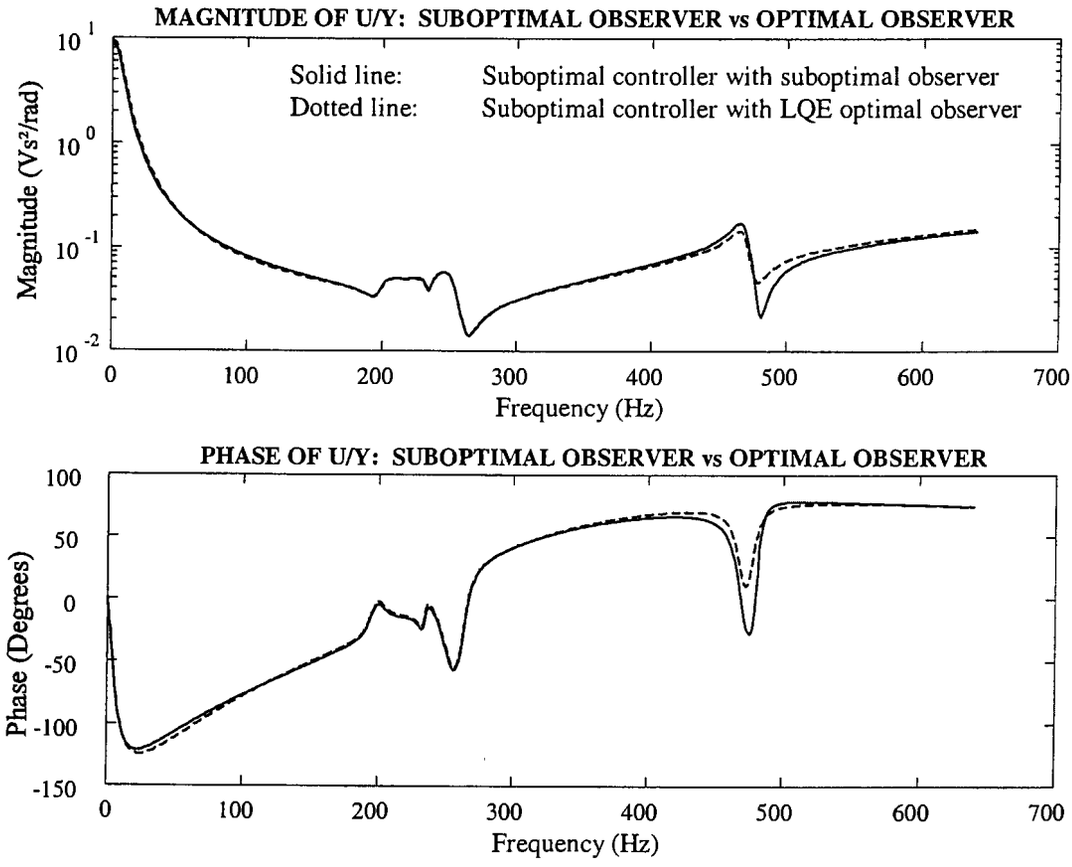

Figure 6.4.5.17: **Output to control *TF* magnitude and phase spectra: Suboptimal controller, suboptimal observer vs optimal observer**

The effect of output integral feedback on the attenuation factor spectra and stability of the closed-loop system are discussed next.

Suboptimal controller with suboptimal observer and output integral feedback

In this study, the optimal integral feedback gain is determined with the aid of simulations. Before the simulation results are given, the effects of the gain on the attenuation factor and closed-loop stability are indicated. The maximum allowable gain at the stability limit, determined by trial-and-error, is 2237. The closed-loop attenuation spectra, for gains of 0, 1000 and -50000, are shown in figure 6.4.5.18. It can be seen that, for the above three gains, the lowest (best) attenuation is achieved with a gain of -50000.

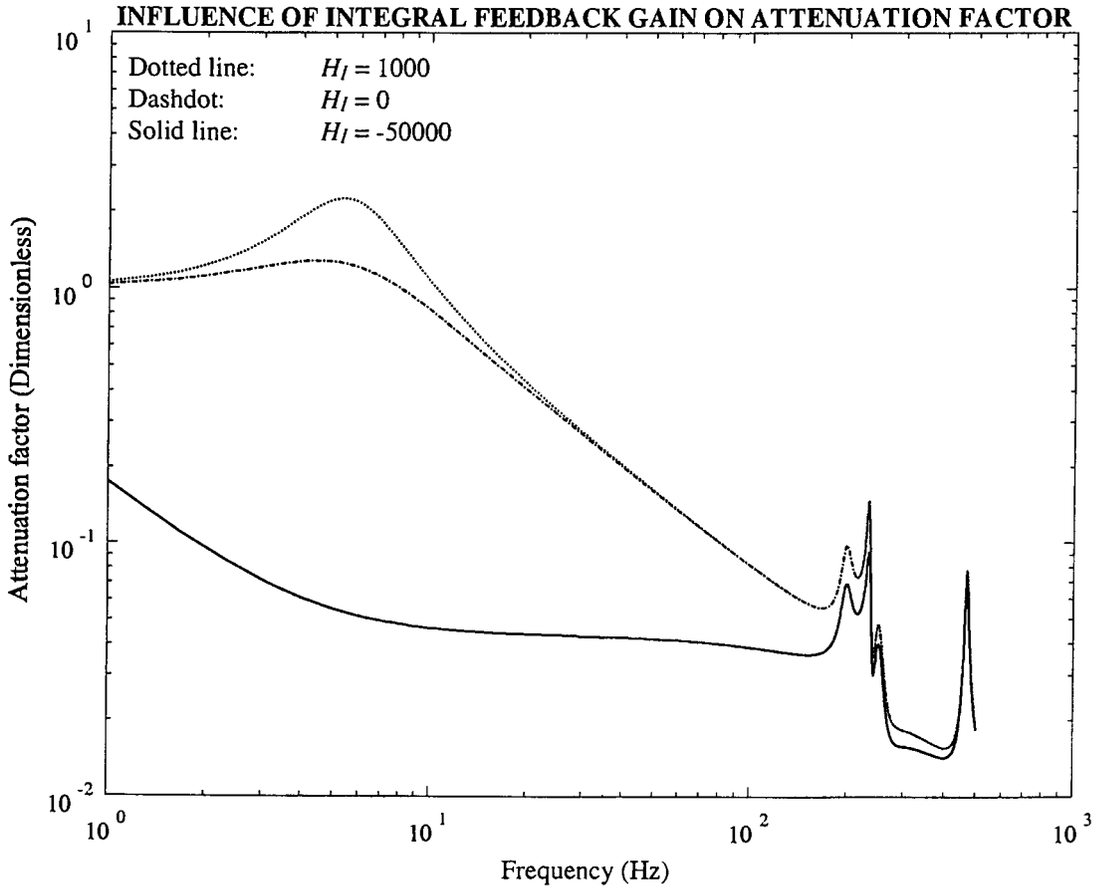

Figure 6.4.5.18: Attenuation factors for suboptimal controller with suboptimal observer and various output integral feedback gains

The design of equivalent digital filters for the disturbance feedforward (*U/D*), output feedback (*U/Y*) and output integral feedback *TF*'s are given next.

Equivalent digital filters

The equivalent digital filters for the disturbance to control and output to control transfer functions *U/D* and *U/Y* are respectively given by:

$$G\left(z^{-1}\right)=\frac{\sum_{i=0}^{12} b_{gi}\left(z^{-1}\right)^{i}}{\sum_{i=0}^{12} a_{gi}\left(z^{-1}\right)^{i}} \qquad \textbf{(6.4.5.15a)}$$

$$H\left(z^{-1}\right)=\frac{\sum_{i=0}^{12} b_{hi}\left(z^{-1}\right)^{i}}{\sum_{i=0}^{12} a_{hi}\left(z^{-1}\right)^{i}} \qquad \textbf{(6.4.5.15b)}$$

The numerator and denominator coefficients of the two digital filters, for a sample frequency of 2,5 kHz, are given in table 6.4.5.11. (Only the first five digits after the decimal point are shown.)

Table 6.4.5.11: Numerator and denominator filter coefficients for $G(z^{-1})$ and $H(z^{-1})$

i	b_{gi}	a_{gi}	b_{hi}	a_{hi}
0	0,05593	1,00000	0,17840	1,00000
1	-0,31316	-6,86194	-1,51049	-7,24684
2	0,69647	21,71518	6,17473	24,48686
3	-0,40650	-40,88123	-16,06805	-50,24938
4	-1,71159	48,39971	29,60721	67,85216
5	5,64420	-32,27825	-40,65931	-59,48195
6	-9,37469	1,15975	42,62427	27,33570
7	10,41497	22,41063	-34,31553	5,90594
8	-8,23882	-25,61932	21,01443	-20,38617
9	4,65344	15,38907	-9,52534	16,49180
10	-1,80623	-5,27795	3,02686	-7,29457
11	0,43651	0,86682	-0,60429	1,76323
12	0,05013	-0,02246	0,05722	-0,17677

In order to determine the coefficients tabled above, the real pole at 25,65 kHz and the real zero of *U/D* at 17,68 kHz, are removed. These frequencies are well in excess of the Nyquist frequency (1,25 kHz). The resulting filter orders are therefore 12, instead of 13. Both filters are the closed-loop system are stable.

Equivalent digital filter for output integrator and filter gain

The feedback integrator is replaced by the following digital filter:

$$H_I\left(z^{-1}\right) = 0{,}0002\frac{1+z^{-1}}{1-0{,}99z^{-1}} \qquad \textbf{(6.4.5.16)}$$

The filter *TF* is compared with that of a pure integrator in figure 6.4.5.19.

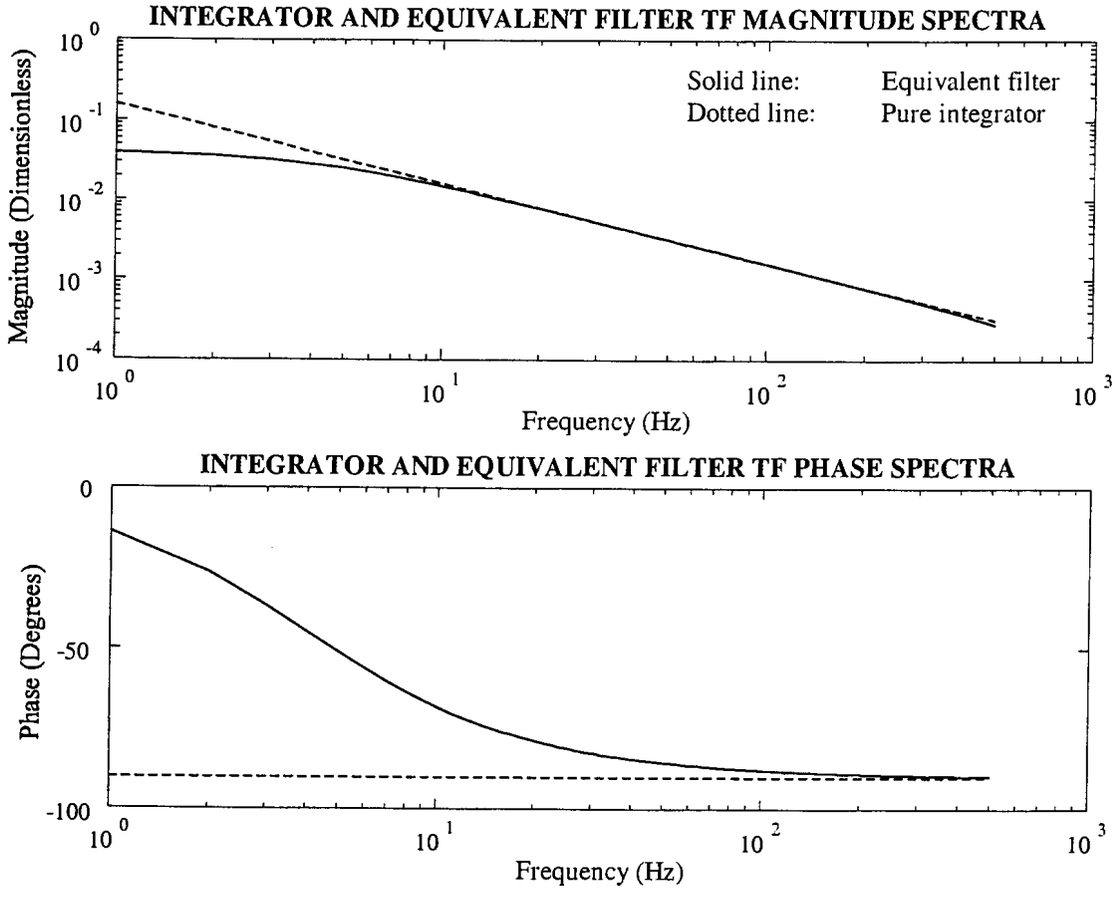

Figure 6.4.5.19: Integrator and equivalent filter magnitude and *TF* phase spectra

The minimum attenuation factor, for a frequency band of 0 Hz to 100 Hz, is achieved with a gain of –61,3.

6.5 Controller test setup and equipment

The controller test setup and test equipment are described in this section. The equipment mainly consists of a test bench, disturbance generation equipment, power amplifiers for the disturbance and control signals, the plant, sensors, sensor signal amplifiers, control equipment and data capturing equipment. A schematic layout of the test setup is shown in figure 6.5.1.

The test bench that was used for characterization of the magnetostrictive LOS stabilization system, as shown in figure 4.3.1.3, is used for testing the controller. The bench serves as a platform for the optical instrument stabilization system and electrodynamic shaker, which excites the base.

The base disturbance signal is generated in Visual Designer, which is a graphical simulation environment, similar to Simulink. The software operates with a low-cost Burr-Brown / Intelligent Instrumentation data card, model PCI 20428-W1, which is normally used for test signal generation and data capturing. Data is generated and captured in buffers, with selectable length, type and sample frequencies. The card is supplied with two D/A and sixteen A/D channels.

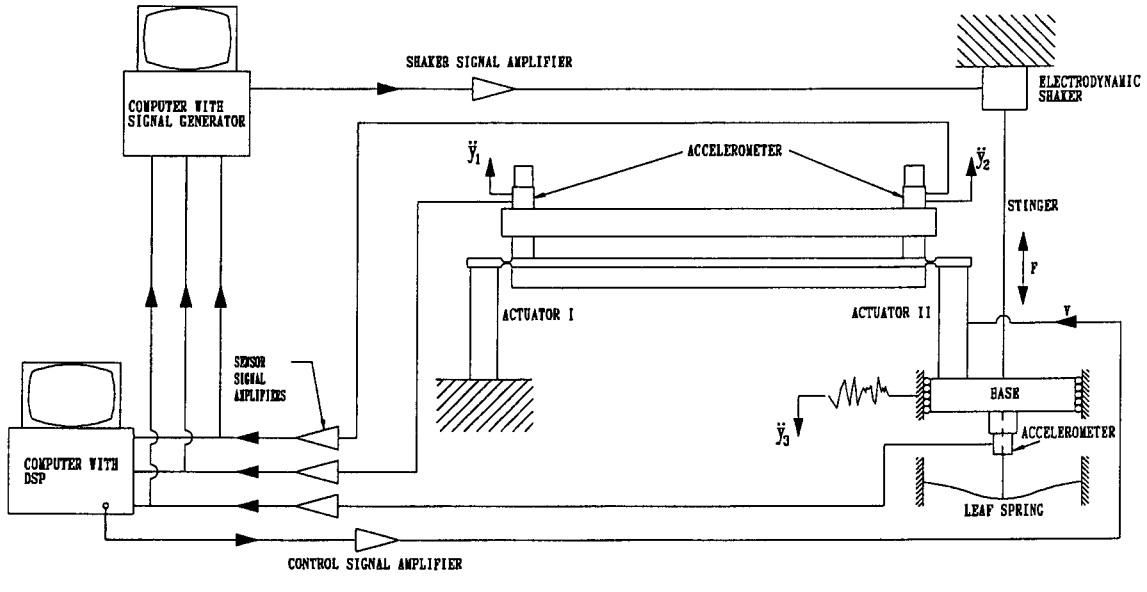

Figure 6.5.1: Controller test setup

The computer communicates with the card through direct memory access (DMA). Processing speed is determined by the computer CPU speed. Contrary to the dSpace card which was used to characterize the plant, this particular Burr-Brown card does not contain a DSP and is not suitable for real-time control, due to excessive throughput lag.

The base disturbance signal is supplied to the electrodynamic shaker via a matched power amplifier. According to the manufacturer, MB Dynamics, frequency bandwidth and maximum power output of the amplifier are 0 Hz to 30 kHz and 750 W respectively.

The shaker excites the base by means of a stinger (a thin steel string). The base is guided by linear bearings, in order to eliminate stick-slip motion, shock feedbacks to the shaker and angular motion of the base. The shaker cannot support the base statically, therefore the latter is suspended by a leaf spring. Spring stiffness and base mass are 7,16 MN/m and 8 kg respectively (see table 5.6.1).

The plant consists of the two actuators, the "dummy" optical instrument and its support structure. Dimensional details of the plant are given in section 4.2, while the dynamic coil and plant characteristics are given in sections 5.4 and 5.6 respectively.

An MB Dynamics SS 250 amplifier, similar to the shaker amplifier, powers the coils of actuator II. The amplifier was discussed in more detail in section 4.3.2. Its TF magnitude and phase spectra, for different output levels and a constant input level, are shown in figure 4.3.2.2.

Three accelerometers are used to measure the base and instrument *translational* motion. Two of the accelerometers are attached to the "dummy" optical instrument, one at each end of the instrument, while the third is placed upside down underneath the base. (A preferred position for accelerometer III would be on top of the base, next to actuator II. However, this space is taken up by the stinger).

Each sensor signal is amplified by a battery-powered amplifier. Amplifier gains are logarithmically adjustable, with gains of 2, 10 or 20, for accelerometers I and II, and gains of 1, 10 or 100 for accelerometer III. The instrument accelerometer amplifiers can also be powered by the main electrical supply, through a transformer, during lengthy test periods.

The amplified signals are captured by a separate PC, which houses the digital signal processor (DSP). The DSP has four analogue input and four analogue output channels. It is timed by a built-in clock, which runs at 40 MHz, and operates independently of the computer CPU clock. The DSP converts the accelerometer signals to digital form, carries out the control calculations, converts the control signal to analogue form and supplies it to the actuator coil via the power amplifier. The software supporting the DSP codes the Simulink block diagram in C, compiles it and loads it onto the DSP. (The DSP was discussed in more detail in section 4.3.2.)

The amplified sensor signals are displayed on a Visual Designer scope and stored in files for later processing.

6.6 Controller implementation and test procedure

Controller implementation and the test procedure are discussed in this section. Excitation of the disturbance is discussed in section 6.6.1, followed by controller implementation in section 6.6.2. The test procedure and test execution are described in sections 6.6.3 and 6.6.4 respectively.

6.6.1 Disturbance excitation

An iterative approach is followed to excite the required disturbance. A description of the procedure is as follows: A filtered random voltage signal excites the base through the electrodynamic shaker (see figure 6.6.1.1 for a diagrammatic representation of the experimental setup). Test duration is 80 s. The base translational acceleration is measured and compared with that of the required disturbance signal. If the RMS-value of the measured signal differs by more than 5% from that of the required signal, the voltage signal amplitude is adjusted and the test is repeated. The procedure is repeated until the RMS-value of the measured signal is within 5% of that of the required signal.

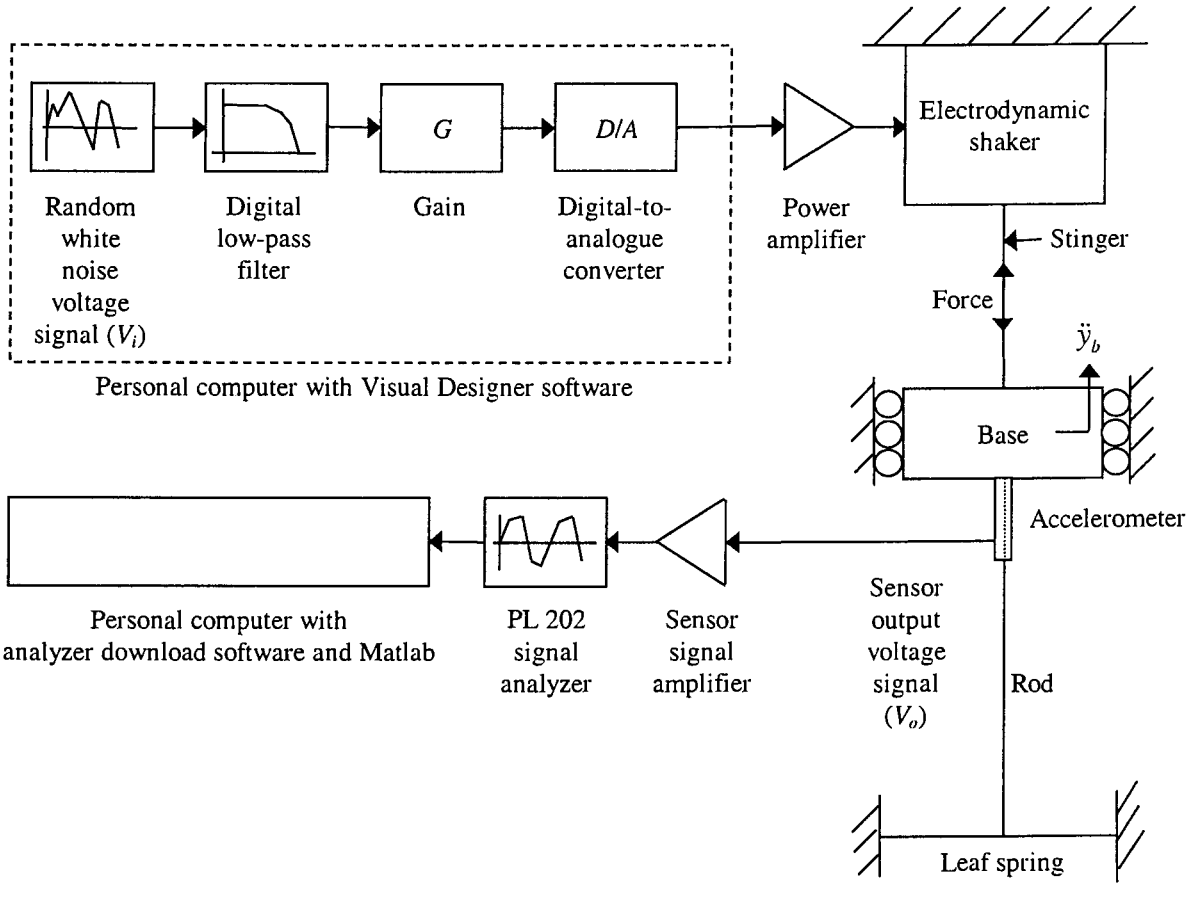

Figue 6.6.1.1: Disturbance excitation experimental setup

The random white-noise signal V_i is generated in Visual Designer. The signal is sampled at 2 kHz, which is 20 times the control bandwidth (100 Hz) and 4 times the maximum frequency of the disturbance signal (500 Hz). The signal is digitally filtered above 500 Hz, by means of a 2nd order low-pass (LP) filter.

The filter *TF* is given by:

$$TF = G(z^{-1}) = 0{,}29289\frac{1+2z^{-1}+1(z^{-1})^2}{1+0.(z^{-1})+0{,}17157.(z^{-1})^2} \qquad \textbf{(6.6.1.1)}$$

where the term z^{-1} represents a single sample-period delay.

Filter *TF* magnitude and phase spectra are shown in figure 6.6.1.2. Filter *TF* magnitude at 500 Hz is 0,707, or -3dB.

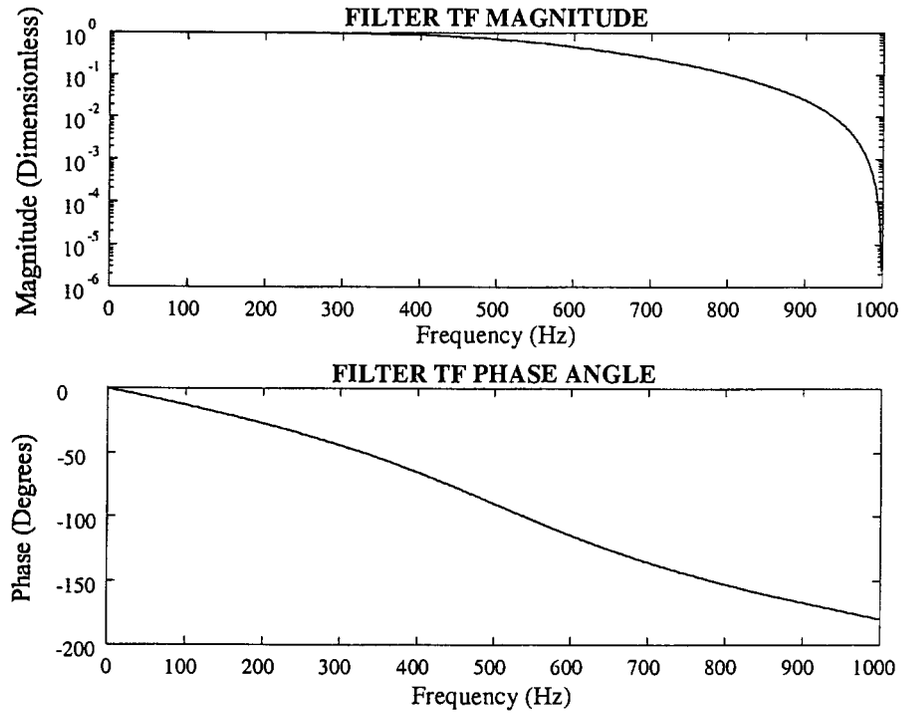

Figure 6.6.1.2: Second order digital LP filter *TF* magnitude and phase spectra

The signal is gained to facilitate amplitude adjustment. The resulting signal is supplied to the shaker through a built-in digital-to-analogue (*D/A*) converter and an external power amplifier, whose gain is held constant. (The amplifier was discussed in more detail in section 4.3.2). The base is excited by the shaker through a steel string, or stinger. Accelerometer output voltage V_o is captured with a PL202 signal analyzer. The captured signal is downloaded to a personal computer and processed in Matlab.

The base translational acceleration $\ddot{y}_b$ is obtained from the accelerometer output voltage signal V_o by means of the following equation:

$$\ddot{y}_b = V_o \times \underbrace{(-1)}_{Factor\,1} \times \underbrace{1000\left(\frac{mV}{V}\right)}_{Factor\,2} \times \underbrace{\frac{1}{10}\left(\frac{mV}{mV}\right)}_{Factor\,3} \times \underbrace{\frac{1}{83{,}1326}\left(\frac{g}{mV}\right)}_{Factor\,4} \times \underbrace{9{,}81\left(\frac{m/s^2}{g}\right)}_{Factor\,5} \qquad \textbf{(6.6.1.2)}$$

Factor 1 compensates for the accelerometer being mounted upside-down. Factor 2 converts the measured accelerometer voltage signal unit from volt to millivolt. This factor is included because the accelerometer calibration factor is given in mV/g. Factor 3 is the inverse of the accelerometer signal amplifier gain factor, i.e. 10. Factor 4 is the inverse of the accelerometer calibration factor, i.e. 83,1326 mV/g. Factor 5 converts the unit of acceleration from g to m/s^2. The resulting conversion factor between the accelerometer output signal V_o and base acceleration $\ddot{y}_b$ in equation 6.6.1.2, is -11,8 $m/s^2/V$.

The base angular acceleration $\ddot{\theta}_b$ is obtained by division of $\ddot{y}_b$ by 0,25m (the base length). The overall conversion factor between the accelerometer output voltage and base angular acceleration, i.e. $\ddot{\theta}_b / V_o$, is therefore -47,2 $rad/s^2/V$.

Once a base angular acceleration with an acceptable RMS-value is achieved, its crest factor, amplitude at 96,75 Hz and percentage energy in the control band, are calculated. If any of these values differ by more than 5% from those of the required acceleration signal, a new voltage signal is generated. The procedure is as follows: The complex Discrete Fourier Transform (*DFT*) of the required acceleration signal is divided by that of the measured signal, at each frequency in the spectrum, and multiplied with that of the random voltage signal:

$$V_{i1}(j\omega_k) = V_{i\,random}(j\omega_k)\frac{\ddot{Y}(j\omega_k)\big|_{required\ signal}}{\ddot{Y}(j\omega_k)\big|_{measured\ signal\ 1}} \qquad \textbf{(6.6.1.3)}$$

where ω_k is the k-th frequency in the spectrum and $\ddot{Y}(j\omega_k)$ is the DFT of $\ddot{y}$ at the k-th frequency. The voltage signal $V_{i1}(t)$ is obtained from the spectrum of voltages $V_{i1}(j\omega_k)$ by means of an inverse Fast Fourier Transform. The test is repeated with $V_{i1}(t)$ as input. Base acceleration is measured and its RMS-value, crest factor, amplitude at 96,75 Hz and percentage energy in the control band, are calculated. If all of these parameters are within 5% of those of the required signal, $V_{i1}(t)$ is the voltage signal which will be used to excite the base.

If not, the base acceleration spectrum is calculated and the *DFT* of V_{i2} is obtained as follows:

$$V_{i2}(j\omega_k) = V_{i1}(j\omega_k)\frac{\ddot{Y}(j\omega_k)\big|_{required\ signal}}{\ddot{Y}(j\omega_k)\big|_{measured\ signal\ 2}} \qquad \textbf{(6.6.1.4)}$$

The voltage signal $V_{i2}(t)$ is obtained from the spectrum of voltages $V_{i2}(j\omega_k)$ by means of an inverse Fast Fourier Transform. The procedure is repeated until the base acceleration RMS-

value, crest factor, amplitude at 96,75 Hz and percentage energy in the control band, are within 5% of those of the required signal.

Parameters of the experimentally generated disturbance signal are compared with those of the required disturbance signal in table 6.6.1.1. The amplitude spectrum of the experimentally generated signal is shown in figure 6.6.1.3.

Table 6.6.1.1: Comparison between measured and required disturbance parameters

Parameter	Required disturbance	Measured disturbance	Relative error
RMS angular acceleration	4,56 rad/s^2	4,59 rad/s^2	0,66 %
Crest factor	2,21	2,14	-3,17 %
Maximum amplitude (@ 96,75 Hz)	4,14 rad/s^2	4,06 rad/s^2	-1,93 %
Percentage energy in control band	91 %	93,7 %	2,97 %

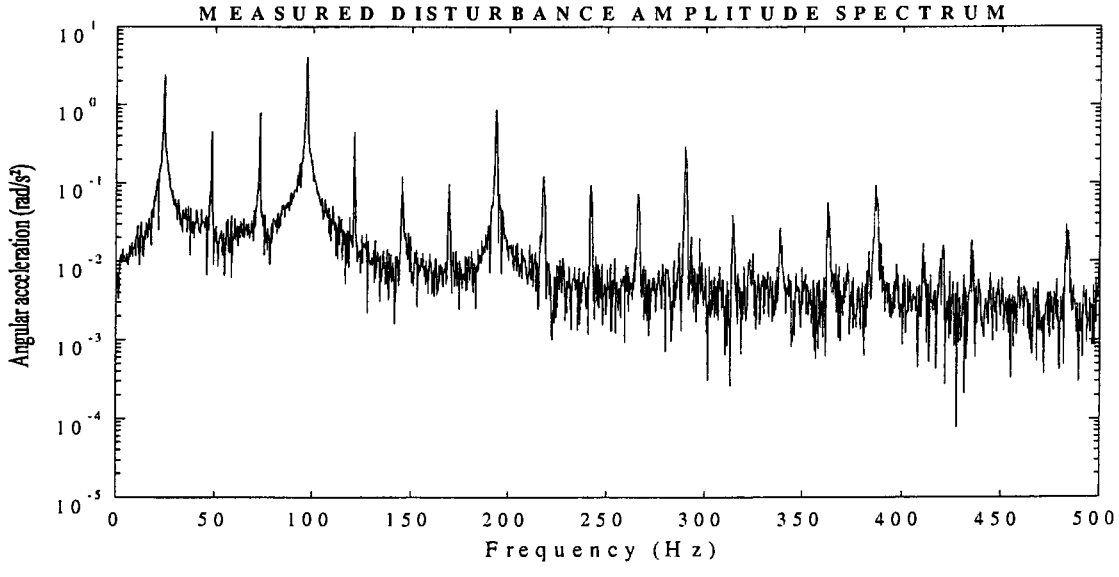

Figure 6.6.1.3: Measured disturbance amplitude spectrum

6.6.2 Controller implementation

The controller block diagram is generated in Simulink, coded in C, compiled and loaded onto the DSP. The block diagram is based on that of the simulated controller, shown in figure 6.4.4.1. For the control experiments, certain elements of the simulated block diagram are retained, some elements are deleted, and a number of elements are added. Elements that are retained, are the high-pass filters, disturbance feedforward and output feedback filter elements, bias signal generation blocks (i.e. step and rate limiter blocks), and gain and summation blocks.

Elements that are deleted, are the plant blocks and noise inputs. During testing, the noise inputs and plant outputs are automatically replaced by the true plant response and measurement noise signals.

Elements that are added, are A/D and D/A converter blocks, overall sensor calibration factor blocks and a "triggering" block, which synchronizes the bias signal with the sensor signals. The latter block is required to force the DSP to cut off the control signal whenever it is unbiased. Synchronization is achieved by multiplication of the bias signal, gained by the inverse of its maximum value, with the control signal.

The resulting experimental block diagram is shown in figure 6.6.2.1. The disturbance sensor signal is V_d and the two output accelerometer signals are V_{a1} for accelerometer I and V_{a2} for accelerometer II. K_{cd}, K_{ca1} and K_{ca2} are the calibration factors for the disturbance and output accelererometers I and II respectively.

Numerical values of the overall sensor calibration factors, DC voltage, rate-of-rise, soft start gain, bias gain, power amplifier gain, clipper limits and DSP card gain are determined. The card gain is unity for throughput signals, i.e. sensor-to-control signals, and 10 for signals generated in Simulink, i.e. the bias signal. The soft start gain and bias gain are scaled accordingly, by dividing the required values by 10. The numerical values used in the block diagram are given in table 6.6.2.1.

Table 6.6.2.1: Constant factors applicable to experimental control block diagram

Constant factor	Value	Unit of measurement
Disturbance accelerometer calibration factor K_{cd}	-45,39	rad/s^2/V
Output accelerometer I calibration factor K_{ca1}	76,27	rad/s^2/V
Output accelerometer II calibration factor K_{caII}	46,37	rad/s^2/V
DC voltage	9,2	V
Rate-of-rise	100	V/s
Soft start gain	0,0927	Dimensionless
Bias gain	0,1087	Dimensionless
Power amplifier gain	1,7	Dimensionless
Clipper limits: Upper; lower	9,9	V
	-9,9	V

Feedforward, feedback and integrator feedback gains are adjustable. The values depend on the controller type to be tested, i.e. open-loop feedforward, closed-loop feedback or feedforward plus feedback. The required values will be given in section 6.6.3, where the controller test procedure will be discussed.

The selected method for integration of the dynamic control equations, i.e. the 5th order Runge-Kutta method, is entered, as well as the integration time-step, i.e. 400μs. The latter is constant, since adaptive time-stepping is not available for real-time implementation of the controller on the DSP (see also section 4.3.2). The block diagram, with its filter, control, bias voltage, gain, clipper and integration parameters, are coded in C, compiled and loaded onto the DSP.

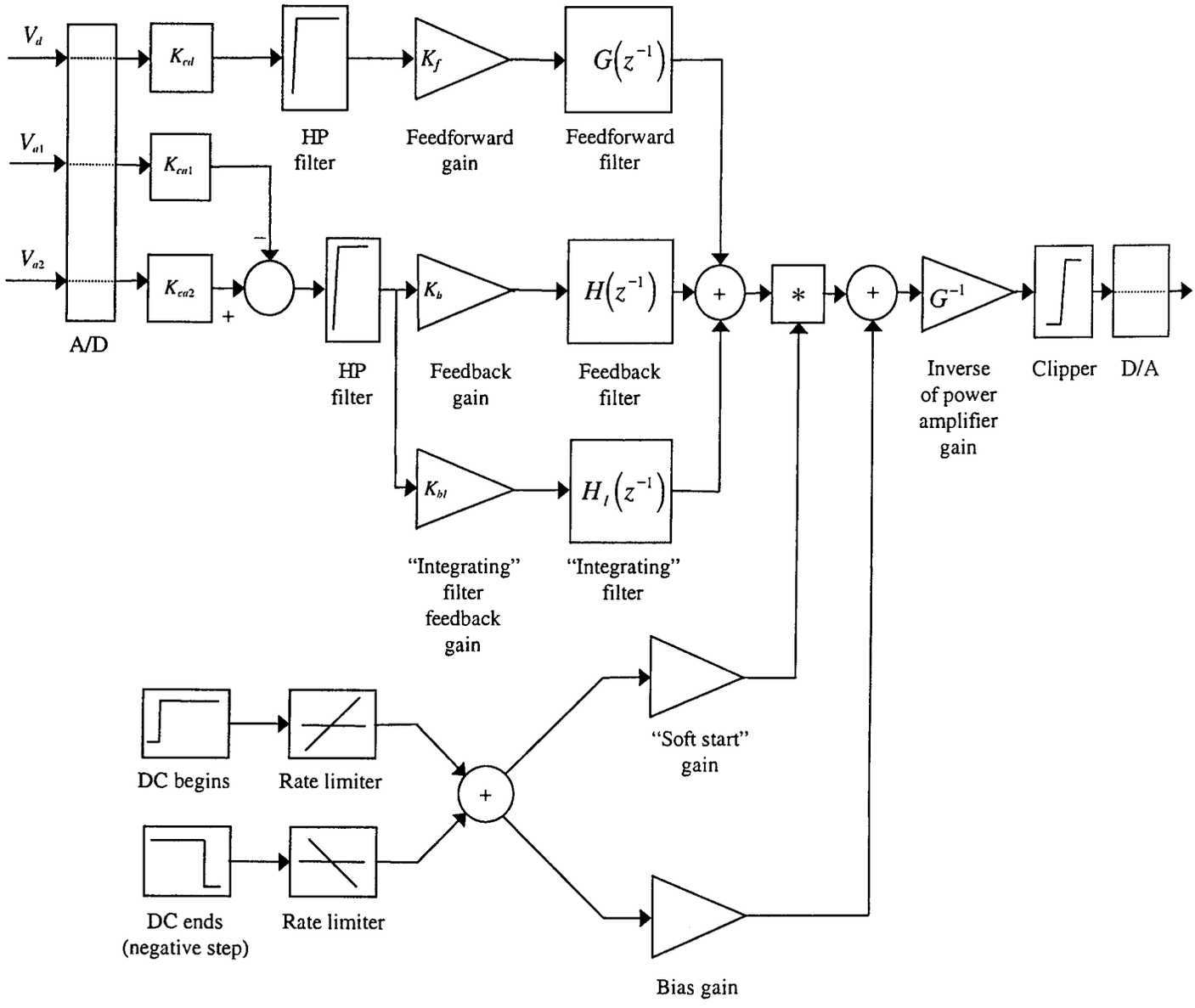

Figure 6.6.2.1: Experimental control block diagram

6.6.3 Test procedure

Three configurations of the controller, i.e. the disturbance feedforward, output feedback and disturbance feedforward plus output feedback configurations, are tested separately. The feedforward controller is tested first. This is to ensure that as large a percentage of the disturbance as possible is removed before the feedback loop is closed.

During the feedforward controller tests, zero output feedback and output integral feedback gains are used. The feedfoward gain is adjusted in increments of 5%, starting at 5%. After incrementing the gain, a test is carried out, the data is captured, processed, and the RMS attenuation factor is calculated. The attenuation factor is compared with that obtained during

the previous test. If an improvement is noticed, the gain is increased and the test is repeated, until no further improvement is achieved. The gain of the last test carried out with this configuration, is the maximum practically achievable feedforward gain.

The feedback loop is subsequently closed. The feedback gain, like the feedforward gain, is adjusted in 5% increments. For this configuration, a zero feedforward gain is used. The output integral feedback gain is initially zero. The feedback gain is increased until the system becomes unstable. The gain at the stability limit, is the maximum feedback gain. The output feedback gain, at the limit, is then held constant and the output integral feedback gain is adjusted in 5% increments, until the system becomes unstable. The gain at the stability limit is the maximum output integral feedback gain.

The disturbance feedfoward plus output feedback controller is subsequently tested. The maximum feedforward gain, output feedback and output integral feedback gains are used during the tests.

6.6.4 Test execution

The disturbance feedforward, output feedback and output integral feedback filter coefficients, sensor calibration factors, feedforward and / or feedback gains, DC voltage, rate limiter slope, clipper limits, sample rate, test duration and integration method are entered into the Simulink block diagram and parameter menu. The block diagram is compiled and loaded onto the DSP. The disturbance signal is excited in Visual Designer and the power amplifier gain is adjusted. An open-loop test is run, the time trace of the disturbance signal is captured and shown on a Visual Designer scope. It is processed and its RMS value is compared with that in table 6.6.1.1. If it differs by more than 5% from that in the table, it is corrected by adjusting the power amplifier gain.

While the disturbance signal is active, the gain of the power amplifier that drives the actuator coils, is adjusted. The DSP, which is inactive at this stage of the test, is activated and the control signal is supplied to the actuator coils, via the power amplifier. The time traces of the base and output signals are captured in Visual Designer and stored in a file for later processing. The time duration of the test corresponds with that of the known disturbance, i.e. 4s. Since this duration is relatively short, the test is repeated 22 times, giving a total duration of 88s for each controller configuration.

Although the same signal analyzer that was used for the characterization tests (as described in section 4.3.3) is available for the tests, it is not used. The reason is that its number of channels is limited to two, and its sample frequencies and window lenghts are only adjustable is fixed increments. The Visual Designer software, on the other hand, gives more flexibility in terms of number of channels, sample frequencies and window lengths. The disadvantage of capturing time traces, however, is that post-processing of the time-domain data is required to obtain the attenuation factor.

6.7 Controller test results

The controller test results are processed, presented and discussed in this section. Processing of the results is described in section 6.7.1. The results are presented in section 6.7.2 and discussed in section 6.7.3.

6.7.1 Processing of test results

The time domain data is processed for each test run of 4s. The captured accelerometer signals are multiplied by their overall calibration factors to obtain the vertical accelerations. The base acceleration signal is divided by the base length to obtain the base angular acceleration. The acceleration measured by accelerometer I is subtracted from that measured by accelerometer II, and divided by the distance between the accelerometers to obtain the output angular acceleration.

The transfer function spectrum of each test is calculated, using the following equation:

$$G(\omega) = \frac{P_{yd}(\omega)}{P_{dd}(\omega)} \qquad \textbf{(6.7.1.1)}$$

where P_{yd} is the cross spectral density between the disturbance and output, and P_{dd} is the disturbance power spectral density. A Hanning window is used to take start- and end effects into account. The frequency resolution is 0,25 Hz, which is the inverse of the test duration of every test, i.e. 4s. The average of the test spectra is calculated for each configuration. The magnitudes of the spectra, i.e. the attenuation factors, are plotted for the disturbance frequency band of 0 Hz to 100 Hz. The attenuation factors at the dominating frequencies in the disturbance spectrum, i.e. at 24 Hz, 48,5 Hz, 72,5 Hz and 96,75 Hz, are tabulated.

The isolation factors, i.e. the complement of the attenuation factors, are calculated at each of the dominating frequencies. The attenuation factors, in terms of the ratio of output RMS to disturbance RMS, in the frequency band of 0 Hz to 100 Hz, are calculated from the time-domain data.

6.7.2 Experimental test results

The maximum feedforward gain achieved during the tests, is 0,76. The maximum feedback and integral feedback gains achieved during the tests are 0,76 and -87,5 respectively. These gains are at the limit of stability.

The experimentally determined attenuation factor of the feedforward controller, for a 0,76 disturbance feedforward gain, zero output feedback gain and zero integral output feedback gain, is shown in figure 6.7.2.1. The frequency range is 0 Hz to 100 Hz, with a resolution of 0,25 Hz. The dashed line indicates a unit attenuation factor accross the spectrum, i.e. the attenuation that would be achieved in the absence of an isolation system. The RMS attenuation for the disturbance feedforward controller, for a frequency bandwidth of 0 Hz to 100 Hz, is 0,44 (-7,06 dB).

The experimentally determined attenuation factor of the feedback controller, for a zero disturbance feedforward gain, output feedback gain of 0,76 and output integral feedback gain of -87,5 is shown in figure 6.7.2.2. The RMS attenuation factor for the feedback controller is 0,7 (-3,1 dB).

The experimentally determined attenuation factor of the feedforward plus feedback controller, for feedforward and feedback gains of 0,76 and an output integral feedback gain of -87,5 is shown in figure 6.7.2.3. The RMS attenuation factor for the disturbance feedforward plus feedback controller is 0,32 (-9,75 dB).

The test results for the three configurations are summarized in table 6.7.2.1.

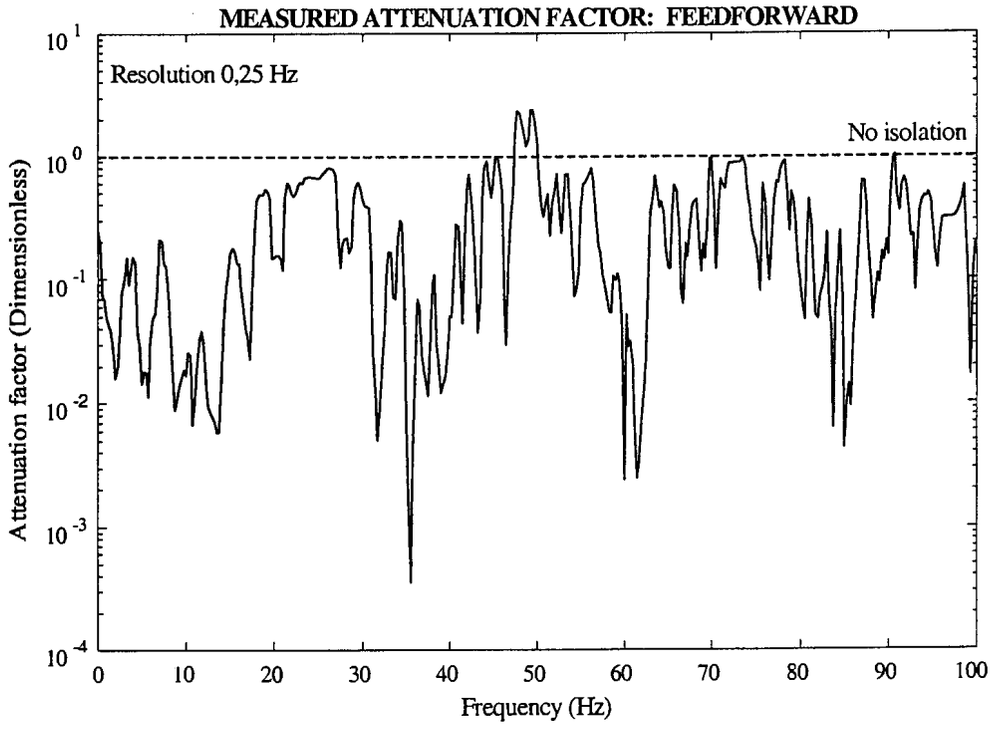

Figure 6.7.2.1: Attenuation factor spectrum for disturbance feedforward controller

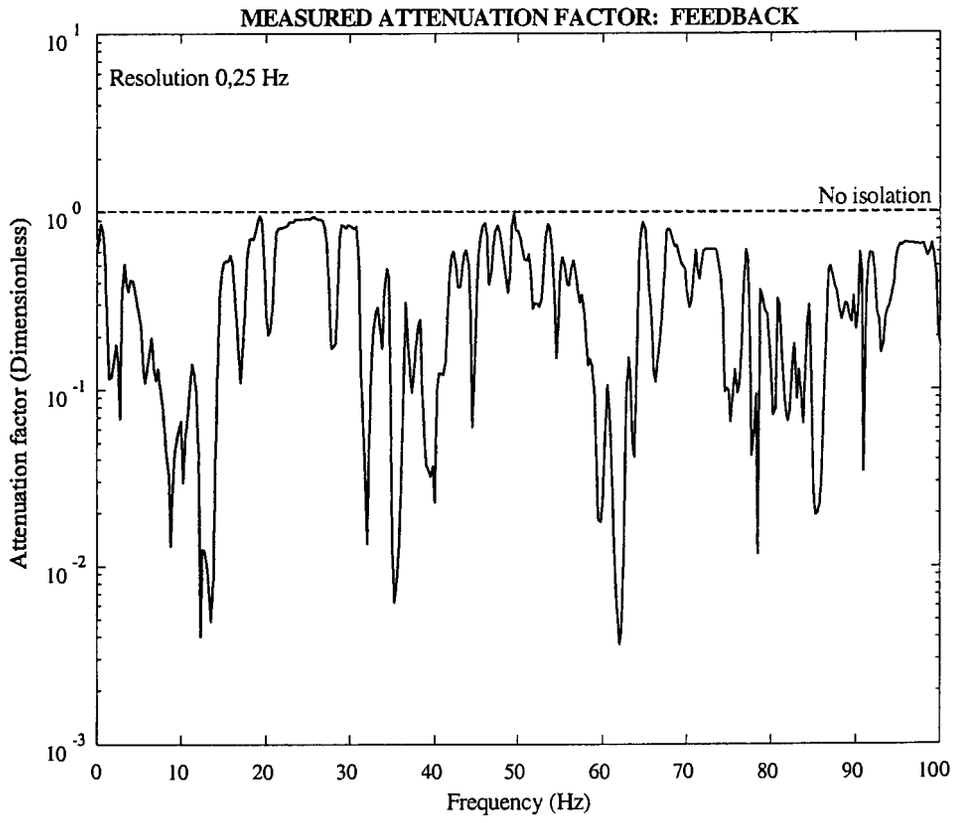

Figure 6.7.2.2: Attenuation factor spectrum for output feedback controller

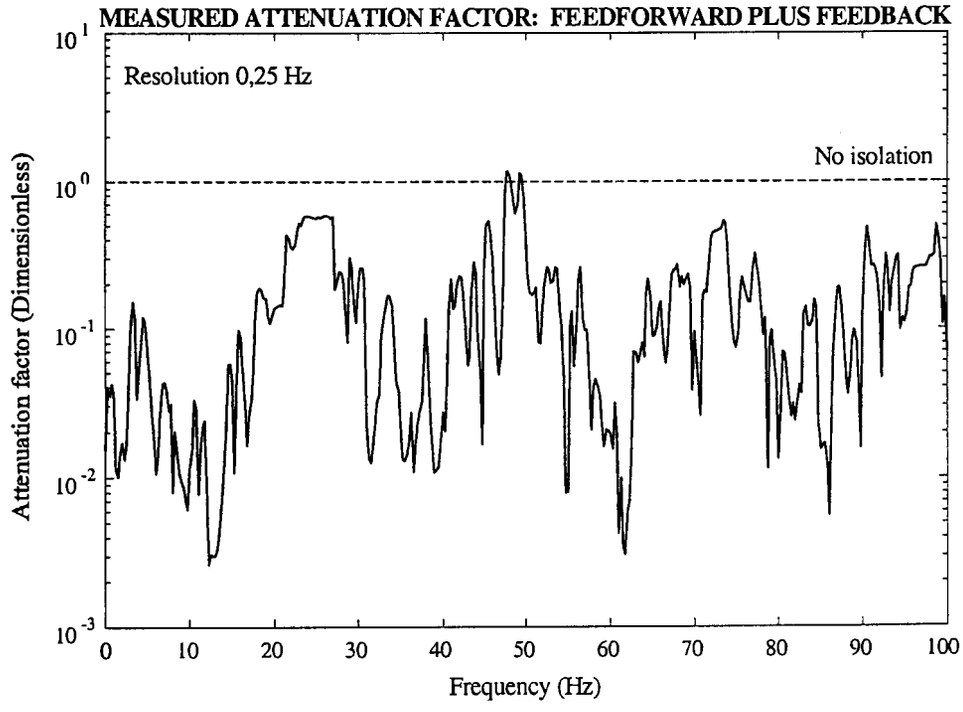

Figure 6.7.2.3: Attenuation factor spectrum for disturbance feedfoward plus output feedback controller

Table 6.7.2.1: Summary of controller test results

Configuration:	Feedforward	Feedback	Feedforward plus feedback
RMS attenuation	0,44	0,70	0,32
Attenuation in dB	-7,06 dB	-3,1 dB	-9,75 dB
Isolation	0,56	0,3	0,68
Target isolation	0,85	0,85	0,85
% of target achieved	66%	35%	80%
dB attenuation at 24 Hz	-3,41	-0,75	-4,73
dB attenuation at 48,5 Hz	3,38	-7,47	-2,58
dB attenuation at 72,5 Hz	-1,11	-4,11	-6,82
dB attenuation at 96,75 Hz *	-10,08	-3,55	-11,66

* Dominant disturbance frequency

A comparison between modelled and experimental transmissibilities of the three controller configurations, at the frequencies where the disturbance peaks (24 Hz, 48,5 Hz, 72,5 Hz and 96,75 Hz) is given in table 6.7.2.2. The tranmissibilities compare favourably at 72,5 Hz for the feedback controller and at 24 Hz for the feedforward plus feedback controller. At the dominant disturbance frequency, i.e. 96,75 Hz, the difference varies from 13,7 % for the feedback controller, to 28,7% for the feedforward controller. The difference is large at 48,5 Hz for all the controllers, and at 72 Hz for the feedforward and feedforward-plus-feedback controllers. Measured and modelled overall attenuations differ by 13,6% for the feedforward controller, -11,4% for the feedback controller and -3,12% for the feedforward plus feedback controller.

Table 6.7.2.2: Comparison between measured and modelled TR's at disturbance peaks

Frequency (Hz):		24	48,5	72,5	96,75#	Overall (RMS)
Feedfoward	Measured (dB):	-3,41	3,38	-1,11	-10,08	0,44
	Modelled (dB):	-2,06	-3,29	-4,53	-7,89	0,5
	***Difference (%):**	**16,8**	**-53,6**	**-32,5**	**28,7**	**13,6**
Feedback	Measured (dB):	-0,75	-7,47	-4,11	-3,55	0,7
	Modelled (dB):	-1,76	-3,31	-4,19	-4,83	0,62
	***Difference (%):**	**-10,99**	**61,44**	**-0,92**	**-13,7**	**-11,4**
Feedforward plus feedback	Measured (dB):	-4,73	-2,58	-6,82	-11,66	0,32
	Modelled (dB):	-5,13	-10,06	-12,65	-13,62	0,31
	***Difference (%):**	**-4,5**	**-57,73**	**-48,89**	**-20,2**	**-3,12**

* Relative to measured transmissibility # Dominant disturbance frequency

Experimental and modelled transmissibilities over the entire disturbance band, for the three controller configurations, are compared in figures 6.7.2.4 to 6.7.2.6. The circles and crosses respectively indicate the measured and modelled transmissibilities at the frequencies where the disturbance peaks. Modelled and measured transmissibilities differ considerably between

peaks, which can be attributed to low signal-to-noise ratios (the disturbance is approximately two orders of magnitude lower between the peaks than at the peaks – see figure 6.6.1.3).

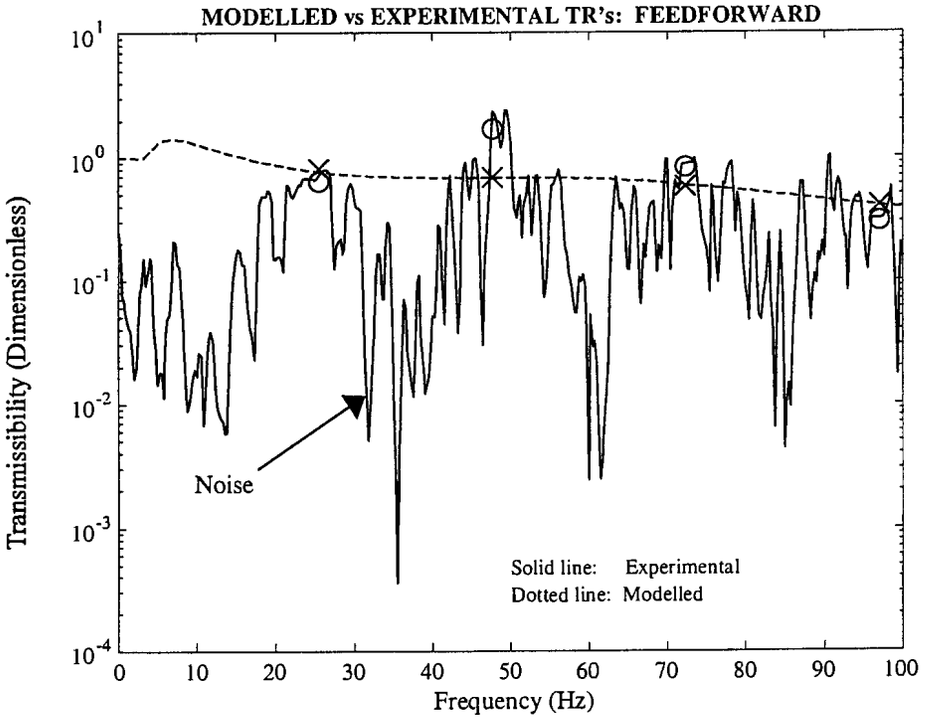

Figure 6.7.2.4: Modelled and measured TR's: Feedforward

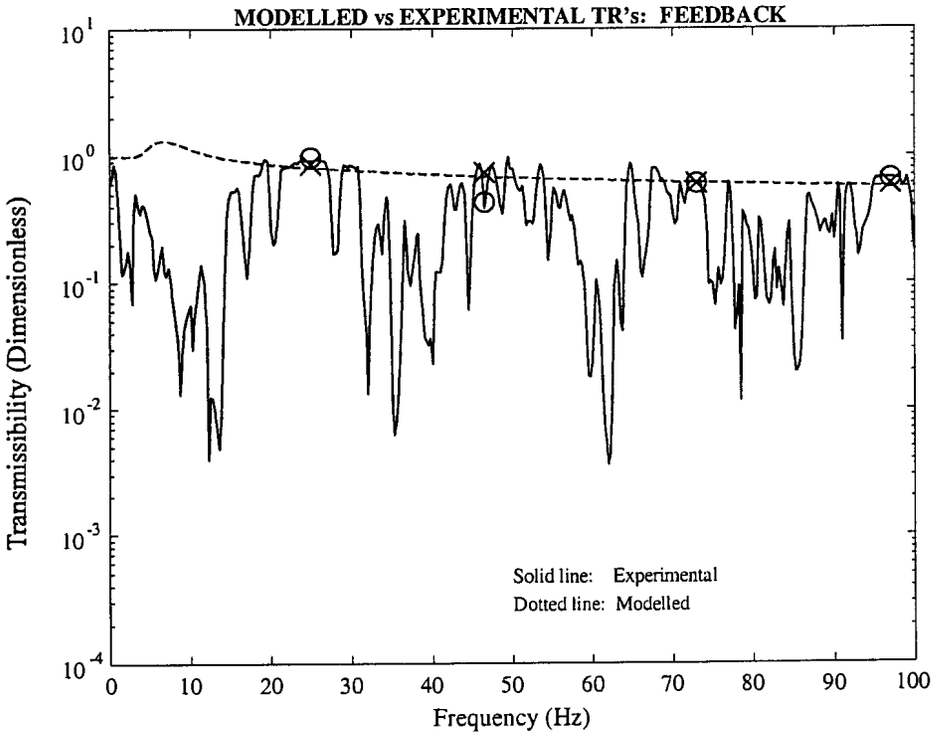

Figure 6.7.2.5: Modelled and measured TR's: Feedback

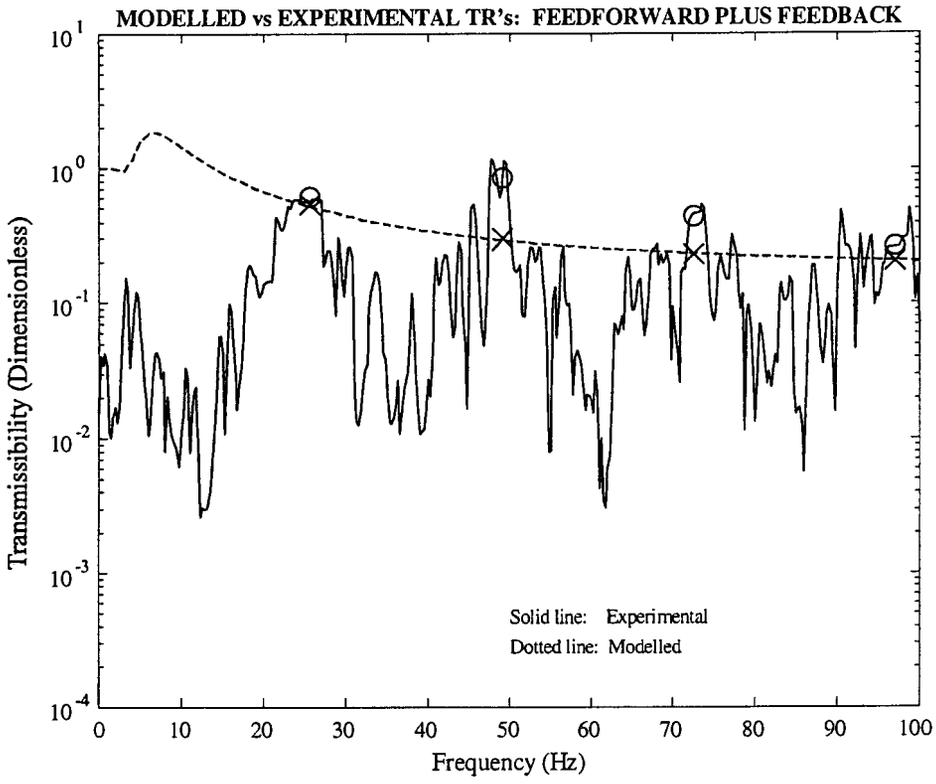

Figure 6.7.2.6: Modelled and measured TR's: Feedforward plus feedback

6.7.3 Discussion of test results

A comparison of the attenuation factor graphs and table 6.7.2.1 show that the best attenuation accross the frequency spectrum is achieved with the disturbance feedforward plus output feedback controller. The RMS attenuation factor achieved with this controller is 80% of the required RMS attenuation. The feedforward controller is ranked second, in terms of RMS attenuation, while the feedback controller is ranked last.

All three controllers display weak performance at 48,5 Hz, which is close to the frequency of the electricity supply network, i.e. 50 Hz. The feedback controller gives the best attenuation at 48,5 Hz, while the feedforward controller amplifies the disturbance. The disturbance feedforward plus output feedback controller attenuates at this frequency, but amplifies slightly in the vicinity of 50 Hz.

A logical choice of the best controller, in terms of overall performance, is the disturbance feedforward plus output feedback controller. Although it slightly amplifies the disturbance at 48,5 Hz, its performance across the rest of the frequency band is acceptable. Furthermore, it is doubtful if the problem at 48,5 Hz will ever be experienced on a vehicle, where the frequency of the power supply varies with engine speed.

Possible reasons for the differences between modelled and experimental results are as follows: Firstly, controller design was based on measured open-loop transfer functions, obtained using a white-noise drive signal, LP-filtered at 130 Hz (see section 4.4.5). This signal did not correspond with the closed-loop drive signal. Secondly, due to the LP filter, open-loop drive signal magnitude above 130 Hz decreased with frequency, resulting in a noisy signal and possibly an inaccurate transfer function magnitude at the dominant plant natural frequency, i.e. 301 Hz. Thirdly, the differences at 47,5 Hz are attributed to (unsuppressed) noise caused by the electricity supply network. Lastly, while feedforward and feedback gains of unity could be achieved during the modelling stage (see section 6.4.4), this was not possible during experimental testing, possibly due to plant nonlinearities.

To summarize, a stable, linear disturbance feedforward plus output feedback controller was tested, which gave an RMS attenuaton of 80% of the target attenuation, in a frequency band of 0 Hz to 100 Hz.

6.8 Summary of chapter 6

The design, implementation and experimental evaluation of a controller for the LOS stabilization system were described in this chapter. A background on various basic controller types was given, followed by a more detailed description of disturbance attenuation methods.

The design of a suitable controller was described in detail. General requirements of controllers were discussed, followed by a specification of the controller performance. The requirements and specification were used to select a suitable controller, i.e. a linear disturbance feedforward plus output feedback regulator, with output integral feedback.

A linear quadratic optimal regulator was subsequently designed. Robustness of the regulator was improved by increasing the lowest natural frequency and damping factors of the attenuation factor zeroes. A suboptimal controller was thus obtained. An optimal state regulator was designed next. The regulator was coupled to the plant and controller. The disturbance-to-control and output-to-control *TF*'s were determined. Zero elements in the observer gain matrix were replaced by nonzero elements. The resulting suboptimal observer was coupled to the plant and suboptimal controller. The integral feedback gain was determined with the aid of simulations of the closed-loop system behaviour. The integrator gain which produced the minimum attenuation factor, was thereby obtained. The disturbance to control and output to control *TF*'s were converted to digital filter form. An "equivalent" digital filter was designed to replace the output feedback integrator.

The control apparatus and test procedure were described. Three configurations of the controller were tested, i.e. disturbance feedforward, output feedback, and disturbance feedforward plus output feedback. The test results were processed and presented. It was found that the disturbance feedforward plus output feedback controller gave the best overall performance in terms of RMS attenuation over the frequency band of 0 Hz to 100 Hz. The controller achieved an RMS attenuation of -9,75 dB in this frequency band. A weak point of the controller is the fact that it does not perform well in the vicinity of 50 Hz, which may be attributed to the electricity supply.

Chapter 7
Summary, conclusions and recommendations

This study covered the line of sight stabilization of an optical instrument by means of gained magnetostrictive actuators. The stabilization system was modelled, designed, manufactured and tested. Modelled and experimental results were compared and inaccuracies of the model were discussed and explained. The model was updated, using the experimental results. A control system was modelled, designed, implemented and tested.

This chapter gives a summary of the work done, conclusions that can be drawn from the results and contributions made by the study, problems encountered and recommendations for future work in the field. The summary is given in section 7.1. Conclusions and contributions are discussed in section 7.2, followed by the problems experienced, in section 7.3. Finally, recommendations for future study are made in section 7.4.

7.1 Summary

Magnetostrictive active LOS stabilization of an optical instrument, excited by a known base disturbance, was motivated in chapter 1. The differences between passive and active isolation methods were discussed and the advantages of active isolation were given. Different actuation methods, i.e. hydraulic, electrodynamic, piezoelectric and magnetostrictive actuation, were compared. Magnetostrictive actuation was selected as the most appropriate isolation method for this study. The cost advantage of magnetostrictive actuators over conventional stabilization devices, e.g. gyroscopes, was pointed out. The limitation of magnetostrictive active isolation, i.e. that a gain mechanism would be required to enhance actuator stroke length, was mentioned. A literature survey of the theory and applications of magnetostriction, and the "giant" magnetostrictive material Terfenol-D, was given.

An analytical model of the magnetostrictive active isolation system was derived in chapter 2. Material characteristics, as obtained from the literature, were used for this purpose. The model would firstly serve as a design aid, and secondly, as a theoretical basis to obtain an accurate, updated model from experimentally determined transfer functions.

The nonlinear and linear magnetostrictive and magnetization characteristics of Terfenol-D were discussed. Strain was modelled as a function of applied mechanical stress and magnetic field strength. Special attention was paid to the two most important nonlinearities, i.e. saturation and hysteresis. The nonlinearities were modelled as range-dependent linearities, in order to facilitate system characterization.

A nonlinear state-space model of a magnetostrictive actuator was derived. The model consisted of an SDOF (2^{nd} order) mechanical subsystem model, coupled to a 1^{st} order electrical coil model. The actuator model was subsequently linearized and coupled to an MDOF structural model of the optical instrument and its support structure. For this purpose, a number of system modelling techniques were evaluated, i.e. the Galerkin, Finite Element, Finite Difference and Rayleigh-Ritz methods. The latter method was selected as the most

suitable modelling technique. The system model was obtained in state-space and transfer function forms. System natural frequencies, normal mode shapes, damping factors, frequency bandwidth and modal forces were obtained from the model.

System design was described in chapter 3. The required system performance parameters, i.e. actuator stroke length and force, system bandwidth and coil resistance to inductance ratio, were calculated from the results obtained in chapter 2. Design concepts for the system components were discussed and evaluated and the most suitable design concepts were selected. An octagonal flexural gain mechanism was selected in favour of resonance spring, hydraulic and elliptical structure mechanisms. Electrodynamic field biasing was considered to be more suitable than permanent magnet biasing, while coil springs were selected in favour of Belleville washers for rod prestressing. Actuator and system concepts were presented.

A detailed system design followed. The required rod lengths, rod diameters and gain factors were calculated and practical design aspects were discussed. The gain mechanisms, field coils, prestress springs and support structure were designed. Detailed drawings of the system components and an assembly drawing of the system, were included. Static and dynamic buckling of the rods, as well as eddy current losses, were checked. The manufacturing procedure was described in short.

Experimental testing of the actuators and LOS stabilization system was dicsussed in chapter 4. The objective of the tests was to obtain quasi-static and dynamic system characteristics. A summary of the most important technical details of the test specimens, i.e. the two actuators and system, was given. These details were required to develop a test procedure and to specify the test equipment.

Two test setups were described, i.e. one for quasi-static characterization of the actuators, and one for dynamic characterization of the system. The quasi-static tests served two purposes, i.e. to ascertain that the actuator stroke lenghts would be sufficient to reject the disturbance, and to determine the most suitable bias voltage for the dynamic tests. The quasi-static test equipment was described in short. The tests were designed and executed and the results were processed. An iterative procedure was followed to obtain the required rod prestress. Graphs of deflection versus coil voltage were obtained for the two actuators. The most suitable bias voltage was calculated.

Different types of dynamic test signals were evaluated and compared and the appropriate signal type was selected. Two dynamic test setups, i.e. and "ideal" and an "available" setup were presented. The latter was chosen by necessity. The tests were designed and executed and the results were processed. The coil voltage to angular acceleration transfer function of the system, for a frequency bandwidth of 0 Hz to 500 Hz, was obtained. It was shown that the modelled results given in chapter 2, differed significantly form the experimentally determined results. Possible reasons for the differences were given and updating of the model was motivated.

Chapter 5 was devoted to updating the model. Identification theory was discussed in short and the most suitable identification technique, i.e. linear, frequency domain identification, was selected and described. An accurate nonparametric transfer function model was identified from the experimentally determined results. The model was adequate for control purposes,

but failed to provide insight into the system dynamic characteristics. To overcome this limitation, a parametric model was derived.

Parametric modelling was facilitated by separating the electrical and mechanical subsystem models. A 3rd order coil model was obtained in state-space and transfer function forms. A mechanical subsystem model, consisting of two 2DOF actuator models, an MDOF model for the optical instrument and support structure, and an SDOF model for the elastically mounted base, was subsequently derived.

The 2DOF actuator models differed from the original SDOF models derived in chapter 2, while the original MDOF model of the optical instrument, was retained. The actuator, base and instrument models were coupled by means of the component mode synthesis method. The mechanical subsystem model was subsequently written in state-space form and coupled to the coil model. The updated system state-space model was converted to transfer function form. The transfer function magnitude and phase spectra of this model compared favourably with the experimentally determined spectra. System natural frequencies, normal mode shapes, damping factors, frequency bandwidth, modal forces and open-loop transmissibility were obtained.

Chapter 6 described the analysis, modelling, simulation, design and experimental evaluation of the control system. General control theory was given as a background. Various controller types, i.e. feedforward, output and state feedback feedback controllers, linear and nonlinear controllers, tracking controllers, regulators and optimal controllers, were discussed in short.

Principles of disturbance attenuation were discussed in more detail. The attenuation factor was defined and the nature of the disturbance was discussed. Requirements for disturbance and noise attenuation were given. An attenuation method for a known disturbance entering a system at a given point, was described. A short summary of optimal control, in terms of H_2 and H_∞ optimal criteria, was given. Other modern disturbance attenuation techniques, such as preshaping of command inputs, attenuation of a continuous disturbance by means of digital regulation, and "two-way" isolation, were discussed. Motion controllers, i.e. relative and absolute motion controllers, were described in detail.

Control system design specifications were given, followed by a discussion of general control system requirements, such as accuracy, stability, sensitivity, reaction speed, control effort, robustness, observability and controllability. The specifications and general requirements were used to select a suitable controller type. A linear, disturbance feedforward plus output feedback controller, with output integral feedback, was selected. The control system design procedure was described and a detailed exposition of the controller design was given. The design of a suboptimal controller, coupled to a suboptimal observer, was described. The controller and observer designs were derived from optimal controller and observer designs. Controller characteristics were expressed in terms of state-space parameters, transfer functions, and closed-loop poles and zeroes. In order to facilitate implementation of the controller, the controller transfer functions were converted to digital filter form.

The test apparatus, test procedure and execution were described. Three controller configurations, i.e. disturbance feedforward, output feedback and feedforward plus feedback configurations, were tested. Test data was processed and the test results were presented and discussed. The attenuation factor spectra were shown graphically and RMS attenuation factors were given. It was shown that the linear disturbance feedforward plus output feedback

controller, with output integral feedback, could achieve 80% of the target attenuation in a disturbance band of 0 Hz to 100 Hz.

7.2 Contributions and conclusions

Firstly, it is possible to stabilize the line of sight of the given optical instrument, over a disturbance frequency bandwidth of 0 to 100 Hz, using gained magnetostrictive actuators. This result shows that magnetostrictive stabilization is a feasible alternative to the more expensive gyroscopic systems normally used for LOS stabilization. Due to the relatively large magnetostrictive strains of 1400 $\mu\varepsilon$ obtainable with Terfenol-D rods, a relatively small displacement gain of 2,7 was sufficient to produce the required actuator stroke length of 75 μm. By comparison, piezoelectric materials, with maximum strains of 200 $\mu\varepsilon$, would require significantly larger gain factors. This, in turn, would result in excessive gain mechanism stresses and an insufficient isolation frequency bandwidth.

Due to the low frequency response of the magnetostrictive LOS stabilization system (as low as 0 Hz), it is superior to electrodynamic systems for low frequency isolation. On the other side of the frequency scale, the high frequency response of the magnetostrictive system (well in excess of 100 Hz – see figure 5.6.7), makes it more suitable than hydraulic isolation for this application. A practical consequence is that hydraulic pumps and valves are eliminated, with an accompanying reduction in maintenance cost.

Secondly, an updated model, based on experimental system identification, must be employed. Since the theoretical model is too inaccurate for controller design purposes (figure 4.5.4.3), it should be combined with the updated model to compose an accurate plant system representation for control design.

Model updating is facilitated by separately modelling the mechanical and electrical subsystems. The mechanical subsystem model, consisting of simple linear lumped mass and stiffness actuator models, coupled to the original distributed optical instrument model, can be obtained using component mode synthesis (section 5.5). The system state-space and transfer function model, which couples the updated mechanical subsystem model to the coil model (section 5.6), gives physically interpretable characteristics, i.e. normal mode shapes, natural frequencies, damping factors and forces, coil DC resistance, voltage to current transfer function and -3dB cutoff frequency. Compared with the experimentally-determined transfer function, the updated model is sufficiently accurate for control design (figure 5.6.4).

Thirdly, reasonable attenuation can be achieved with a linear regulator, in spite of the highly nonlinear saturation and hysteresis characteristics of Terfenol-D. The controller, which consists of a suboptimal disturbance feedforward plus output feedback regulator, with output integral feedback to improve robustness, can be designed using linear state control theory (see section 6.4.4). The tedious work required to construct input-versus-state functions, to linearize and stabilize nonlinear state feedback controllers, is thus eliminated, thereby significantly simplifying controller design. In addition, the regulator employed in this study is relatively easily implemented digitally and can be run on a commercial DSP, using standard Simulink block diagram elements (figures 6.4.4.1 and 6.6.2.1).

In the fourth place, it was experimentally shown (table 6.7.2.1) that the magnetostrictive active LOS stabilization system developed in this study, achieves an attenuation of -9,75 dB, i.e. 80% of the target isolation, in a frequency band of 0 Hz to 100 Hz. This is an indication of the effectiveness of the system.

Lastly, a theoretical model, though inaccurate, can be derived from first principles, to serve as an input to actuator design. The lumped mass and stiffness models of the actuators, coil resistance and inductance equations derived in chapter 2, are a useful design aid. The model makes it possible to calculate the required Terfenol-D rod length and diameter, displacement gain factor, actuator stroke length, rod prestress, number of coil windings, coil resistance to inductance ratio and system isolation frequency bandwidth.

As a final comment: The LOS stabilization system was specifically developed to isolate a lightweight video camera with a mass of 1 kg and length of 250 mm, against a random base disturbance with a frequency bandwidth of 0 to 100 Hz, encountered on a military tank. The given disturbance spectrum (figure 1.1.3) is unique to tracked vehicles and will normally not be encountered in other vehicle types.

Alternative applications of the LOS stabilization system are not the topic of discussion in this thesis. However, extensions to the application are possible under certain circumstances, provided the system bandwidth of 199 Hz and actuator stroke of 75 μm are not exceeded. Applications which may require alterations to the plant and controller, are as follows: An increase in instrument length, for example, will necessitate actuators with longer stroke lengths, since the angular displacement of the isolation system will decrease. If the disturbance frequency spectrum deviates from that of the given disturbance, the controller may have to be redesigned. A change in instrument mass will change the system natural frequencies and isolation bandwidth, but small increases in mass will not decrease the bandwidth to below 100 Hz. Pole and zero shifts due to mass changes must necessarily be accounted for in the control design.

7.3 Problems encountered

A number of problems were experienced in this study. In the first place, design of the gain mechanisms proved problematic and a "worse-than-average" solution had to be accepted. Secondly, the measured -3dB coil cutoff frequency was lower than the required frequency (84 Hz versus 100 Hz). Lastly, an additional personal computer and signal processing board had to be acquired to generate the base motion. These problems are discussed in more detail below.

Design of octagonal gain mechanisms

The octagonal gain mechanisms used in the actuators, are supplied with notched flexures in the corners, in order to allow translational deflection (see figure 3.4.1.5). Although the flexures are sufficiently soft to allow translational deflection, they are too soft to prevent rotational deflection. If the normal mode shapes of a single actuator, in the absence of the optical instrument and other actuator, are analyzed, it is found that the first normal mode

shape is an undesirable rocking mode. (The actuator normal mode shapes were not discussed in this study). Rocking modes place the Terfenol-D rods under fluctuating bending moments, which can cause breakages.

An alternative gain mechanism, with slotted flexures, instead of notched flexures, was originally considered in this study. The mechanism prevents rocking motion and only allows translational motion. A quarter model of the gain mechanism is shown in figure 7.3.1. The forces and bending moment acting on the mechanism, are indicated.

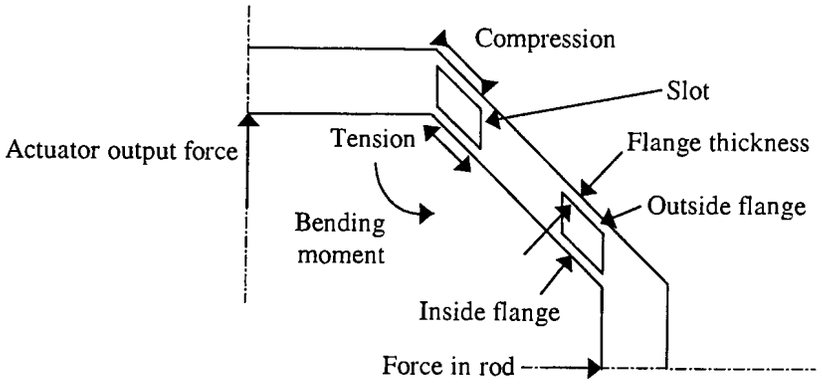

Figure 7.3.1: Quarter model of gain mechanism with slotted flexures

The bending moment causes a tensile force in the inside flange of the flexure and a compressive force in the outside flange. During evaluation of the design concepts, a finite element analysis revealed that the compressive force in the outside flange would exceed the critical buckling force. An effort was made to increase the critical buckling force, by increasing flange thickness and by decreasing flange length, while maintaining the required bending stiffness. Unfortunately, the efforts were unsuccessful and the concept was shelved.

Coil design

One of the design objectives was to obtain a coil with a –3dB cutoff frequency of more than 100 Hz, that could be matched to amplifiers with often-used input impedances of 4 Ω or 8 Ω (see section 3.5.2). The design was based on magnetostrictive and magnetization characteristics of Terfenol-D, as published in the literature. In order to allow a margin of error in the design, the target cutoff frequency was set at 150 Hz, which exceeded the required frequency by 50%.

Initially, a coil with an 8 Ω impedance was selected in favour of a 4 Ω coil, since this measure would make it easier to obtain a sufficiently high cutoff frequency. The higher impedance could be obtained in two ways, i.e. by means of a longer wire, or by means of a wire with a smaller diameter. The longer wire was preferred, since the thinner wire would be too fragile.

The resulting coil was however too heavy and didn't produce the minimum required cutoff frequency of 100 Hz. (The design of the 8 Ω coil is not included in this study).

In order to obtain a lighter coil, with a relatively strong wire, and which could be matched to the available amplifier, it was decided to design an entirely new coil with a 4 Ω impedance, at the cutoff frequency of 100 Hz. The lower impedance was achieved with a shorter and thinner wire, resulting in a significantly smaller and lighter coil. The design of the coil was explained in detail in section 3.5.2.

Experimental identification of the system revealed that the coil cutoff frequency was 84 Hz (see section 5.4.2). This frequency differed from the design cutoff frequency of 150 Hz and the minimum required cutoff frequency of 100 Hz. The differences were attributed to differences between the modelled and true Terfenol-D characteristics. It was mentioned in section 2.7.3 that especially hysteresis characteristics would be difficult to model. The initial hysteresis model was derived from published quasi-static magnetostrictive and magnetization characteristics (see section 2.3), while experimental characterization of the actuators and optical instrument was done dynamically (see section 4.4).

However, although the coil –3dB bandwidth was lower than 100 Hz, the system –3dB bandwidth was sufficient (see section 5.6). The low-pass filtering effect of the coil was to a certain extent cancelled by the mechanical characteristics of the system, due to resonance at frequencies above the disturbance band (see also figure 5.6.7).

Excitation of base motion

Excitation of the disturbance required an additional personal computer and signal processing board (see section 6.6). A more convenient solution would be to generate the signal digitally, e.g. on a computer with signal generation software and D/A converters (as in section 4.3.2), record the signal with an analogue data recorder and save it on a magnetic tape. During controller tests, the base could be excited by playing back the recorded signal through a power amplifier, and by supplying it to the electrodynamic shaker. The suggested procedure is schematically shown in figure 7.3.2.

The abovementioned setup would make it possible to repeat controller tests as many times as required without the need of an additional computer or signal processing board. Unfortunately, a data tape recorder was not available for this purpose.

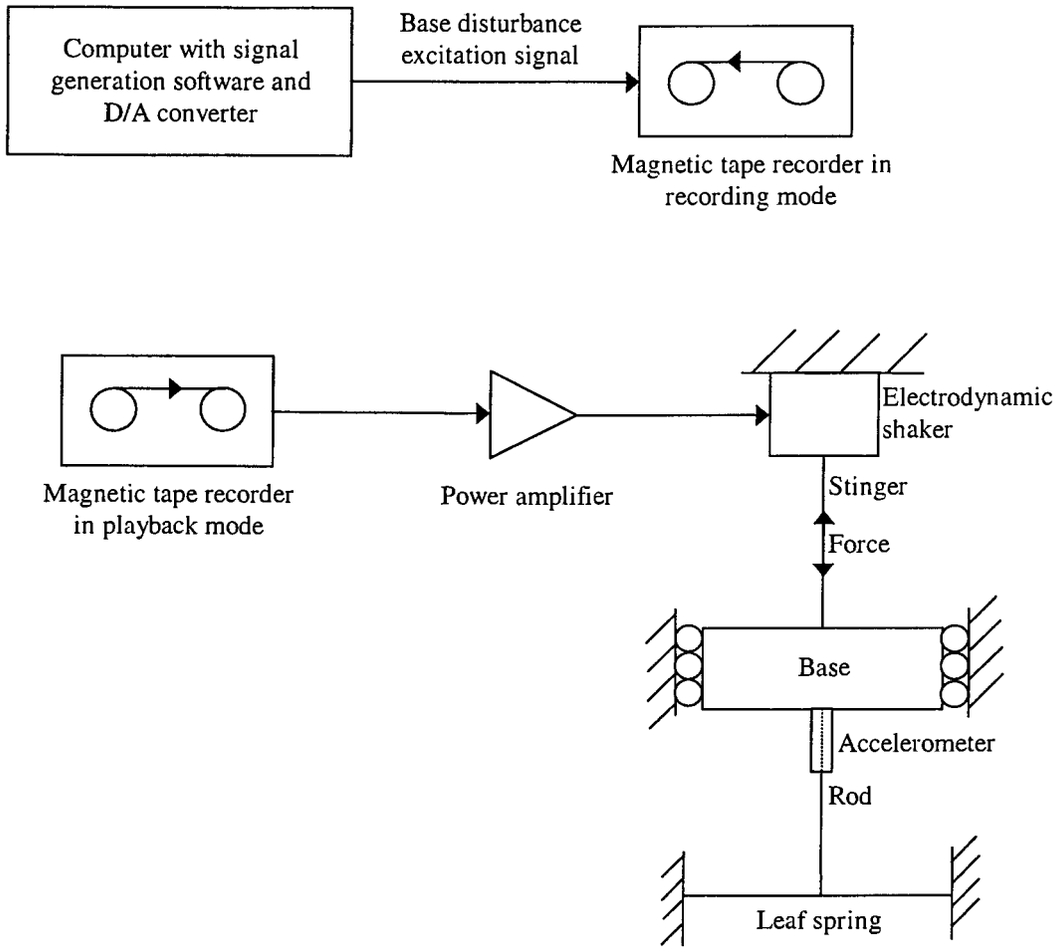

Figure 7.3.2: Suggested disturbance excitation procedure

7.4 Recommendations for future work

A number of recommendations can be made for future work in the field. Firstly, excitation of the optical instrument with both actuators, instead of one, should be considered. This would make it possible to obtain the required output angular acceleration, when exciting the system with the full base angular acceleration.

Secondly, simultaneous translational and rotational isolation of the instrument would both stabilize the line of sight, and isolate the instrument against vertical vibrations that could damage the instrument. In the third place, optimization of the plant and controller during the design phase would make it possible to obtain the optimal plant parameters, before manufacture. Parameters which could be optimized, include, inter alia, plant mechanical and electrical characteristics, sensor types and positions, control inputs and plant outputs.

In the fourth place, more powerful control methods, such as two-way isolation and nonlinear control, could be implemented. A fifth recommendation is to apply permanent magnet biasing, instead of electrodynamic baising. This measure would significantly reduce coil input power

and would eliminate the need for additional biasing signals. A last recommendation is to do away with the mechanical biasing springs altogether and to adjust prestress in the Terfenol-D rods by means of the prestress bolts.